INTERNATIONAL ATOMIC ENERGY AGENCY

INDC(BLR)-017
Distr. J+TU/EL

I N D C INTERNATIONAL NUCLEAR DATA COMMITTEE

Neutron Data Evaluation of ^{234}U

V.M. Maslov[1], Yu.V. Porodzinskij[1], N.A. Tetereva[1]
A.B. Kagalenko[1*], N.V. Kornilov[1*]
M. Baba[2], A. Hasegawa[3]

[1]) Joint Institute of Nuclear and Energy Research – SOSNY
220109, Minsk-Sosny, Belarus

[2]) Cyclotron and Radioisotope Center, Tohoku University,
Sendai, Japan

[3]) Department of Nuclear Energy System, Tokai Research
Establishment, Japan Atomic Energy Research Institute,
Tokai-mura, Naka-gun, Ibaraki-ken

*) Permanent address: Institute of Physics and Power Engineering,
249020, Obninsk, Russia

March 2003

Documents in the EL series are available in only limited quantities in hardcopy form. They may be downloaded in electronic form from http://www-nds.iaea.or.at/indc_sel.html or sent as an e-mail attachment. Requests for hardcopy or e-mail transmittal should be directed to services@iaeand.iaea.org or to:

Nuclear Data Section
International Atomic Energy Agency
PO Box 100
Wagramer Strasse 5
A-1400 Vienna
Austria

Produced by the IAEA in Austria
March 2003

INDC(BLR)-017
Distr. J+TU/EL

Neutron Data Evaluation of ^{234}U

V.M. Maslov[1], Yu.V. Porodzinskij[1], N.A. Tetereva[1]
A.B. Kagalenko[1*], N.V. Kornilov[1*]
M. Baba[2], A. Hasegawa[3]

[1]) Joint Institute of Nuclear and Energy Research – SOSNY
220109, Minsk-Sosny, Belarus
[2]) Cyclotron and Radioisotope Center, Tohoku University,
Sendai, Japan
[3]) Department of Nuclear Energy System, Tokai Research
Establishment, Japan Atomic Energy Research Institute,
Tokai-mura, Naka-gun, Ibaraki-ken

*) Permanent address: Institute of Physics and Power Engineering,
249020, Obninsk, Russia

Abstract

Consistent evaluation of ^{234}U measured data base is performed. Hauser-Feshbach-Moldauer theory, coupled channel model and double-humped fission barrier model are employed. Total, differential scattering, fission and (n,*x*n) data are calculated, using fission cross section data description as a major constraint. The direct excitation of ground state and higher band levels is calculated within rigid rotator and soft (deformable) rotator model, respectively. Average resonance parameters are provided, which reproduce evaluated cross sections in the range of 1.5 – 140 keV.

This work is performed under the Project Agreement B-404 with the International Science and Technology Center (Moscow). The Financing Party for the Project is Japan.

March 2003

Contents

1 Introduction

Uranium-234 can initiate ^{232}U production in uranium- and uranium-thorium-fueled nuclear reactors by high-energy neutrons in (n,3n) reactions and in neutron capture reactions after α– decay. It turns out that fission data description maintains almost the only constraint for ^{234}U capture, neutron elastic and inelastic scattering, (n,2n), (n,3n) and secondary neutron spectra evaluation. Current approach was validated recently in case of ^{238}U and ^{232}Th neutron data description [1, 2, 3].

2 Resolved resonance energy range

Here we will briefly review the status of resolved neutron resonance parameters of ^{234}U. Resolved resonance region of ENDF/B-VI [4] data file extends up to 1.5 keV. Resolved resonance parameters are adopted from BNL-325 [5], resolved resonance parameters are assumed to be multi-level Breit-Wigner parameters. Thermal capture and fission cross sections are equal to 0.464 barns and 103.034 barns and are compatible with BNL-325 estimates (see Table 1). Region of resolved resonances in JENDL-3.2 [6] also extends up to 1.5 keV. Parameters recommended by James et al. [7] are modified for the lower value of average radiative width $\langle\Gamma_\gamma\rangle$ = 26 meV. A bound level was added at E_r =-2.06 eV to reproduce thermal total, elastic and capture cross section of BNL-325 [5].

In present evaluation basically resonance parameters of JENDL-3.2 [6] are adopted, fission width of bound resonance is varied to fit recent thermal fission cross section by Wagemans et al. [8] of 67±14 mbarn. This value was derived after revision of previous value of 300±20 mbarn by Wagemans et al. [9], using corrected mass of the ^{234}U sample, as well as corrected mass of ^{235}U impurity in the sample. The revised value is in agreement with the value of 100±70 mbarn, reported by Borzakov et al. [10]. Figures 1 demonstrates a comparison of evaluated fission cross sections around thermal point energy. Calculated thermal cross section and resonance integral values are compared in Table 1.

The resonance parameters by James et al. [7], basically accepted in present data file of ^{234}U, might provide a test of neutron width and resonance spacing distributions. We performed a resonance parameter analysis based on maximum likelihood estimates [11] both of mean level spacing $\langle D_{l=0}\rangle$ and neutron strength function S_o. Correction for the missing of levels based on simultaneous analysis of level spacing distribution and neutron width distribution gives estimates of average $s-$wave neutron resonance spacing $\langle D_{l=0}\rangle$ =11.4±0.55 eV and strength function estimate $S_o = (0.96\pm0.13)\times10^{-4}$. This estimate is lower than that of Reference Input Parameter Library File [12] ($\langle D_{l=0}\rangle$ =12±0.8 eV), but higher than $\langle D_{l=0}\rangle$ =10.6 eV, adopted in JENDL-3.2 [6] and ENDF/B-VI [4] data files. The latter estimate is accepted following the analysis of missing of weak levels by

James et al. [7]. They assumed missing of ~ 23 levels up to 1500 eV based on the share of levels with $\Gamma_n^o \leqslant 0.02$ meV. Cumulative sum of $s-$resonances up to 1.5 keV is shown on Fig. 2, it seems resonance missing starts above $\sim$250 eV, within our approach missing of ~ 18 levels is anticipated at 1.5 keV. Cumulative sum of reduced neutron widths of $s-$resonances Γ_n^o is described with present strength function estimate of $S_o = (0.96 \pm 0.13) \times 10^{-4}$ on Fig. 3.

The resolution function parameters as well as $\langle \Gamma_n^o \rangle$ and $\langle D_{l=0} \rangle$ are obtained by maximum likelihood method when comparing experimental distributions of reduced neutron width and resonance spacing with Porter-Thomas and Wigner distributions, modified for the resonance missing. The latter distributions will be called expected distributions. Figures 4 and 5 demonstrate the comparison of predicted level spacing $D_{l=0}$ and reduced neutron width Γ_n^o distributions with present resonance parameter set. Quantiles on Fig. 4 show eight equal probability intervals ($P(x \leq x_{0.125} = \int p(x)dx = 0.125)$ for expected level spacing distribution of $s-$wave resonances $D_{l=0}$. Expected level spacing distribution, which takes into account missing of weak resonances and unresolved doublets, is compatible with experimental distribution. Expected distribution is qualitatively similar to Wigner distribution. However, one may notice that expected distribution would correspond to Wigner distribution with value of $\langle D_{l=0} \rangle$ higher by $\sim$15%, in other words that leads to the $\sim$15% difference of mean values of distributions. In case of using pure Wigner distribution with $\langle \widetilde{D}_{l=0} \rangle \sim 1.15 \langle D_{l=0} \rangle$, there would be predicted no missing of resonances up to $\sim$1.5 keV and $\langle D_{l=0} \rangle$ value would be overestimated.

Table 1

Thermal cross sections and resonance integrals

Reaction	σ^{th},barns	RI	σ^{th},barns	RI	σ^{th},barns	RI	σ^{th},barns	RI
	Present		JENDL-3.2 [6]		ENDF/B-VI [4]		BNL-325 [5]	
Total	119.23	-	119.2	-	115.799		119.1±1.3	
Elastic	19.409	-	19.41		12.301		19.6±1.0	
Fission	0.06696	6.637	0.00622	6.72	0.464	6.542	<0.65	6.5
Capture	99.75	631.98	99.75	632	103.034	660.619	99.8±1.3	660±70

Quantiles on Fig. 5 show six equal probability ($P(x \leq x_{0.125} = \int p(x)dx = 0.167)$ intervals for Γ_n^o expected distribution. It demonstrates that reduced neutron width distribution with account of missing is compatible with observed distribution also in the range of small reduced neutron width values. Experimental width distribution, when plotted in quantiles of pure Porter-Thomas distribution, would be much different from the latter distribution the range of $\Gamma_n^o \lesssim 0.05 \langle \Gamma_n^o \rangle$.

Figure 6 shows a comparison of experimental distribution of reduced neutron widths with cumulative Porter-Thomas distribution of reduced neutron widths

with (expected distribution) and without resonance missing correction. Cumulative Porter-Thomas distribution of reduced neutron widths without resonance missing correction (solid line on Fig. 6) is plotted for the number of resonances N =136, which takes into account present estimate of missing 14.4% levels. Actually, it gives an estimate of missing of levels with small neutron widths as ~ 18 levels at 1.5 keV.

3 Unresolved resonance region

Here we will briefly review the status of unresolved neutron resonance parameters of ^{234}U and provide a cross section parameterization of total, capture, elastic and inelastic scattering cross sections.

The unresolved resonance energy region of ENDF/B-VI [4] extends from 1.5 keV up to 100 keV. Provided are energy independent average resonance parameters $\langle D_{l=0}\rangle = 10.6$ eV, $\langle D_{l=1}\rangle = 5.3$ eV, $\langle D_{l=2}\rangle = 3.53$ eV and $\langle \Gamma_\gamma\rangle = 0.025$ eV, other average resonance parameters might be energy dependent or not. In JENDL-3.2 [6] unresolved resonance region extends from 1.5 keV up to 50 keV. Provided are energy independent average resonance parameters, fission width $\langle \Gamma_f\rangle$ being equal to zero, while $\langle D_{l=0}\rangle = 10.6$ eV, $\langle D_{l=1}\rangle = 5.3$ eV, $\langle \Gamma_\gamma\rangle = 0.026$ eV are adopted.

The assume that lower energy of unresolved resonance energy region in present evaluation is the end-point of resolved resonance region, i.e. 1.5 keV, the upper energy is 140 keV, about the same as in our recent evaluations of ^{238}U and ^{232}Th [2, 3]. We suppose $s-$, $p-$ and $d-$wave neutron-nucleus interactions to be effective.

3.1 Average resonance parameters

Average resonance parameters $S_o = (0.96\pm0.13)\times10^{-4}$, $\langle D_{l=0}\rangle$= 11.4 eV, $\langle \Gamma_\gamma\rangle$ =26 meV are applied for the cross section calculation from 1.5 keV up to 140 keV.

3.1.1 Neutron resonance spacing

Neutron resonance spacing $\langle D_J\rangle$ was calculated with the phenomenological model [14], which takes into account the shell, pairing and collective effects. The main parameter of the model, asymptotic value of level density parameter $\widetilde{a}$, was normalized to the observed neutron resonance spacing $\langle D_{l=0}\rangle = 11.4$ eV.

3.1.2 Neutron width

Average neutron width is calculated as follows

$$\langle \Gamma_n^{lJ} \rangle = S_l \langle D_J \rangle E_n^{1/2} P_l \nu_n^{lJ}, \quad (1)$$

where E_n is the incident neutron energy, P_l is the transmission factor for the $l-$th partial wave, which was calculated within black nucleus model, ν_n^{lJ} is the number of degrees of freedom of Porter-Thomas distribution (see Table 2). The p-wave neutron strength function $S_1 = 1.997 \times 10^{-4}$ at 1.5 keV was calculated with the optical model, using the deformed optical potential, described below.

3.1.3 Radiative capture width

Energy and angular momentum dependence of radiative capture width are calculated within a two-cascade γ-emission model with allowance for the (n,γn') [16] and (n,γf) [15] reactions competition to the (n,$\gamma\gamma$) reaction. The (n,$\gamma\gamma$) reaction is supposed to be a radiative capture reaction. The radiative capture width was normalized to the value of $\langle \Gamma_\gamma \rangle = 26$ meV.

3.1.4 Neutron inelastic width

Average neutron inelastic width is calculated as follows

$$\langle \Gamma_{n'}^{lJ} \rangle = S_l \langle D_J \rangle (E_n - E_1)^{1/2} P_l (E_n - E') \nu_{n'}^{lJ}, \quad (2)$$

where $\nu_{n'}^{lJ}$ is number of degrees of freedom of Porter-Thomas distribution (see Table 2). For actual compound nucleus states, formed by $s-$, $p-$ and $d-$wave neutrons one obtains

$$\begin{aligned}
\langle \Gamma_{n'}^{0,1/2} \rangle &= S_2 \langle D_{1/2} \rangle (E_n - E_1)^{1/2} P_2 (E - E_1) \cdot 2, \\
\langle \Gamma_{n'}^{1,1/2} \rangle &= S_1 \langle D_{1/2} \rangle (E_n - E_1)^{1/2} P_1 (E_n - E_1), \\
\langle \Gamma_{n'}^{1,3/2} \rangle &= S_1 \langle D_{3/2} \rangle (E_n - E_1)^{1/2} P_1 (E_n - E_1) \cdot 2 \\
\langle \Gamma_{n'}^{2,3/2} \rangle &= S_0 \langle D_{3/2} \rangle (E_n - E_1)^{1/2} + S_2 \langle D_{3/2} \rangle (E_n - E_1)^{1/2} P_2 (E_n - E_1) \cdot 2 \\
\langle \Gamma_{n'}^{2,5/2} \rangle &= S_0 \langle D_{5/2} \rangle (E_n - E_1)^{1/2} + S_2 \langle D_{5/2} \rangle (E_n - E_1)^{1/2} P_2 (E_n - E_1) \cdot 2 \quad (3)
\end{aligned}$$

3.1.5 Fission width

Fission widths are calculated within a double-humped fission barrier model. Energy and angular momentum dependence of fission width is defined by the transition state spectra at inner and outer barrier humps. We constructed transition spectra by supposing the axiality of inner saddle and mass asymmetry at outer saddle [12, 13]. Number of degrees of freedom ν_f^{lJ} of Porter-Thomas distribution is defined in Table 2. They will be described below.

Table 2.
Number of degrees of freedom

l, J	ν_n^{lJ}	$\nu_{n'}^{lJ}$	ν_f^{lJ}
0,1/2	1	2	3
1,1/2	1	1	3
1,3/2	1	2	4
2,3/2	1	1	4
2,5/2	1	1	4

3.2 Average cross sections in the region 1.5-140 keV

3.2.1 Total section

There is no total cross section measurements above 1.5 keV, only rather old data at lower energies [17, 18, 19, 20]. Above 10 keV total cross section was estimated assuming a decreasing trend of S_o and S_1 strength function values as the latter and potential radius, which was adopted from optical calculations, define total cross section up E_n =140 keV. To reproduce total cross section, calculated with optical model, we assume S_o value linearly decreasing starting from 10 keV to 0.8×10^{-4},while S_1 - to 1.6×10^{-4} at 140 keV (see Fig. 7).The d-wave neutron strength function was assumed to be equal to $S_2 = 1.257\times10^{-4}$. In JENDL-3.2 [6] evaluation potential scattering radius is R =0.97 fm, while in ENDF/B-VI [4] $R = 0.893$ fm, we assumed $R = 0.9381$ fm, that is consistent with the results of coupled channel optical model calculations. This difference of potential scattering radii explains low total cross section level of ENDF/B-VI [4] (see Fig. 7).

3.2.2 Elastic scattering cross section

Elastic scattering cross section estimate is rather insensitive to the fission cross section estimate. The discrepancy of present, ENDF/B-VI [4] and JENDL-3.2 [6] estimates from ∼1.5 keV and up to ∼150 keV, shown on Fig. 8, appears to be correlated with the different estimates of potential scattering radius (see Fig. 8).

3.2.3 Fission cross section

Only one set of the measured fission cross section data by James et al. [7] is available below ∼140 keV. We fitted these data by varying $s-$wave $\langle\Gamma_f^{0,1/2}\rangle$ fission width (see Fig. 9)

3.2.4 Inelastic scattering cross section

Calculated inelastic scattering cross section increases not that fast as in case of ^{238}U target nuclide, however it reaches ∼0.75 b at 140 keV. Direct scattering contribution seems to be rather important even at this low incident neutron energies, since it comprises ∼15% at 140 keV, this contribution is ∼1.5 times larger than in case of ^{238}U+n interaction. Conventional ENDF/B processing codes (i.e. RECENT [21], NJOY [22]) exemplify Hauser-Feshbach-Moldauer formalism and do not take into account direct scattering component of inelastic scattering. Total and capture data could be described within Hauser-Feshbach-Moldauer formalism, adopted in these codes, while it fails in case of inelastic scattering cross section because of appreciable direct scattering contribution. This discrepancy above ∼100 keV could be compensated by increasing inelastic neutron widths $\langle\Gamma_{n'}^{lJ}\rangle$ for the channels giving major contributions to inelastic scattering. Figure 10 shows partial contributions to the inelastic scattering coming from different (l, J)-channels. Major contribution, like in case of ^{238}U+n interaction, comes from $p-$wave channels $(l = 1, J = 1/2)$ and $(l = 1, J = 3/2)$, the intermediate comes from $s-$wave channel $(l = 0, J = 1/2)$, though only $d-$wave neutrons could excite 2^+ excited level of ^{234}U. The lowest contribution comes from $(l = 2, J = 3/2)$ and $(l = 2, J = 5/2)$ entrance channels, since both $s-$wave and $d-$wave neutrons contribute to exit channel. The direct contribution missing could be compensated by linear increase of S_1 neutron strength function in the exit channels from 1.997×10^{-4} $(\text{eV})^{-1/2}$ up to 4.0×10^{-4} $(\text{eV})^{-1/2}$ at 140 keV. To keep capture cross section unaffected we should increase capture widths in the same linear manner, up to ∼15% at 140 keV. Evaluated inelastic scattering cross section of ENDF/B-VI [4] is much different from present calculation, being lower for $E_n \lesssim 80$ keV, but ∼1.5 times higher for E_n ∼140 keV (see Fig. 10).

3.2.5 Capture cross section

We adopted $s-$wave radiative strength function $\text{S}_{\gamma 0} = 22.81\times10^{-4}$ ($\Gamma_\gamma = 26$ meV and $\langle D_{l=0}\rangle = 11.4$ eV). The $s-$wave radiative strength function estimate of $\text{S}_{\gamma 0} = 35.09\times10^{-4}$ ($\Gamma_\gamma = 40$ meV and $\langle D_{l=0}\rangle = 11.4$ eV) produces higher capture cross section, notwithstanding the scatter of measured capture data by Muradyan et al. [23] lower value of radiative strength function seems to be more justified. The important peculiarity of the calculated ^{238}U(n,γ) capture cross section, Wigner cusp above first excited level threshold, is also pronounced in case of calculated ^{234}U(n,γ) reaction cross section (see Fig. 11). The pattern of $s-, p-$and $d-$wave channel contributions to the capture cross section in the energy range of 1.5 - 140 keV is also rather similar to that of ^{238}U target nuclide. The $p-$wave contribution is higher than that of $s-$wave above ∼10 keV, while that of $d-$wave neutrons is the lowest. In case of ^{238}U(n,γ) reaction main contribution comes from $p-$wave neutrons above ∼5 keV, while that of $d-$wave neutrons becomes higher than that

of $s-$wave above $\sim$130 keV. These peculiarities might be attributed to the increased fission competition in $p-$ and $d-$wave entrance channels. Competition of (n,γf) reaction [15] to capture reaction is not that essential as in case of ^{232}U(n,γ) reaction (see Fig. 11). The decrease of S_1 strength function above $\sim$43.5 keV is essential for consistent description of capture and total cross section, calculated with a Hauser-Feshbach-Moldauer approach. Capture cross sections in present data file and those of JENDL-3.2 [6] and ENDF/B-VI [4] are of rather different shapes, however they are only slightly different around $\sim$1.5 keV, while for higher incident neutron energies, up to $\sim$60 keV, the estimate of JENDL-3.2 [6] is systematically lower than present and ENDF/B-VI [4] estimates (see Fig. 12). The discrepancies could be attributed to the energy dependence of radiative strength functions, which is missing in JENDL-3.2 [6] and ENDF/B-VI [4] estimates as well as to different estimates of reduced neutron widths.

3.2.6 Comparison of average resonance parameters

Figures 13-17 compare reduced neutron widths $\langle\Gamma_n^{lJ}\rangle$. Differences are pronounced either in $s-$wave, $p-$wave and $d-$wave reduced neutron widths. Non-smooth energy dependence of ENDF/B-VI [4] $s-$ and $p-$wave reduced neutron widths seems to be unnecessary to reproduce calculated total and capture cross sections up to E_n =140 keV.

Figures 18-22 compare present fission widths $\langle\Gamma_f^{lJ}\rangle$ with those of ENDF/B-VI [4]. We fitted averaged fission data by James et al.[7] by varying fission width of $s-$wave channel $\langle\Gamma_f^{0,1/2}\rangle$, other fission widths $\langle\Gamma_f^{lJ}\rangle$ are calculated with double-humped fission barrier.

The advantage of present evaluation is that it provides average energy dependent resonance parameters which reproduce evaluated cross sections, using conventional ENDF/B processing codes [21, 22] up to 140 keV. The price paid for that is slight increase of inelastic and capture widths for $p-$wave channels. Without that increase competitive inelastic width would correspond to inelastic scattering cross section, which is lower than inelastic cross section of smooth cross section file above 140 keV. That would be pronounced as a step in total cross section at 140 keV, since according to ENDF/B conventions, total cross section is calculated as a sum of elastic, capture, fission and inelastic scattering cross section, the latter is taken from tabulated cross section data file. The other cross sections are calculated using average energy dependent parameters. Present estimate of $\langle D_{l=0}\rangle$ is consistent with adopted set of $s-$wave resonances, while estimates of S_l and $S_{\gamma 0}$ values (see Table 3) are consistent with total and capture data trends.

Table 3
Average resonance parameters for ^{234}U

	$D_{l=0}$,eV	Γ_γ,meV	$S_0 \times 10^{-4}$	$S_1 \times 10^{-4}$	R, fm
JENDL-3.2	10.6	26	.96	1.197	0.97
ENDF/B-VI	10.6	25	0.976	2.269	0.893
Present	11.4	26	.96	1.997	0.9381

4 Optical Potential

A coupled channel model is employed for estimating differential scattering and total cross sections. Another important application of coupled channel model is calculation of direct inelastic scattering contribution of discrete levels. The direct excitation of ground state rotational band levels 0^+-2^+-4^+-6^+-8^+ is estimated within rigid rotator model, five levels of ground state band are assumed coupled. To calculate the direct excitation cross sections for β-vibration (K^π= 0^+), γ-vibration (K^π= 0^+, 2^+), as well as octupole ($K^\pi = 0^-$) band levels a soft rotator model [24, 1] was used.

We adopted here the optical potential parameters obtained for ^{232}Th [1] by fitting total cross section data, angular distributions and $s-$wave strength function. Then we fitted ^{234}U $s-$wave strength function $S_o = (0.96\pm0.13)$ $\times 10^{-4}$ with β_2 and β_4 deformation parameters. The optical potential parameters are as follows:

$$W_D = \begin{cases} V_R = 45.722 - 0.334E_n, MeV, r_R = 1.2668\ fm, a_R = 0.6468\ fm \\ 3.145 + 0.455E_n, MeV, \quad E_n \leq 10MeV, r_D = 1.25\ fm, a_D = 0.5246\ fm \\ 7.695\ MeV, \qquad\qquad 10 < E_n < 20\ MeV \\ V_{SO} = 6.2\ MeV, r_{SO} = 1.120\ fm, a_{SO} = 0.47\ fm, \\ \beta_2 = 0.190, \beta_4 = 0.072 \end{cases}$$

4.1 Total and elastic cross sections

Present total cross section is compared with JENDL-3.2 [6] and ENDF/B-VI [4] evaluated cross section on Fig. 23. Present and JENDL-3.2 [6] estimates are not much different, while shape of ENDF/B-VI [4] cross section is rather discrepant from both evaluations up to ∼10 MeV. Figure 24 compares elastic cross sections estimates of present coupled channels optical potential and that of JENDL-3.2 [6] with estimate of elastic scattering cross section of ENDF/B-VI [4] as a difference of total and partial reaction cross sections.

5 Statistical Model

As distinct from the previous evaluations JENDL-3.2 [6] and ENDF/B-VI [4] we calculate neutron cross sections within Hauser-Feshbach theory, coupled channel optical model and double-humped fission barrier model. The relative importance of direct excitation of rotational and vibrational levels is increased even in a few MeV incident neutron energy range, as compared with ^{238}U+n interaction, due to the lowered compound neutron scattering to the ^{234}U discrete and continuum levels.

Hauser-Feshbach-Moldauer [25] statistical theory is employed for partial cross section calculations below emissive fission threshold. Fissioning and residual nuclei level densities as well as fission barrier parameters are key ingredients, involved in actinide neutron-induced cross section calculations. First, level density parameters are defined, using neutron resonance spacing $\langle D_{l=0} \rangle$ estimate for ^{234}U target nuclide. Constant temperature level density parameters T_o, E_o, U_c are defined by fitting cumulative number of low-lying levels of ^{232}U, ^{233}U, ^{234}U and ^{235}U (see Fig. 25, 26) [11].

In case of fast neutron ($E_n \leq 6$ MeV) interaction with ^{234}U target nucleus, the main reaction channel is fission, fission cross section description serves as a major constraint for the neutron inelastic scattering and radiative neutron capture cross section estimate. Below there is an outline of the statistical model [28, 29] employed.

Neutron-induced reaction cross section (n, x) for excitation energies up to emissive fission threshold is defined as

$$\sigma_{nx}(E_n) = \frac{\pi \, \acute{\lambda}^2}{2(2I+1)} \sum_{ljJ\pi} (2J+1) T_{lj}^{J\pi}(E_n) P_x^{J\pi}(E_n) S_{nx}^{ljJ\pi}, \tag{4}$$

the compound nucleus decay probability $P_x^{J\pi}$ $(x = n, f, \gamma)$ is

$$P_x^{J\pi}(E_n) = \frac{T_x^{J\pi}(U)}{T_f^{J\pi}(U) + T_n^{J\pi}(U) + T_\gamma^{J\pi}(U)}, \tag{5}$$

where $U = B_n + E_n$ is the excitation energy of the compound nucleus, B_n is the neutron binding energy, $T_{lj}^{J\pi}$ are the entrance neutron transmission coefficients for the channel $(ljJ\pi)$, I is the target nucleus spin. Decay probability $P_x^{J\pi}(E_n)$ of the compound nucleus with excitation energy U for given spin J and parity π, depends on $T_f^{J\pi}$, $T_n^{J\pi}(U)$ and $T_\gamma^{J\pi}(U)$, transmission coefficients of the fission, neutron scattering and radiative decay channels, $S_{nx}^{ljJ\pi}$ denotes partial widths Porter-Thomas fluctuation factor. Below incident neutron energy equal to the cut-off energy of discrete level spectra, neutron cross sections are calculated within Hauser-Feshbach approach with correction for width fluctuation by Moldauer [25]. For width fluctuation correction calculation only Porter-Thomas fluctuations are taken into account. Effective number of degrees of freedom for fission channel is

defined at the higher fission barrier saddle as $\nu_f^{J\pi} = T_f^{J\pi}/T_{f\,\max}^{J\pi}$, where $T_{f\,\max}^{J\pi}$ is the maximum value of the fission transmission coefficient $T_f^{J\pi}$. At higher incident neutron energies the Tepel et al. [26] approach is employed, it describes cross section behavior in case of large number of open channels correctly.

5.1 Level Density

Level density is the main ingredient of statistical model calculations. Level density of fissioning, residual and compound nuclei define transmission coefficients of fission, neutron scattering and radiative decay channels, respectively. We will briefly discuss here level densities of even-even ^{234}U and even-odd ^{235}U nuclides.

The level densities were calculated with a phenomenological model by Ignatyuk et al. [14], which takes into account shell, pairing and collective effects in a consistent way

$$\rho(U, J, \pi) = K_{rot}(U, J) K_{vib}(U) \rho_{qp}(U, J, \pi), \tag{6}$$

where quasiparticle level density

$$\rho_{qp}(U, J, \pi) = \frac{(2J+1)\omega_{qp}(U)}{4\sqrt{2\pi}\sigma_\perp^2 \sigma_\parallel} \exp\left(-\frac{J(J+1)}{2\sigma_\perp^2}\right), \tag{7}$$

$\omega_{qp}(U, J, \pi)$ is state density, $K_{rot}(U, J)$ and $K_{vib}(U)$ are factors of rotational and vibrational enhancement of the level density. The collective contribution of the level density of deformed nuclei is defined by the nuclear deformation order of symmetry. The actinide nuclei at equilibrium deformation are axially symmetric. The order of symmetry of nuclear shape at inner and outer saddles were adopted from calculations within shell correction method (SCM) by Howard & Möller [30], uranium nuclei of interest (A$\leq$235) are assumed to be axially symmetric, then

$$K_{rot}(U) = \sigma_\perp^2 = F_\perp t, \tag{8}$$

where $\sigma_\perp^2$ is the spin cutoff parameter, $F_\perp$ is the nuclear momentum of inertia (perpendicular to the symmetry axis), which equals the rigid-body value at high excitation energies, where the pairing correlations are destroyed, experimental value at zero temperature and is interpolated in between, using the pairing model, $F_\parallel = 6/\pi^2 < m^2 > (1 - 2/3\varepsilon)$, where $< m^2 >$ is the average value of the squared projection of the angular momentum of the single-particle states, and ε is quadrupole deformation parameter. The closed-form expressions for thermodynamic temperature and other relevant equations which one needs to calculate $\rho(U, J, \pi)$ are provided by Ignatyuk et al. model [14].

To calculate the residual nucleus level density at the low excitation energy, i.e. just above the last discrete level excitation energy where $N^{exp}(U) \sim N^{theor}(U)$, we employ a Gilbert-Cameron-type approach. The constant temperature approximation of

$$\rho(U) = dN(U)/dU = T^{-1}\exp((U-U_o)/T) \tag{9}$$

is extrapolated up to the matching point U_c to the $\rho(U)$ value, calculated with a phenomenological model by Ignatyuk et al. [14] with the condition

$$U_c = U_o - Tln(T\rho(U_c)). \tag{10}$$

In this approach $U_o \simeq -n\triangle_o$, where $\triangle_o$ is the pairing correlation function, $\triangle_o = 12/\sqrt{A}$, A is the mass number, $n = 0$ for even-even, 1 for odd nuclei, i.e. U_o has the meaning of the odd-even energy shift. The value of nuclear temperature parameter T is obtained by the matching conditions at the excitation energy U_c.

In present approach the modelling of total level density

$$\rho(U) = K_{rot}(U)K_{vib}(U)\frac{\omega_{qp}(U)}{\sqrt{2\pi}\sigma} = T^{-1}\exp((U-U_o)/T) \tag{11}$$

in Gilbert-Cameron-type approach looks like a simple renormalization of quasiparticle state density $\omega_{qp}(U)$ at excitation energies $U < U_c$. The cumulative number of observed levels for even-even ^{234}U and even-odd ^{235}U are compared with constant temperature approximation on Figs. 25 and 26. In case of ^{234}U missing of levels above pairing gap ($\sim$1.3 MeV) is markedly pronounced. In case of ^{235}U nuclide missing seems to be pronounced above excitations of $\sim$0.5 MeV.

Few-quasiparticle effects which are due to pairing correlations are essential for state density calculation at low intrinsic excitation energies either for equilibrium (^{234}U) or saddle (^{235}U) deformations. The step-like structure in ^{238}Pu(n,f) reaction cross section above fission threshold was shown to be a consequence of threshold excitation of three-quasiparticle states in fissioning ^{239}Pu nuclide and two-quasiparticle configurations in residual even-even nuclide ^{238}Pu [31]. Strong vibrational resonance is observed in the reaction ^{234}U(n,f) around $\sim$0.8 MeV, this complicates the analysis of step-like irregularity in fission cross section around $\sim$1-2 MeV incident neutron energy, which could be evidenced in measured fission data and also might be attributed to the step in the level density of odd fissioning nuclide ^{235}U. We argue also that few-quasiparticle effects are important also for reasonable prediction of inelastic scattering cross section for even-even target nuclide ^{234}U at low energies.

The partial $n-$quasiparticle state densities, which sum-up to intrinsic state density of quasiparticle excitations could be modelled using the Bose-gas model prescriptions [32, 33]. The intrinsic state density of quasiparticle excitations $\omega_{qp}(U)$ could be represented as a sum of $n-$quasiparticle state densities $\omega_{nqp}(U)$:

$$\omega_{qp}(U) = \sum_n \omega_{nqp}(U) = \sum_n \frac{g^n(U-U_n)^{n-1}}{((n/2)!)^2(n-1)!}, \tag{12}$$

where $g = 6a_{cr}/\pi^2$ is a single-particle state density at the Fermi surface, n is the number of quasiparticles. The important model parameters are threshold values

U_n for excitation of $n-$quasiparticle configurations $n = 2, 4...$ for even-even nuclei and $n = 1, 3...$ for odd-A nuclei [33]. The detailed treatment of this approach and approximations employed, as applied for fission, inelastic scattering or capture reaction calculations, is provided in [34].

Nuclear level density $\rho(U)$ of even-even nucleus ^{234}U above the pairing gap up to the four-quasiparticle excitation threshold was extracted by fitting fission cross section data of ^{234}U(n,f) reaction. The total level density for even nuclide ^{234}U at equilibrium deformation, as compared with the Gilbert-Cameron-type approximation of $\rho(U)$ is shown on Fig. 27. The arrows on the horizontal axis of Fig. 27 indicate the excitation thresholds of even $n-$quasiparticle configurations. Below the excitation threshold U_2, i.e. within pairing gap the constant temperature model fits cumulative number of ^{234}U levels [35].

In case of and even-odd nucleus ^{235}U the partial contributions of $n-$quasiparticle states $\omega_{nqp}(U)$ to the total intrinsic state density $\omega_{qp}(U)$ produces distinct "jump" only below three-quasiparticle excitation threshold U_3 (see Fig. 28). The arrows on the horizontal axis of Fig. 28 indicate the excitation thresholds of odd $n-$quasiparticle configurations. Nuclear level density $\rho(U)$ up to the three-quasiparticle excitation threshold U_3 is virtually independent on the excitation energy, since the intrinsic state density ($\omega_1 \sim g$) is constant. The numerical values of nuclear level density $\rho(U)$ parameters of ^{235}U, defining one- and three quasiparticle state densities, are fitted to ^{234}U(n,f) cross section data.

Main parameters of the level density model for equilibrium, inner and outer saddle deformations are as follows: shell correction δW, pairing correlation functions Δ and Δ_f, at equilibrium deformations $\Delta = 12/\sqrt{A}$, quadrupole deformation ε and momentum of inertia at zero temperature $F_o/\hbar^2$ are given in Table 4. For ground state deformations the shell corrections were calculated as $\delta W = M^{exp} - M^{MS}$, where M^{MS} denotes liquid drop mass (LDM), calculated with Myers-Swiatecki parameters [36], and M^{exp} is the experimental nuclear mass. Shell correction values at inner and outer saddle deformations $\delta W_f^{A(B)}$ are adopted following the comprehensive review by Bjornholm and Lynn [37].

Table 4

Level density parameters of fissioning nucleus and residual nucleus

Parameter	inner saddle	outer saddle	neutron channel
δW, MeV	1.5	0.6	LDM
$\triangle$, MeV	$\triangle_o + \delta^*$	$\triangle_o + \delta^*$	$\triangle_o$
ε	0.6	0.8	0.24
$F_0/\hbar^2$, MeV^{-1}	100	200	73

*)$\delta = \Delta_f - \Delta$ value is defined by fitting fission cross section in the plateau region.

5.2 Fission Cross Section

Fission data fit is used as a major constraint for capture, elastic and inelastic scattering, (n,2n) and (n,3n) cross sections as well as secondary neutron spectrum estimation. Description of measured fission cross section might justify a validity of level density description and fission barrier parameterization.

5.3 Fission Channel

Neutron-induced fission in a double humped fission barrier model could be viewed as a two-step process, i.e. a successive crossing over the inner hump A and over the outer hump B. Hence, the transmission coefficient of the fission channel $T_f^{J\pi}(U)$ can be represented as

$$T_f^{J\pi}(U) = \frac{T_{fA}^{J\pi}(U) T_{fB}^{J\pi}(U)}{(T_{fA}^{J\pi}(U) + T_{fB}^{J\pi}(U))}. \tag{13}$$

The transmission coefficient $T_{fi}^{J\pi}(U)$ is defined by the level density $\rho_{fi}(\varepsilon, J, \pi)$ of the fissioning nucleus at the inner and outer humps (i = A,B, respectively):

$$T_{fi}^{J\pi}(U) = \sum_{K=-J}^{J} T_{fi}^{JK\pi}(U) + \int_0^U \frac{\rho_{fi}(\epsilon, J, \pi) d\epsilon}{(1 + \exp(2\pi(E_{fi} + \epsilon - U)/h\omega_i))}, \tag{14}$$

where the first term denotes the contribution of low-lying collective states and the second term that from the continuum levels at the saddle deformations, ϵ is the intrinsic excitation energy of fissioning nucleus. The first term contribution due to discrete transition states depends upon saddle symmetry. The total level density $\rho_{fi}(\epsilon, J, \pi)$ of the fissioning nucleus is determined by the order of symmetry of nuclear saddle deformation.

Inner and outer fission barrier heights and curvatures as well as level densities at both saddles are the model parameters. They are defined by fitting fission cross section data at incident neutron energies below emissive fission threshold. Fission barrier height values and saddle order of symmetry are strongly interdependent. The order of symmetry of nuclear shape at saddles was defined by Howard and Möller [30] within shell correction method (SCM) calculation. We adopt the saddle point asymmetries from SCM calculations. According to shell correction method (SCM) calculations of Howard and Möller [30] the inner barrier was assumed axially symmetric. This helped to interpret the non-threshold fission cross section behavior of ^{232}U(n,f) [38] assuming a lowered height of axially symmetric inner hump of ^{233}U, as anticipated by Howard and Möller [30] with SCM calculations. Outer barrier for uranium nuclei is assumed mass-asymmetric.

5.3.1 Fission transmission coefficient, level density and transition state spectrum

Adopted level density description allows to describe shape of measured fission cross section data of ^{234}U (see Figs. 29, 30). Incident neutron energy $E_3 = U_3 + E_{fA(B)} - B$ correspondent to excitation of three-quasiparticle states is ~ 1.5 MeV. The one-quasiparticle neutron states of even-odd fissioning nuclide, lying below the three-quasiparticle states excitation threshold define the shape of fission cross section below incident neutron energy of $E_n \leq E_{fA(B)} + U_3 - B_n$. At higher excitation energies three-quasiparticle states are excited. Two-quasiparticle states in even residual nuclide ^{234}U could be excited at incident neutron energies $E_n > U_2$. At lower energies fission cross section shape is controlled by one-quasiparticle state density. The transition state spectra were constructed using values of $F_0/\hbar^2$ at the inner and outer saddles shown in Table 5.

Each one-quasiparticle state in odd fissioning nucleus is assumed to have a rotational band built on it with a rotational constant, dependent upon the respective saddle deformation. We construct the discrete transition spectra up to $\sim$100 keV, using one-quasiparticle states by Bolsterli et al. [39] (see Table 5). The discrete transition spectra, as well as continuous level contribution to the fission transmission coefficient are dependent upon the order of symmetry for fissioning nucleus at inner and outer saddles. The negative parity bands $K^\pi = 1/2^-$,$3/2^-$, $5/2^-$ ... at outer saddle are assumed to be doubly degenerate due to mass asymmetry. With transition state spectra thus defined the fission barrier parameters are obtained.

Table 5.
Transition spectra band-heads, Z-even, N-odd nuclei

inner saddle		outer saddle	
K^π	E_{K^π}, MeV	K^π	E_{K^π}, MeV
$1/2^+$	0.0	$1/2^+$	0.0
$5/2^+$	0.08	$1/2^-$	0.0
$1/2^-$	0.05	$3/2^+$	0.08
$3/2^-$	0.0	$3/2^-$	0.08
		$5/2^+$	0.0
		$5/2^-$	0.0

5.4 Fission Data Analysis

Fission cross section data for ^{234}U(n,f) were measured by Behrens et al. [40], Fursov et al.[41], James et al. [7], Goverdovsky et al. [42, 43, 44], Kanda et al. [45], Meadows [46, 47], Lamphere [48, 49], White et al. [50, 51] and Arlt et al.[52].

First comprehensive measurement of ^{234}U(n,f) reaction cross section was done by Behrens et al. [40]. They covered neutron energy range of E_n ∼0.1-30 MeV (see Figs. 29, 30). Data by Lamphere [49] for E_n ∼0.6-1.3 MeV differ from them in energy scale (shifted to higher side) and are lower by ∼5%. Data by White et al. [51] for E_n ∼2.5, 5.4, 14.1 MeV are also lower by ∼5%. Data by James et al. [7] in the range above 100 keV up to 8.9 MeV were normalized to Lamphere [49] data for E_n ∼1-1.3 MeV, this procedure introduces systematic error of at least ∼5%. Data by James et al. [7] are discrepant with data Behrens et al. [40], being higher below E_n ∼2 MeV and systematically lower for $E_n \gtrsim 2$ MeV. Data by Goverdovsky et al. [44] near vibrational resonance of ∼0.8 MeV are compatible with data by Behrens et al. [40].

Data on ^{234}U(n,f) by Behrens et al. [40], Meadows [46] (E_n ∼0.2-10 MeV), Kanda et al. [45] (E_n ∼0.5-7.8 MeV) and Fursov et al.[41] (E_n ∼0.13-7.4 MeV) are compatible (within ∼2%) up to E_n ∼3 MeV. In the energy range of E_n ∼3-5 MeV, these data are systematically discrepant (up to ∼5%), data by Meadows [46] define the highest, while the data by Fursov et al.[41] the lowest cross section level. Above E_n ∼5 MeV data by Behrens et al. [40] are compatible with data by Meadows [46] (up to E_n ∼9.85 MeV) and by Fursov et al.[41] (up to E_n ∼7.4 MeV). Data by Goverdovsky et al. [43], which start at E_n ∼5 MeV, are compatible with the data base up to E_n ∼9.5 MeV, then up to E_n ∼10.5 MeV they predict rather sharp decrease of fission cross section in the second plateau region.

Above (n,2nf) reaction threshold data by White et al. [51] (E_n ∼14 MeV), Meadows [47] (E_n ∼14.8 MeV) and Goverdovsky et al. [42] (E_n ∼16 MeV) seem to be compatible, while data by Behrens et al. [40] at E_n ∼16 MeV predict higher cross section level, while data by Arlt et al.[52] (E_n ∼14.7 MeV) seem to be too low.

Rather peculiar feature of measured data is a change of cross section shape around ∼1 MeV neutron energy. One-quasiparticle neutron states of even-odd ^{235}U fissioning nuclide, lying below three-quasiparticle states excitation threshold define the shape of ^{234}U fission cross section below incident neutron energy of E_n ∼2.5 MeV. At higher energies three-quasiparticle states are excited. We fit the decreasing trend of data above E_n ∼2.5 MeV increasing the correlation function value at outer saddle, which controls the cross section shape. For E_n up to E_n ∼2.5 MeV the step-like irregularity is roughly reproduced by varying the density of one- and three-quasiparticle states at saddle deformations, as described in [31] (see Figs. 29, 30). Discrepancy of the calculated curve with measured data for E_n ∼1.5-2.5 MeV could be easily removed by more detailed fitting of level density $\rho(U)$ of ^{235}U up to the three-quasiparticle excitation threshold U_3. In present evaluation for E_n ∼1.5-2.5 MeV we fitted data by Fursov et al.[41].

5.5 Inelastic Scattering

Fission data fit defines the compound inelastic neutron scattering contribution to the total inelastic scattering cross section. The relative contribution of direct discrete level excitation cross sections is higher than in case of ^{238}U target nuclide because of stronger fission competition to compound neutron scattering.

5.6 Neutron Channel

The lumped transmission coefficient of the neutron scattering channel (see Eqs. (4), (5)) is given by

$$T_n^{J\pi}(U) = \sum_{l'j'q} T_{l'j'}^{J\pi}(E_n - E_q) + \sum_{l'j'I'} \int_0^{U-U_c} T_{l'j'}^{J\pi}(E'_n)\rho(U - E'_n, I', \pi)dE'_n, \quad (15)$$

where $\rho(U - E'_n, I', \pi)$ is the level density of the residual nucleus. Levels of residual nuclide ^{234}U [35] are provided in Table 6. The entrance channel neutron transmission coefficients $T_{lj}^{J\pi}$ are calculated within a rigid rotator coupled channel approach. For the compound nucleus formation cross section calculation, the cross sections of the direct excitation of ground state band levels were subtracted from the absorption cross section. The compound and direct inelastic scattering components are added incoherently.

The exit neutron transmission coefficients $T_{l'j'}^{J\pi}(E'_n)$ were calculated using the re-normalized deformed optical potential of entrance channel without coupling, which describes a neutron absorption cross section.

5.7 Ground State Rotational Band

Predicted discrete level excitation cross section shape, calculated within a rigid rotator model, depends upon optical potential used. Calculated compound contribution is controlled mainly by fission competition. Due to lower fission threshold of ^{235}U fissioning nuclide, as compared with that of ^{239}U, compound inelastic scattering makes lower contributions to excitation cross sections of 1st, 2nd and 3d levels of ^{234}U around E_n ~1 MeV (see Figs. 31, 32, 33). Figure 34 shows that direct scattering essentially defines the excitation cross section of $J^\pi = 8^+$ level. The discrepancies with previous evaluations are due to both compound and missing (in evaluation of ENDF/B-VI [4]) direct contribution estimates. The compound component tends to be zero above ~3 MeV incident neutron energy.

Table 6

Levels of ^{234}U

	E_q, keV	J^π	K^π
1	0.	0^+	0^+
2	43.498	2^+	0^+
3	143.350	4^+	0^+
4	296.070	6^+	0^+
5	497.040	8^+	0^+
6	741.2	10^+	0^+
7	786.29	1^-	0^-
8	809.88	0^+	0^+
9	849.3	3^-	0^-
10	851.7	2^+	0^+
11	926.74	2^+	2^+
12	947.85	4^+	0^+
13	962.6	5^-	0^-
14	968.6	3^+	2^+
15	989.45	2^-	2^-
16	1023.7	4^+	2^+
17	1023.8	12^+	0^+
18	1023.83	3^-	2^-
19	1044.5	0^+	0^+
20	1069.3	4^-	2^-
21	1085.3	2^+	0^+
22	1090.9	5^+	2^+
23	1095.9	6^+	0^+
24	1125.2	7^-	0^-
25	1126.7	2^+	
26	1127.6	5^-	2^-
27	1150.0	4^+	0^+
28	1165.2	3^+	
29	1172.1	6^+	2^+
30	1174.2	1^+	

5.8 Soft rotator model

We assume strong missing of levels above excitations of ∼1.35 MeV (see Fig. 25), so only levels up to this excitation energy were included when calculating inelastic scattering cross sections. For excitation energies up to ∽1.35 MeV six bands with $K^\pi = 0^+_1$, 0^+_2, 0^+_3, $K^\pi = 0^-$, $K^\pi \backsimeq 2^-$ and $K^\pi \backsimeq 2^+$ could be distinguished in

^{234}U level scheme [35] within a soft rotator model [24] (see Table 7). Excitation energies of members of even parity collective bands $K^\pi = 0_1^+,\ 0_2^+,\ 0_3^+,\ K^\pi \backsimeq 2^+$ and first octupole band $K^\pi = 0^-$ as well as second octupole band $K^\pi \backsimeq 2^-$ are reproduced. Levels of $K^\pi = 0_2^+$ band ($E_{0_2^+}$ =0.80988 MeV) are classified as quadrupole longitudinal $\beta-$vibrations, while levels of $K^\pi = 0_3^+$ band ($E_{0_3^+}$ =1.04453 MeV) as quadrupole $\gamma-$transversal vibrations.

Table 7

Comparison of experimental ^{234}U levels [35] with soft rotator model calculations

19	1044.53	0^+						1044.5
18	1023.83	3^-					1019.9	
17	1023.8	12^+	1004.0					
16	1023.7	4^+				1012.0		
15	989.45	2^+					989.45	
14	968.6	3^+				965.2		
13	962.6	5^-		932.27				
12	947.85	4^+			966.22			
11	926.74	2^+				930.0		
10	851.70	2^+			855.42			
9	849.30	3^-		838.67				
8	809.88	0^+			806.73			
7	786.29	1^-		786.13				
6	741.2	10^+	730.94					
5	497.04	8^+	492.39					
4	296.071	6^+	294.58					
3	143.351	4^+	143.16					
2	43.498	2^+	43.553					
1	0.0	0^+	0.0	$n_{\beta_3}=0$	$n_{\beta_2}=1$			$n_\gamma=1$
	E_q^{exp},keV	J^π	$K^\pi=0^+$	$K^\pi=0^-$	$K^\pi=0_2^+$	$K^\pi=2^+$	$K^\pi=2^-$	$K^\pi=0_2^+$

Levels of negative parity band with $K^\pi = 0^-$ are defined by octupole deformation parameter β_3 and parameter of softness to the octupole vibrations μ_{β_3}. This peculiarity prohibits unanimous definition of β_3-parameter value by fitting $K^\pi = 0^-$ band level positions only. Values of β_3-parameter are defined by fitting angular distribution data, level positions are kept unaffected by varying softness parameter μ_{β_3}. Experimental inelastic cross section data [53] for excitation of groups of octupole band levels of ^{238}U up to ~ 3 MeV allow to define β_3- and $\mu_{\beta_3}-$parameter values. We adopted these β_3- and $\mu_{\beta_3}-$parameter values for ^{234}U and other nuclides, i.e. ^{232}Th, and ^{232}U (see Table 8). Other model parameters - the scaling factor $\hbar\omega_0$, μ_{β_2} and μ_γ softness parameters to quadrupole longitudinal and transversal vibrations, respectively, and non-axiality parameter γ_0, were obtained by fitting positions of $K^\pi = 0_1^+,\ 0_2^+,\ 0_3^+,\ 0_4^+,\ K^\pi \backsimeq 2^+$ band heads.

Table 7 (continued)

Comparison of experimental ^{234}U levels with soft rotator model calculations

33	1340.8	14^+	1309.1					
32	1335.9	9^-		1235.5				
31	1292.6	8^+			1349.6			
30	1277.48	7^-					1240.5	
29	1261.84	7^+				1218.0		
28	1194.73	6^-					1170.6	
27	1172.10	6^+				1139.3		
26	1150.0	4^+						1158.8
25	1127.6	5^-					1110.8	
24	1125.27	7^-		1065.3				
23	1095.9	6^+			1133.3			
22	1090.9	5^+				1069.7		
21	1085.3	2^+						1079.0
20	1069.3	4^-					1060.4	
				$n_{\beta_3}=0$	$n_{\beta_2}=1$			$n_\gamma=1$
	E_{exp},keV	J^π	$K^\pi=0^+$	$K^\pi=0^-$	$K^\pi=0^+$	$K^\pi=2^+$	$K^\pi=2^-$	$K^\pi=0^+$

Table 8. Deformation parameter values for soft rotator model

Nuclide	$h\omega_0$	μ_{β_2}	μ_γ	γ_0	μ_{β_3}	β_2	β_3	β_4
^{238}U	.989	.216	.293	.146	.626	.195	.052	.078
^{234}U	.807	.244	.270	.158	.626	.190	.052	.072
^{232}U	.691	.273	-	.168	.626	.188	.052	.071
^{232}Th	.725	.279	.279	.187	.626	.220	.052	.071

Quadrupole longitudinal β-vibration $K^\pi = 0^+$ band levels and quadrupole transversal $\gamma-$vibration $K^\pi= 0^+$ band levels are defined by softness parameters to respective vibrations μ_{β_2} and μ_γ. Anomalous rotational $K^\pi \backsimeq 2^+$ $\gamma-$band levels are defined by non-axiality parameter γ_o, which is correlated with positions of $K^\pi \backsimeq 2^+$ levels in ^{238}U,^{234}U, ^{232}U and ^{232}Th.

In case of ^{234}U, levels of second $K^\pi = 0_2^+$ band ($E_{0_2^+}$ =0.80988 MeV) are classified as quadrupole longitudinal $\beta-$vibrations, excitation energies are defined by softness parameter μ_{β_2} (see Table 8). Position of this $K^\pi = 0^+$ $\beta-$vibration band-head is lower than in case of ^{238}U, but higher than in case of ^{232}U nuclide. As regards the position of quadrupole transversal vibrations K^π=0_3^+ band ($E_{0_3^+}$ =1.04453 MeV), it lies much higher than in case of ^{238}U, but lower than in case of ^{232}U.

In other words, ^{234}U turns out to be less soft to γ-vibrations, than ^{238}U, but more soft than ^{232}U. These peculiarities might be correlated with positions of anomalous rotational band $K^\pi = 2^+$ in ^{232}U, ^{234}U and ^{238}U, here ^{234}U band again occupies intermediate position, as compared with ^{238}U and ^{232}U nuclides. Anomalous rotational $K^\pi \backsimeq 2^+$ band level positions are defined by non-axiality parameter γ_0 (see Table 8).

Direct excitation of vibrational levels $K = 0_2^+$, $K^\pi = 0_3^+$, $K = 0^-$ and $K \simeq 2^+$ could be described within a soft rotator model [24, 1]. Specifically, direct excitation cross sections for the $K^\pi = 0_2^+$ and $K^\pi = 0_3^+$ bands, anomalous rotational band $K^\pi = 2^+$ as well as first octupole ($K^\pi = 0^-$) band levels are calculated for deformed non-axial, soft to quadrupole vibrations rotator (see Figs. 35-48). Values of coupling strength parameters were fixed as follows: octupole deformation parameter β_3 was adopted to be the same as for the ^{238}U nuclide, then level positions of $K = 0^-$ band were fitted with softness parameter μ_{β_3}. Levels of second $K^\pi = 0_2^+$ band (0.69121 MeV) are classified as quadrupole longitudinal $\beta-$vibrations, excitation energies are defined by softness parameter μ_{β_2} (see Table 8).

Actually the calculations of direct inelastic scattering cross sections were made adding each of 17 levels of $K^\pi = 0_2^+$, $K = 0^-$ and $K^\pi \simeq 2^+$ bands (see Table 9), one by one, to the 0^+-2^+-4^+-6^+-8^+ coupling basis, instead of the last 8^+-member, since the coupling with ground state band levels is the strongest for any band level. This procedure was checked in case of ^{238}U and ^{232}Th target nuclides. However, coupling basis could be extended to include all 18 collective levels simultaneously. Obviously, the extension of the coupling basis leads to the renormalization of optical potential parameters. After they are fitted to neutron cross sections and strength functions, the calculated direct excitation cross sections are changed only slightly .

5.8.1 Octupole bands

Pronounced is the direct excitation contribution for the $K^\pi = 0^-$ band-head state 0.78629 MeV ($J^\pi = 1^-$) (see Fig. 35). Relative contribution of direct level excitation increases for the higher lying members $J^\pi = 3^-$ and $J^\pi = 5^-$ of this band (see Figs. 37, 41). Previous estimate of JENDL-3.2 [6] of excitation cross sections of these levels is rather discrepant with present calculations above $E_n \sim 1.5$ MeV due to missing direct scattering contribution.

Compound scattering components for excitation cross section of $K^\pi = 2^-$ band-head state 0.98945 MeV ($J^\pi = 2^-$) (see Fig. 43) of present calculation and estimate of JENDL-3.2 [6] are severely discrepant. At the other hand, they almost coincide in case of second member of this band, 1.02383 MeV ($J^\pi = 3^-$) (see Fig. 45), in both cases direct component is extremely low.

5.8.2 Quadrupole bands

Discrepancies of present calculation of excitation cross sections of β-vibration band K^π=0_2^+ levels with JENDL-3.2 [6] estimate, which are observed above E_n $\sim$1 MeV, are due to missing direct scattering components (see Figs. 36, 38, 40). In case of ENDF/B-VI [4] compound scattering component seems to be unreasonably high.

Table 9

Coupling scheme for ^{234}U

				1.27748; 7^-	
		1.26184; 7^+			
				1.19473; 6^-	
			1.1721; 6^+		
					1.150; 4^+
				1.1276; 5^-	
	1.12527; 7^-				
		1.0959; 6^+			
			1.0909; 5^+		
					1.0853; 2^+
				1.0693; 4^-	
					1.04453; 0^+
				1.02383; 3^-	
1.0238; 12^+					
			1.0237; 4^+		
				0.98945; 2^-	
			0.9686; 3^+		
	0.9626; 5^-				
		0.94785; 4^+			
			0.92674; 2^+		
		0.85170;2^+			
	0.83867; 3^-				
		0.80988; 0^+			
	0.78629; 1^-				
0.49704;8^+					
0.296071; 6^+					
0.143351; 4^+					
0.043498; 2^+					
0.0000; 0^+	$n_{\beta_3}=0$	$n_{\beta_2}=1$			$n_\gamma=1$
K^π= 0^+	$K^\pi=0^-$	$K^\pi=0_2^+$	$K^\pi\simeq 2^+$	$K^\pi\simeq 2^-$	$K^\pi=0_3^+$

Discrepancies of present calculation of excitation cross sections of anomalous rotation band-head K^π=2^+ with JENDL-3.2 [6] estimate, which are observed above ∼1 MeV, are due to missing direct scattering components (see Fig. 39). For other levels of this band(See Figs. 42, 44, 48) direct scattering contribution is rather low and discrepancies might be attributed to the compound scattering differences.

Discrepancies of present calculation of excitation cross sections of β-vibration band K^π=0_2^+ levels with JENDL-3.2 [6] estimate, which are observed above ∼1 MeV, are again due to missing direct scattering components (see Figs. 46, 47). In case of ENDF/B-VI [4] compound scattering component again seems to be unreasonably high (see Fig. 46).

5.9 Total inelastic cross section

Calculated total inelastic cross section is compared with previous evaluated data on Fig. 49. Lumped contribution of direct excitation of ground state band levels, octupole K^π=0^- and K^π=2^- bands, β-vibration $K^\pi = 0_2^+$, $\gamma-$vibration $K^\pi = 0_3^+$ and anomalous rotation band $K^\pi = 2^+$ levels is shown to attain ∼20% of total inelastic cross section at $E_n \gtrsim 2$ MeV. The calculated curve is consistent with JENDL-3.2 evaluation [6] up to E_n ∼1 MeV, while at higher energies the discrepancy might be attributed to missing direct excitation of octupole K^π=0^- and K^π=2^- bands, β-vibration, $\gamma-$vibration and anomalous rotation band levels. Our estimate is roughly compatible with ENDF/B-VI [4] evaluation above E_n ∼1.5 MeV, though this consistency is explained by rather high estimate of continuum inelastic scattering in ENDF/B-VI [4] evaluation (see Fig. 50). At lower excitations the discrepancy might be attributed to overestimation of compound excitation cross sections of second and third members of ground state rotational band in ENDF/B-VI [4].

Shape of calculated continuum inelastic scattering cross section is rather similar to that of JENDL-3.2 [6] evaluated total inelastic scattering cross section (see Fig. 50). Continuum inelastic scattering cross section of ENDF/B-VI [4] evaluation seems to be too high.

Above emissive fission threshold evaluations of inelastic scattering cross section differ severely, present estimate being the highest (see Fig. 51). In our calculations pre-equilibrium neutron emission contribution is defined by description of ^{238}U secondary neutron spectra and consistent description of ^{238}U(n,f), ^{238}U(n,2n) and ^{238}U(n,3n) reaction cross sections [34]. At E_n ∼10 MeV it is∼ 3 times higher than that of JENDL-3.2 evaluation [6]. Pre-equilibrium neutron emission contribution allowed to reproduce also observed fission cross section of ^{234}U(n,f) up to E_n ∼20 MeV.

6 Capture cross section

We have demonstrated by the analysis of measured capture cross sections of ^{238}U(n,γ) and ^{232}Th(n,γ) [54] that neutron capture data could be described within a Hauser-Feshbach-Moldauer statistical model. Specifically, in a few-keV energy region calculated capture cross section is defined by the radiative strength function value $S_\gamma = \Gamma_\gamma/D$. At incident neutron energies above ∼100 keV calculated capture cross section shape is defined by the energy dependence of radiative strength function S_γ. Energy dependence of S_γ is controlled mainly by the energy dependence of the level density of the compound nuclide ^{235}U. Low fission threshold for the ^{235}U nuclide necessitates the inclusion of the competition of fission [15] alongside with neutron emission [16] at the second $\gamma-$cascade, i.e. after first $\gamma-$quanta emission . Then "true" capture reaction cross section (n,$\gamma\gamma$) is defined using transmission coefficient $T^{J\pi}_{\gamma\gamma}(U)$ defined in a two-cascade approximation as

$$T^{J\pi}_{\gamma\gamma} = \frac{2\pi C_{\gamma 1}}{3(\pi hc)^2}\int \varepsilon^2_\gamma \sigma_\gamma(\varepsilon_\gamma) \sum_{I=|J-1|}^{I=J+1} \rho(U-\varepsilon_\gamma, I, \pi)\frac{T^{I\pi}_\gamma}{T^{I\pi}_f + T^{I\pi}_{n'} + T^{I\pi}_\gamma} d\varepsilon_\gamma \ , \quad (16)$$

The last term of the integrand describes the competition of fission, neutron emission and γ-emission at excitation energy $(U-\varepsilon_\gamma)$ after emission of first γ-quanta, $C_{\gamma 1}$ is the normalizing coefficient. That means that transmission coefficients $T^{I\pi}_\gamma$, $T^{I\pi}_{n'}$ and $T^{I\pi}_f$ are defined at excitation energy $(U-\varepsilon_\gamma)$. The neutron emission after emission of first $\gamma-$quanta strongly depends on the ^{234}U residual nuclide level density at excitations just above paring gap U_2. The contribution of (n,γf)$-$reaction [15] to fission cross section is defined by $T^{J\pi}_{\gamma f}$ value. The energy dependence of (n,γf) reaction transmission coefficient $T^{J\pi}_{\gamma f}$ was calculated with the expression

$$T^{J\pi}_{\gamma f} = \frac{2\pi C_{\gamma 1}}{3(\pi hc)^2}\int \varepsilon^2_\gamma \sigma_\gamma(\varepsilon_\gamma) \sum_{I=|J-1|}^{I=J+1} \rho(U-\varepsilon_\gamma, I, \pi)\frac{T^{I\pi}_f}{T^{I\pi}_f + T^{I\pi}_{n'} + T^{I\pi}_\gamma} d\varepsilon_\gamma \ , \quad (17)$$

The capture cross section is shown on Fig. 52. The (n,γf) reaction competition to the "true" capture (n,$\gamma\gamma$) reaction competition is rather strong above E_n ∼3 MeV. The competition of (n,γn') reaction to the "true" capture (n,$\gamma\gamma$) reaction is essential above E_n ∼1 MeV. We adopted here radiative capture strength function $S_{\gamma o}$, which actually corresponds to $\langle\Gamma_\gamma\rangle$ = 26 meV and $\langle D_{l=0}\rangle$ = 11.4 eV. The important peculiarity of the calculated ^{238}U(n,γ) capture cross section - Wigner cusp above first excited level threshold, is also pronounced in case of ^{234}U(n,γ) reaction cross section (see Fig. 52). Another capture cross section drop is observed around ∼0.8 MeV. It might be correlated with strong increase of inelastic scattering competition due to vibrational levels of $K^\pi = 0^+_2, K^\pi = 0^+_3$, $K = 0^-$

and $K^{\pi} \simeq 2^{+}$ bands. Above $E_n \sim 1$ MeV capture cross section decrease is defined by (n,γf) and (n,γn') reactions competition.

Previous evaluated capture cross sections are drastically discrepant with present calculation at $E_n \gtrsim 100$ keV (see Fig. 53). Some consistency is observed only with ENDF/B-VI [4] up to $\sim$15 keV. For higher incident neutron energies competition of fission and inelastic scattering with $\gamma-$emission seems to be modelled correctly within present approach. A consistent description of a most complete set of measured data on the (n,γ), (n,f) and (n,n') reaction cross sections for the ^{238}U and ^{232}Th target nuclides [1, 2, 3, 54] enables one to consider the statistical theory estimates of ^{234}U(n,γ) reaction as fairly realistic.

7 Cross sections above emissive fission threshold

At incident neutron energies when fission reaction of ^{234}U or ^{233}U nuclides is possible after emission of 1 or 2 pre-fission neutrons, the observed ^{234}U(n,f) fission cross section being a superposition of non-emissive or first chance fission of ^{235}U and xth-chance fission contributions. These contributions are weighted with a probability of x neutron emission before fission. For fixed statistical model parameters of residual nuclei ^{234}U and ^{233}U, fissioning in ^{234}U(n,nf) or ^{234}U(n,2nf) reactions, the behavior of the first-chance fission cross section σ_{nf} should make it possible to reproduce the measured fission cross section σ_{nF} of ^{234}U(n,f) reaction. A consistent description of a most complete set of measured data on the (n,f), (n,2n), (n,3n) and (n,4n) reaction cross sections for the ^{238}U target nuclide up to 20 MeV enables one to consider the estimates of first neutron spectra of initial ^{235}U nuclide as fairly realistic.

7.1 Fission cross section

Above emissive fission threshold contributions of emissive fission to the observed fission cross section coming from (n,$x$nf), $x = 1, 2, 3...X$, fission reactions of relevant equilibrated uranium nuclei, could be calculated as

$$\sigma_{nF}(E_n) = \sigma_{nf}(E_n) + \sum_{x=1}^{X} \sigma_{n,xnf}(E_n), \tag{18}$$

emissive fission contributions could be calculated using fission probability estimates $P_{fi}^{J\pi}(U)$ as

$$\sigma_{n,xnf}(E_n) = \sum_{J\pi} \int_0^{U_{max}} W_{x+1}^{J\pi}(U) P_{f(x+1)}^{J\pi}(U) dU, \tag{19}$$

where $W_x^{J\pi}(U)$ is the population of $(x+1)-$th nucleus at excitation energy U after emission of x neutrons, excitation energy U^{max} is defined by incident neutron energy E_n and energy, removed from the composite system by ^{234}U(n,$x$nf) reaction neutrons. Fission probabilities $P_{fx}^{J\pi}$ for fissioning $x-$th nuclei, could be estimated by fitting neutron-induced fission cross sections of relevant target nuclides, i.e. ^{233}U and ^{232}U. Neutron-induced fission cross section of ^{234}U, shown on the Fig. 54 demonstrates a step-like structures, relevant to contributions of (n,$x$nf) reactions to the total fission cross section. For these calculations modified version of Hauser-Feshbach code STAPRE [27] is employed.

Contribution of first-chance fission is defined by the pre-equilibrium emission of first neutron and level densities of fissioning ^{235}U and residual ^{234}U nuclides. The behavior of the first-chance fission cross section σ_{nf} is obviously related to the energy dependence of the fission probability of the ^{235}U nuclide P_{f1}:

$$\sigma_{nf} = \sigma_r(1 - q(E_n))P_{nf}. \tag{20}$$

Once the contribution of first neutron pre-equilibrium emission $q(E_n)$ is fixed [1], the first-chance fission probability P_{nf} of the ^{235}U composite nuclide depends only on the level density parameters of fissioning and residual nuclei. Actually, it depends on the ratio of shell correction values $\delta W_{fA(B)}$ and δW_n. The results of different theoretical calculations of the shell corrections as well as of the fission barriers vary by $1 \sim 2$ MeV. The same is true for the experimental shell corrections, which are obtained with a smooth component of potential energy calculated according to the liquid-drop or droplet model. However the isotopic changes of $\delta W_{fA(B)}$ and δW_n [37] are such that P_{nf} viewed as a function of the difference $(\delta W_{fA(B)} - \delta W_n)$ is virtually independent on the choice of smooth component of potential energy. Therefore, we shall consider the adopted $\delta W_{fA(B)}$ estimates (see Table 4) to be effective, provided that δW_n are obtained with the liquid drop model.

Above (n,nf) reaction threshold (see Fig. 54) calculated curve is compatible with measured data by Behrens et al. [40], Meadows [46] (E_n ~9.5 MeV), Kanda et al. [45] (E_n ~0.5-7.8 MeV) and Fursov et al.[41] (E_n ~0.13-7.4 MeV). Data by Goverdovsky et al. [43] are compatible with calculated cross section up to 9.5 MeV, then they predict rather sharp decrease of fission cross section in the second plateau region.

Above (n,2nf) reaction threshold calculated curve is compatible with measured data by White et al. [51] (E_n ~14 MeV), Meadows [47] (E_n ~14.8 MeV), and and Goverdovsky et al. [42] (E_n ~16 MeV). Data point by Behrens et al. [40] at E_n ~16 MeV predict higher cross section level, though the other two data point are compatible with calculated curve, while data by Arlt et al.[52] (E_n ~14.7 MeV) seem to be too low.

The trend of the first-chance fission cross section σ_{nf}, shown in Fig. 55 corresponds to estimate of σ_{nf}, obtained by fit of ^{238}U(n,f), ^{238}U(n,2n), ^{238}U(n,3n)

and ^{238}U(n,4n) reaction cross section data. Contribution of second-chance fission of ^{234}U nuclide is defined by pre-equilibrium contribution of first neutron spectrum and subsequent sharing of $\sigma_r = \sigma_{nf} + \sigma_{n,nx}$ reaction cross section into first-chance fission and neutron emission cross sections. First-, second- and third-chance fission contributions to the total neutron-induced fission cross section of ^{234}U are compared with relevant contributions for neutron-induced fission of ^{238}U target nuclide on Fig. 55. The contribution of first-chance fission to the ^{234}U(n,f) reaction cross section is rather smooth function of incident neutron energy, as distinct from ^{238}U(n,f) reaction. In the latter case a local minimum is observed near ^{238}U(n,nf) reaction threshold. The second-chance fission contribution ^{234}U(n,nf) is a smooth increasing function of excitation energy up to E_n ∼13 MeV. Calculated with present level density approach cross section of ^{233}U(n,f) reaction is shown on Fig. 56. The contribution of ^{234}U(n,2nf) reaction to the total fission cross section is somewhat higher than in case of ^{238}U(n,2nf) reaction. It corresponds to neutron-induced fission cross section of ^{232}U(n,f) reaction. Calculated with present level density approach cross section of ^{232}U(n,f) reaction is shown on Fig. 57.

7.2 ^{234}U(n,xn) cross section

There is no measurements of ^{234}U(n,2n) or ^{234}U(n,3n) reaction cross section. These cross sections would be estimated using ^{234}U(n,f) fission cross section fit up to E_n =20 MeV as the only constraint. Present estimate of ^{234}U(n,2n) cross section for $E_n \lesssim$10 MeV is about twice lower that that of JENDL-3.2 [6], the estimate of ENDF/B-VI shows unrealistic structures around E_n ∼10 MeV (Fig. 58). For $E_n \gtrsim$10 MeV calculated (n,2n) reaction cross section shape corresponds to pre-equilibrium emission contribution to the first neutron spectrum.

Present estimate of ^{234}U(n,3n)^{232}U cross section is much lower than those of JENDL-3.2 [6] and ENDF/B-VI [4], both seem to be unrealistically high (see Fig. 59).

8 Neutron emission spectra

Neutron emission spectra are inclusive of both fission and scattered neutrons. First we will describe the approach used for prompt fission neutron number ν_p and prompt fission neutron spectra (PFNS) calculation and then return to the discussion on neutron emission spectra. A brief survey of the model used to estimate prompt fission neutron number ν_p value and PFNS is provided below.

8.1 Prompt fission neutron number ν_p

There is no experimental data for prompt fission neutron spectra for ^{234}U, there is only one measurement of the prompt neutron multiplicity ν_p in the energy range E_n ∼1- 4 MeV [55]. The evaluated data of JENDL-3.2 [6] and ENDF/B-VI [4] were based on this experiment after re-normalization to the present thermal value of neutron multiplicity for ^{252}Cf (ν_p^{th} =3.756). The predicted data on ν_p for ^{234}U of systematic [56] are ∼3% lower than experimental data by Mather et al.[55]. Since systematic of [56] is based on the fission energy balance, we corrected TKE value for the first chance fission reaction of ^{234}U(n,f) to fit data by Mather (see Fig. 60).

At incident neutron energies above emissive fission threshold the number of prompt fission neutron $\nu_p(E_n)$ was calculated as

$$\begin{aligned}\nu_p(E_n) &= \beta_o\nu_o(E_n) + \beta_1(1 + \nu_1(E_n - B_{nA} - \overline{E}_1)) + \\ &\quad \beta_2(2 + \nu_2(E_n - B_{nA} - B_{nA-1} - \overline{E}_1 - \overline{E}_2)). \qquad (21)\end{aligned}$$

Here, $\nu_i(E_n)$ is a prompt fission neutron number for $i-$th fissioning nucleus, B_{nA} - neutron binding energy for the A nucleus, $\overline{E}_i$- average energy of $i-$th pre-fission neutron. To calculate the ν_p for ^{234}U(n,f) reaction up to E_n =20 MeV we need to estimate ν_p values for ^{233}U and ^{232}U target nuclides, which contribute to the observed ν_p-value of ^{234}U target nuclide via (n,$x$nf) emissive fission processes. Relevant contributions are shown on Fig. 61. We assumed that excitation energy

$$U_i = E_n - \sum_j (B_{nj} + \langle E_{ij} \rangle), \qquad (22)$$

is brought into A_i nucleus with the reaction: $n + (A_i - 1) \rightarrow fission$. Incident neutron energy in this hypothetical reaction equals to $U_i - B_{nA_i}$. In this way the $\nu_i(E_n)$ functions for all nuclides in the mass chain $A+1, A, A-1$ were calculated.

Energy dependence of ν_p versus incident neutron energy estimated with this equation is compared on Fig. 60 with previous evaluations. Bump in ν_p above (n,nf) reaction threshold is due to pre-fission neutrons emitted in ^{234}U(n,nf) reaction. The similar behavior was evidenced in measured data for ^{232}Th(n,f) and ^{238}U(n,f) and was reproduced in the framework of present model. The first-chance ν_p-values [56] for ^{232,233,234}U target nuclides below relevant emissive fission threshold are shown in Table 10. The delayed neutrons yield and decay parameters were taken to be the same as in JENDL-3.2 [6], i.e from [57], [58].

Table 10

Evaluated first chance ν-values for ^{232,233,234}U target nuclides

Target	ν_p^{th}	$\nu_p(E_n$, MeV)	$\nu_p(E_n$ =6 MeV)
^{232}U	2.506	2.677 (1.92)	3.196
^{233}U	2.486	2.584 (1.02)	3.237
^{234}U	2.352	2.688(2.53)	3.165

8.2 Prompt fission neutron spectra

Prompt Fission Neutron Spectra (PFNS) for ^{234}U have been calculated with the model that was previously applied for ^{238}U and ^{232}Th PFNS data analysis [1, 59]. Here is enclosed a brief description of the PFNS model.

8.2.1 Model for PFNS evaluation

For the first chance fission reaction the PFNS are calculated as a sum of two Watt distributions [60]:

$$S_i(E, E_n) = 0.5 \cdot \sum_{j=1,2} W_i(E, E_n, T_{ij}(E_n), \alpha) \tag{23}$$

where

$$T_{ij} = k_{ij} \cdot \sqrt{E^*} = \sqrt{E_r + E_n + B_n - TKE} \tag{24}$$

is the temperature parameters of light and heavy fragments (j=1,2) for nucleus "i", is the ratio of the total kinetic energy (TKE) at the moment of the neutron emission to the TKE value at full acceleration limit. Ratio α was used as a free parameter to fit PFNS experimental data for a number of actinide nuclei, its values for various nuclei scatter only slightly. The ratio of the "temperatures" for light and heavy fragment was the second semi-empirical fitting parameter, it also varies from one target nucleus to another only slightly, we assumed r=1.248 for all actinide nuclei.

Above emissive fission threshold PFNS are described by the equation

$$\begin{aligned} S(E, E_n) &= \nu^{-1}(E_n)(\nu_o(E_n) \cdot \beta_o(E_n) \cdot S_o(E, E_n) + \\ &\quad \nu_1(E_n) \cdot \beta_1(E_n) \cdot S_1(E, E_n) + \beta_1(E_n) \cdot P_{11}(E, E_n) + \\ &\quad \nu_2(E_n) \cdot \beta_2(E_n) \cdot S_2(E, E_n) + \\ &\quad \beta_2(E_n) \cdot [P_{21}(E, E_n) + P_{22}(E, E_n)] + ...), \\ \int P_{ik}(E, E_n)dE &= 1, \end{aligned}$$

$$\nu(E_n) \;=\; \sum_{i=0} \left[(\nu_i(E_n) + i) \cdot \beta_i(E_n) \right], \tag{25}$$

where subscript i denotes i-th chance fission reaction of the $A+1$, A, $A-1$ nuclei after emission of i pre-fission neutrons, $\beta_i(E_n)$ is the i-th chance fission contribution to the observed fission cross section (see Figs. 54 and 55), $\nu_i(E_n)$ is the number of the prompt fission neutron for relevant nucleus, $S_i(E, E_n)$ is the PFNS spectrum without pre-fission neutrons, $P_{ik}(E, E_n)$ is the spectrum of k-th pre-fission neutron for $i-$th chance fission. To estimate observed PFNS, $\nu_i(E_n)$, $\beta_i(E_n)$ and T_{ij} values should be calculated.

The pre-fission neutron spectra $P_{ik}(E, E_n)$ were calculated as described in [59]. The pre-equilibrium pre-fission neutron emission was also taken into account.

The excitation energy U_i of the nucleus $A_i = A + 1 - i$ after emission of i-neutrons was calculated as:

$$U_i = B_n + E_n - \sum_j (B_j + \langle E_{ij} \rangle), \tag{26}$$

where B_j is the neutron binding energy. This allows to estimate the excitation energy of fission fragments as $E^* = E_r + U - TKE$ and calculate the $T_{ij}(E_n)$ energy for each nucleus in the mass chain. The equation for the $\nu_i(E_n)$ calculation is given in previous section.

For $E_n \gtrsim$10 MeV we incorporated an additional correction to remove a discrepancy between measured and calculated data for PFNS of ^{238}U(n,f) and ^{232}Th(n,f) reactions [1]. We assume that the same correction for CMS energy per nucleon E_{v0} should be introduced for ^{234}U(n,f) reaction. The CMS energy was calculated as

$$E_v = \alpha \cdot \alpha_1 \cdot E_{v0}, \tag{27}$$

α_1=1 for $E_n \leq$10 MeV and α_1=0.8 for $E_n >$12 MeV and linearly interpolated for 10$< E_n <$12 MeV. This correction was made either for non-emissive and emissive fission reactions.

8.2.2 Pre-fission (n,$x$nf) neutron spectra

Partial neutron energy distributions $P_{ik}(E, E_n)$ of (n,$x$nf), x = 1, 2, 3, reactions are calculated with Hauser-Feshbach model taking into account fission and gamma-emission competition to neutron emission, actually neutron spectra are calculated simultaneously with fission and (n,xn) reaction cross sections [59]. The pre-equilibrium emission of first neutron is fixed by the description of high energy tails of (n,2n) reaction cross sections and (n,f) reaction cross sections for ^{238}U and ^{232}Th target nuclides. First neutron spectrum of the ^{234}U(n,nf) reaction is the sum of evaporated and pre-equilibrium emitted neutron contributions. Second and third neutron spectra for ^{234}U(n,$x$nf) fission reactions are assumed

to be evaporative. Pre-fission neutron spectrum of ^{234}U(n,nf) reaction, especially its hard energy tail, is sensitive to the description of fission probability of ^{234}U nuclide near fission threshold (see below).

Partial neutron spectra are shown on Figs. 62-68. Components of first, second and third neutron spectra for E_n =20 MeV are shown on Figs. 62, 63 and 64. Components of first and second neutron spectra for E_n =14 MeV are shown on Figs. 65, 66, for E_n =8 MeV - on Figs. 67, 68.

At E_n =20 and 14 MeV major contribution to the first neutron spectrum comes from (n,nf) reaction spectrum (see Figs. 62, 65), at lower energy E_n =8 MeV its soft part is lower than the first neutron component of (n,2nγ) reaction, while hard part of (n,nf) reaction neutron is comparable with soft energy tail of (n,nγ) reaction spectrum (see Fig. 67). Spectrum of (n,nγ) reaction actually is just hard energy tail of 'pre-equilibrium' component of first neutron spectrum. Shapes of first neutron spectra of (n,nγ) and (n,2nγ) reactions at E_n =20 (Fig. 62) and 14 MeV (Fig. 65) are rather similar, soft part being defined by neutron emission competition of higher neutron multiplicity reactions. This lowering of soft part of first neutron spectrum of (n,2nγ) reaction disappears for E_n =8 MeV.

At E_n =20 MeV major contribution to the second neutron spectrum (up to $E \sim$8 MeV) comes from (n,2nf) reaction (see Fig. 63), it is defined by the fission probability of ^{233}U. Soft parts of the second neutron spectra of (n2n) and (n,3n) reactions are comparable. At lower incident neutron energy E_n =14 MeV major contribution to the second neutron spectrum comes from (n,2nγ) reaction (see Fig. 66). At lower energy E_n =8 MeV major contribution to the second neutron spectrum also comes from (n,2nγ) reaction (see Fig. 68)

At E_n =20 MeV most contribution to the third neutron spectrum comes from (n,3nγ) reaction (see Fig. 64), that of the (n,3nf) reaction being rather low.

8.2.3 Comparison with previous evaluations

The PFNS for the ^{234}U data file of ENDF/B-VI [4] library were assumed to be Maxwellian, while for the JENDL-3.2 [6] PFNS were calculated with Madland-Nix [61] model. The peculiarities similar to ^{238}U, ^{232}Th nuclei [59] for which the experimental data are available, are also noticed. The PFNS calculated with present model demonstrate more complicated shape as compared with simple Maxwellian estimate for E_n =2 MeV (Fig. 69). At the same time the Madland-Nix [61] model predicts very low contribution of soft neutrons with $E \lesssim$2 MeV. The excess of higher energy neutrons ($E \gtrsim$2 MeV) can be explained by the higher average energy for the PFNs that was assumed in calculations for JENDL-3.2 [6].

Above emissive fission threshold at E_n =7 MeV the contribution of the second chance fission reaction ^{234}U(n,f) is comparable with that of non-emissive fission (see Figs. 54, 55). The average energy removed by first pre-fission neutron is much smaller than the average energy of post-fission neutrons. This peculiarity explains appearance of low energy bump in the spectrum of fission neutrons (Fig.

70). At higher incident neutron energies of E_n =14 and 20 MeV (Figs. 71 and 72), the PFN spectrum also consists of several components. One of them is connected with pre-equilibrium first neutron emission and produces bump at $E_{th} \sim E_n - B_{fA}$ ~7 MeV prompt fission neutron energy for E_n =14 MeV or E_{th} ~12 MeV for E_n = 20 MeV, B_{fA} is the effective fission barrier of ^{234}U. Soft neutron component connected with pre-fission neutrons from (n,2nf) reaction is noticed on Fig. 71 for E_n =14 MeV. Irregularity around 7 MeV for PFNS for E_n = 20 MeV (see Fig. 72) might be correlated with the first neutron spectrum of ^{234}U(n,2nf) reaction, $P_{21}(E, E_n)$ ((n,2nf)[1]), it is sensitive to the description of fission probability of ^{233}U near fission threshold.

Calculated PFNS of ^{238}U(n,f) spectra reproduce available measured data. We will compare with them calculated PFNS of ^{234}U(n,f) to define the influence of different partial chance fission contributions. In the domain of emissive fission rather different contribution of (n,nf) reaction for the ^{234}U(n,f) reaction, than in case of ^{238}U(n,f) reaction [1] is observed (see Figs. 54, 55). Relative contribution of ^{234}U (n,nf) reaction is lower than in case of ^{238}U (n,nf) reaction for $E_n \lesssim 8$ MeV, but it is much higher for $E_n \gtrsim 8$ MeV. The low energy spectrum component due to pre-fission neutrons makes a strong influence on the PFNS shape. For ^{234}U(n,f) reaction the contribution of pre-fission neutrons from (n,nf) reaction to the observed PFNS in fission neutron energy range $E_{th} \sim E_n - B_f$ should be less pronounced than in case of ^{238}U(n,f) for $E_n \lesssim$8 MeV and more pronounced for higher incident neutron energies. Actually, the energy dependence of PFNS for ^{234}U(n,f) and ^{238}U(n,f) reactions at fission neutron energies $E_n \lesssim E_{th}$ resembles the shape of fission probability of ^{234}U or ^{238}U nuclide, respectively. Figure 55 shows the comparison of emissive chance fission contributions to the total fission cross section of ^{234}U (n,f) and ^{238}U (n,f) reactions. The contribution of ^{234}U(n,nf) reaction cross section to the observed fission cross section ^{234}U(n,f) is shown on Fig. 54.

At E_n =7 MeV (see Fig. 70) low energy components due to pre-fission neutrons from (n,nf) reaction reduce average energy very much as it was observed for ^{238}U(n,f) and ^{232}Th(n,f) reactions. Since the contribution of (n,nf) reaction at E_n =7 MeV is higher in case of ^{238}U(n,f), than in case of ^{234}U(n,f), it is pronounced in the low energy part of PFNS (see Fig. 70). However, the situation is quite different for higher incident energies $E_n \gtrsim$8 MeV (see Fig. 71, 72), the contribution of (n,nf) reaction in PFNS now is higher in case of ^{234}U(n,f) reaction. As shown on Fig. 61, the contribution of ^{234}U(n,2nf) reaction to the observed ν_p-value is lower than in case of ^{238}U(n,f) reaction.

The average energy of the fission neutron versus incident energy is shown in fig. 73. At incident neutron energy $E_n \lesssim 6$ MeV, the ν_p-value energy dependence is proportional to $\sqrt{U_i}$, however, at higher excitations we have more complicated excitation energy dependence. At E_n ~7 MeV the average energy reduces by ~150 keV due to the contribution of low energy neutrons from (n,nf) reaction. This tendency, visible in measured data for the ^{238}U(n,f) PFNS, is predicted for

the ^{234}U(n,f) reaction.

8.3 Neutron emission spectra comparison

There is no measured data on neutron emission spectra for ^{234}U+n interaction. Relative contribution of prompt fission neutron spectra to the neutron emission spectra is higher than in case of ^{238}U+n interaction. In case of ^{238}U calculated neutron emission spectra reproduce structures in measured data, these structures are correlated with excitation of first octupole band ($K^\pi = 0^-$) levels and levels of $\beta-$ vibration ($K^\pi = 0_2^+$) and $\gamma-$bands ($K^\pi = 0_3^+, 2^+$). Estimates of inelastic scattering to vibrational levels of first octupole band and higher lying $\beta-$ and $\gamma-$ bands of ^{238}U were shown to be extremely important for incident neutron energies $E_n \leq 3$ MeV. In case of ^{234}U there is no measured data to define a resolution function. The parameters of resolution function usually are fitted to the elastic peak shape. Using the parameters obtained for ^{238}U+n data description in case of ^{234}U+n, one can observe that the structures due to discrete level excitation are present. They could be revealed introducing a better secondary neutron energy resolution. Figures 74–80 show emission spectra, calculated for 1.2, 2.6, 3.55, 6.1, 11.8. 14.05 and 18 MeV, these energies were selected because for these energies emission neutron spectra were measured for ^{238}U target nuclide. Bumps evident in neutron emission spectra for E_n ~2 - 4 MeV could be correlated with excitation of discrete levels of various collective bands. The elastic as well as inelastic scattering to 2^+, 4^+, 6^+ and 8^+ levels of ground state rotational band contribution were added to the other inelastic scattered and fission neutrons. They were broadened using model resolution function of Gaussian type with a constant resolution width. PNFS labels prompt fission neutron spectra. Arrows on figures show emitted neutron energy, corresponding to excitation of octupole and $\beta-$vibration levels.

The direct excitation of ground state rotational band levels 0^+, 2^+, 4^+, $6^+$and 8^+ was estimated within rigid rotator model. To calculate the direct excitation cross sections for $\beta-$ vibration ($K^\pi = 0_2^+$), $\gamma-$ vibration ($K^\pi = 0_3^+$) and anomalous rotation band ($K^\pi = 2^+$) as well as octupole ($K^\pi = 0^-$, 2^-) band levels a soft rotator model was employed. For ground state band levels the direct and compound components became comparable above ~1.5 MeV, for octupole ($K^\pi = 0^-$) band levels - above ~2.5 MeV, while for $\beta-$ vibration ($K^\pi = 0^+$) levels - above ~3 MeV. With increase of incident energy the influence of discrete level excitation diminishes, while the role of continuum level excitation grows.

For incident neutron energy higher than emissive fission threshold, emissive neutron spectrum is deconvoluted, components of 1st, 2nd and 3d neutron spectra are provided, where applicable. We have calculated 1st, 2nd and 3d neutron spectra for the (n,nγ), (n,2n) and (n,3n) reactions.

According to the ENDF/B-VI format specifications the secondary neutron spectra are included in the following way. Calculated spectra were summed up

and tabular spectra for the (n,nγ), (n,2n) and (n,3n) reactions were obtained.

Spectrum of (n,nγ) reaction actually is just hard energy tail of 'pre-equilibrium' component of first neutron spectrum. Spectrum of the first neutron of (n,2n) reaction is much softer, although 'pre-equilibrium' component still comprise appreciable part of it. First neutron spectrum of (n,3n) reaction is actually of evaporative nature. First neutron spectrum of (n,nf) reaction has rather long pre-equilibrium high-energy tail. First neutron spectrum of (n,2nf) reaction, as that of (n,3n) reaction, is of evaporative nature.

Figures 81, 82, 83, 84 and 85 compare neutron spectra of (n,nγ) reaction of JENDL-3.2 [6] and ENDF/B-VI [4] with present calculation. Neutron spectra ENDF/B-VI [4] are evaporative. At E_n =20 and 14 MeV hard energy tails of 'pre-equilibrium' component of first neutron spectrum of JENDL-3.2 [6] and present evaluation are rather similar, for lower energies E_n =10 and 8 MeV the former estimate is much softer. Average energies of first neutron spectra for ENDF/B-VI are much lower than that of present evaluation.

Table 11

Average energies of secondary neutron spectra for ^{234}U+n

1st neutron average energy, MeV							
E_n,MeV	(n,n')			(n,2n)	(n,n'f)	(n,3n)	(n,2n'f)
	Present	B-VI	J-3.2	Present			
6.0	1.071	0.790	0.902	0.000	0.264		
8.0	2.419	0.981	1.367	0.549	0.936		
10.0	4.184	1.173	2.800	1.133	1.419		
14.0	8.189	1.556	7.842	2.734	2.448	0.513	0.780
20.0	14.180	1.965	14.058	8.254	4.000	2.300	2.648

<E> for (n,2n), MeV				<E> for (n,3n), MeV		
E_n,MeV	Present	J-3.2	B-VI	Present	J-3.2	B-VI
8.0	0.473	0.415	0.656			
10.0	0.905	0.836	1.162			
14.0	1.824	1.408	1.513	0.402	0.447	0.740
20.0	4.658	4.943	2.929	1.417	1.180	1.738

Figures 86, 87, 88 and 89 show the comparison of (n,2n) reaction spectra of JENDL-3.2, ENDF/B-VI and present evaluation at E_n =20, 14, 10 and 8 MeV. The discrepancies above ~5 MeV and ~3 MeV, ~1 MeV and ~0.5 MeV respectively, are due to first neutron spectra of (n,2n) reaction in present calculation being of hard pre-equilibrium nature. Figure 89 shows the comparison of (n,2n) reaction spectra at 8 MeV. Figures 90 and 91 show spectra of (n,3n) reaction for incident neutron energy of 14 and 20 MeV, respectively.

In summary, inclusion of pre-equilibrium emission changes significantly the average energies of emitted neutron spectra. That is shown in Table 11, where the average secondary neutron energies for current, ENDFB-VI and JENDL-3.2 evaluations are compared. The most significant is the change of neutron spectra of (n,nγ) reaction.

9 Conclusions

The statistical Hauser-Feshbach-Moldauer model calculation of neutron-induced reaction cross sections for ^{234}U target nuclide shows the fair description of available data base on fission cross section. Statistical calculations were employed for predicting total, capture, inelastic, (n,2n) and (n,3n) reaction cross sections. Rigid and soft rotator coupled channel models were used to predict inelastic scattering cross sections for level excitation. Prompt fission neutron spectra are predicted with the model, tested on the PFNS description of ^{238}U(n,f) and ^{232}Th(n,f) reactions.

10 Acknowledgments

This work was supported within the Project B-404 "Actinide Nuclear Data Evaluation" of International Science and Technology Center (Funding Party Japan).

*) Permanent address: Institute of Physics and Power Engineering, 249020, Obninsk, Russia

References

[1] Maslov V.M., Porodzinskij Yu. V., Baba M., Hasegawa A., Kornilov N.V., Kagalenko A.B., Proc. International Conference on Nuclear Data for Science and Technology, October 7-12, 2001, Tsukuba, Japan, p. 148, 2002.

[2] Maslov V.M. , Yu. V. Porodzinskij, M. Baba, A. Hasegawa, Ann. Nucl. Energy, 29, 1707 (2002).

[3] Maslov V.M., Porodzinskij Yu. V., Baba M., Hasegawa A., Nucl. Sci. Eng. (2003).

[4] Roussin R.W., Young P.G., McKnight R., Proc. Int. Conf. Nuclear Data for Science and Technology, Gatlinburg, USA, May 9-13, 1994, p. 692, J.K. Dickens (Ed.), ANS, 1994.

[5] Mughabghab S.F.and Garber D.I., BNL-325, VOL. 1, BRookhaven National Laboratory (2973).

[6] JAERI-Data/Code, 98-006 (Part II), (Eds.) K. Shibata and T. Narita, 1998.

[7] James G.D., Dabbs J.W.T., Harvey J.A., Hill N.W. Phys. Rev. C, 15, 2083 (1977).

[8] Wagemans C., Wagemans J., Serot O., Nucl. Sci. Eng., 141, 171 (2002).

[9] Wagemans C., Wagemans J., Geltenbort P., Zimmer O., Nucl. Sci. Eng. 132, p. 308-311 (1999).

[10] Borzakov S., Florek M.,Konovalov V. et al. Measurement of the subthreshold neutron induced fission cross-sections of ^{234}U, ^{237}Np and ^{243} Am. Proc. Int. Workshop on Fission and Fission-Product Spectroscopy. Seyssins, France, AIP Conf. Proc. 447. P.269-276 (1998).

[11] Maslov V.M., Porodzinskij Yu.V. JAERI-Research 98-038, Japan, 1998.

[12] Handbook for Calculations of Nuclear Reaction Data: Reference input parameter library,IAEA-TECDOC-1034, p.81, 1998, Vienna.

[13] Maslov V.M., INDC(BLR)-013, IAEA, Vienna,1998.

[14] Ignatjuk A.V., Istekov K.K., Smirenkin G.N. Sov. J. Nucl. Phys. 29, 450 (1979).

[15] Stavinskij V.S., Shaker M.O., Nucl. Phys., 62, 667 (1965).

[16] Moldauer P.A., Proc.Conf. on Neutron Cross Sections and Technology, Washington, D.C., USA, March 22-24, 1966, p. 613-622, AEC (1966).

[17] Block R.C., Slauchter G.G., Harvey J.A. Nucl. Sci. Eng. 8, 112 (1960).

[18] McCallum G.J. J. Nucl. Energ. 6, 181 (1958).

[19] Harvey J.A., Huges D.J. Phys. Rev.,109, 471 (1958).

[20] Sokolovskiy V.V. J. Atomnaya Energiya, 2, 2, 129, (1957).

[21] Cullen D. PREPRO2000: 2000 ENDF/B Pre-Processing Codes.

[22] NJOY 94.10 Code System for Producing Pointwise and Multigroup Neutron and Photon Cross Sections from ENDF/B Data, RSIC Peripheral Shielding Routine Collection, ORNL, PSR-355, LANL, Los Alamos, New Mexico (1995).

[23] Muradian G.V., Furman W.I. Private communication, 1998.

[24] Porodzinskij Yu.V., Sukhovitskij E.Sh, Yadernaya Fizika, 59, 247 (1996).

[25] Moldauer P.A., Phys. Rev., C11, 426 (1975).

[26] Tepel J.W., Hoffman H.M., Weidenmuller H.A. Phys. Lett. 49, 1 (1974)

[27] Uhl M., Strohmaier B., IRK-76/01, IRK, Vienna (1976).

[28] Ignatjuk A.V., Maslov V.M., Proc. Int. Symp. Nuclear Data Evaluation Methodology, Brookhaven,USA, October 12-16, 1992, p.440, World Scientific, 1993.

[29] Maslov V.M., Kikuchi Y., JAERI-Research 96-030, 1996.

[30] Howard W.M., Möller P. Atomic Data and Nuclear Data Tables, 25, 219 (1980).

[31] Maslov V.M., Physics of Atomic Nuclei, 63, 161 (2000).

[32] Maslov V.M., Zeit. Phys. A, Hadrons & Nuclei, 347, 211 (1994).

[33] Fu C. Nucl. Sci. Engng. 86, 344 (1984).

[34] Maslov V.M., Porodzinskij Yu.V., Hasegawa A., Shibata K. JAERI-Research 98-040, Japan, 1998.

[35] Y.A. Ellis-Akovali , Nuclear Data Sheets, 40, 567 (1988).

[36] Myers W.O., Swiatecky W.J., Ark. Fyzik, 36, 243 (1967).

[37] Bjornholm S., Lynn J.E. Rev. Mod. Phys., 52, 725 (1980).

[38] V.M. Maslov and Kikuchi Ya., Nucl. Sci. Eng. 124, 492 (1996).

[39] Bolsterli M., Fiset E.O., Nucl. Sci.Eng., 63, 250 (1977).

[40] Behrens J.W., Carlson G.W. Nucl. Sci. Eng., 63, 250 (1977).

[41] Fursov B.I., Baranov E.Yu., Klemyshev M.P., Samylin B.F., Smirenkin G.N., Turchin Yu.M. Atomnaya Energiya, 71, 320 (1991).

[42] Goverdovskiy A.A., Gordyushin A.K., Kuz'minov B.D., Mitrofanov V.F., Sergachev A.I. Atomnaya Energiya, 60, 416 (1986).

[43] Goverdovskij A.A., Gordyushin A.K., Kuz'minov B.D., Mitrofanov V.F., Sergachev A.I. Atomnaya Energiya, 63, 60 (1987).

[44] Goverdovskiy A.A., Gordyushin A.K., Kuz'minov B.D., Mitrofanov V.F., Sergachev A.I. Atomnaya Energiya, 62, 190 (1987).

[45] Kanda K., Imaruoka H., Yoshida K., Sato O., Hirakawa N. Radiation Effects, 93, 233 (1986).

[46] Meadows J.W. Nucl. Sci. Eng., 65, 171 (1978).

[47] Meadows J.W. Ann .Nucl. Ener., 15 , 421 (1988).

[48] Lamphere R. Phys.Rev., 104, 1654 (1956).

[49] Lamphere R. Nucl.Phys., 38, 561 (1962).

[50] White P.H., Hodgkinson J.G., Wall G.J. IAEA Conf. on the Physics and Chemistry of fission, Salzburg, 22-26 March, 1965, vol. 1, p. 219, Paper SM-60/14 (1965).

[51] White P.H. and Warner G.P. J. Nucl. Energy, 21, 671 (1967).

[52] Arlt et al., Proc. International Conference on Nuclear Data for Science and Technology, October 7-12, 1979, Knoxville, USA, p. 995, 1979.

[53] Plompen A.J.M., Goddio C., Maslov V.M., Porodzinskij Yu.V. Proc. VIII International Seminar on Interaction of Neutrons with Nuclei, Dubna, Russia, May 17-20, 2000, p. 153, 2000.

[54] V.M. Maslov, Yu. V. Porodzinskij, M. Baba, A. Hasegawa, Proc. 11th Intern. Symp. on Capture an Gamma-ray Spectroscopy, Sptember 2-6, 2002, Prague, Czhech Republic.

[55] Mather D.S. et al.: Nucl. Phys., 66, 149 (1965).

[56] Malinovskij V.V. VANT (ser. Yadernie constanty), 1987, No.2, 25.

[57] Tuttle R.J.: INDC(NDS)-107/G+Special, p.29 (1979).

[58] Brady M.C. and England T.R.: Nucl. Sci. Eng., 103, 129(1989).

[59] V.M. Maslov, Yu. V. Porodzinskij, M. Baba, A. Hasegawa, N.V. Kornilov, A.B. Kagalenko, Proc. X International Seminar on Interaction of Neutrons with Nuclei, Dubna, Russia, May 17-20, 2002, 2002.

[60] Kornilov N.V., Kagalenko A.B., Hambsch F.-J. Physics of Atomic Nuclei, 62, 173 (1999).

[61] Madland D.C., Nix J.R. Nucl. Sci. Eng., 81, 213 (1982).

11 Figure captions

Fig. 1 Fission cross section of ^{234}U.
Fig. 2 Cumulative sum of levels of ^{234}U.
Fig. 3 Cumulative sum of reduced neutron widths of ^{234}U.
Fig. 4 Level spacing distribution of ^{234}U.
Fig. 5 Reduced neutron width distribution of ^{234}U.
Fig. 6 Cumulative distribution of reduced neutron widths of ^{234}U.
Fig. 7 Total cross section of ^{234}U.
Fig. 8 Elastic cross section of ^{234}U.
Fig. 9 Fission cross section of ^{234}U.
Fig. 10 Inelastic cross section of ^{234}U.
Fig. 11 Capture cross section of ^{234}U.
Fig. 12 Capture cross section of ^{234}U.
Fig. 13 Average reduced neutron width of ^{234}U, $l = 0, J = 1/2$.
Fig. 14 Average reduced neutron width of ^{234}U, $l = 1, J = 1/2$.
Fig. 15 Average reduced neutron width of ^{234}U, $l = 1, J = 3/2$.
Fig. 16 Average reduced neutron width of ^{234}U, $l = 2, J = 3/2$.
Fig. 17 Average reduced neutron width of ^{234}U, $l = 2, J = 5/2$.
Fig. 18 Average fission width of ^{234}U, $l = 0, J = 1/2$.
Fig. 19 Average fission width of ^{234}U, $l = 1, J = 1/2$.
Fig. 20 Average fission width of ^{234}U, $l = 1, J = 3/2$.
Fig. 21 Average fission width of ^{234}U, $l = 2, J = 3/2$.
Fig. 22 Average fission width of ^{234}U, $l = 2, J = 5/2$.
Fig. 23 Total cross section of ^{234}U.
Fig. 24 Elastic scattering cross section of ^{234}U.
Fig. 25 Cumulative number of levels of ^{234}U.
Fig. 26 Cumulative number of levels of ^{233}U.
Fig. 27 Level density of ^{233}U.
Fig. 28 Level density of ^{234}U.
Fig. 29 Fission cross section of ^{233}U.
Fig. 30 Fission cross section of ^{234}U.
Fig. 31 Cross section of ^{234}U: 0.043498 MeV, 2^+ level excitation.
Fig. 32 Cross section of ^{234}U: 0.143351 MeV, 4^+ level excitation..
Fig. 33 Cross section of ^{234}U: 0.296071 MeV, 6^+ level excitation.
Fig. 34 Cross section of ^{234}U: 0.49704 MeV, 8^+ level excitation.
Fig. 35 Cross section of ^{234}U: 0.78629 MeV, 1^- level excitation.
Fig. 36 Cross section of ^{234}U: 0.80988 MeV, 0^+ level excitation.
Fig. 37 Cross section of ^{234}U: 0.8493 MeV, 3^- level excitation.
Fig. 38 Cross section of ^{234}U: 0.8517 MeV, 2^+ level excitation.
Fig. 39 Cross section of ^{234}U: 0.92674 MeV, 2^+ level excitation.
Fig. 40 Cross section of ^{234}U: 0.94785 MeV, 4^+ level excitation.
Fig. 41 Cross section of ^{234}U: 0.9626 MeV, 5^- level excitation.

Fig. 78 Neutron emission spectrum of ^{232}U for incident neutron energy 11.8 MeV.
Fig. 79 Neutron emission spectrum of ^{232}U for incident neutron energy 14.05MeV.
Fig. 80 Neutron emission spectrum of ^{232}U for incident neutron energy 18 MeV.
Fig. 81 Comparison of (n,n'γ) reaction neutron spectra of ^{234}U for incident neutron energy 20 MeV.
Fig. 82 Comparison of (n,n'γ) reaction neutron spectra of ^{234}U for incident neutron energy 14 MeV.
Fig. 83 Comparison of (n,n'γ) reaction neutron spectra of ^{234}U for incident neutron energy 10 MeV.
Fig. 84 Comparison of (n,n'γ) reaction neutron spectra of ^{234}U for incident neutron energy 8 MeV.
Fig. 85 Comparison of (n,n'γ) reaction neutron spectra of ^{234}U for incident neutron energy 6 MeV.
Fig. 86 Comparison of (n,2n) reaction neutron spectra of ^{234}U for incident neutron energy 20 MeV.
Fig. 87 Comparison of (n,2n) reaction neutron spectra of ^{234}U for incident neutron energy 14 MeV.
Fig. 88 Comparison of (n,2n) reaction neutron spectra of ^{234}U for incident neutron energy 10 MeV.
Fig. 89 Comparison of n,2n) reaction neutron spectra of ^{234}U for incident neutron energy 8 MeV.
Fig. 90 Comparison of (n,3n) reaction neutron spectra of ^{234}U for incident neutron energy 20 MeV.
Fig. 91 Comparison of (n,3n) reaction neutron spectra of ^{234}U for incident neutron energy 14 MeV.

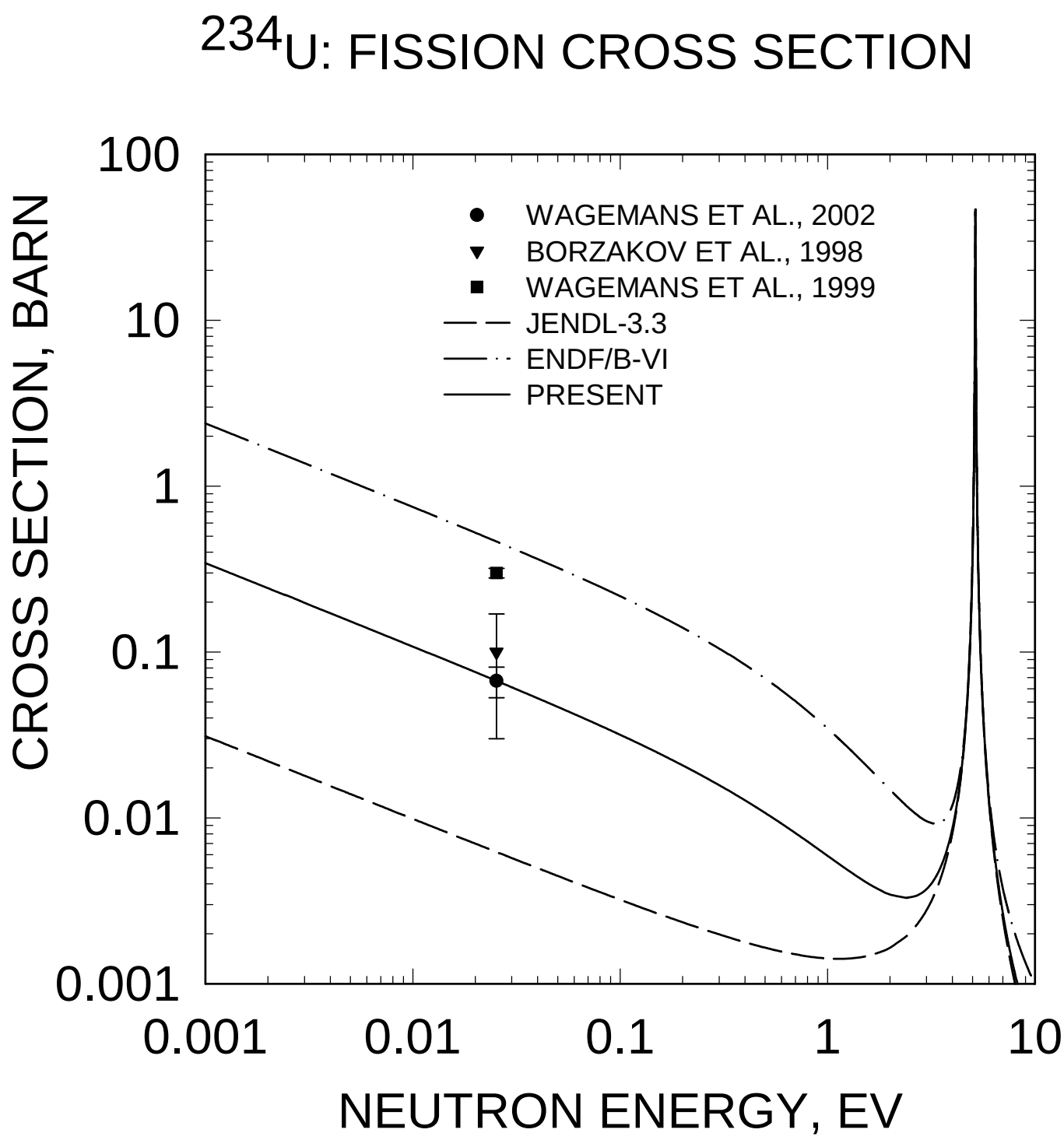
^{234}U: FISSION CROSS SECTION
CROSS SECTION, BARN
100
10
1
0.1
0.01
0.001
0.001
0.01
0.1
1
10
NEUTRON ENERGY, EV
WAGEMANS ET AL., 2002
BORZAKOV ET AL., 1998
WAGEMANS ET AL., 1999
JENDL-3.3
ENDF/B-VI
PRESENT

FIG. 1

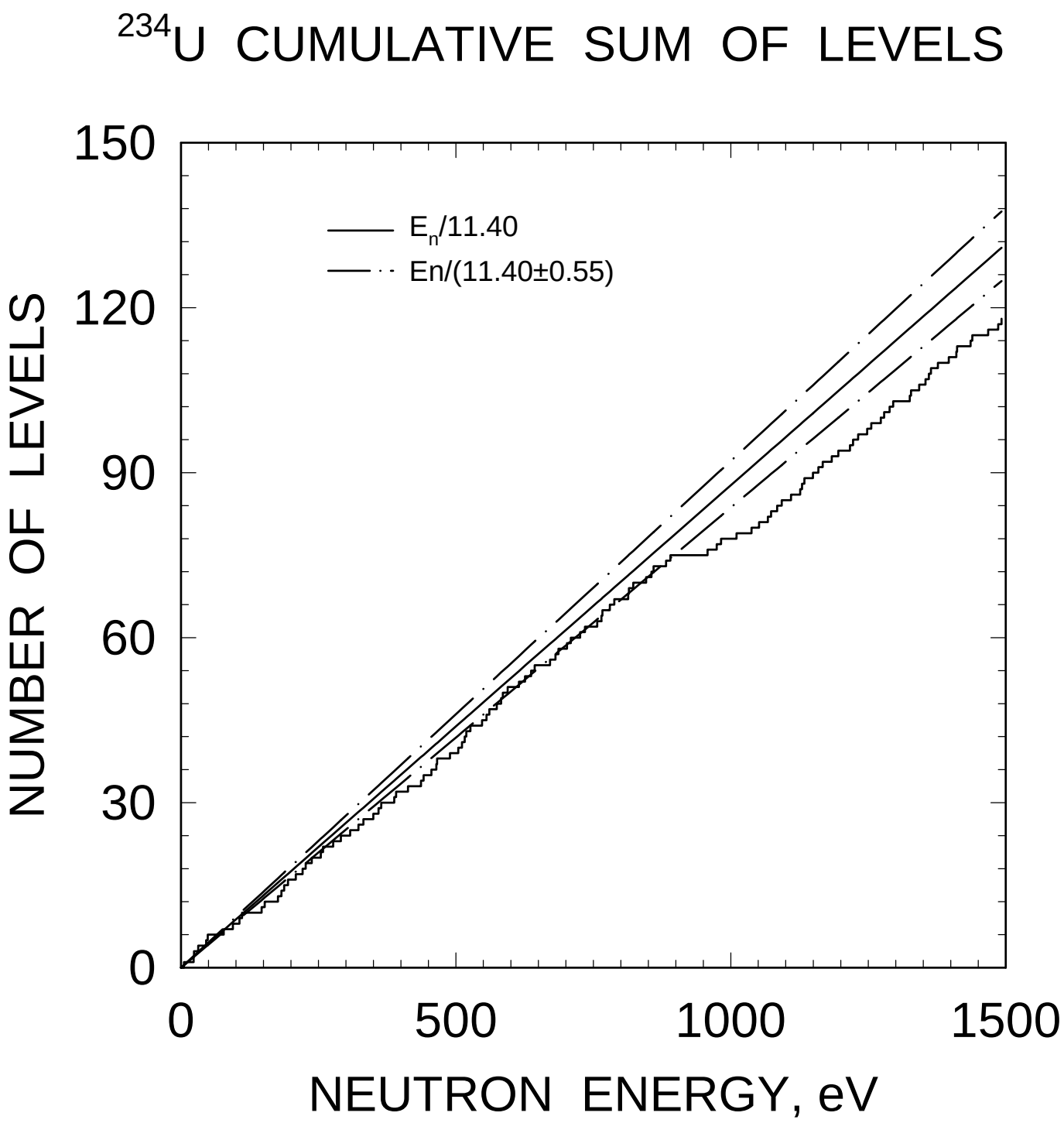
^{234}U CUMULATIVE SUM OF LEVELS
NUMBER OF LEVELS
150
120
90
60
30
0
0
500
1000
1500
NEUTRON ENERGY, eV
E_n/11.40
En/(11.40±0.55)

FIG. 2

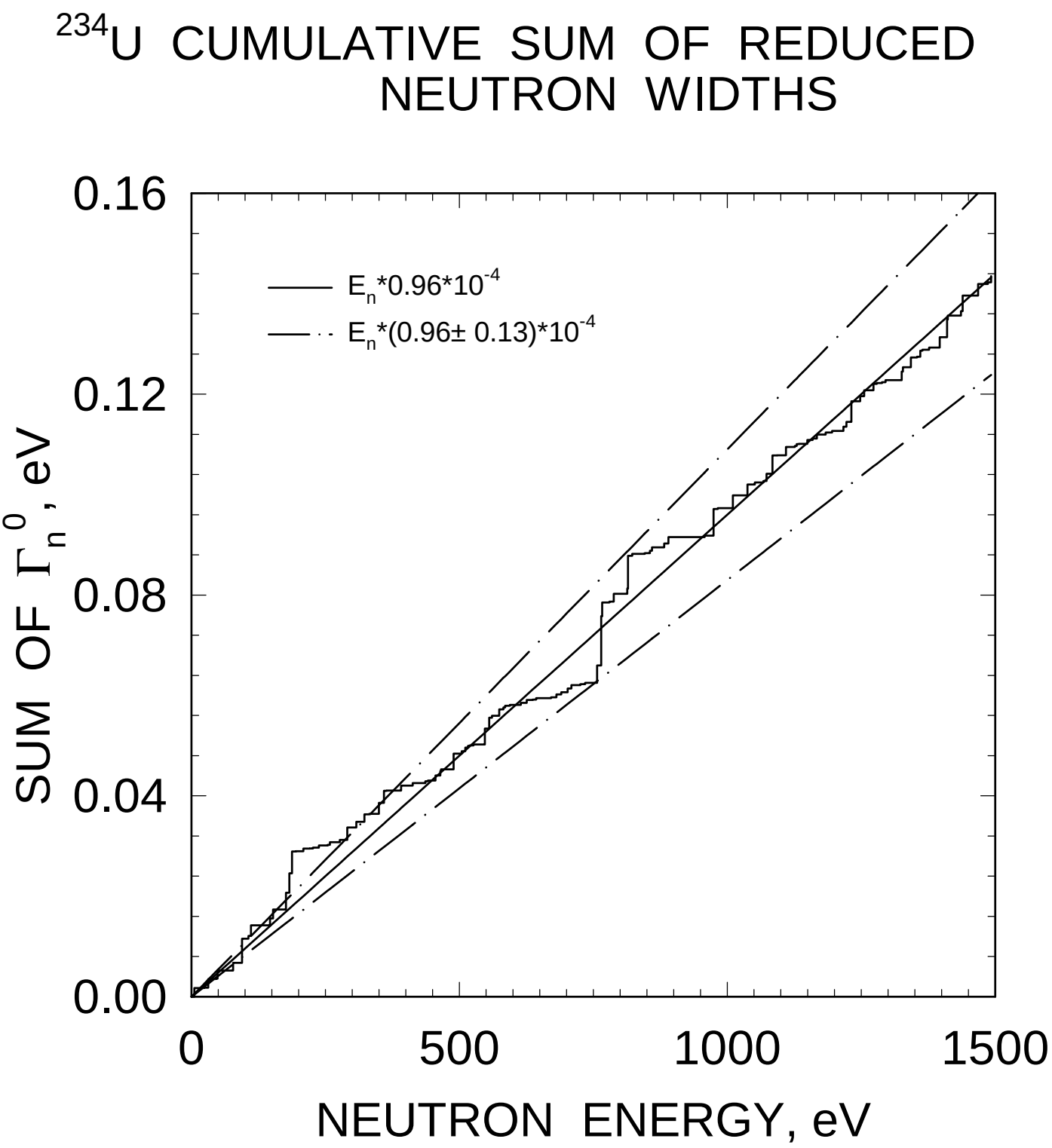
^{234}U CUMULATIVE SUM OF REDUCED NEUTRON WIDTHS
0.16
0.12
0.08
0.04
0.00
SUM OF Γ_n^0, eV
E_n*0.96*10^{-4}
E_n*(0.96± 0.13)*10^{-4}
0
500
1000
1500
NEUTRON ENERGY, eV

FIG. 3

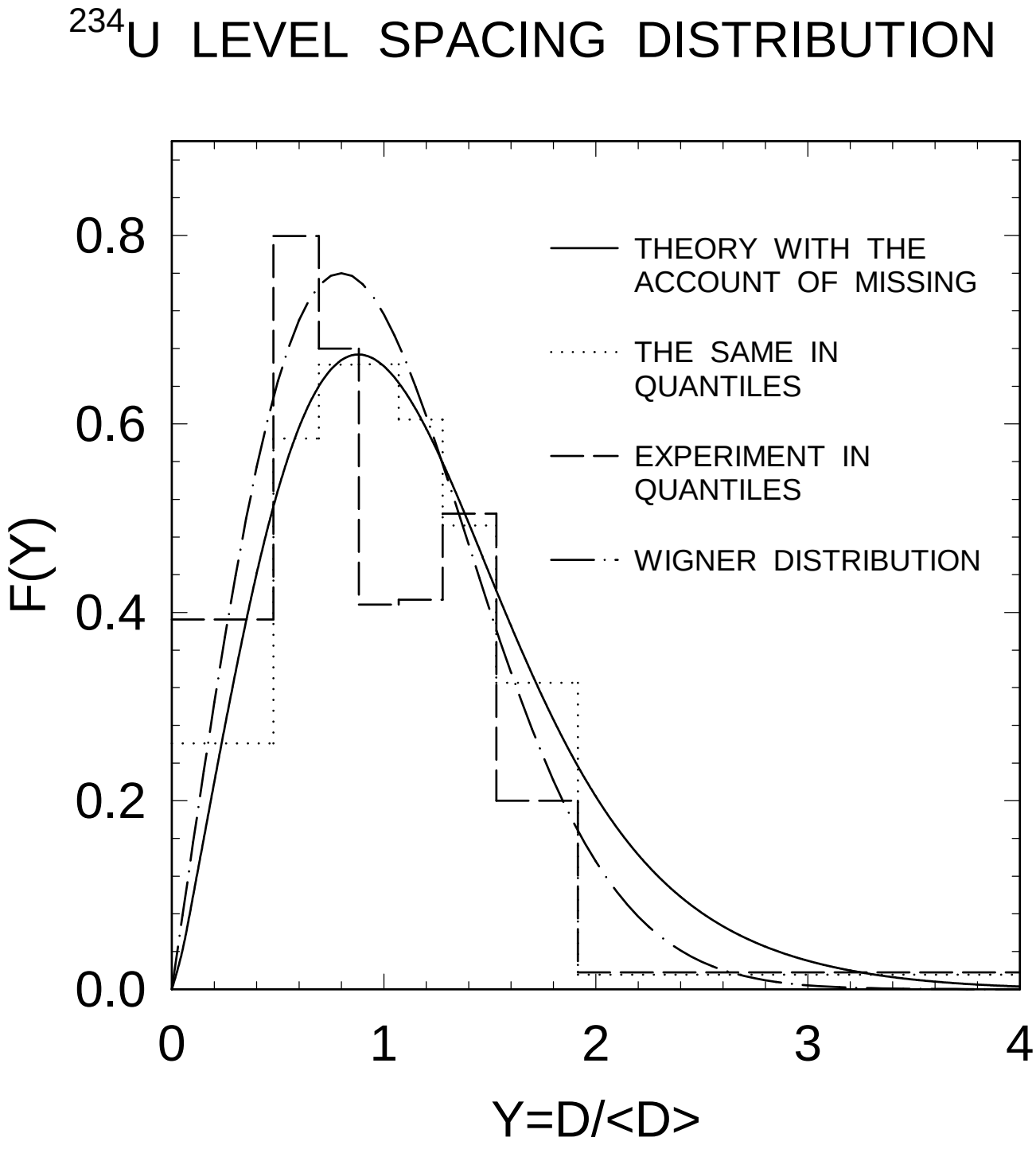
^{234}U LEVEL SPACING DISTRIBUTION
F(Y)
0.0
0.2
0.4
0.6
0.8
0
1
2
3
4
Y=D/<D>
THEORY WITH THE ACCOUNT OF MISSING
THE SAME IN QUANTILES
EXPERIMENT IN QUANTILES
WIGNER DISTRIBUTION

FIG. 4

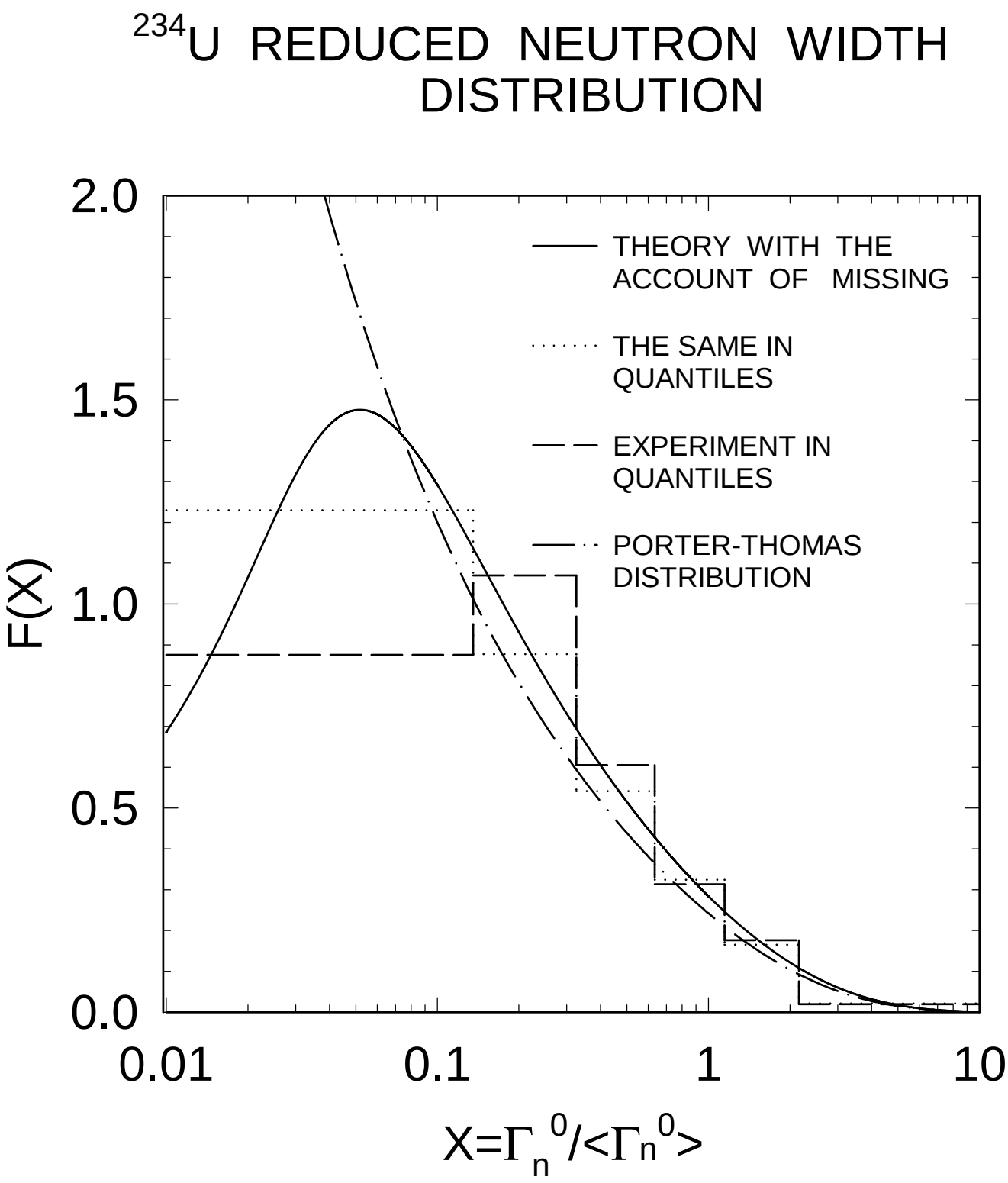
^{234}U REDUCED NEUTRON WIDTH DISTRIBUTION
2.0
1.5
1.0
0.5
0.0
F(X)
0.01
0.1
1
10
X=Γn0/<Γn0>
THEORY WITH THE ACCOUNT OF MISSING
THE SAME IN QUANTILES
EXPERIMENT IN QUANTILES
PORTER-THOMAS DISTRIBUTION

FIG. 5

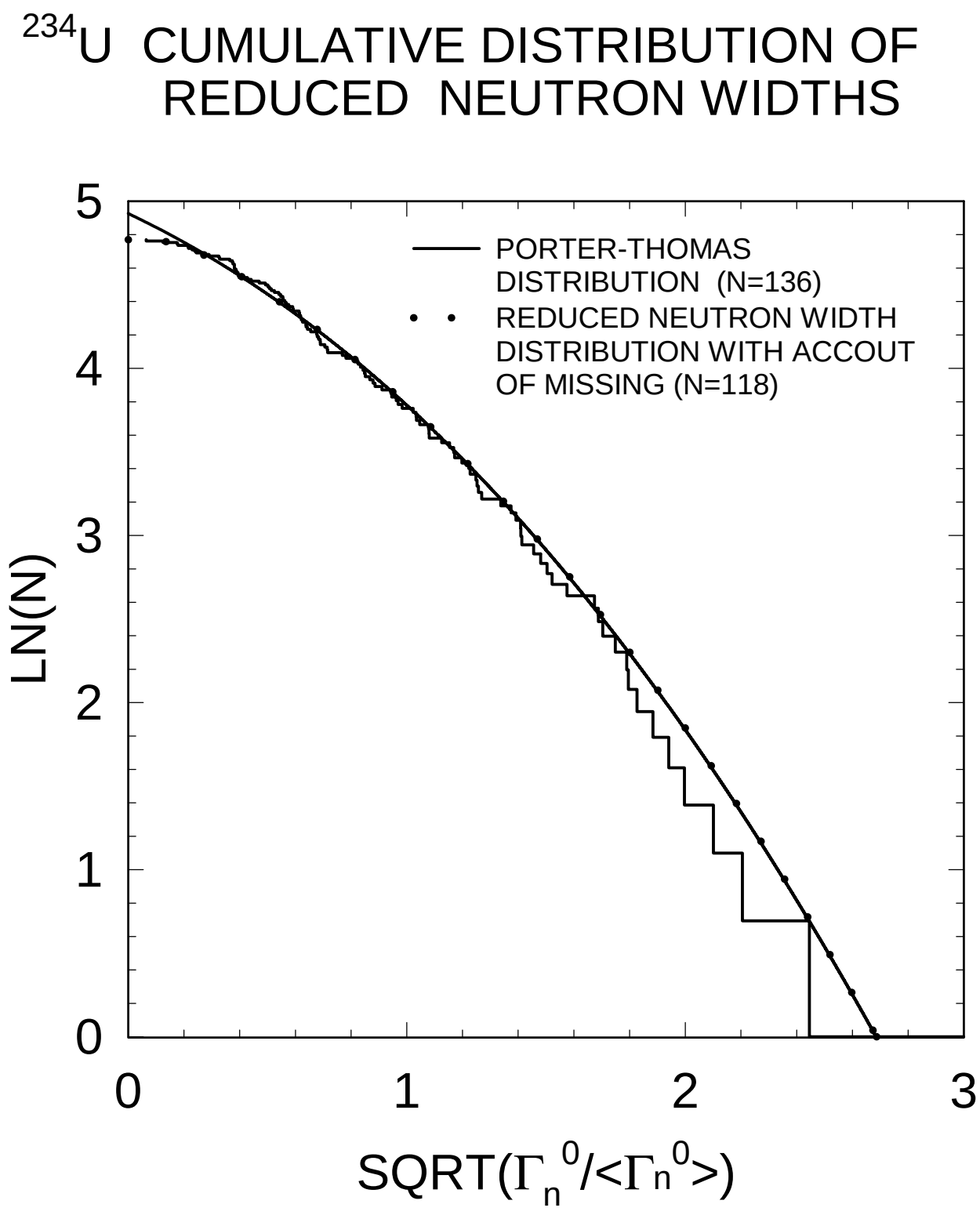
^{234}U CUMULATIVE DISTRIBUTION OF REDUCED NEUTRON WIDTHS
PORTER-THOMAS DISTRIBUTION (N=136)
REDUCED NEUTRON WIDTH DISTRIBUTION WITH ACCOUT OF MISSING (N=118)
LN(N)
SQRT($\Gamma_n^0/\langle\Gamma_n^0\rangle$)
0
1
2
3
4
5

FIG. 6

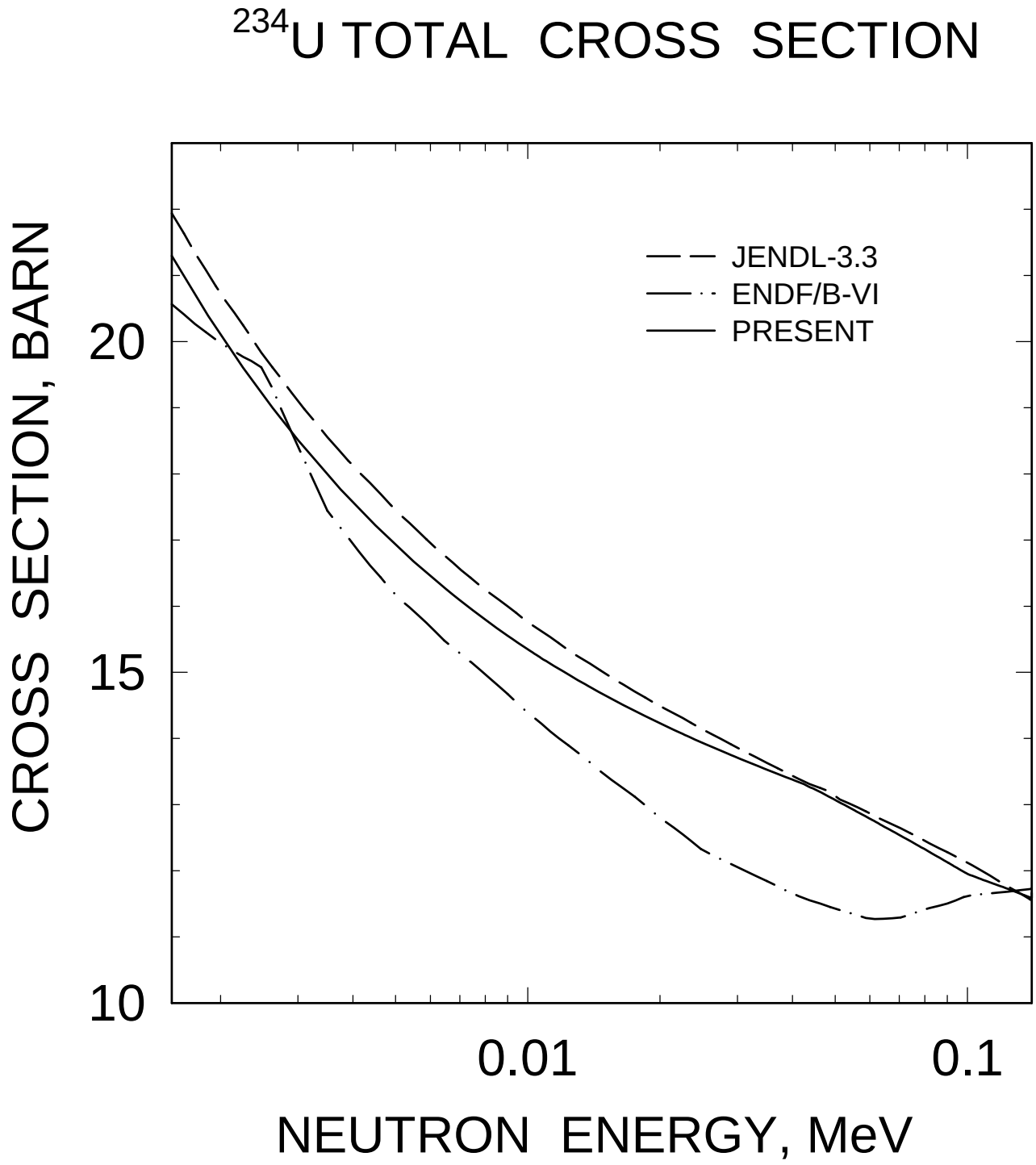
^{234}U TOTAL CROSS SECTION
CROSS SECTION, BARN
20
15
10
0.01
0.1
NEUTRON ENERGY, MeV
JENDL-3.3
ENDF/B-VI
PRESENT

FIG. 7

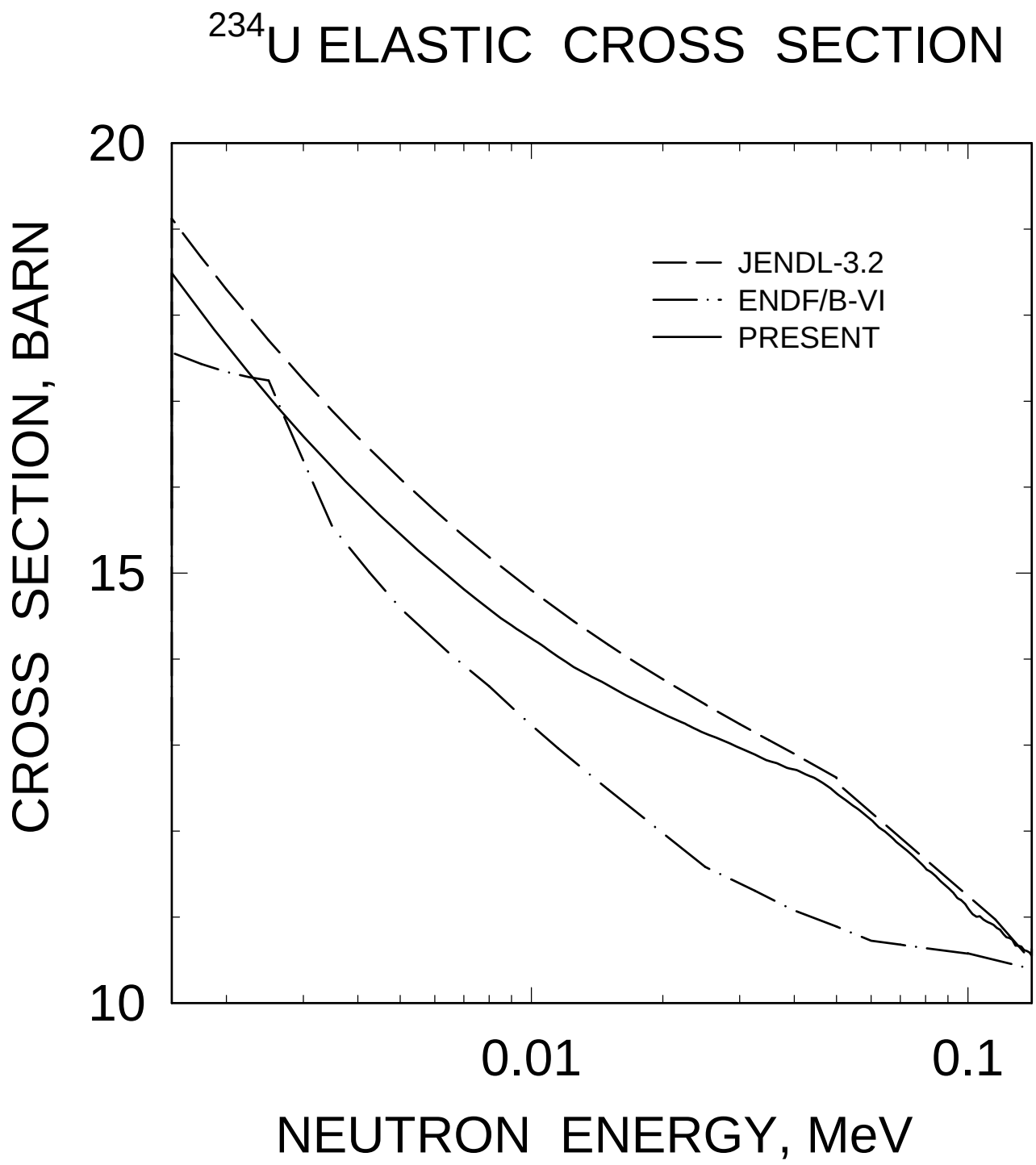
^{234}U ELASTIC CROSS SECTION
20
15
10
CROSS SECTION, BARN
JENDL-3.2
ENDF/B-VI
PRESENT
0.01
0.1
NEUTRON ENERGY, MeV

FIG. 8

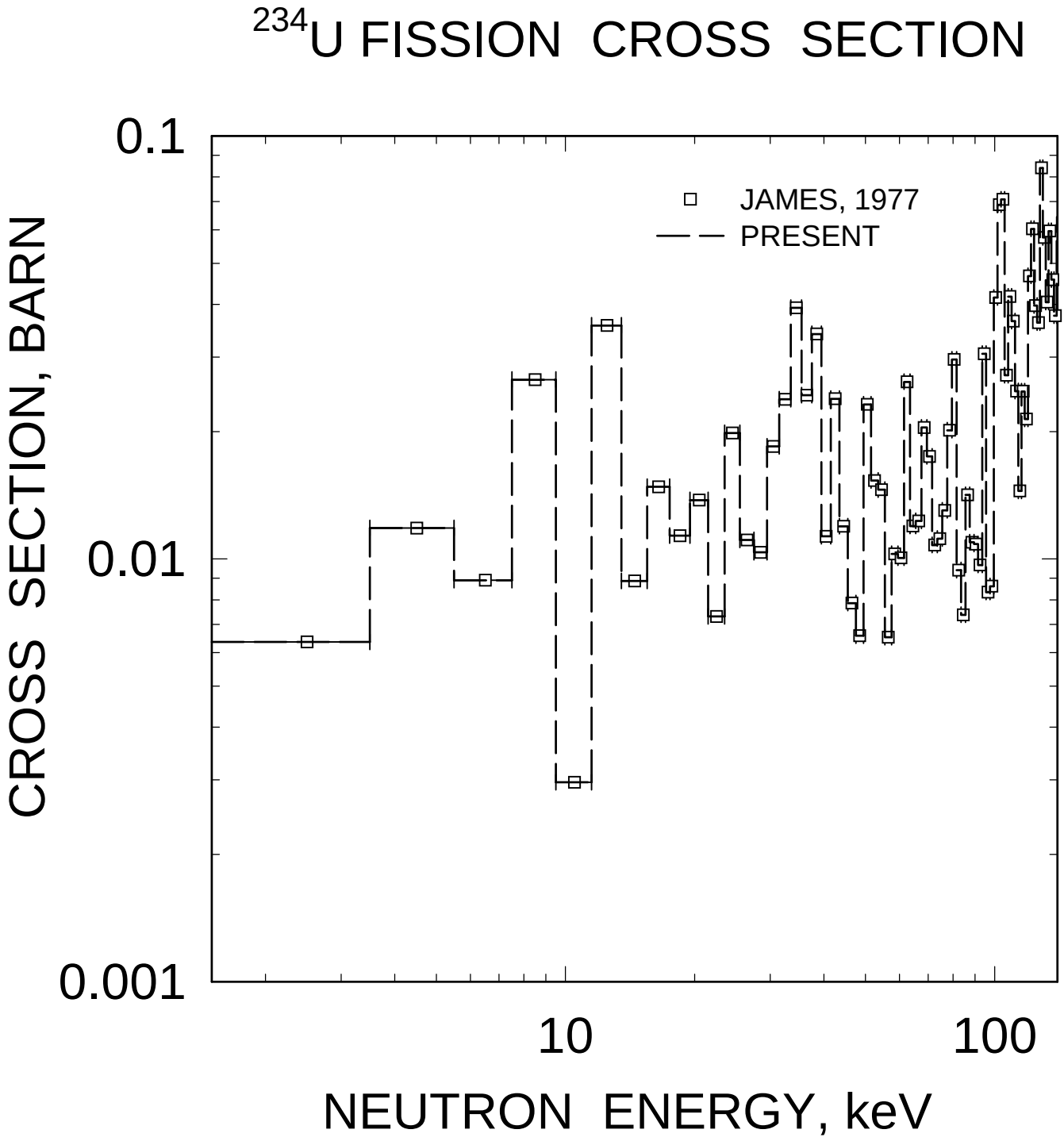
^{234}U FISSION CROSS SECTION
0.1
0.01
0.001
CROSS SECTION, BARN
JAMES, 1977
PRESENT
10
100
NEUTRON ENERGY, keV

FIG. 9

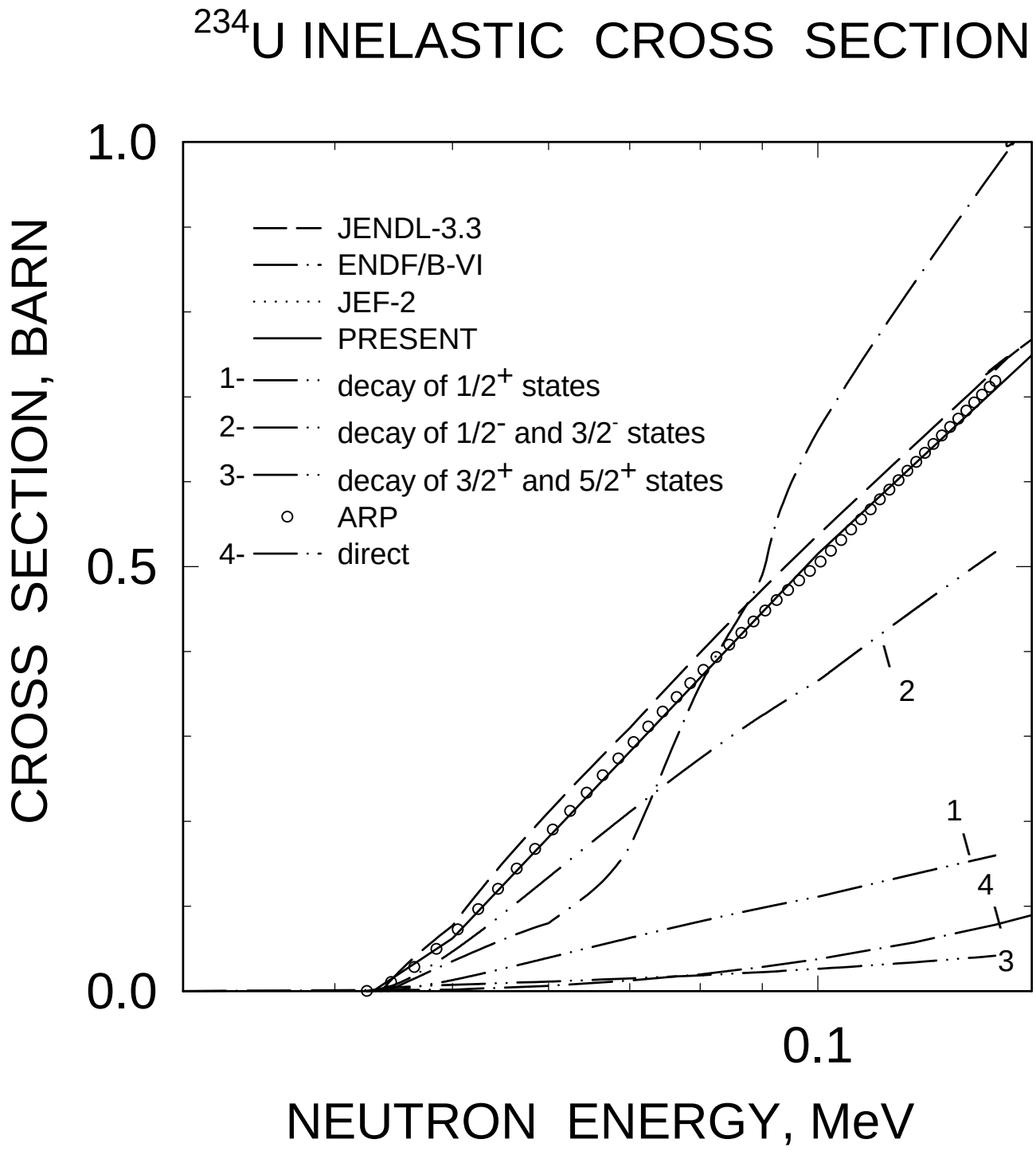
^{234}U INELASTIC CROSS SECTION
1.0
0.5
0.0
CROSS SECTION, BARN
JENDL-3.3
ENDF/B-VI
JEF-2
PRESENT
1- decay of 1/2+ states
2- decay of 1/2- and 3/2- states
3- decay of 3/2+ and 5/2+ states
ARP
4- direct
1
2
3
4
0.1
NEUTRON ENERGY, MeV

FIG. 10

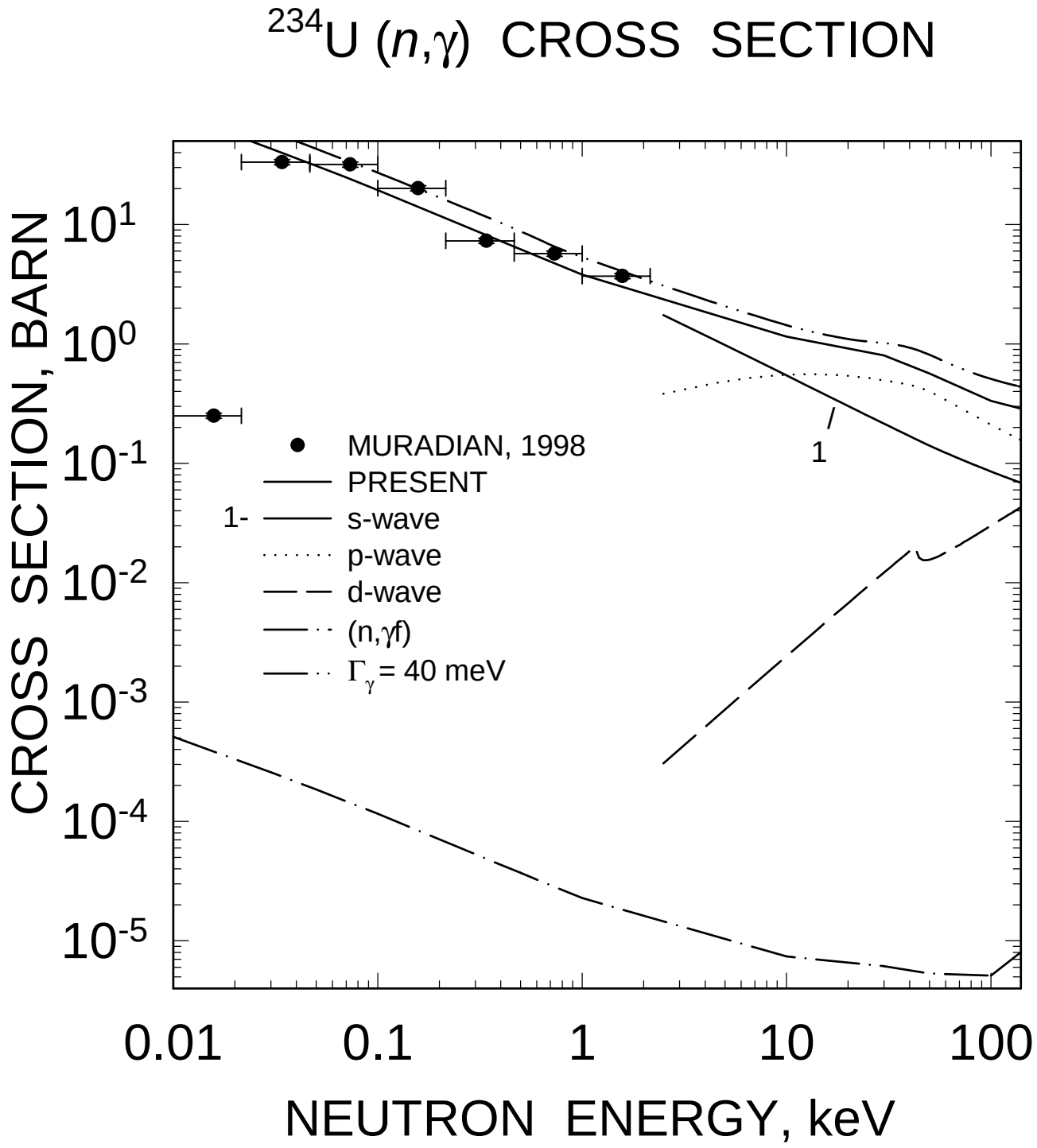
^{234}U (n,γ) CROSS SECTION
CROSS SECTION, BARN
10^{1}
10^{0}
10^{-1}
10^{-2}
10^{-3}
10^{-4}
10^{-5}
MURADIAN, 1998
PRESENT
1-
s-wave
p-wave
d-wave
(n,γf)
Γ_γ = 40 meV
1
0.01
0.1
1
10
100
NEUTRON ENERGY, keV

FIG. 11

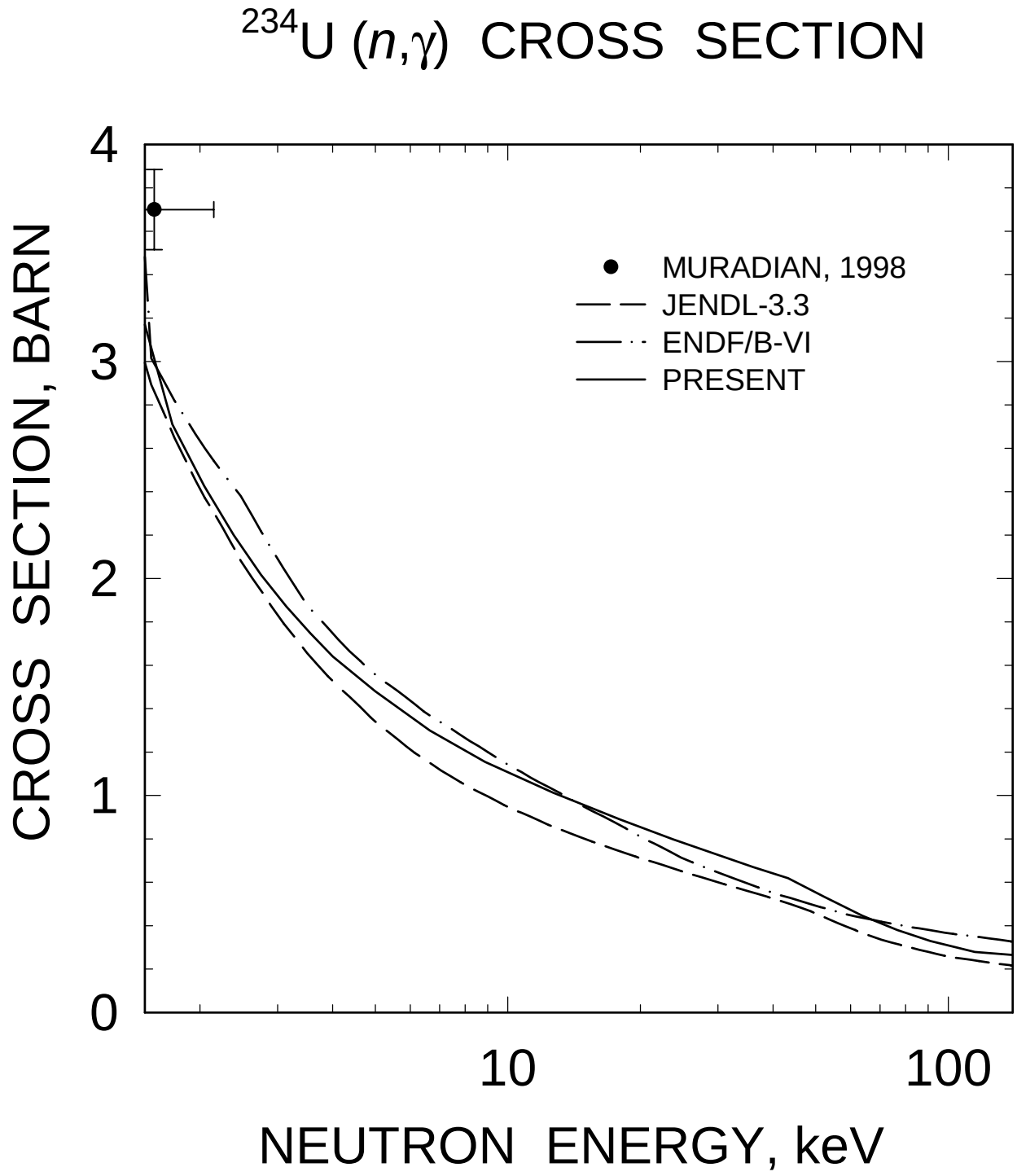
^{234}U (n,γ) CROSS SECTION
CROSS SECTION, BARN
0
1
2
3
4
10
100
NEUTRON ENERGY, keV
MURADIAN, 1998
JENDL-3.3
ENDF/B-VI
PRESENT

FIG. 12

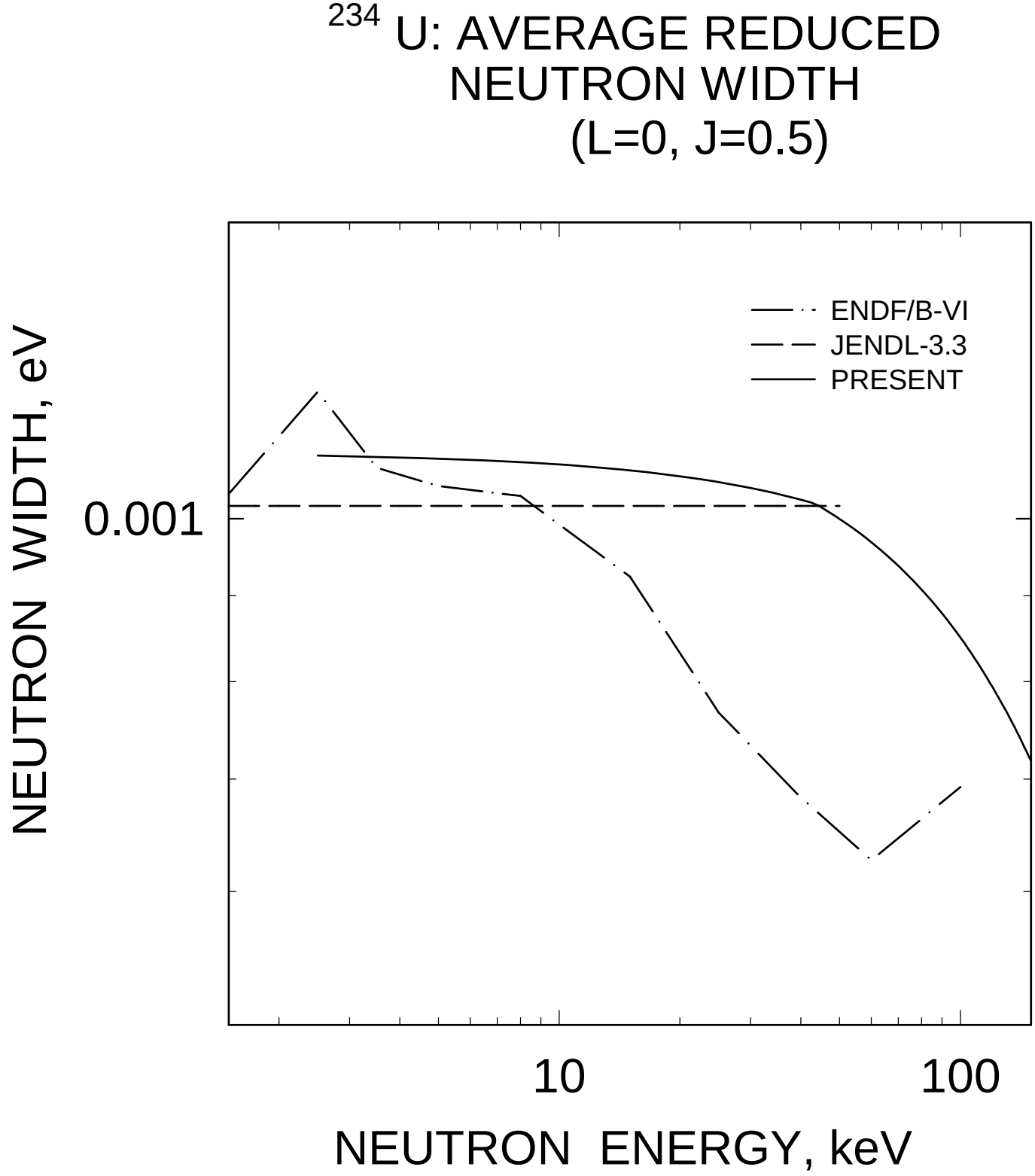
234 U: AVERAGE REDUCED NEUTRON WIDTH (L=0, J=0.5)
ENDF/B-VI
JENDL-3.3
PRESENT
NEUTRON WIDTH, eV
0.001
10
100
NEUTRON ENERGY, keV

FIG. 13

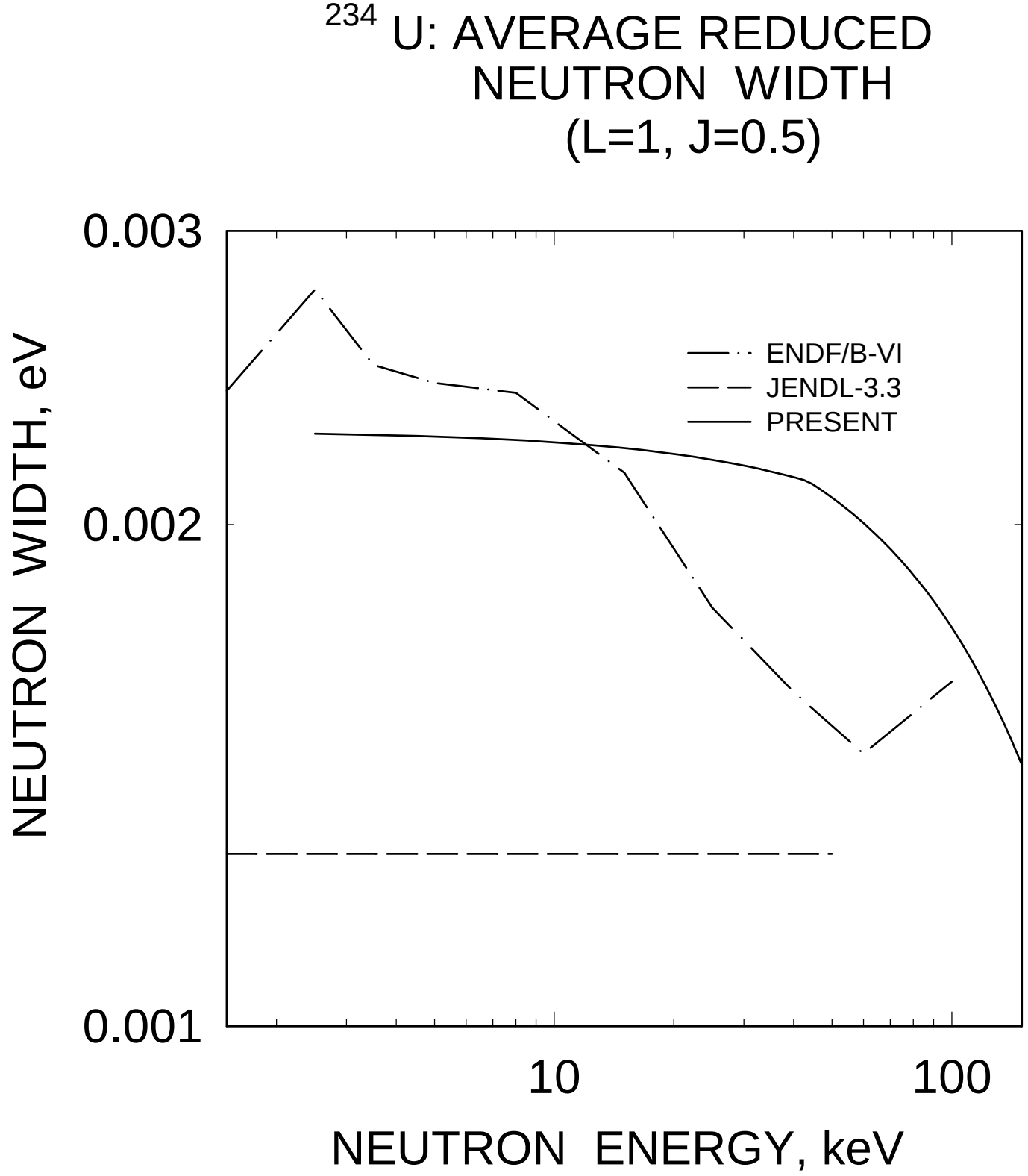
234 U: AVERAGE REDUCED NEUTRON WIDTH (L=1, J=0.5)
0.003
0.002
0.001
NEUTRON WIDTH, eV
ENDF/B-VI
JENDL-3.3
PRESENT
10
100
NEUTRON ENERGY, keV

FIG. 14

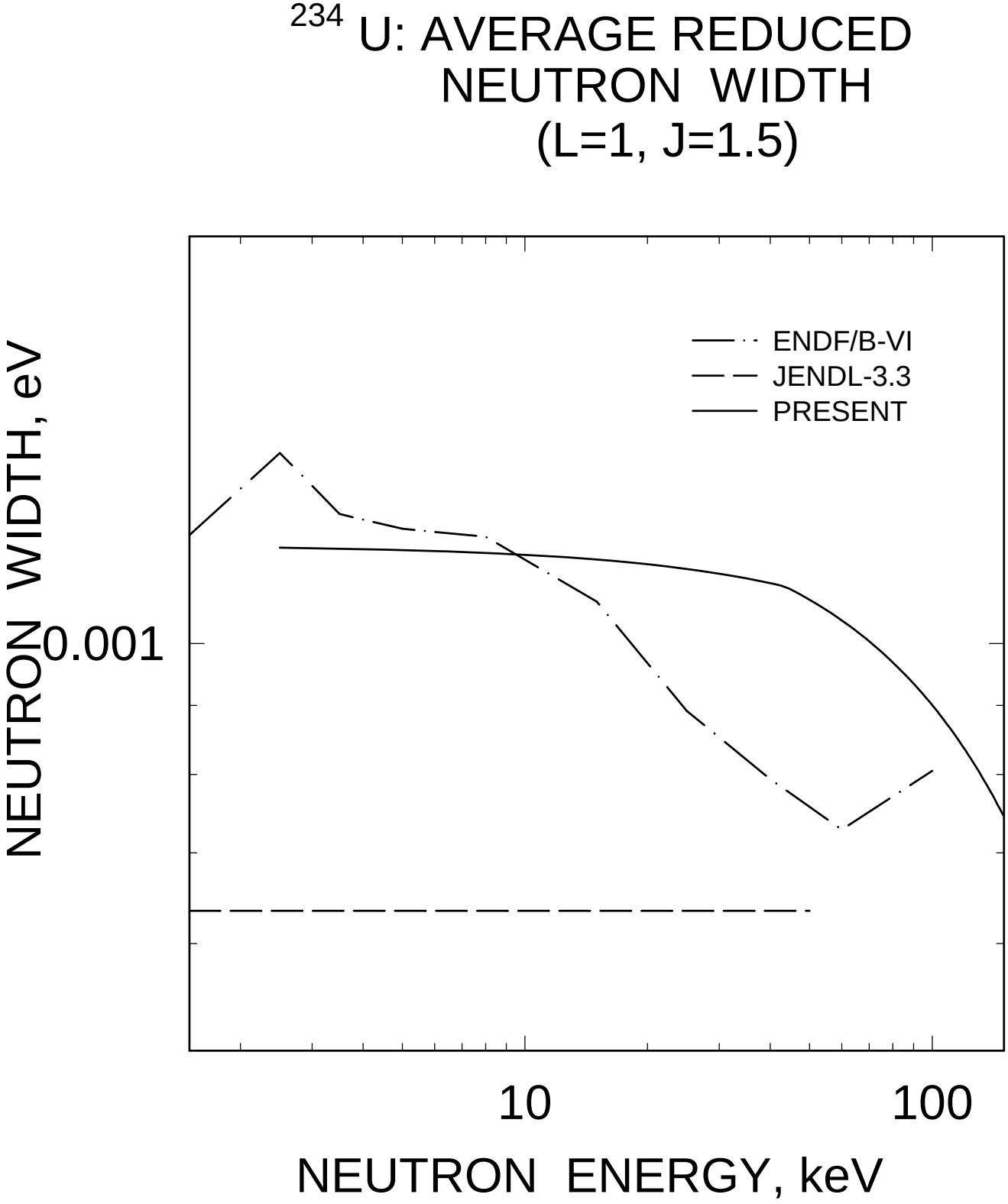
234 U: AVERAGE REDUCED NEUTRON WIDTH (L=1, J=1.5)
ENDF/B-VI
JENDL-3.3
PRESENT
NEUTRON WIDTH, eV
0.001
10
100
NEUTRON ENERGY, keV

FIG. 15

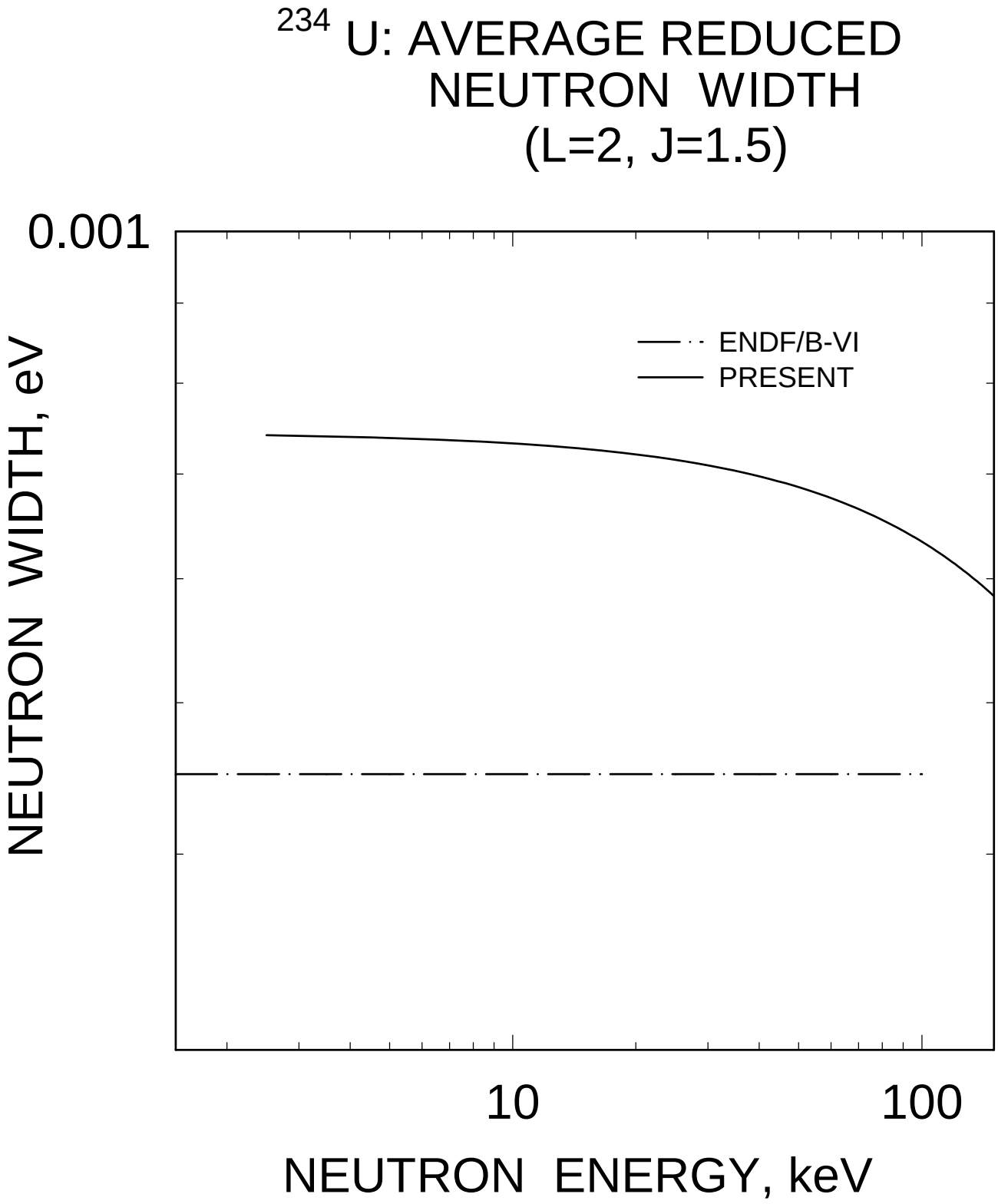
234 U: AVERAGE REDUCED NEUTRON WIDTH (L=2, J=1.5)
0.001
NEUTRON WIDTH, eV
ENDF/B-VI
PRESENT
10
100
NEUTRON ENERGY, keV

FIG. 16

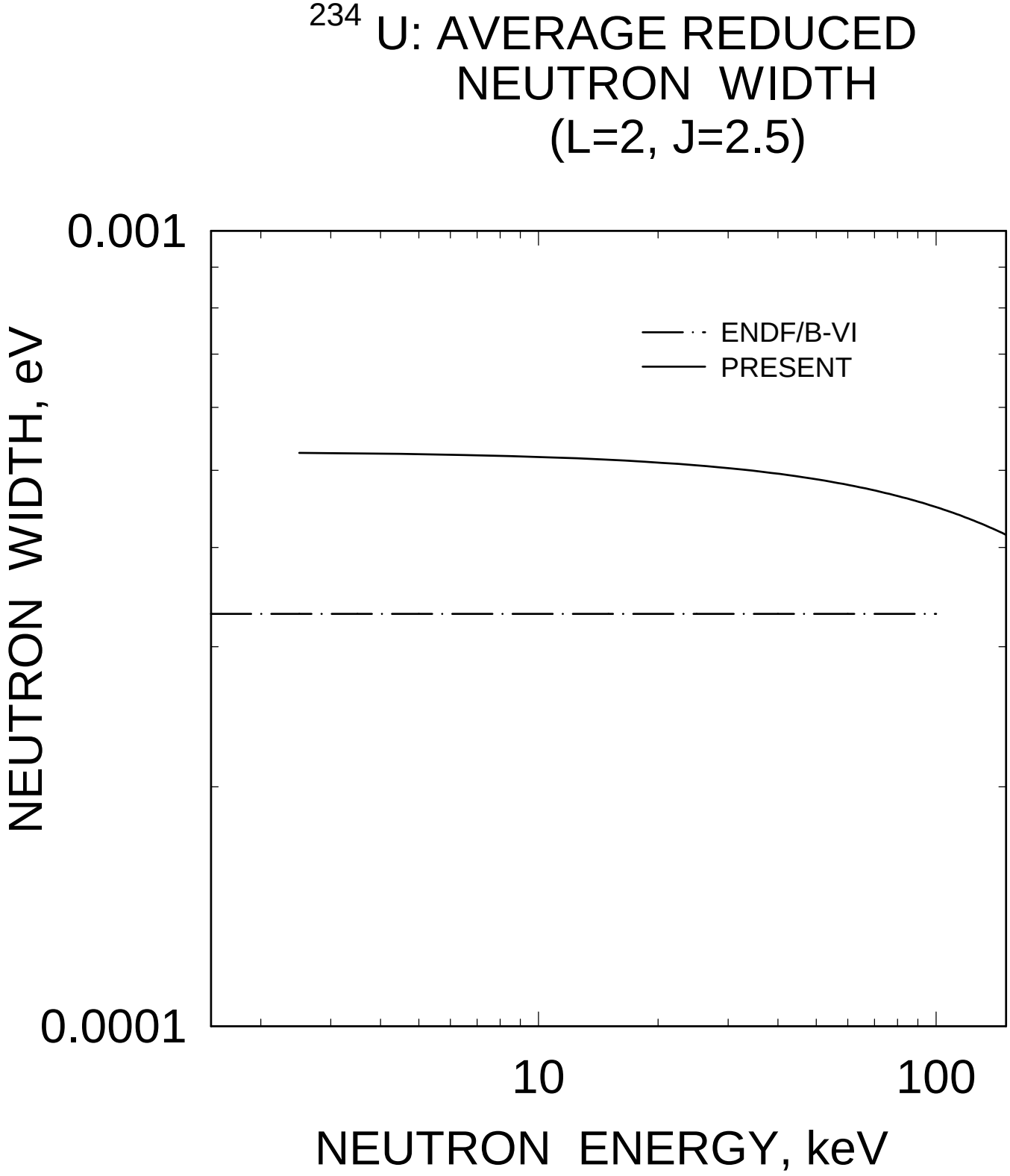
234 U: AVERAGE REDUCED NEUTRON WIDTH (L=2, J=2.5)
0.001
0.0001
NEUTRON WIDTH, eV
ENDF/B-VI
PRESENT
10
100
NEUTRON ENERGY, keV

FIG. 17

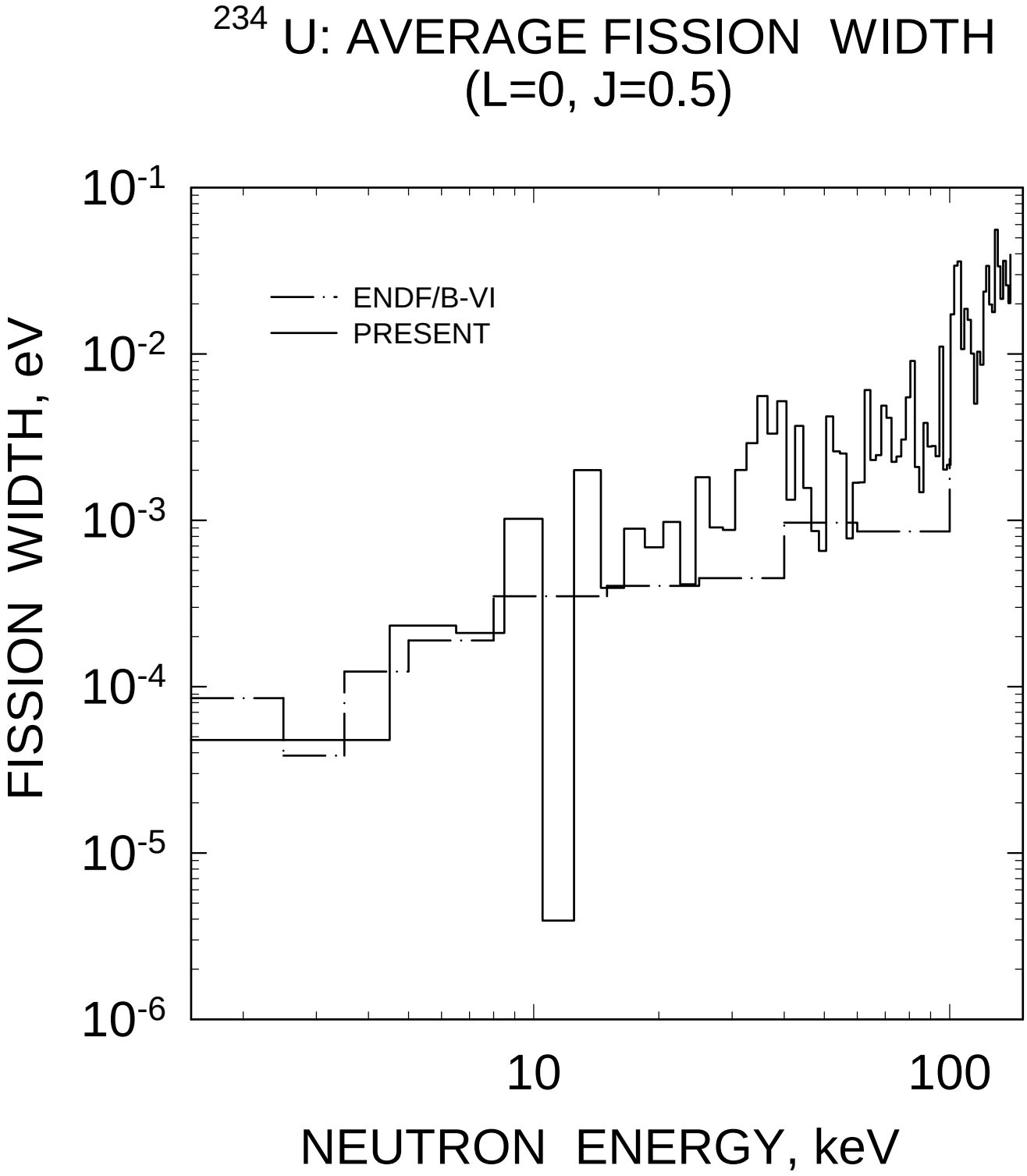
^{234} U: AVERAGE FISSION WIDTH
(L=0, J=0.5)
FISSION WIDTH, eV
10^{-1}
10^{-2}
10^{-3}
10^{-4}
10^{-5}
10^{-6}
ENDF/B-VI
PRESENT
10
100
NEUTRON ENERGY, keV

FIG. 18

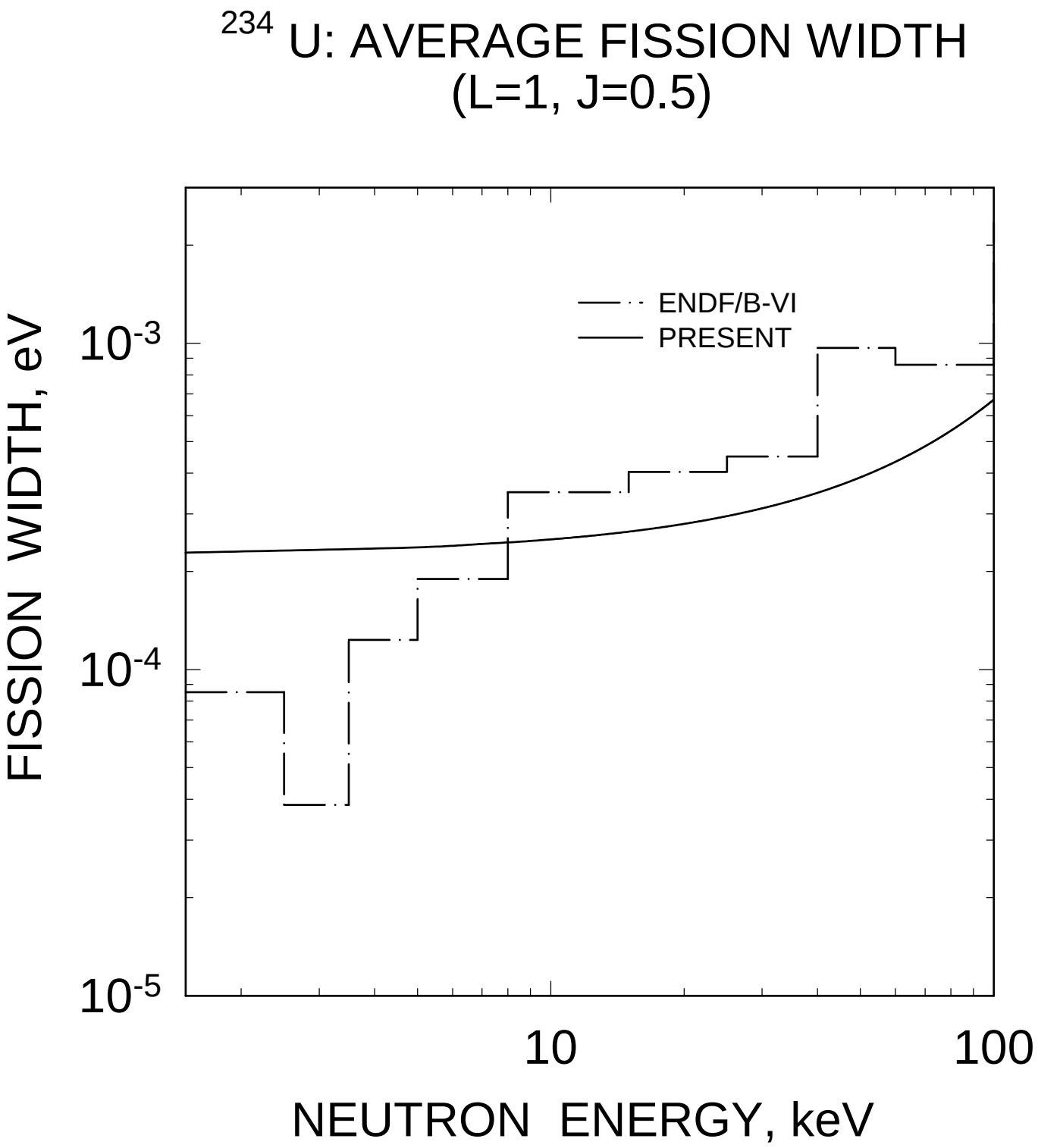
^{234} U: AVERAGE FISSION WIDTH
(L=1, J=0.5)
ENDF/B-VI
PRESENT
FISSION WIDTH, eV
10^{-3}
10^{-4}
10^{-5}
10
100
NEUTRON ENERGY, keV

FIG. 19

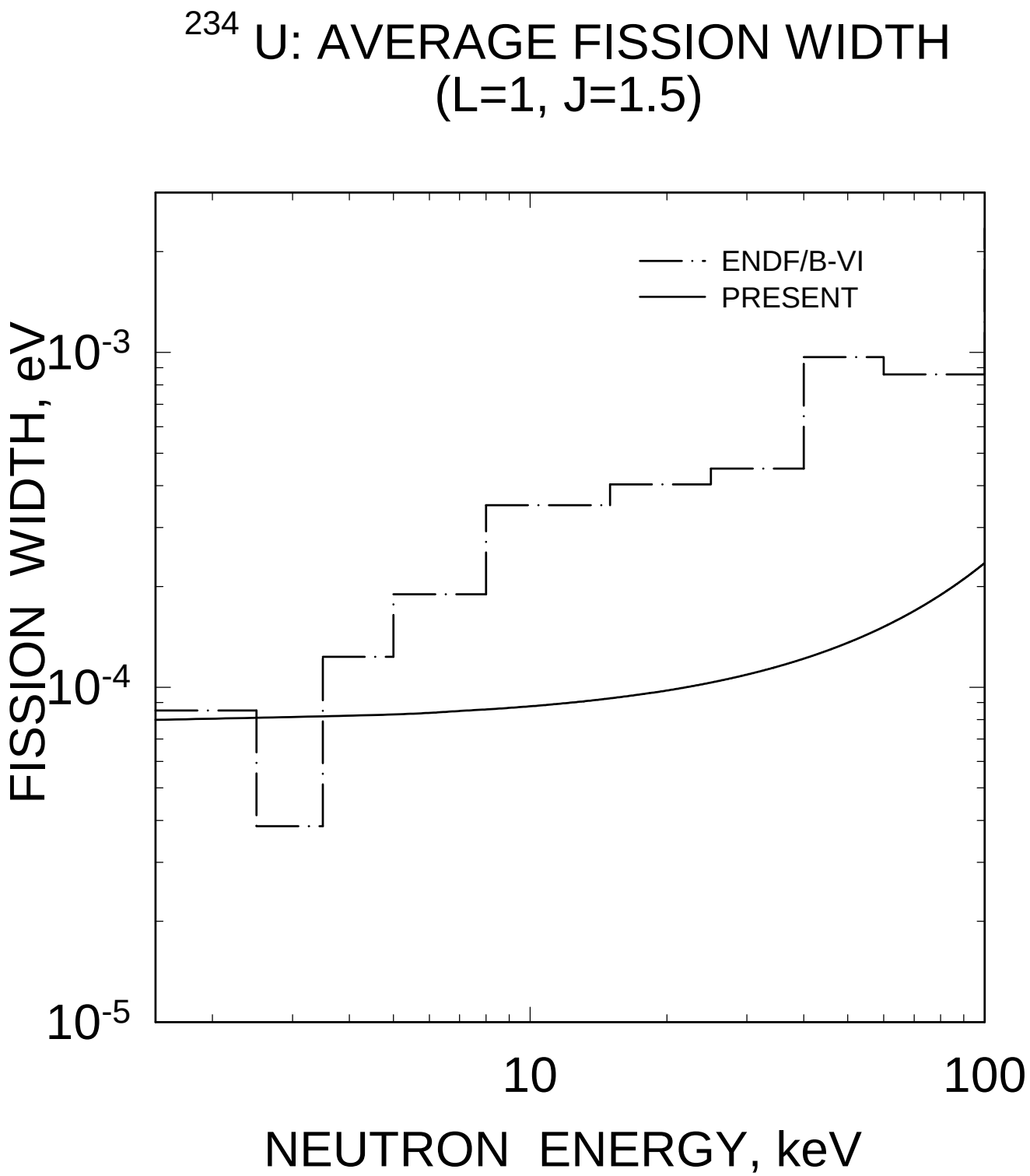
^{234} U: AVERAGE FISSION WIDTH
(L=1, J=1.5)
ENDF/B-VI
PRESENT
FISSION WIDTH, eV
10^{-3}
10^{-4}
10^{-5}
10
100
NEUTRON ENERGY, keV

FIG. 20

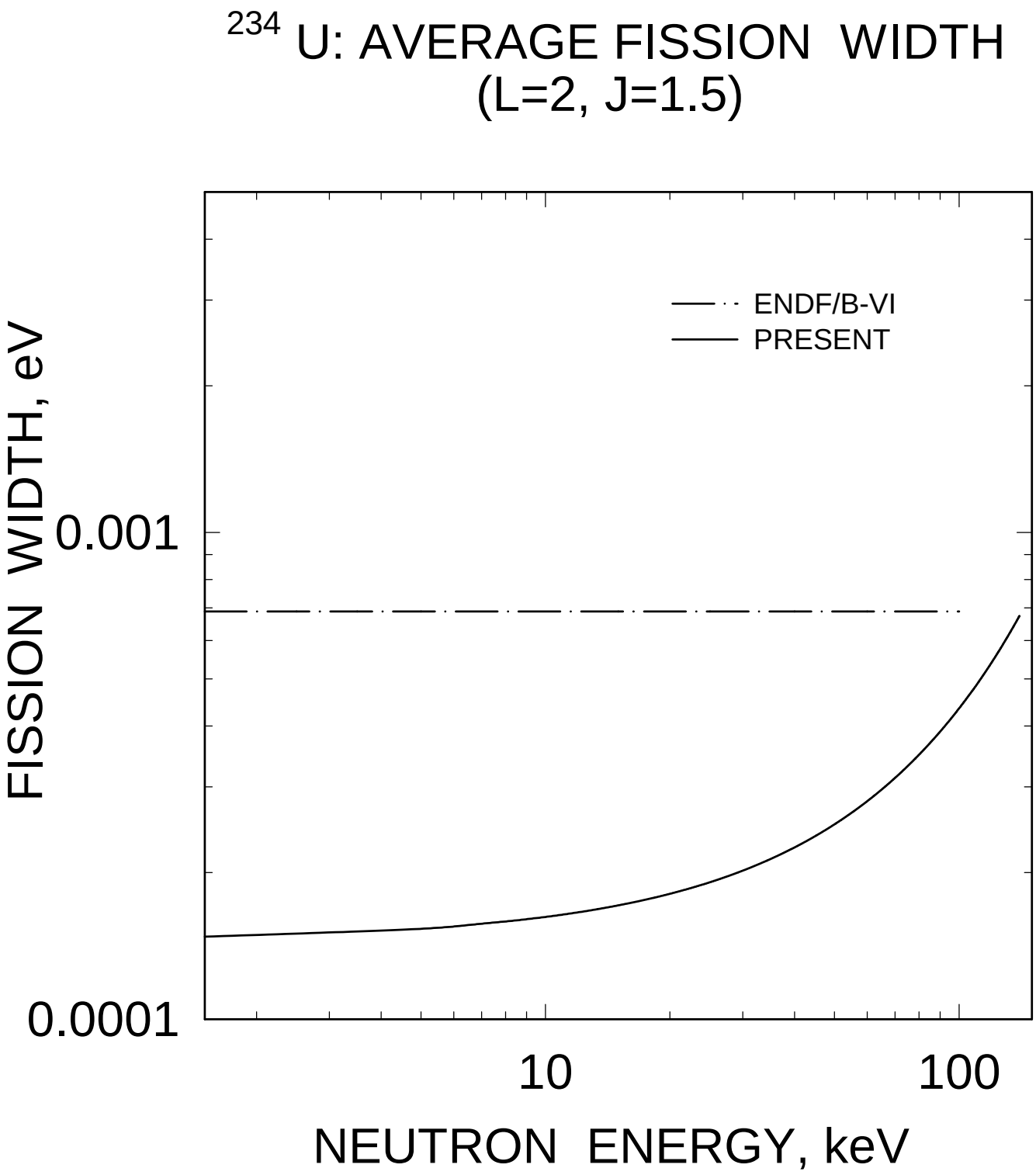
^{234} U: AVERAGE FISSION WIDTH
(L=2, J=1.5)
ENDF/B-VI
PRESENT
FISSION WIDTH, eV
0.001
0.0001
10
100
NEUTRON ENERGY, keV

FIG. 21

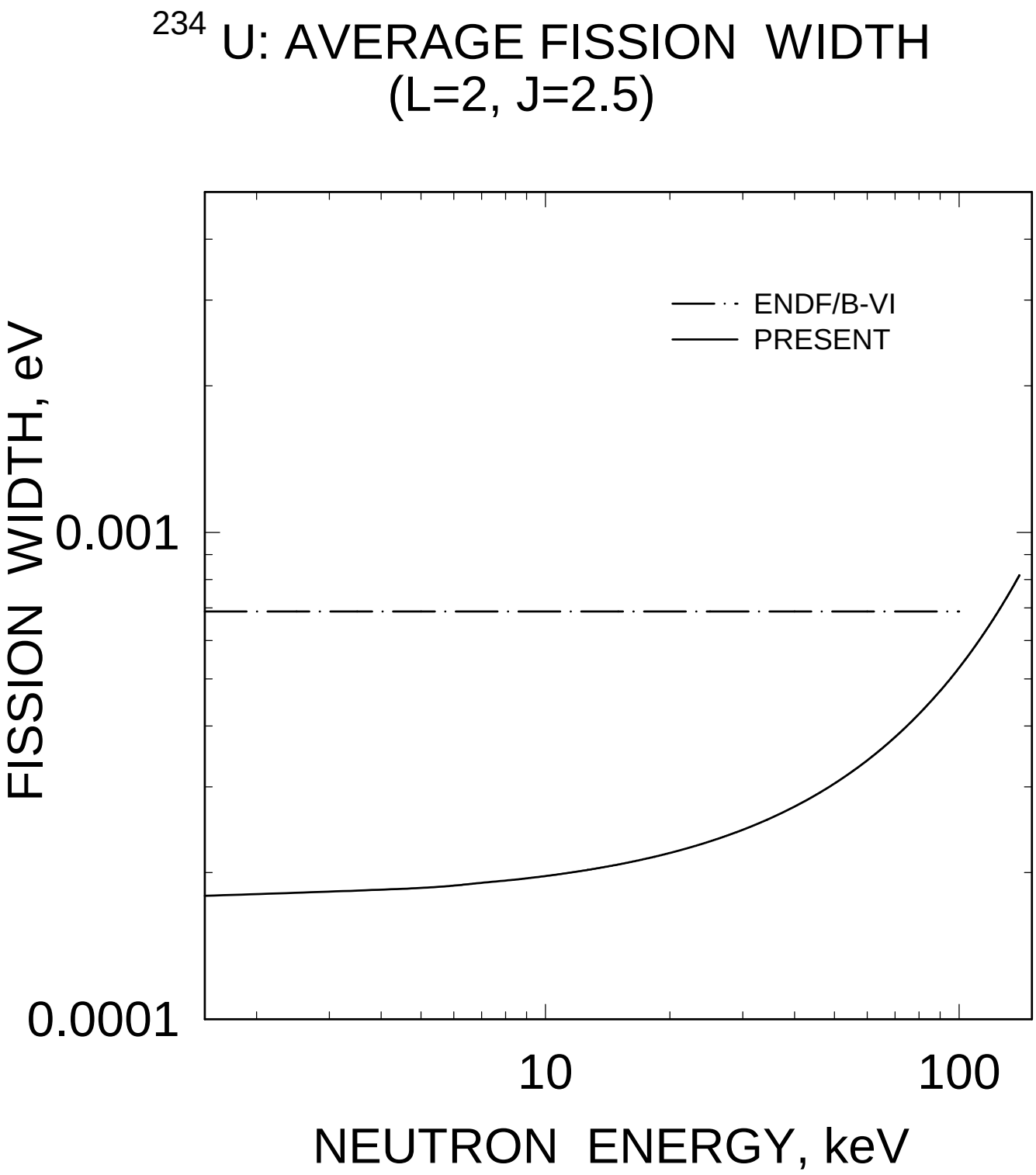
^{234} U: AVERAGE FISSION WIDTH
(L=2, J=2.5)
ENDF/B-VI
PRESENT
FISSION WIDTH, eV
0.001
0.0001
10
100
NEUTRON ENERGY, keV

FIG. 22

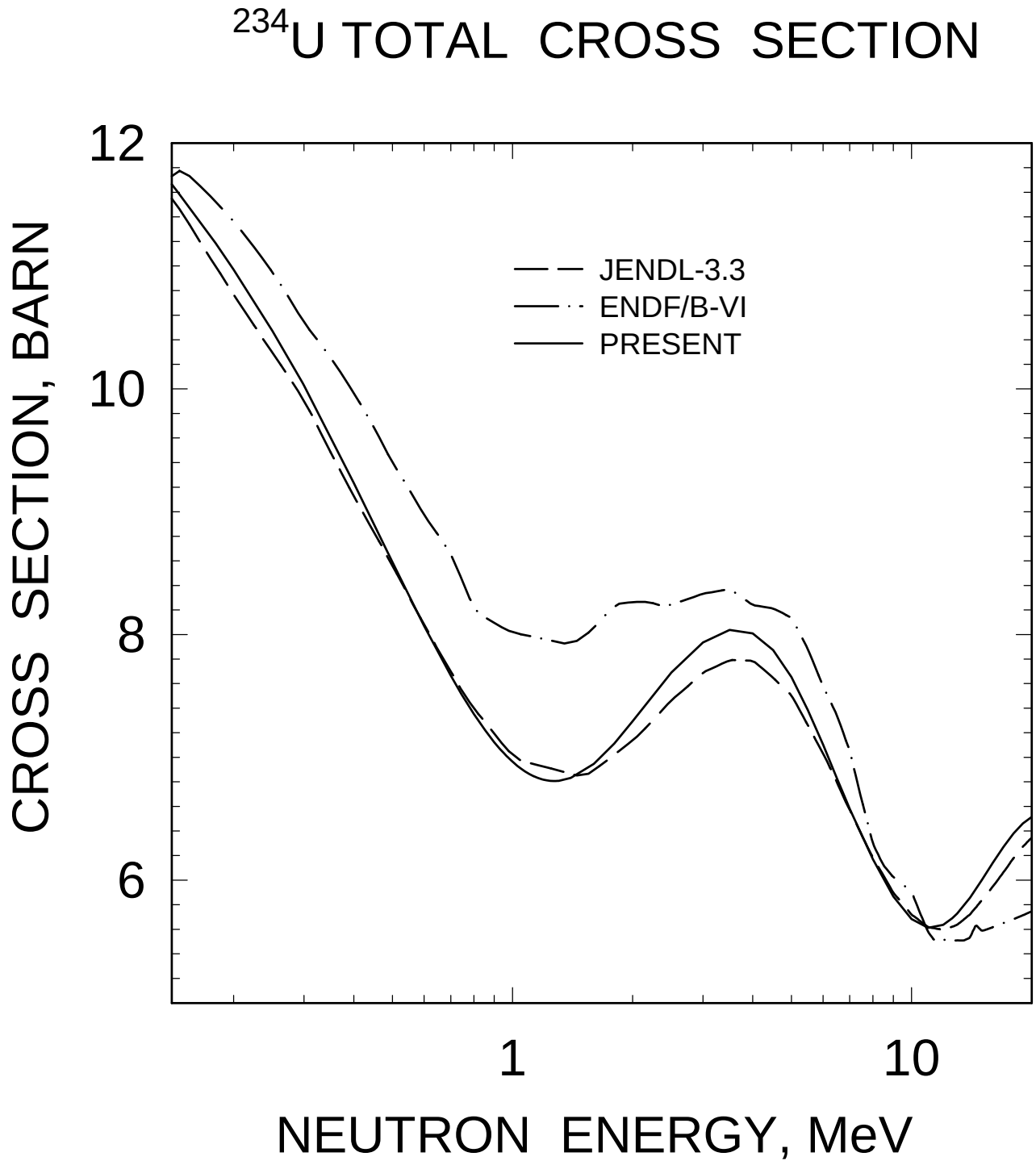
234U TOTAL CROSS SECTION
CROSS SECTION, BARN
12
10
8
6
JENDL-3.3
ENDF/B-VI
PRESENT
1
10
NEUTRON ENERGY, MeV

FIG. 23

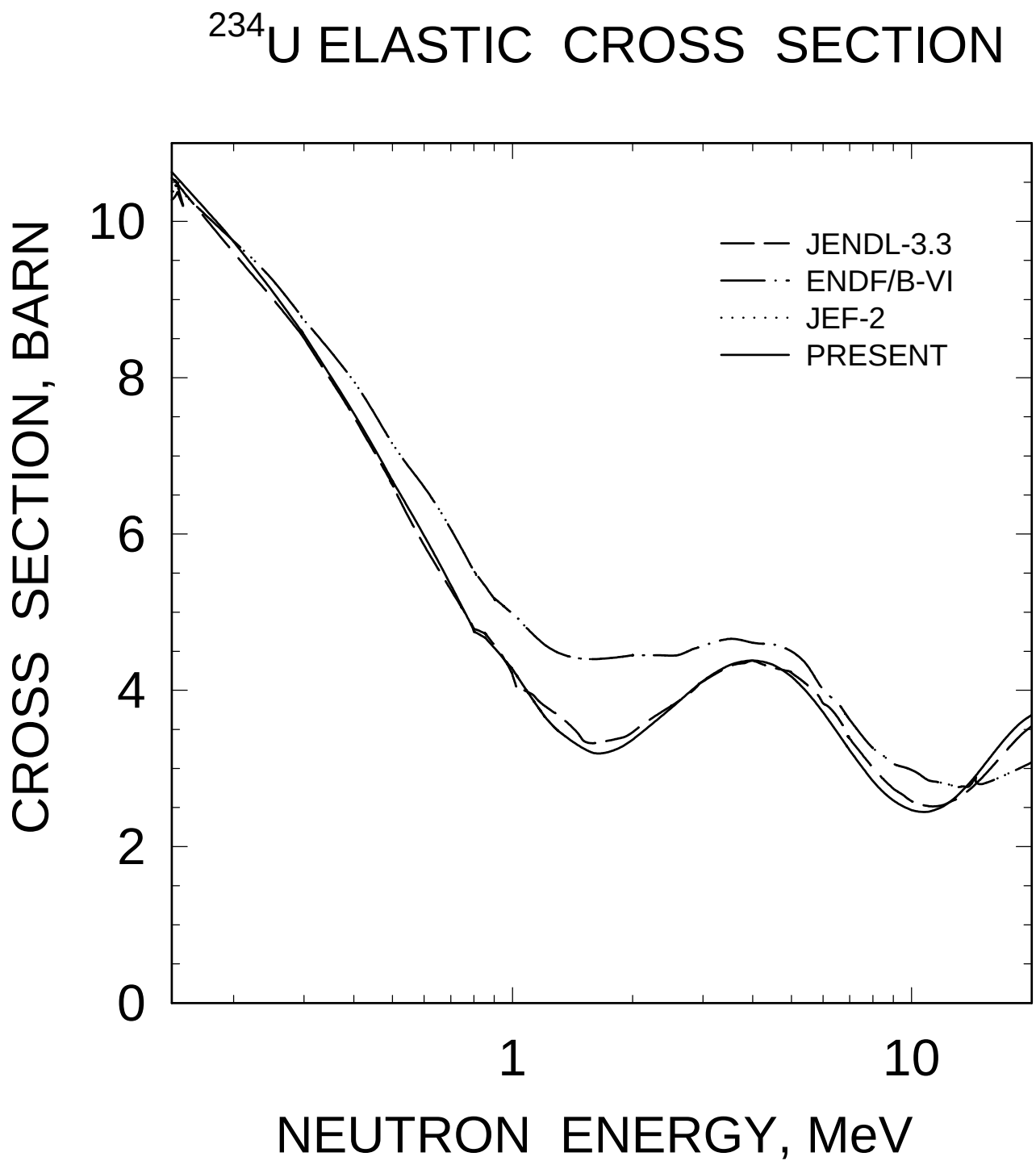
^{234}U ELASTIC CROSS SECTION
CROSS SECTION, BARN
10
8
6
4
2
0
1
10
NEUTRON ENERGY, MeV
JENDL-3.3
ENDF/B-VI
JEF-2
PRESENT

FIG. 24

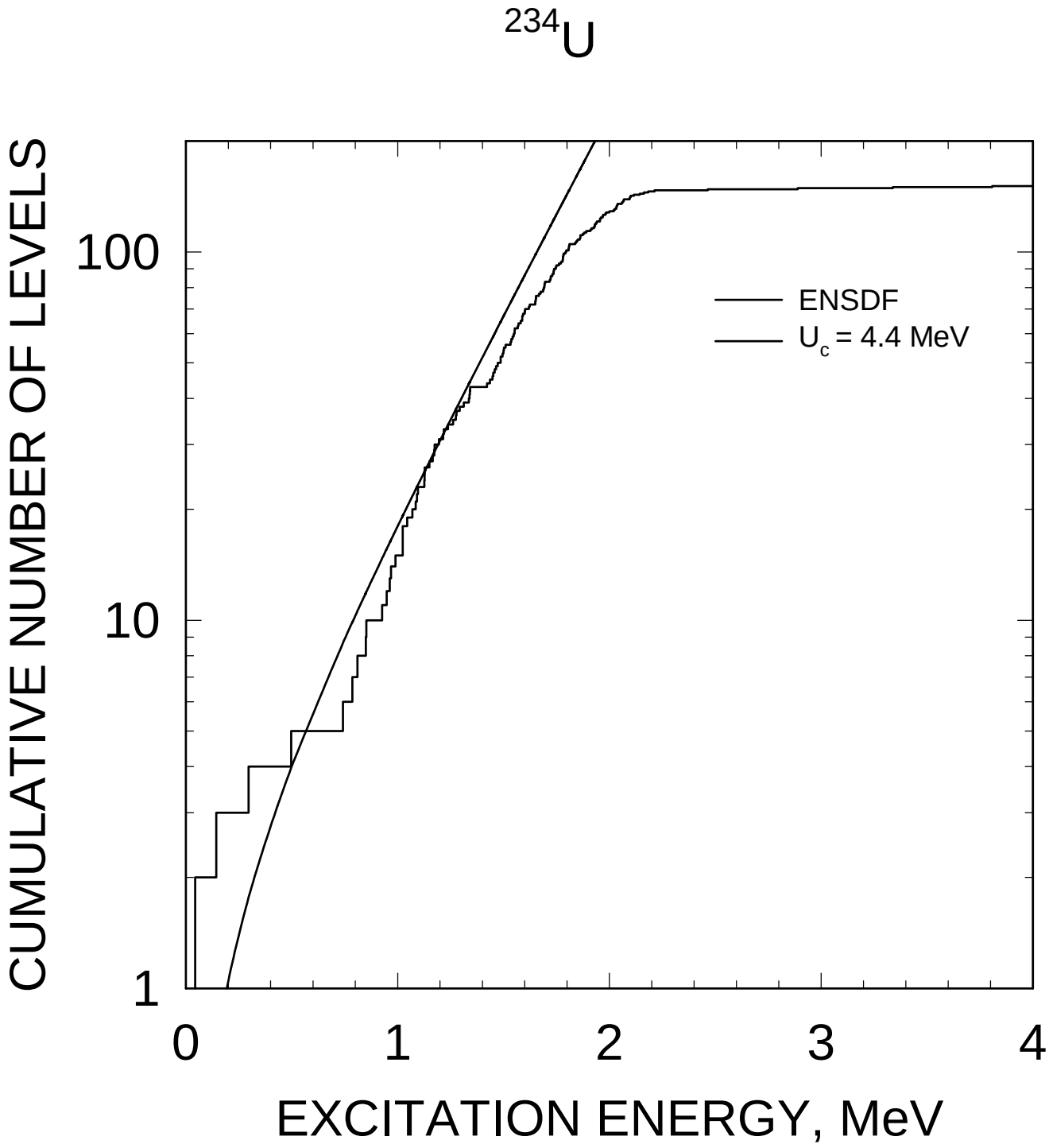
^{234}U
CUMULATIVE NUMBER OF LEVELS
100
10
1
0
1
2
3
4
EXCITATION ENERGY, MeV
ENSDF
U_c = 4.4 MeV

FIG. 25

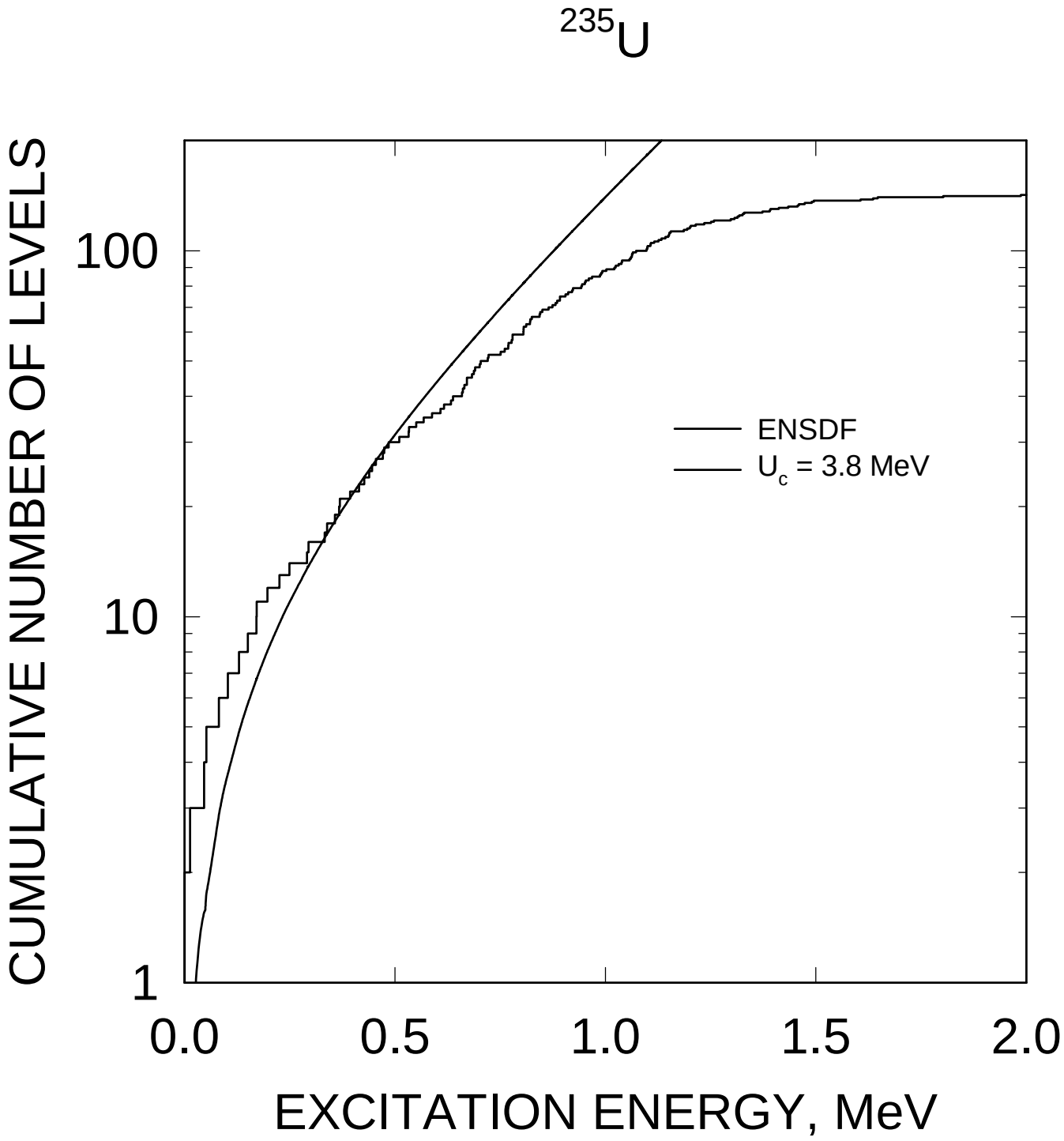
^{235}U
CUMULATIVE NUMBER OF LEVELS
100
10
1
0.0
0.5
1.0
1.5
2.0
EXCITATION ENERGY, MeV
ENSDF
U_c = 3.8 MeV

FIG. 26

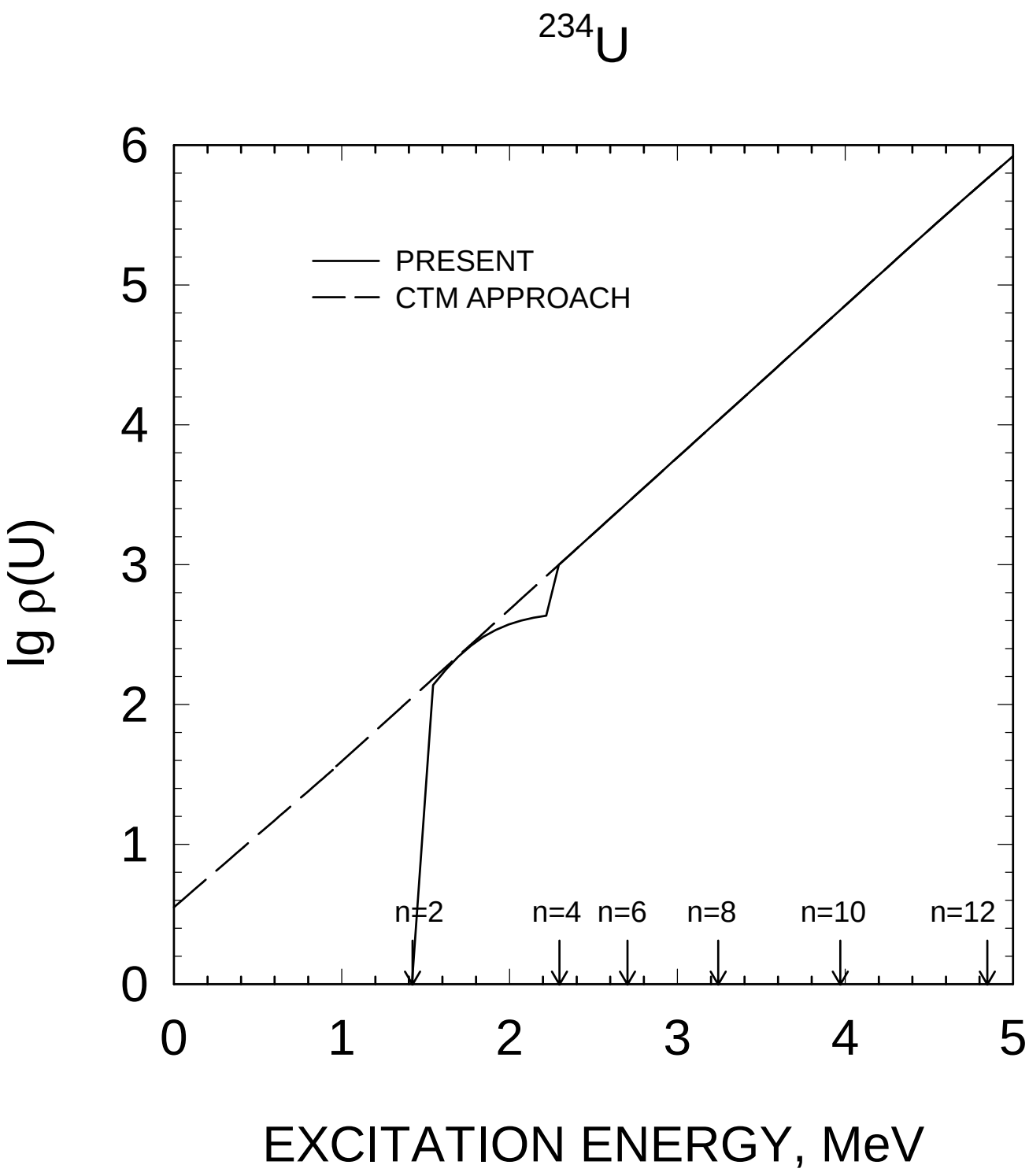
^{234}U
PRESENT
CTM APPROACH
n=2
n=4
n=6
n=8
n=10
n=12
lg ρ(U)
EXCITATION ENERGY, MeV
0
1
2
3
4
5
6

FIG. 27

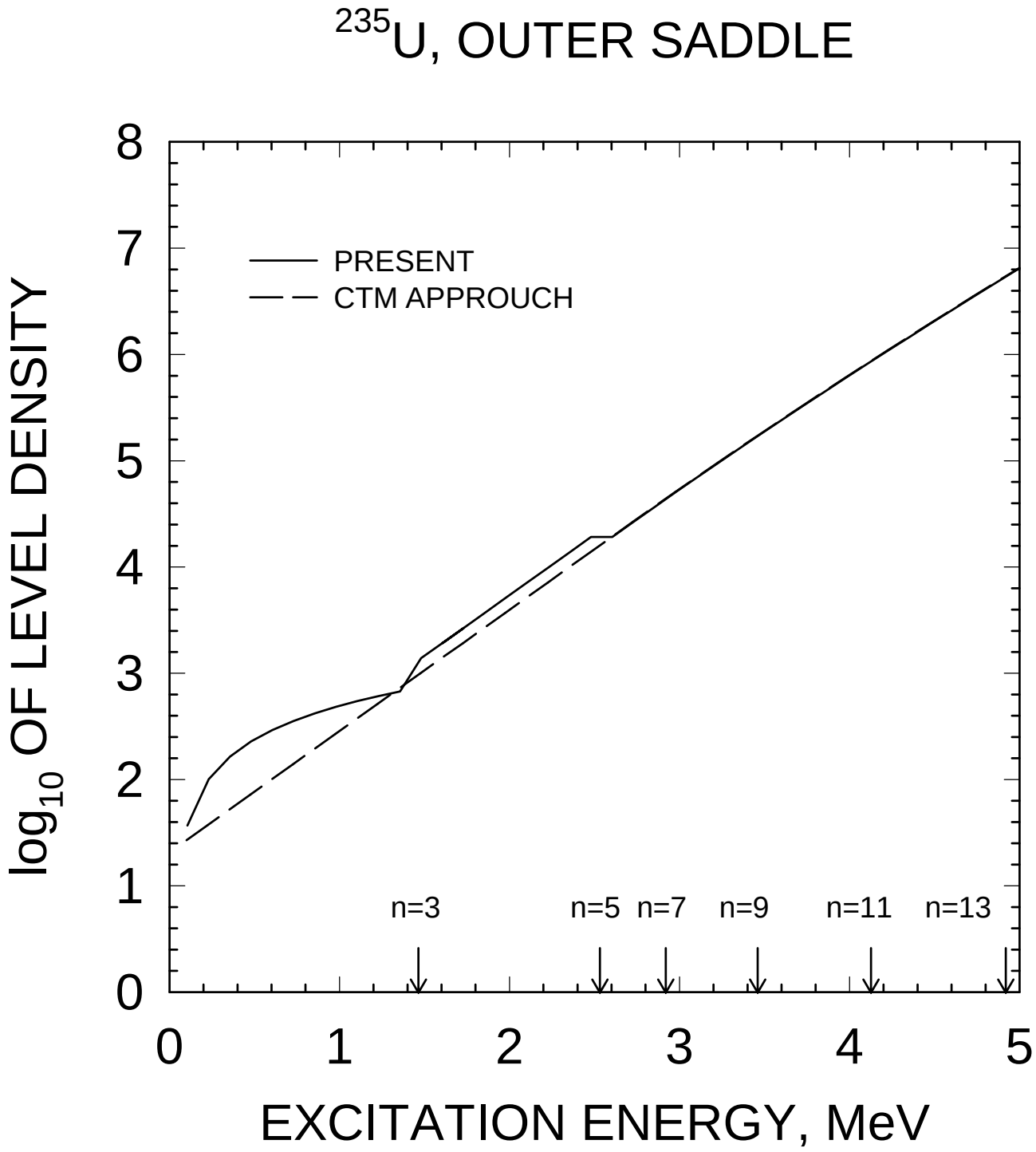
^{235}U, OUTER SADDLE
log$_{10}$ OF LEVEL DENSITY
EXCITATION ENERGY, MeV
PRESENT
CTM APPROUCH
n=3
n=5
n=7
n=9
n=11
n=13
0
1
2
3
4
5
6
7
8

FIG. 28

^{234}U FISSION CROSS SECTION

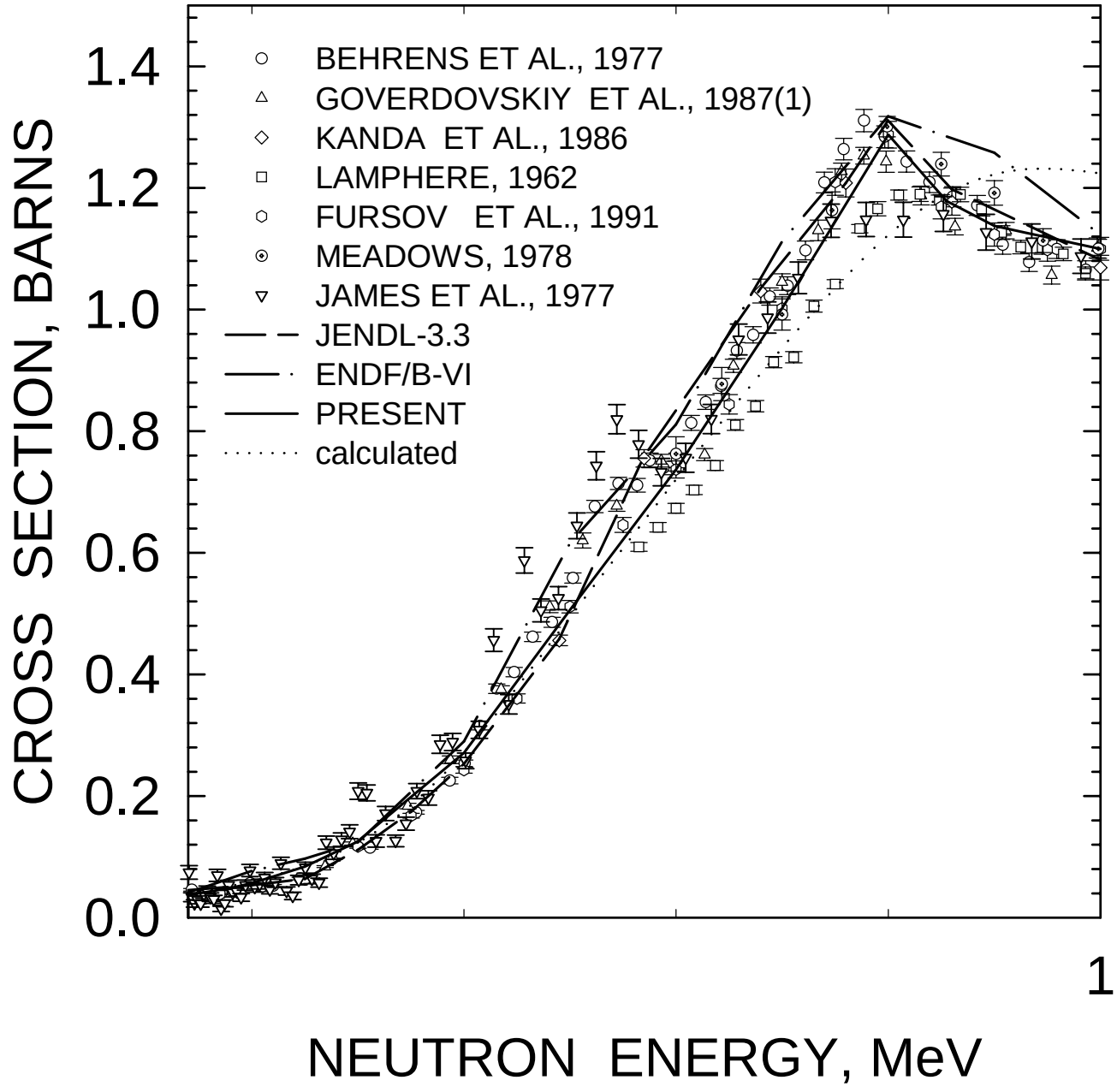

FIG. 29

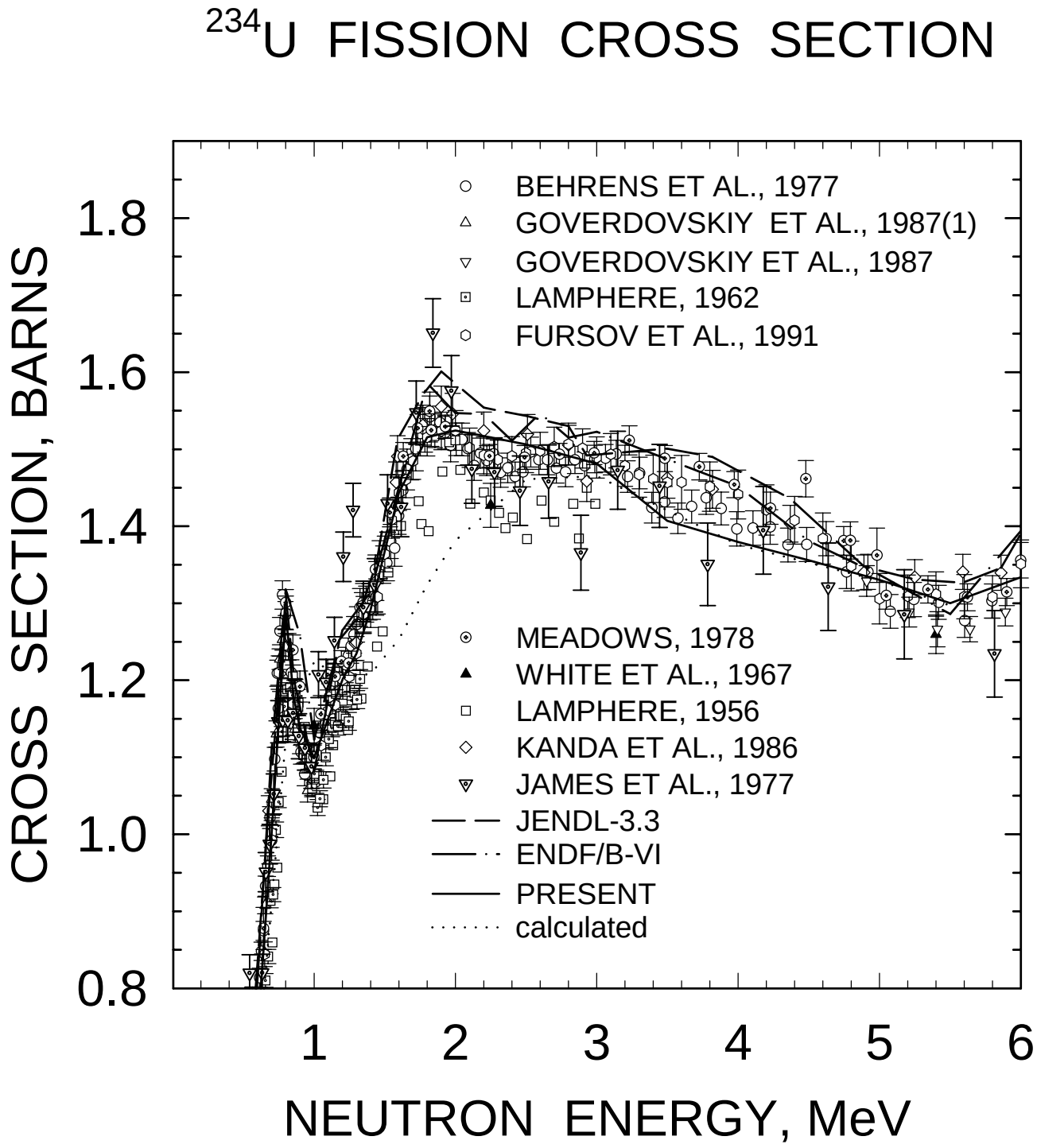
^{234}U FISSION CROSS SECTION
CROSS SECTION, BARNS
NEUTRON ENERGY, MeV
0.8
1.0
1.2
1.4
1.6
1.8
1
2
3
4
5
6
BEHRENS ET AL., 1977
GOVERDOVSKIY ET AL., 1987(1)
GOVERDOVSKIY ET AL., 1987
LAMPHERE, 1962
FURSOV ET AL., 1991
MEADOWS, 1978
WHITE ET AL., 1967
LAMPHERE, 1956
KANDA ET AL., 1986
JAMES ET AL., 1977
JENDL-3.3
ENDF/B-VI
PRESENT
calculated

FIG. 30

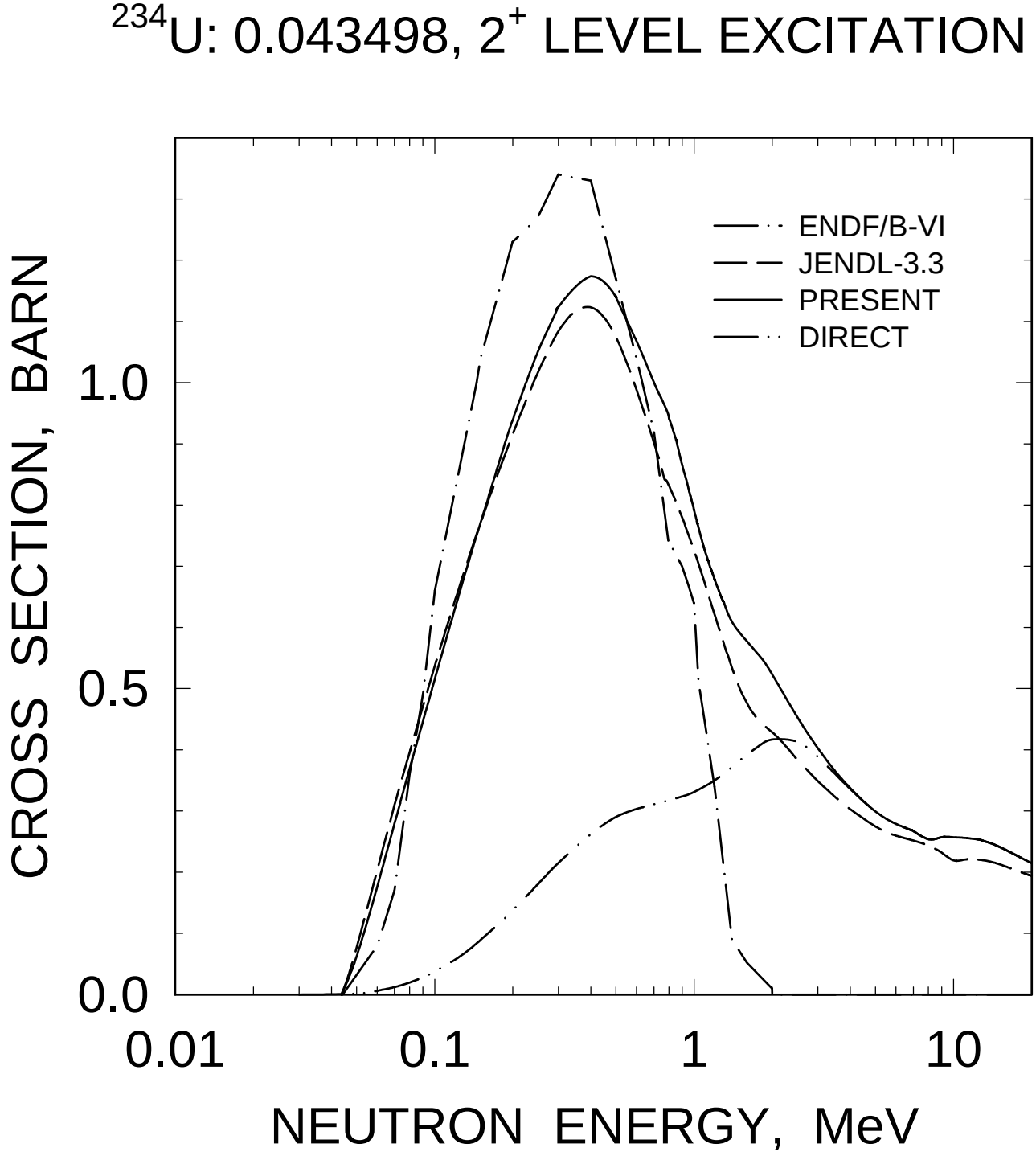
^{234}U: 0.043498, 2^{+} LEVEL EXCITATION
ENDF/B-VI
JENDL-3.3
PRESENT
DIRECT
CROSS SECTION, BARN
0.0
0.5
1.0
0.01
0.1
1
10
NEUTRON ENERGY, MeV

FIG. 31

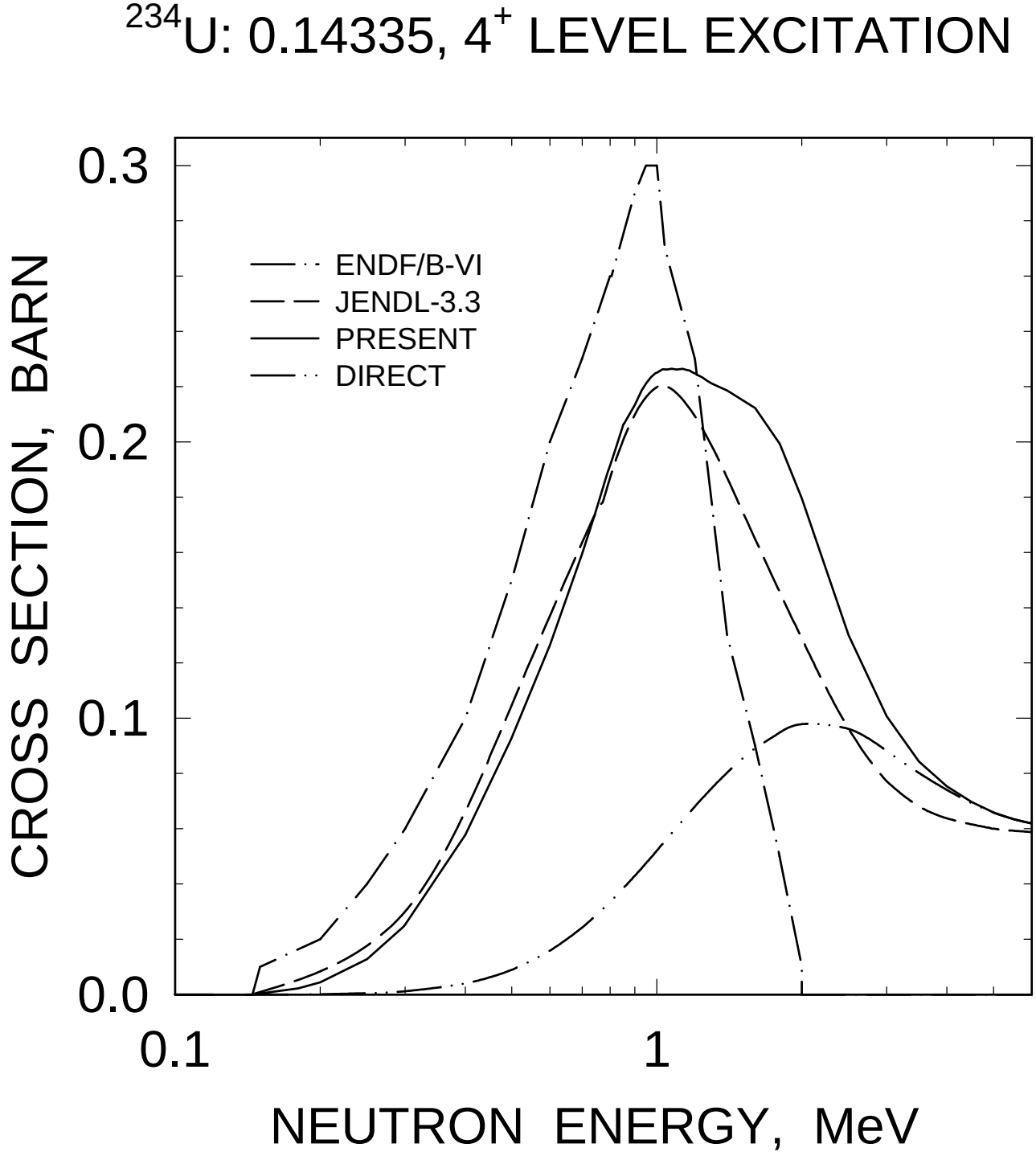
^{234}U: 0.14335, 4^{+} LEVEL EXCITATION
CROSS SECTION, BARN
0.3
0.2
0.1
0.0
0.1
1
NEUTRON ENERGY, MeV
ENDF/B-VI
JENDL-3.3
PRESENT
DIRECT

FIG. 32

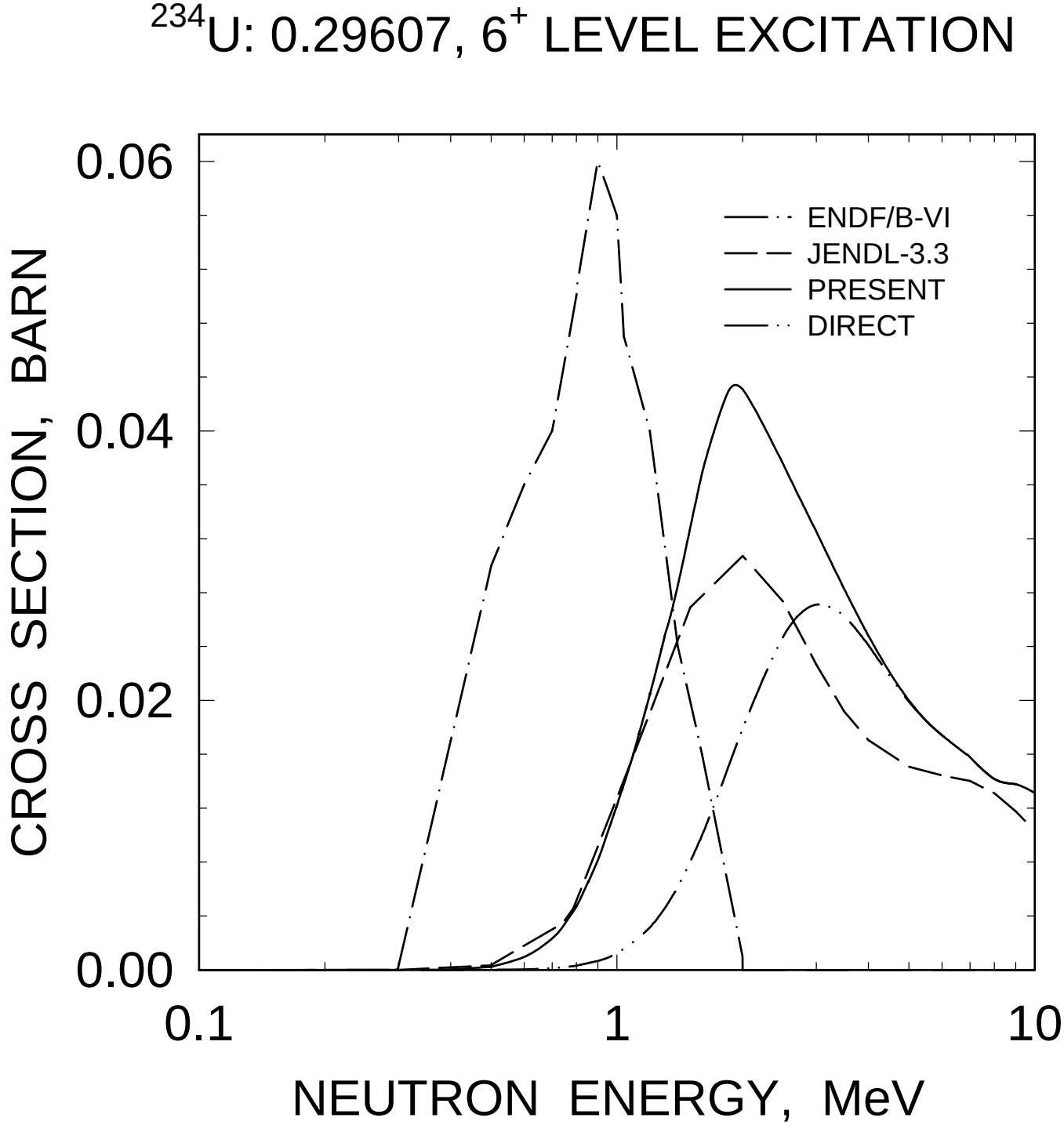
^{234}U: 0.29607, 6^{+} LEVEL EXCITATION
CROSS SECTION, BARN
0.06
0.04
0.02
0.00
0.1
1
10
NEUTRON ENERGY, MeV
ENDF/B-VI
JENDL-3.3
PRESENT
DIRECT

FIG. 33

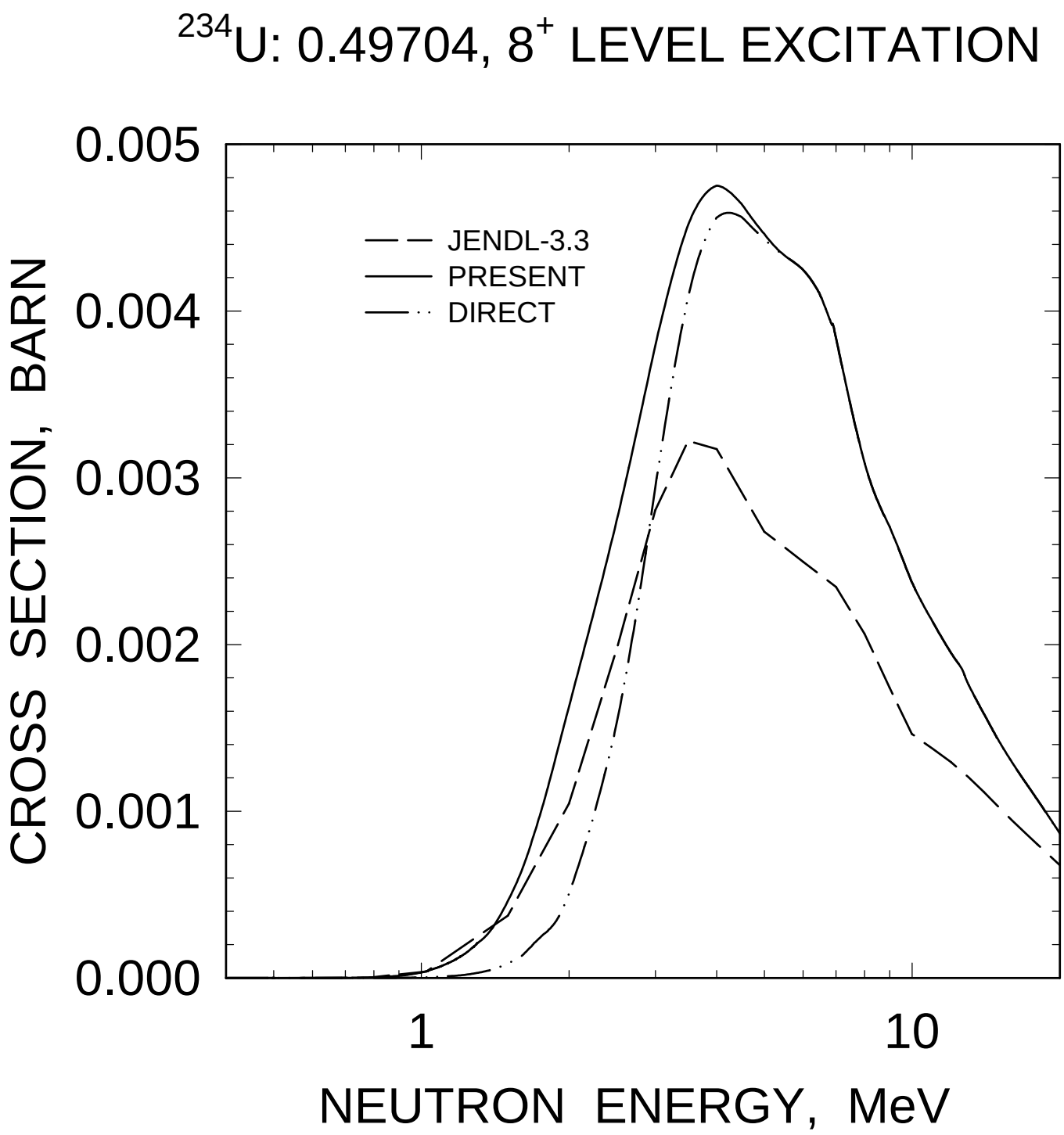
^{234}U: 0.49704, 8^{+} LEVEL EXCITATION
0.005
0.004
0.003
0.002
0.001
0.000
CROSS SECTION, BARN
JENDL-3.3
PRESENT
DIRECT
1
10
NEUTRON ENERGY, MeV

FIG. 34

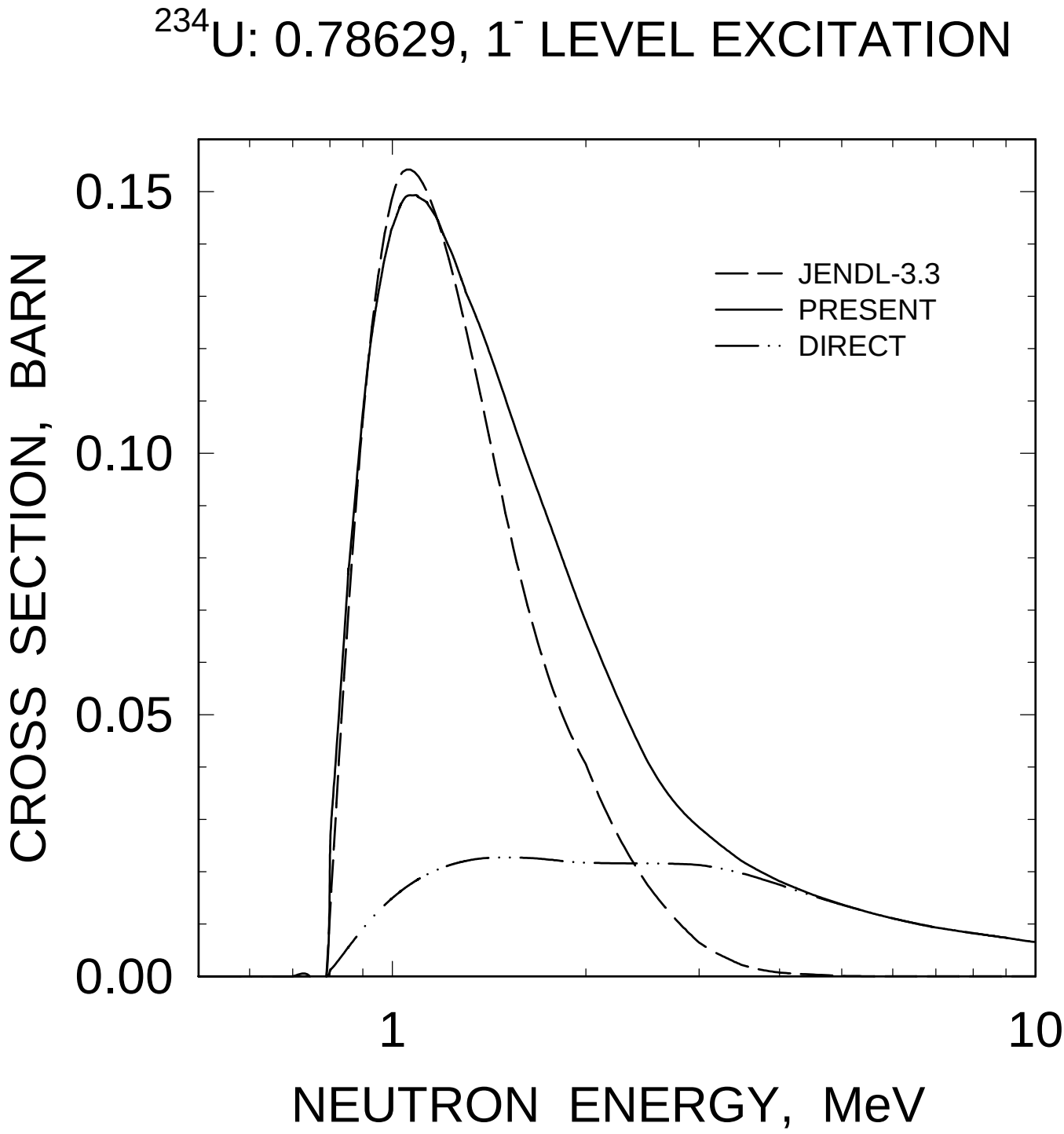
^{234}U: 0.78629, 1^{-} LEVEL EXCITATION
CROSS SECTION, BARN
0.15
0.10
0.05
0.00
1
10
NEUTRON ENERGY, MeV
JENDL-3.3
PRESENT
DIRECT

FIG. 35

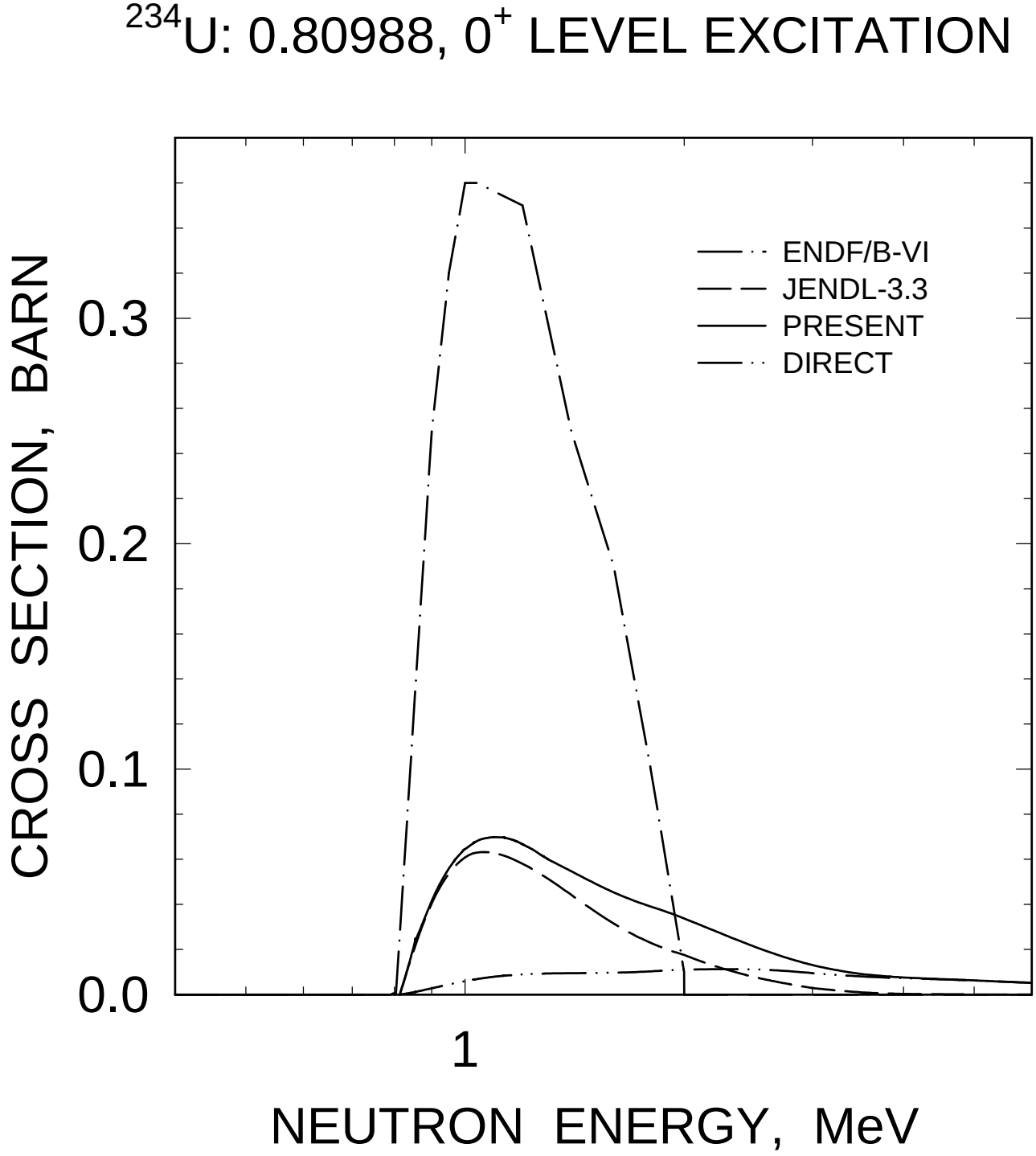
^{234}U: 0.80988, 0^+ LEVEL EXCITATION
CROSS SECTION, BARN
0.0
0.1
0.2
0.3
1
NEUTRON ENERGY, MeV
ENDF/B-VI
JENDL-3.3
PRESENT
DIRECT

FIG. 36

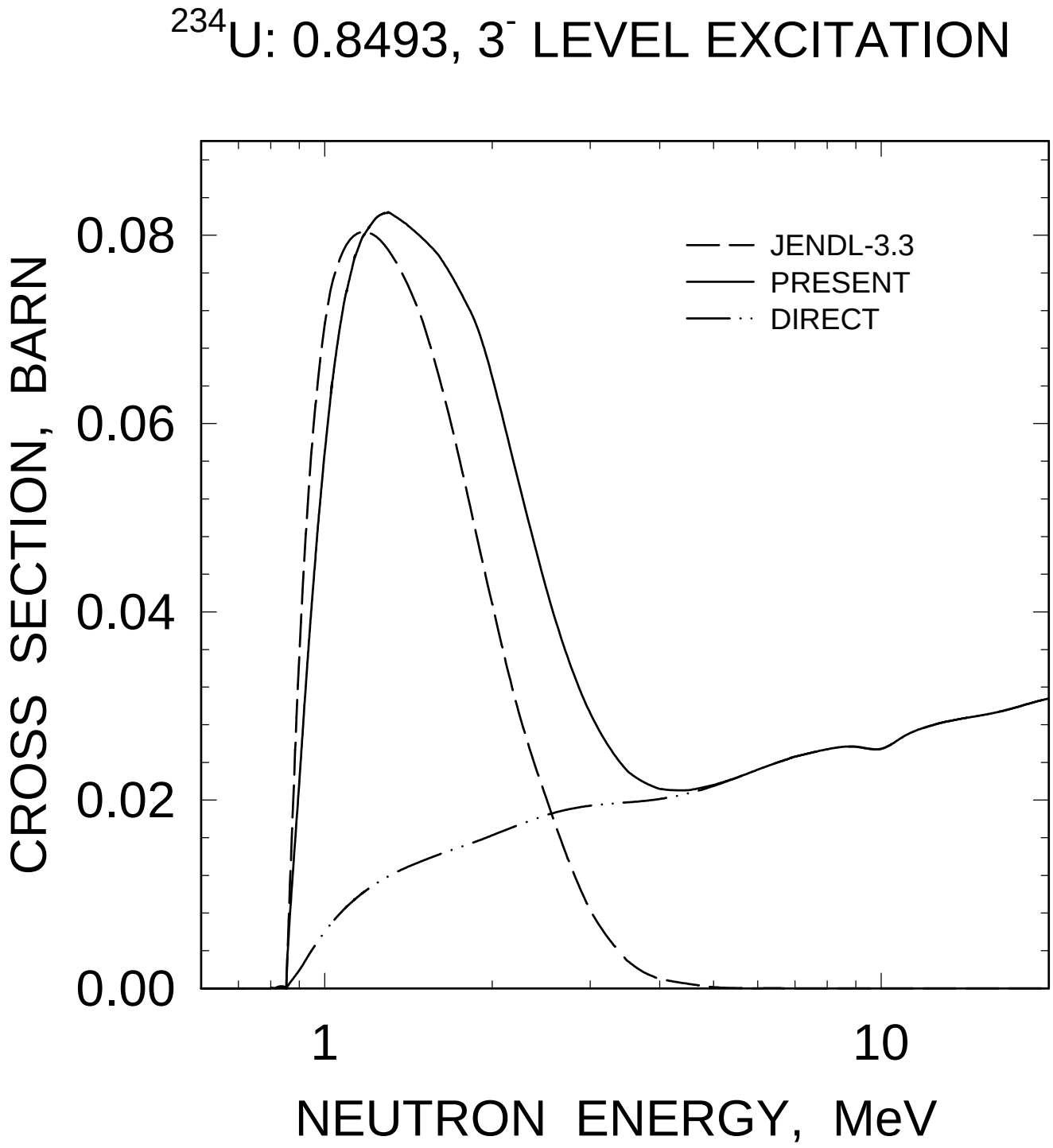
^{234}U: 0.8493, 3$^-$ LEVEL EXCITATION
CROSS SECTION, BARN
0.08
0.06
0.04
0.02
0.00
1
10
NEUTRON ENERGY, MeV
JENDL-3.3
PRESENT
DIRECT

FIG. 37

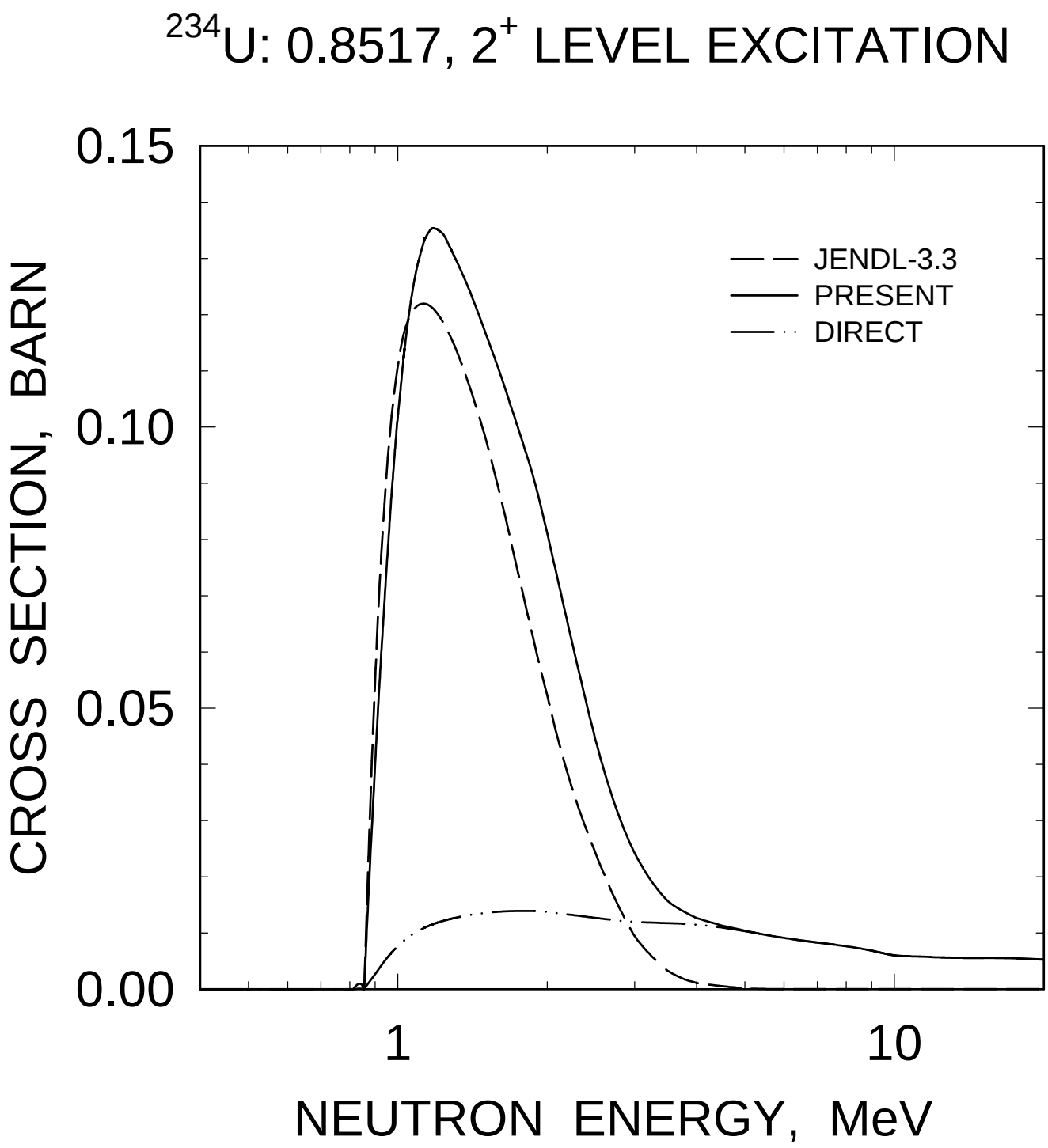
^{234}U: 0.8517, 2^{+} LEVEL EXCITATION
0.15
0.10
0.05
0.00
CROSS SECTION, BARN
JENDL-3.3
PRESENT
DIRECT
1
10
NEUTRON ENERGY, MeV

FIG. 38

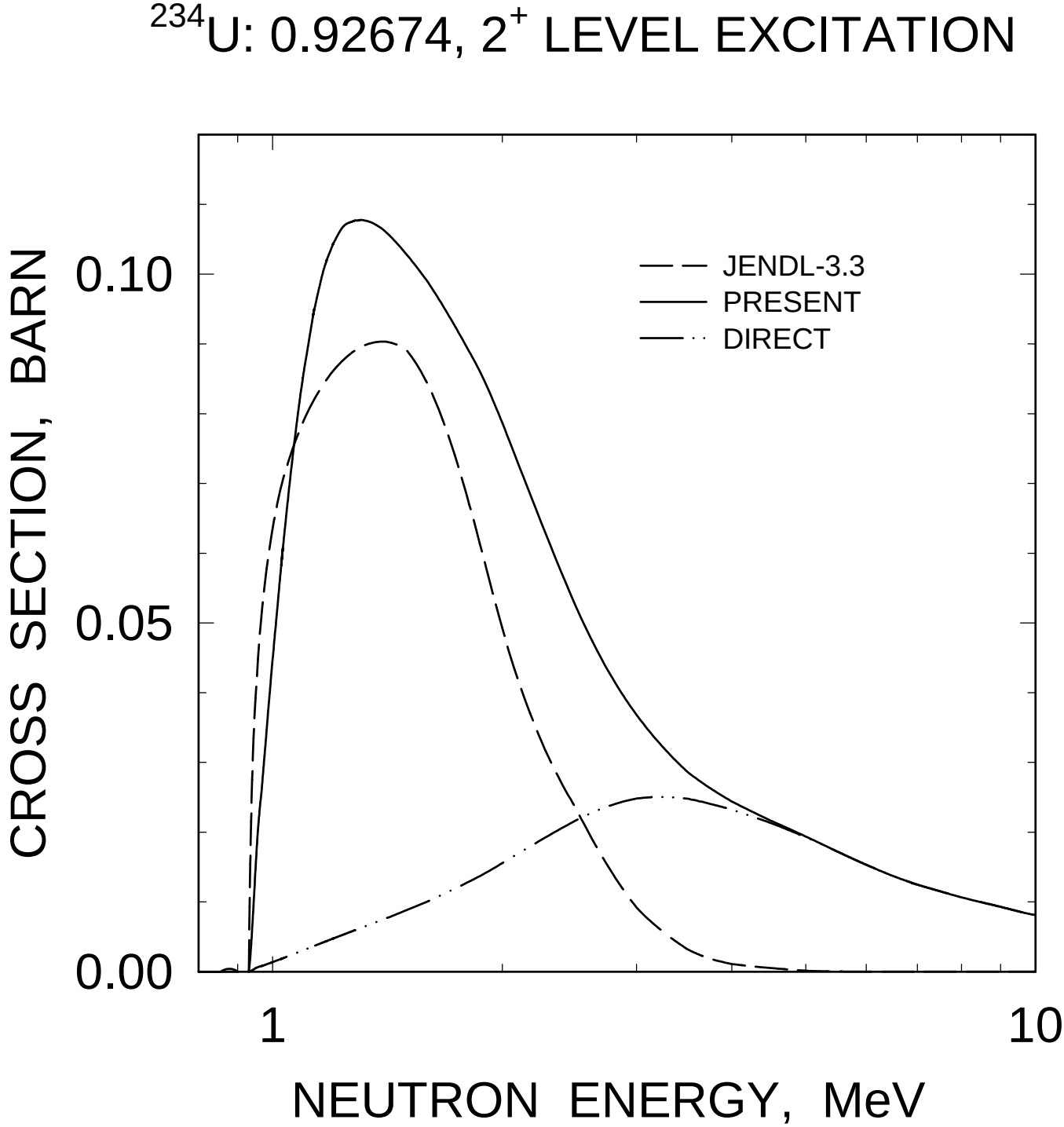
^{234}U: 0.92674, 2^{+} LEVEL EXCITATION
CROSS SECTION, BARN
0.10
0.05
0.00
1
10
NEUTRON ENERGY, MeV
JENDL-3.3
PRESENT
DIRECT

FIG. 39

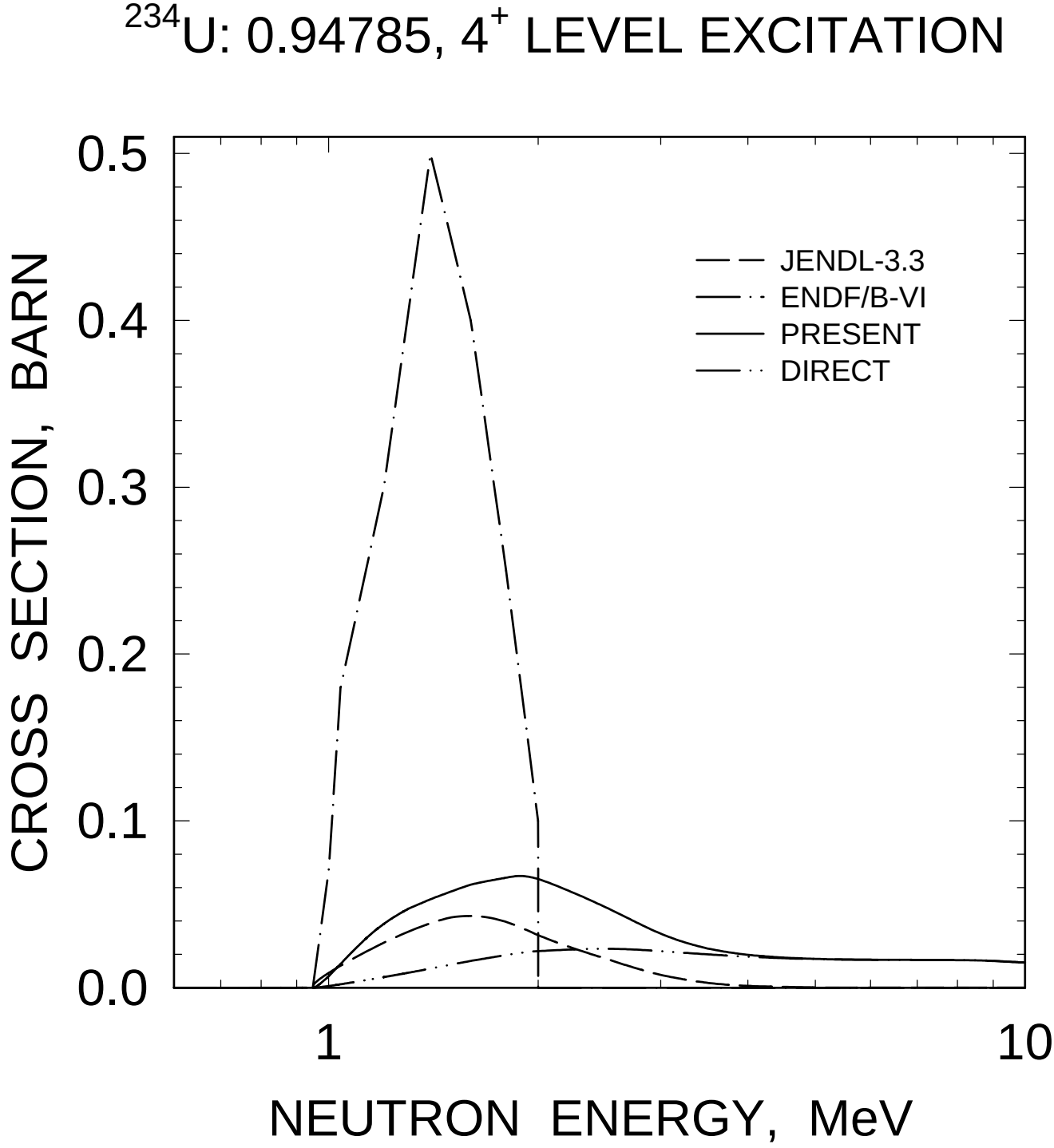
^{234}U: 0.94785, 4^{+} LEVEL EXCITATION
CROSS SECTION, BARN
0.5
0.4
0.3
0.2
0.1
0.0
1
10
NEUTRON ENERGY, MeV
JENDL-3.3
ENDF/B-VI
PRESENT
DIRECT

FIG. 40

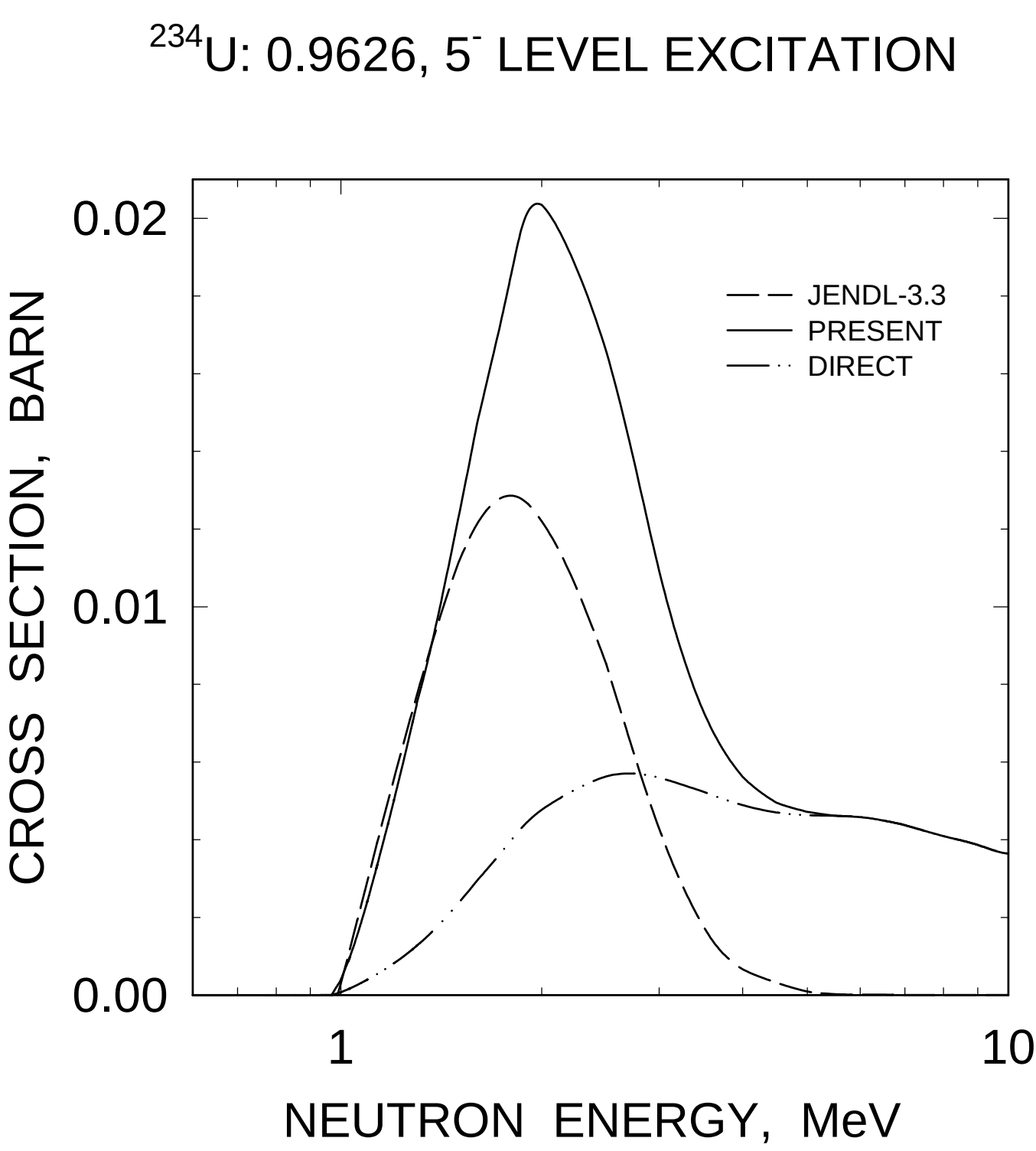
^{234}U: 0.9626, 5^{-} LEVEL EXCITATION
0.02
0.01
0.00
CROSS SECTION, BARN
JENDL-3.3
PRESENT
DIRECT
1
10
NEUTRON ENERGY, MeV

FIG. 41

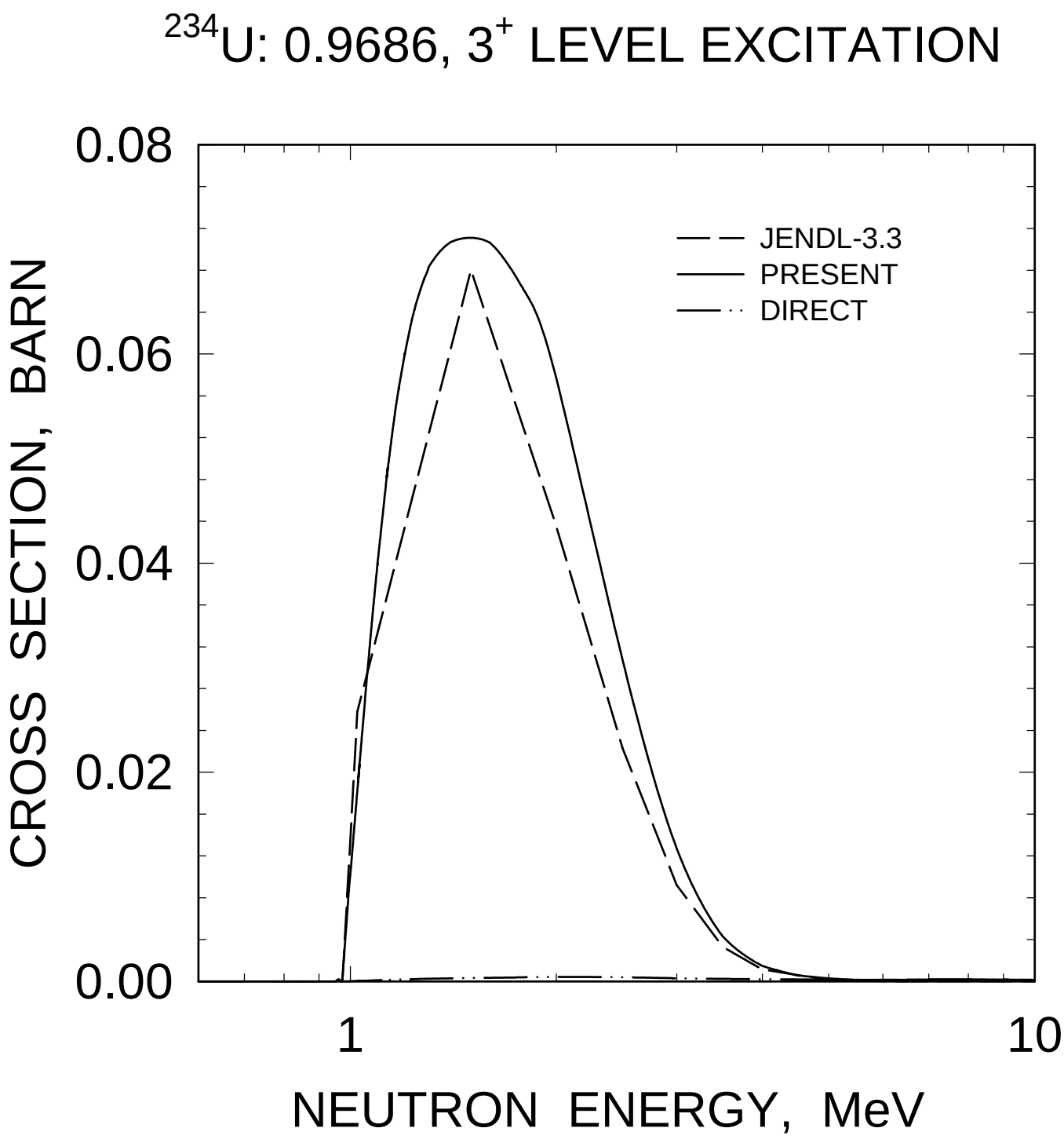
^{234}U: 0.9686, 3^{+} LEVEL EXCITATION
0.08
0.06
0.04
0.02
0.00
CROSS SECTION, BARN
JENDL-3.3
PRESENT
DIRECT
1
10
NEUTRON ENERGY, MeV

FIG. 42

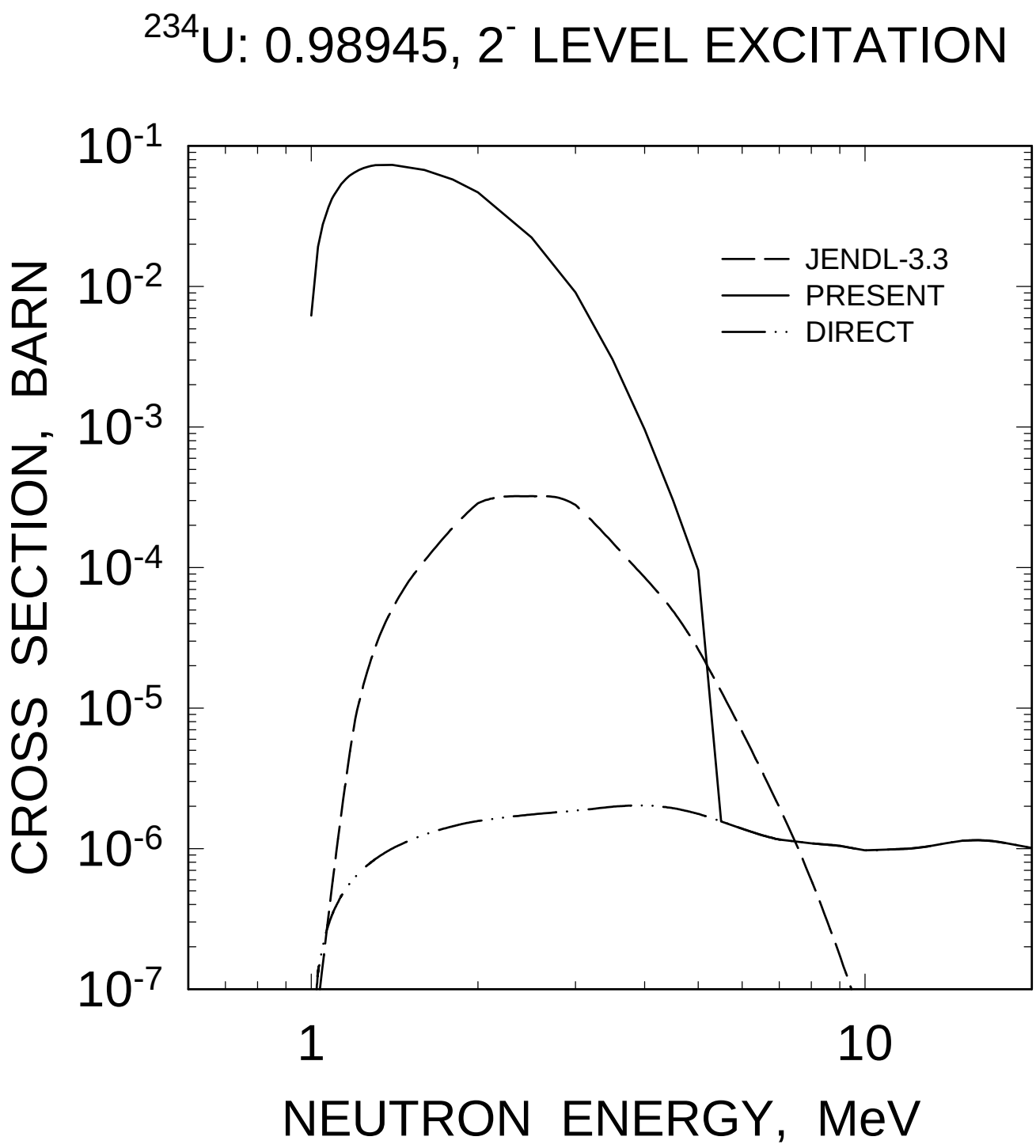
^{234}U: 0.98945, 2^{-} LEVEL EXCITATION
CROSS SECTION, BARN
10^{-1}
10^{-2}
10^{-3}
10^{-4}
10^{-5}
10^{-6}
10^{-7}
JENDL-3.3
PRESENT
DIRECT
1
10
NEUTRON ENERGY, MeV

FIG. 43

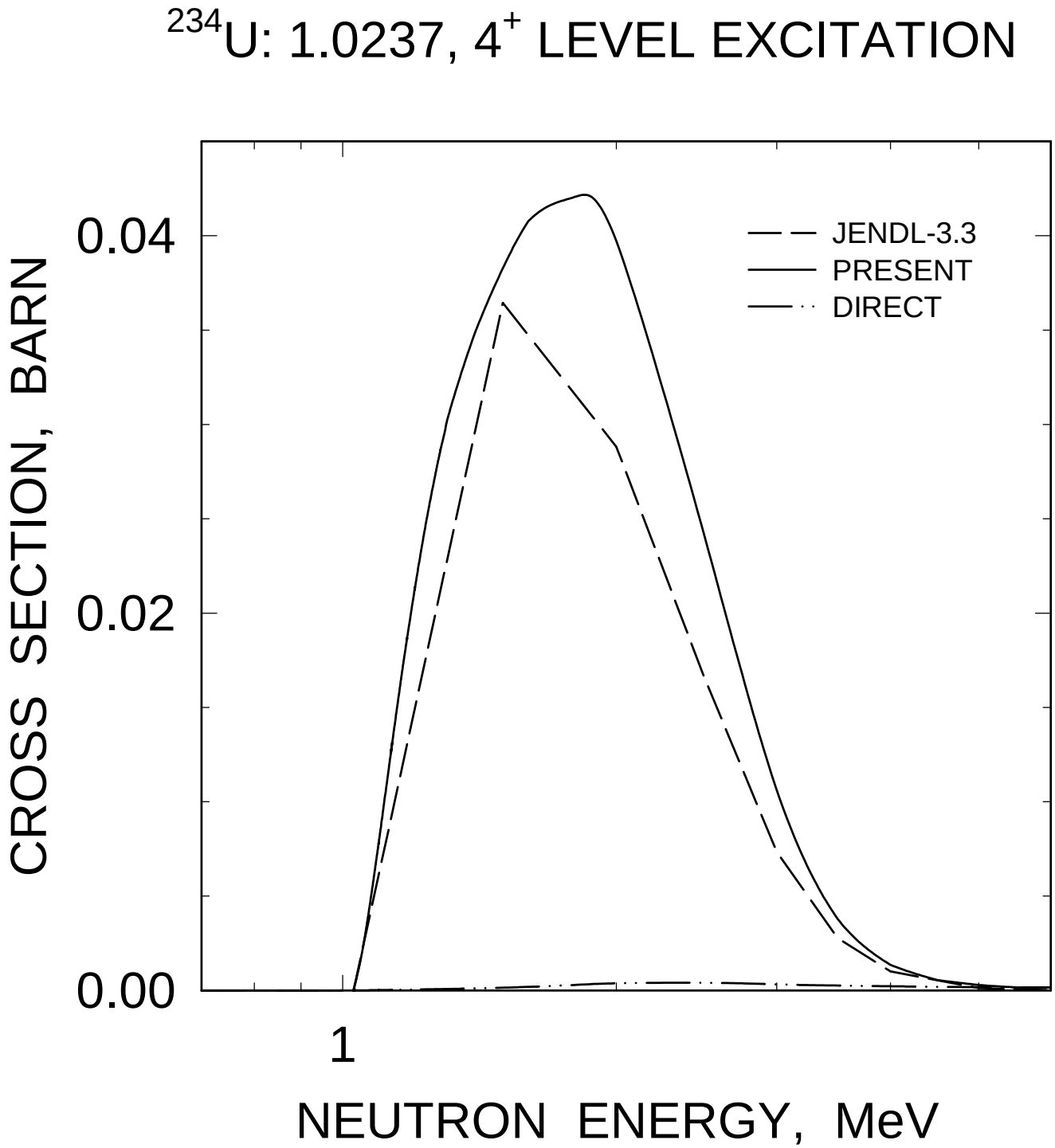
^{234}U: 1.0237, 4^{+} LEVEL EXCITATION
CROSS SECTION, BARN
0.04
0.02
0.00
1
NEUTRON ENERGY, MeV
JENDL-3.3
PRESENT
DIRECT

FIG. 44

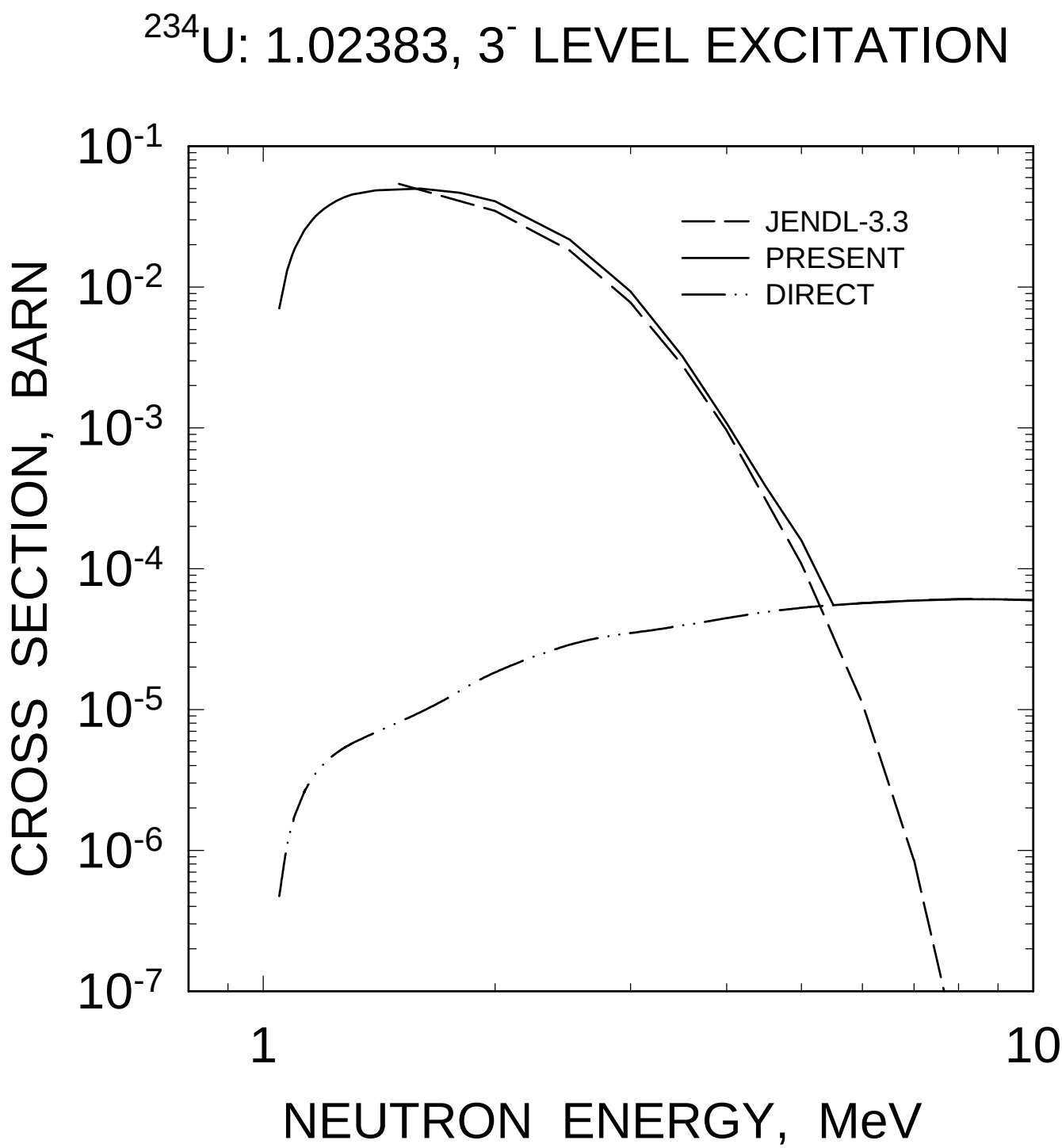
^{234}U: 1.02383, 3^{-} LEVEL EXCITATION
CROSS SECTION, BARN
10^{-1}
10^{-2}
10^{-3}
10^{-4}
10^{-5}
10^{-6}
10^{-7}
JENDL-3.3
PRESENT
DIRECT
1
10
NEUTRON ENERGY, MeV

FIG. 45

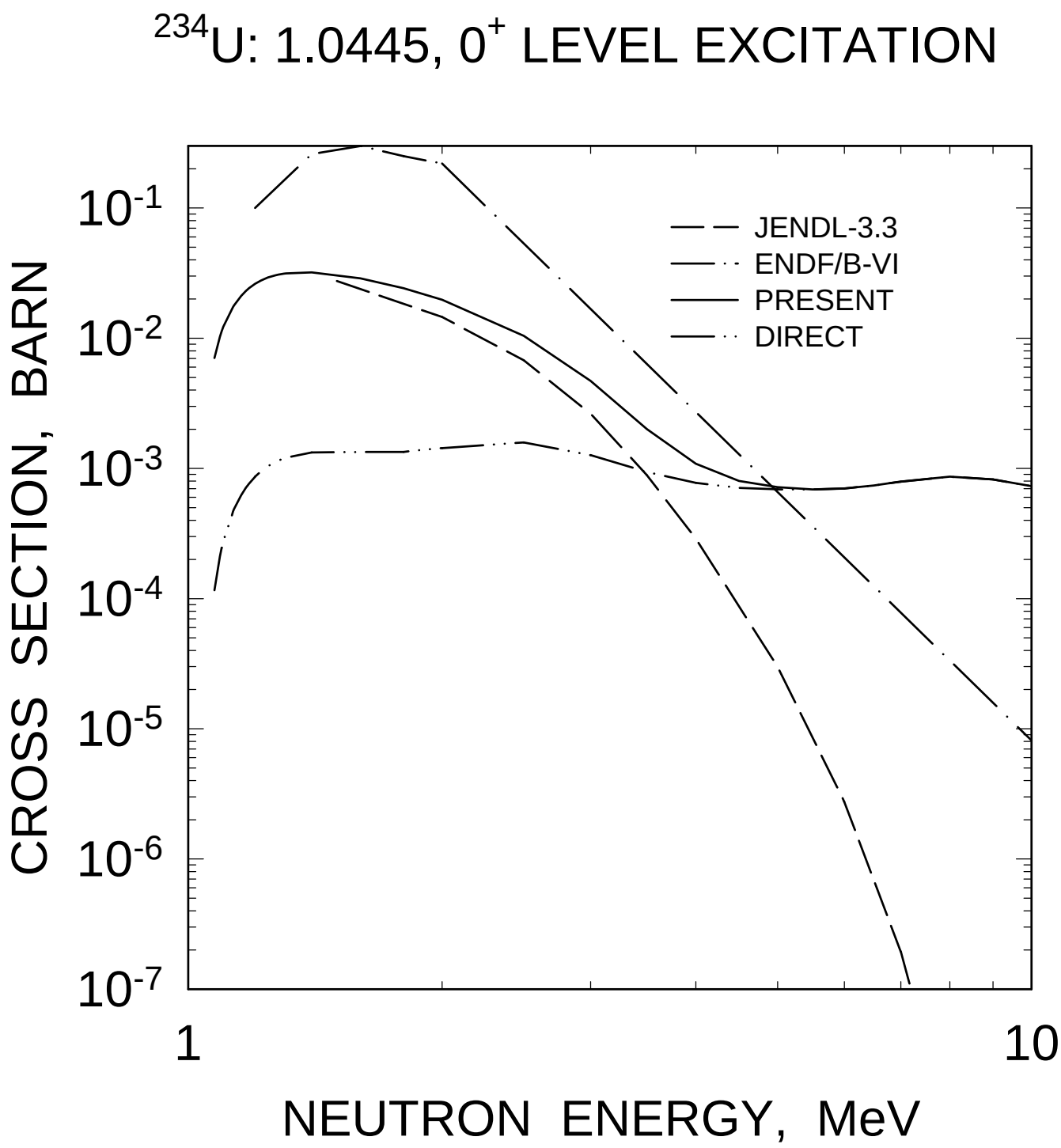
^{234}U: 1.0445, 0^{+} LEVEL EXCITATION
CROSS SECTION, BARN
10^{-1}
10^{-2}
10^{-3}
10^{-4}
10^{-5}
10^{-6}
10^{-7}
1
10
NEUTRON ENERGY, MeV
JENDL-3.3
ENDF/B-VI
PRESENT
DIRECT

FIG. 46

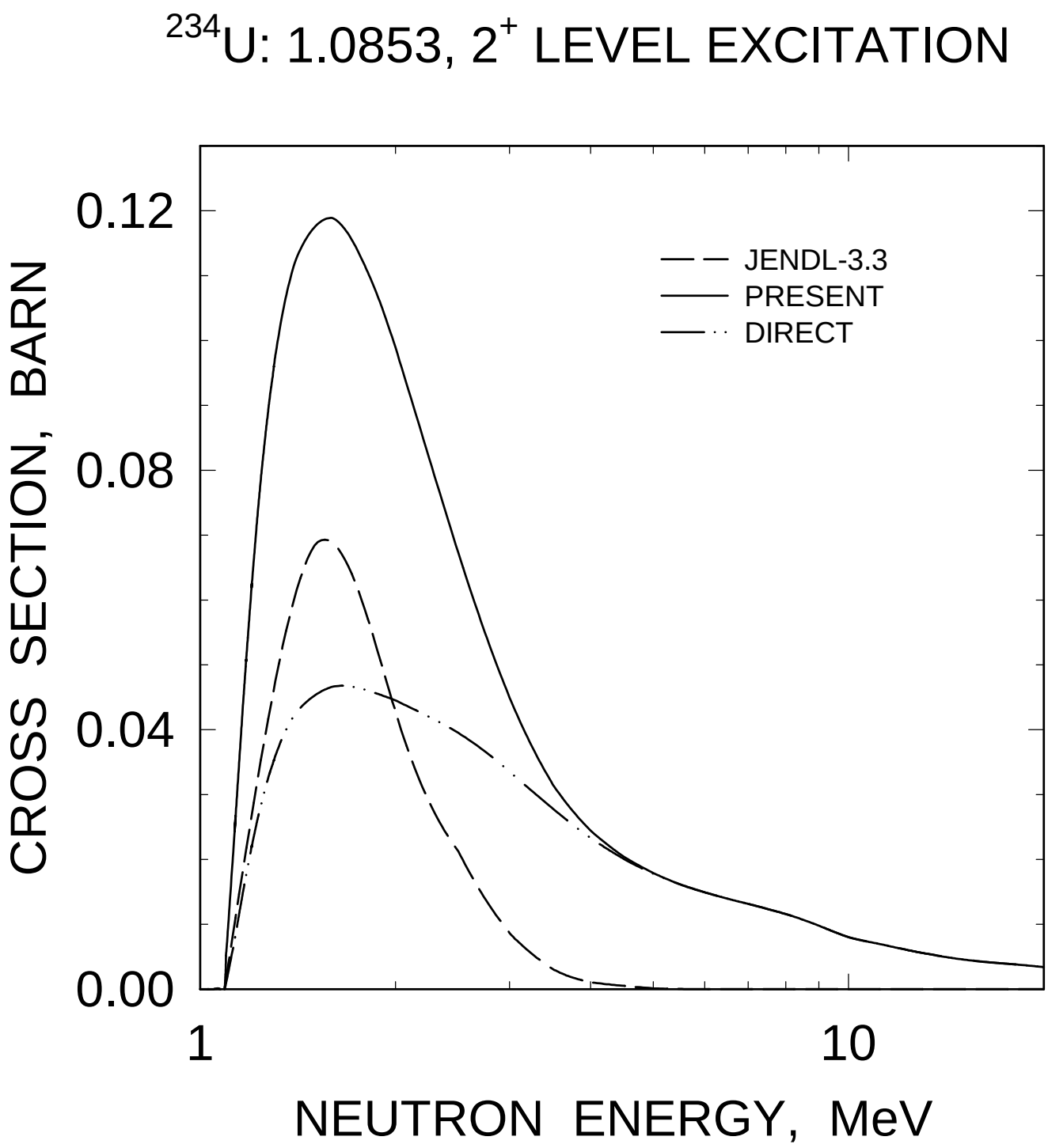
^{234}U: 1.0853, 2^{+} LEVEL EXCITATION
CROSS SECTION, BARN
0.12
0.08
0.04
0.00
1
10
NEUTRON ENERGY, MeV
JENDL-3.3
PRESENT
DIRECT

FIG. 47

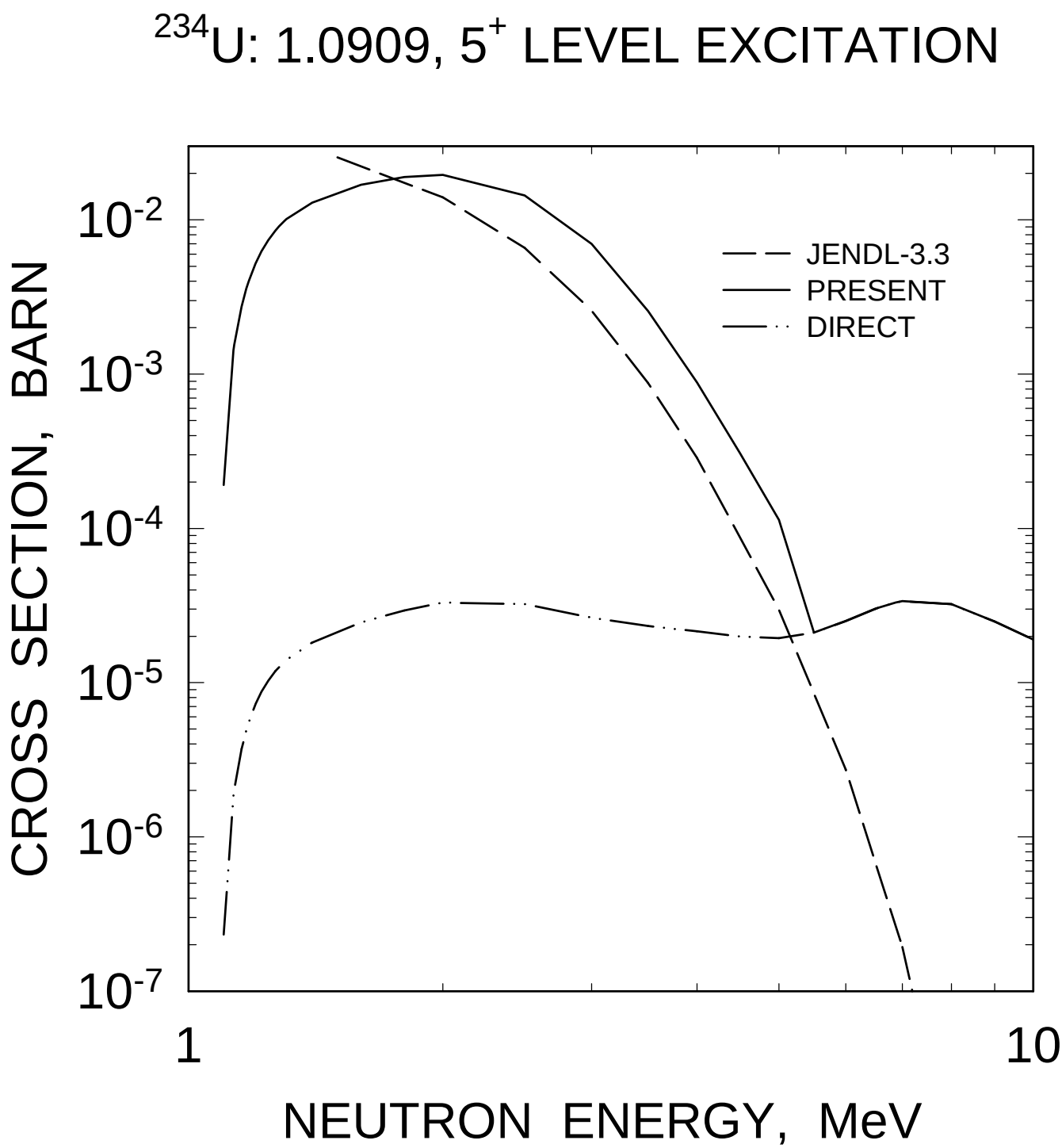
^{234}U: 1.0909, 5^{+} LEVEL EXCITATION
CROSS SECTION, BARN
10^{-2}
10^{-3}
10^{-4}
10^{-5}
10^{-6}
10^{-7}
1
10
NEUTRON ENERGY, MeV
JENDL-3.3
PRESENT
DIRECT

FIG. 48

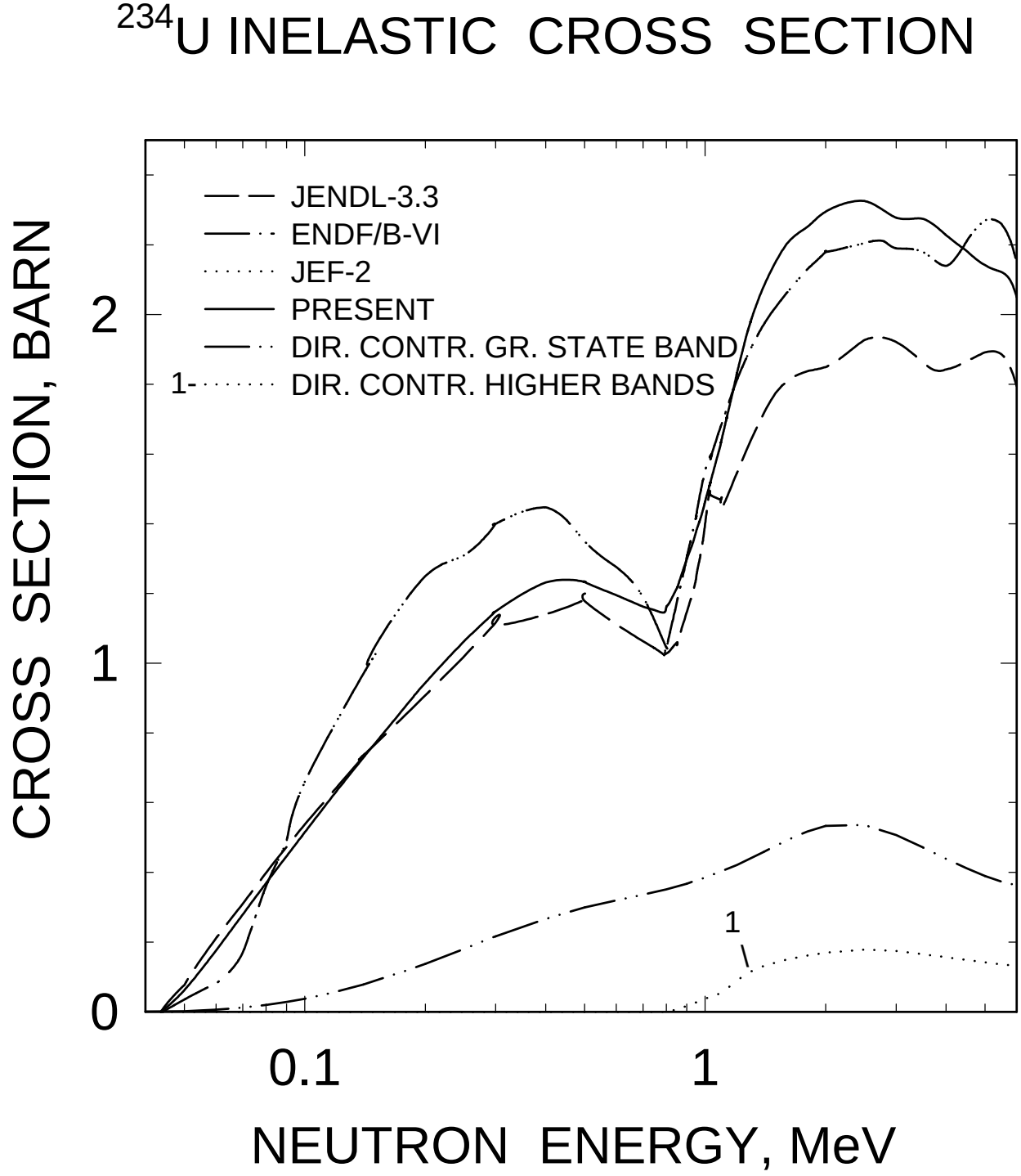
^{234}U INELASTIC CROSS SECTION
JENDL-3.3
ENDF/B-VI
JEF-2
PRESENT
DIR. CONTR. GR. STATE BAND
DIR. CONTR. HIGHER BANDS
CROSS SECTION, BARN
0
1
2
0.1
1
NEUTRON ENERGY, MeV

FIG. 49

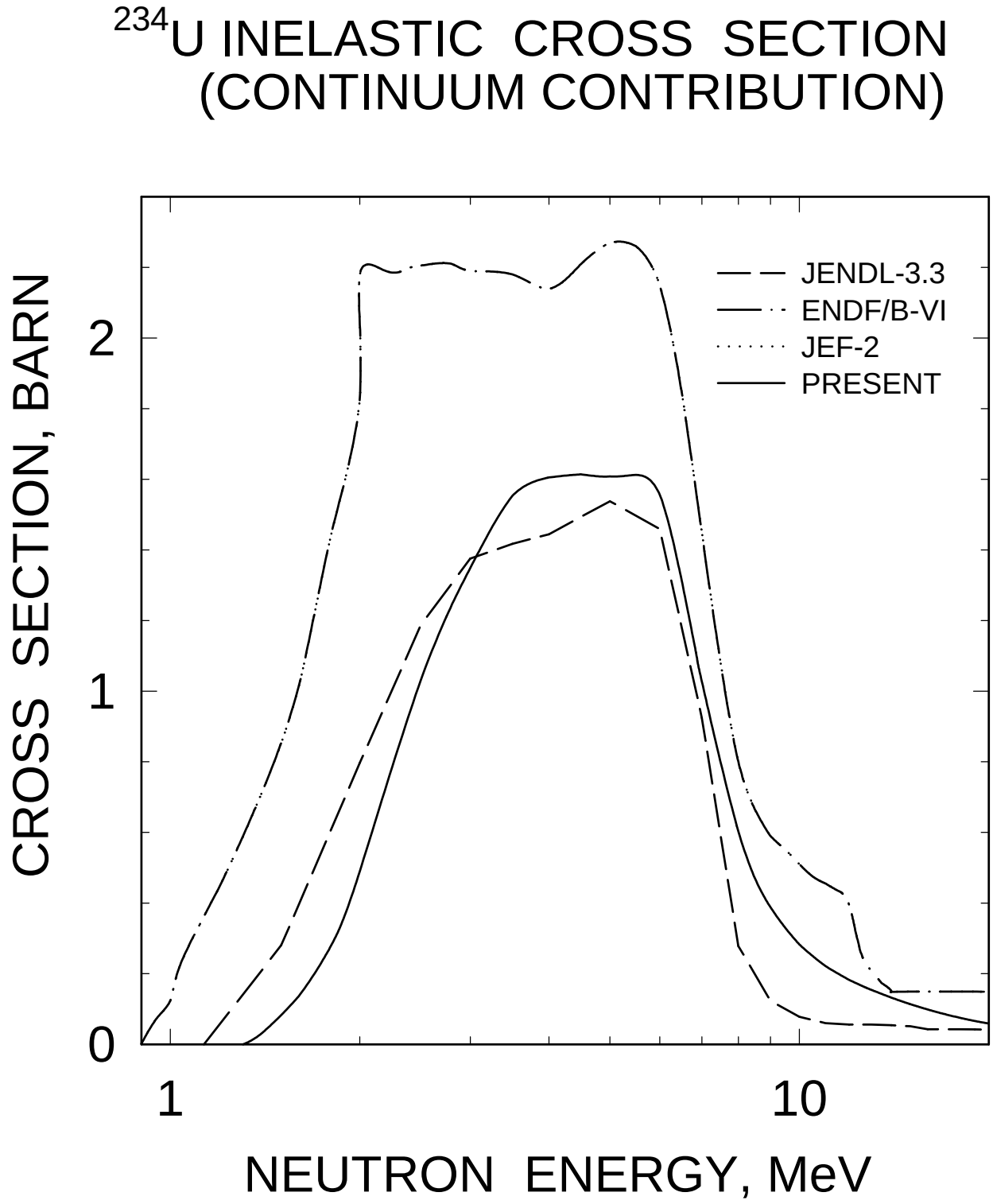
^{234}U INELASTIC CROSS SECTION
(CONTINUUM CONTRIBUTION)
CROSS SECTION, BARN
0
1
2
1
10
NEUTRON ENERGY, MeV
JENDL-3.3
ENDF/B-VI
JEF-2
PRESENT

FIG. 50

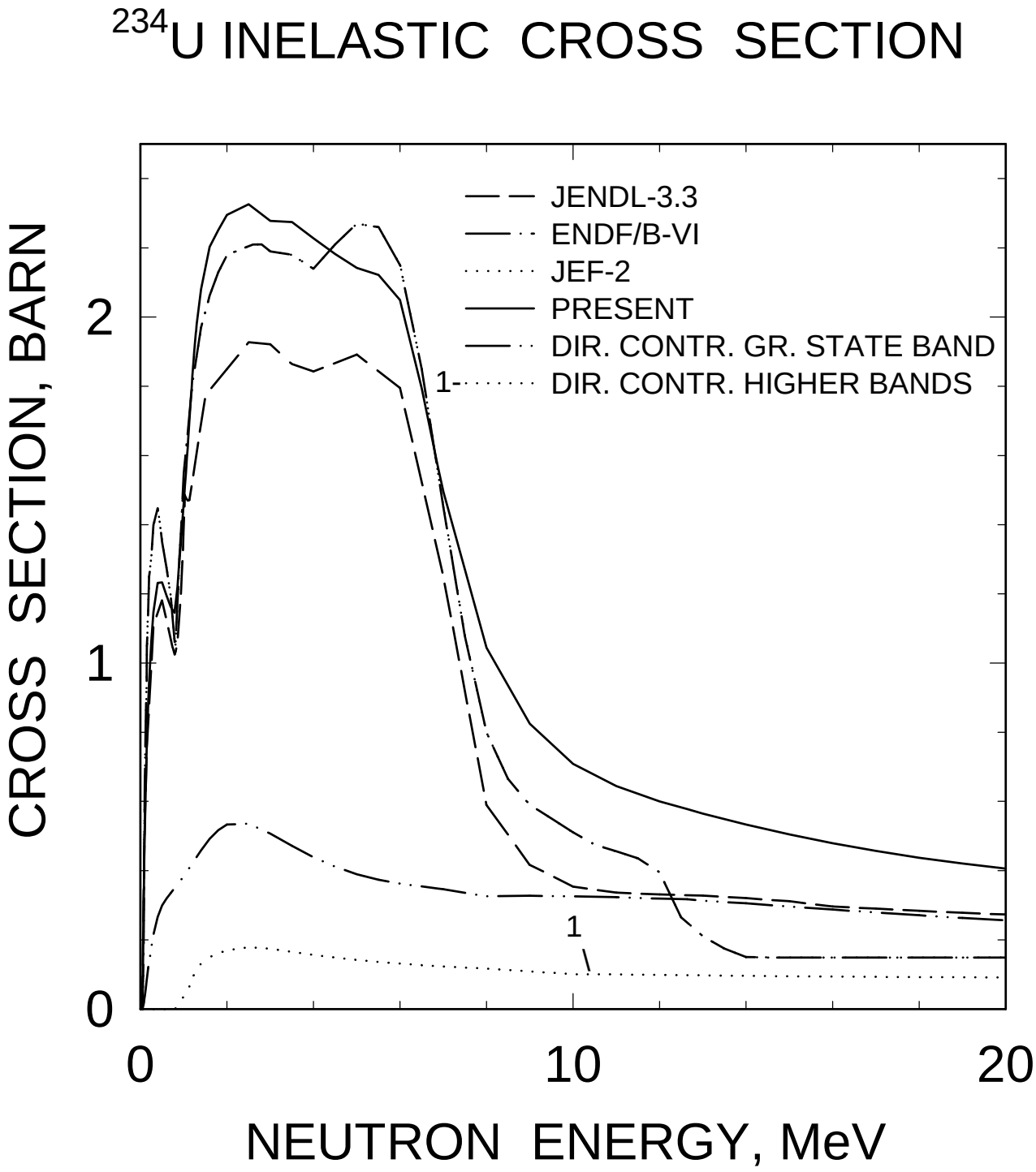
^{234}U INELASTIC CROSS SECTION
JENDL-3.3
ENDF/B-VI
JEF-2
PRESENT
DIR. CONTR. GR. STATE BAND
DIR. CONTR. HIGHER BANDS
CROSS SECTION, BARN
NEUTRON ENERGY, MeV
0
1
2
10
20
1-
1

FIG. 51

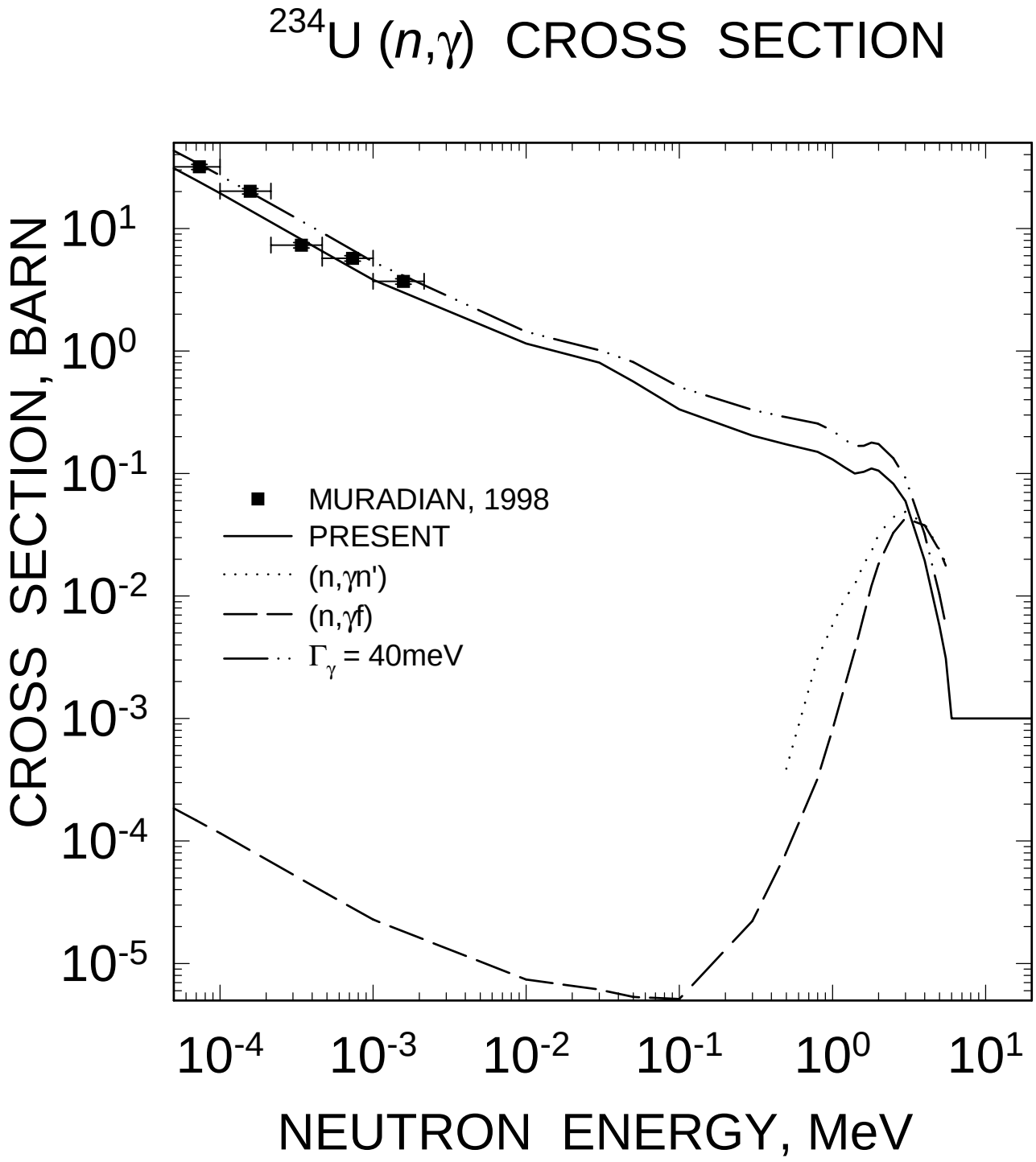
^{234}U (n,γ) CROSS SECTION
CROSS SECTION, BARN
10^{1}
10^{0}
10^{-1}
10^{-2}
10^{-3}
10^{-4}
10^{-5}
MURADIAN, 1998
PRESENT
(n,γn')
(n,γf)
Γ_γ = 40meV
10^{-4}
10^{-3}
10^{-2}
10^{-1}
10^{0}
10^{1}
NEUTRON ENERGY, MeV

FIG. 52

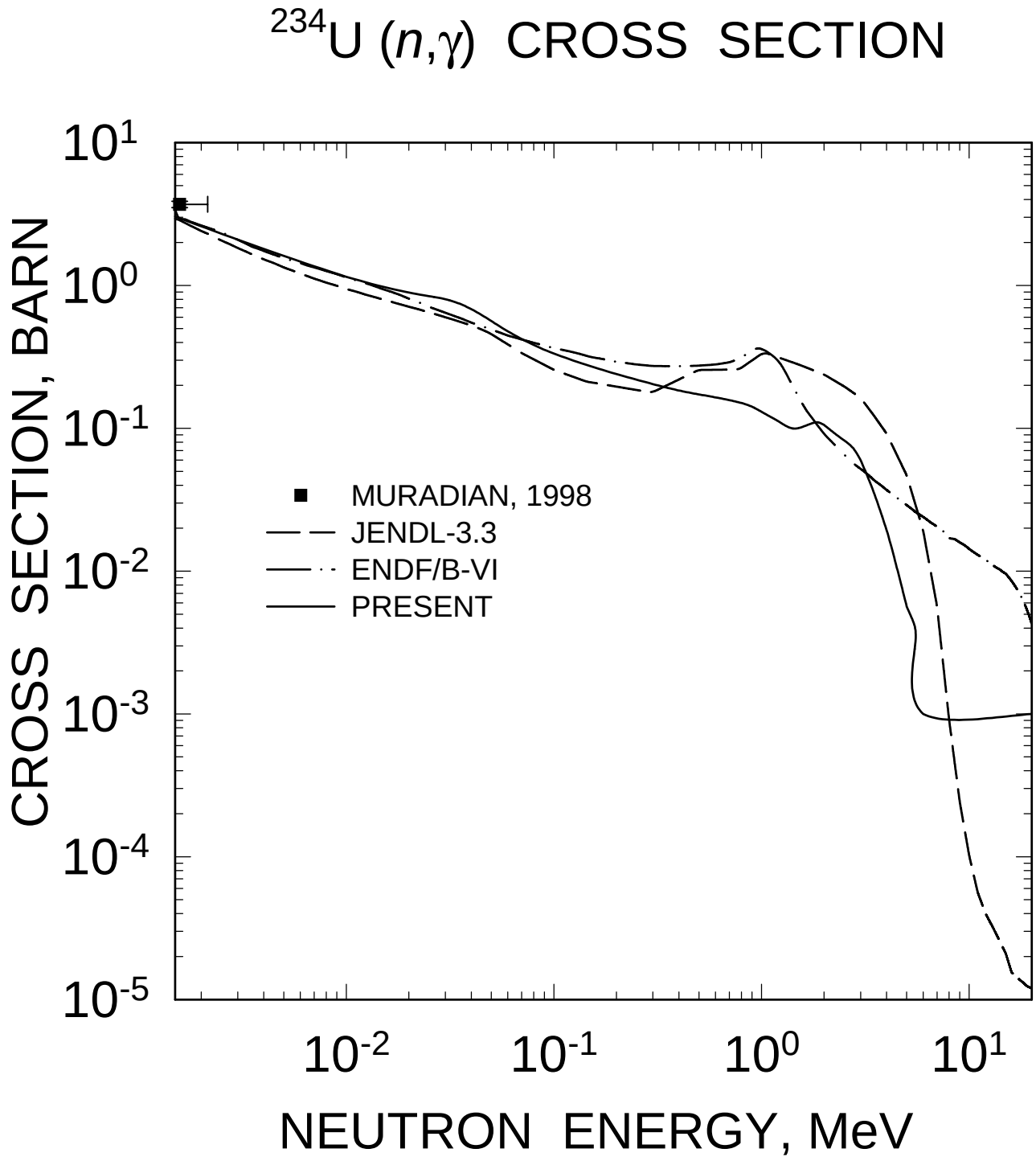
^{234}U (n,γ) CROSS SECTION
CROSS SECTION, BARN
NEUTRON ENERGY, MeV
MURADIAN, 1998
JENDL-3.3
ENDF/B-VI
PRESENT
10^{1}
10^{0}
10^{-1}
10^{-2}
10^{-3}
10^{-4}
10^{-5}
10^{-2}
10^{-1}
10^{0}
10^{1}

FIG. 53

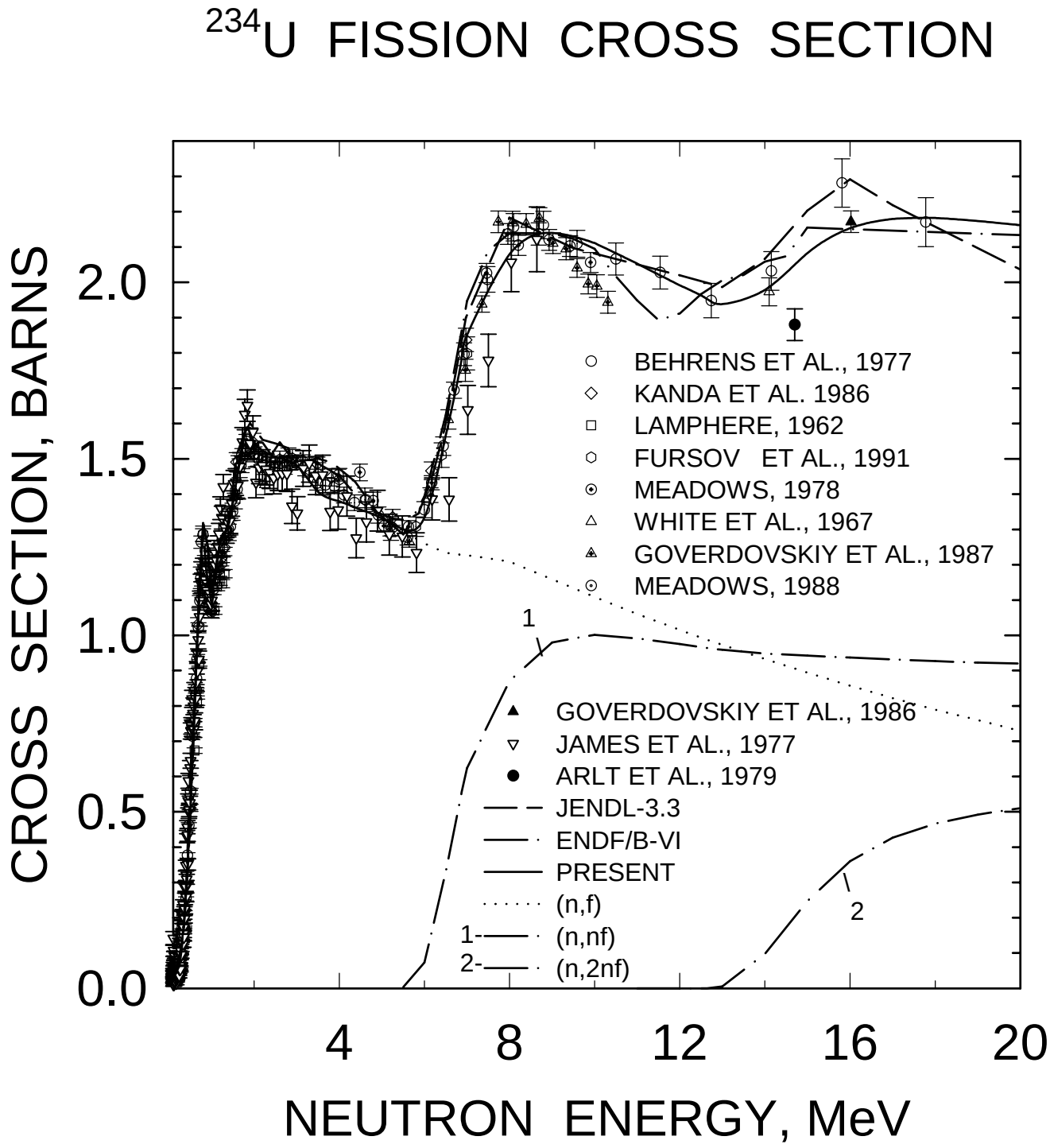
234U FISSION CROSS SECTION
CROSS SECTION, BARNS
0.0
0.5
1.0
1.5
2.0
4
8
12
16
20
NEUTRON ENERGY, MeV
BEHRENS ET AL., 1977
KANDA ET AL. 1986
LAMPHERE, 1962
FURSOV ET AL., 1991
MEADOWS, 1978
WHITE ET AL., 1967
GOVERDOVSKIY ET AL., 1987
MEADOWS, 1988
GOVERDOVSKIY ET AL., 1986
JAMES ET AL., 1977
ARLT ET AL., 1979
JENDL-3.3
ENDF/B-VI
PRESENT
(n,f)
1- (n,nf)
2- (n,2nf)
1
2

FIG. 54

^{234}U(n,f) CHANCE FISSION CONTRIBUTIONS

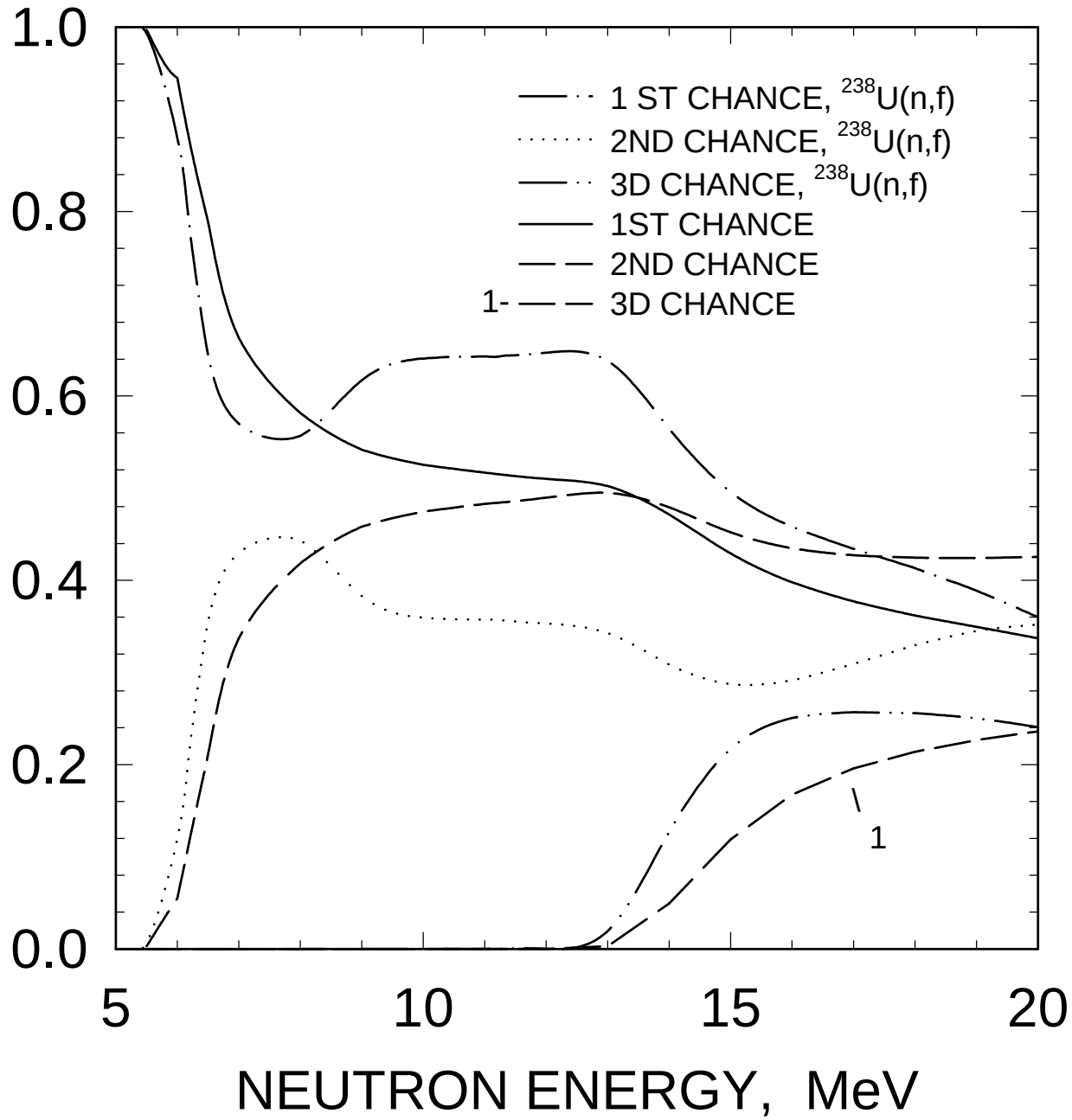

FIG. 55

^{233}U FISSION CROSS SECTION

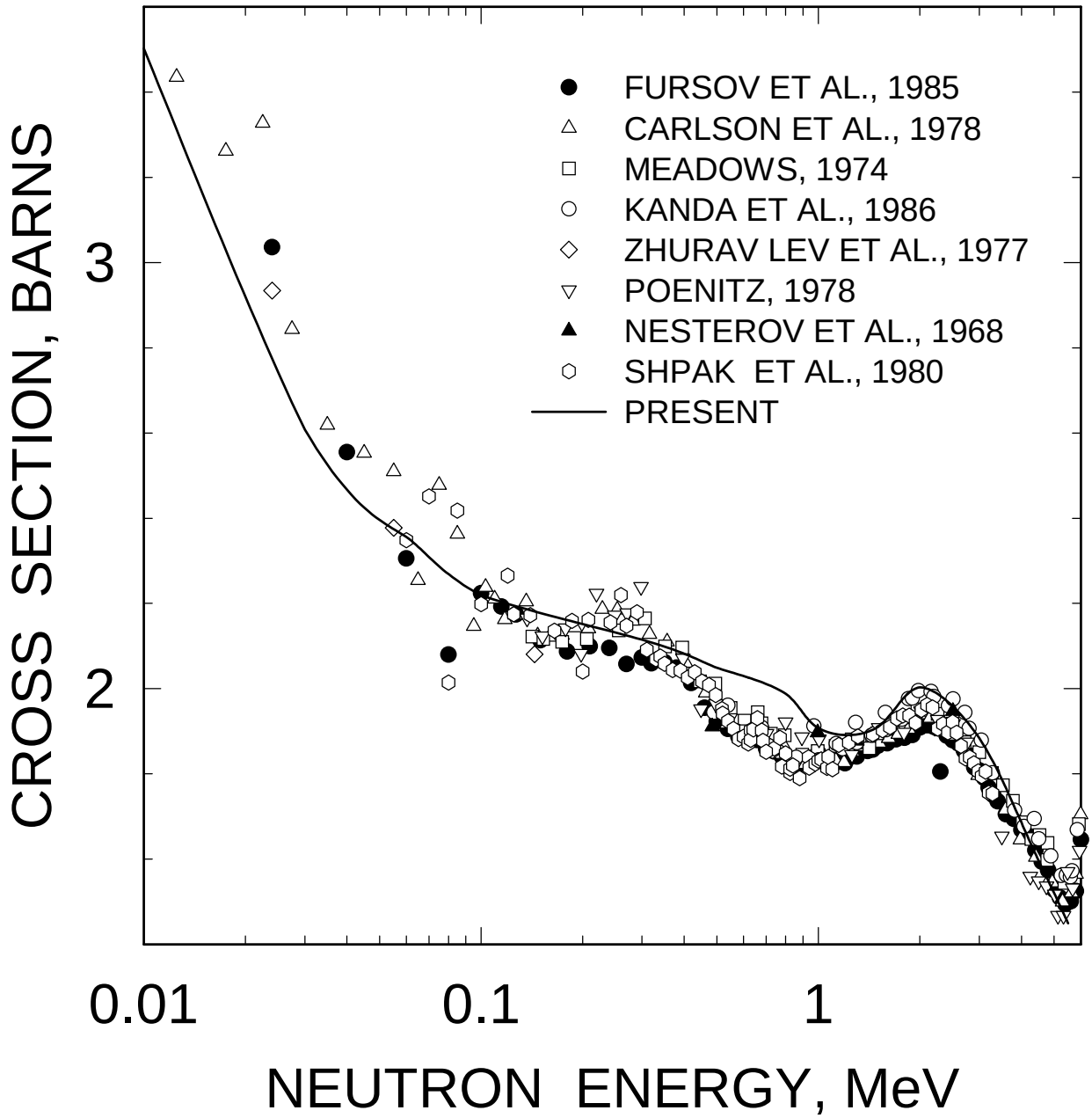

FIG. 56

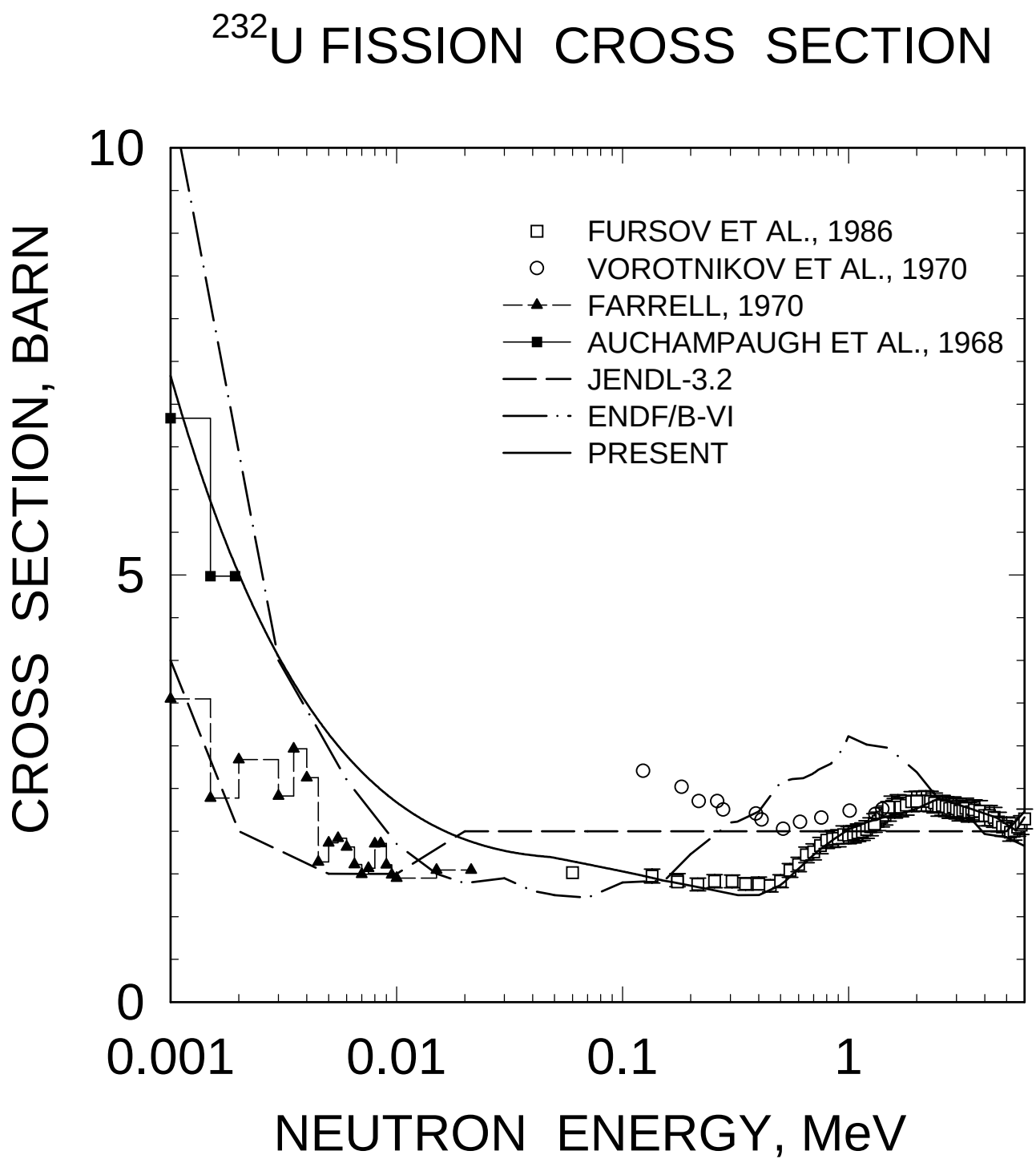
^{232}U FISSION CROSS SECTION
CROSS SECTION, BARN
10
5
0
0.001
0.01
0.1
1
NEUTRON ENERGY, MeV
FURSOV ET AL., 1986
VOROTNIKOV ET AL., 1970
FARRELL, 1970
AUCHAMPAUGH ET AL., 1968
JENDL-3.2
ENDF/B-VI
PRESENT

FIG. 57

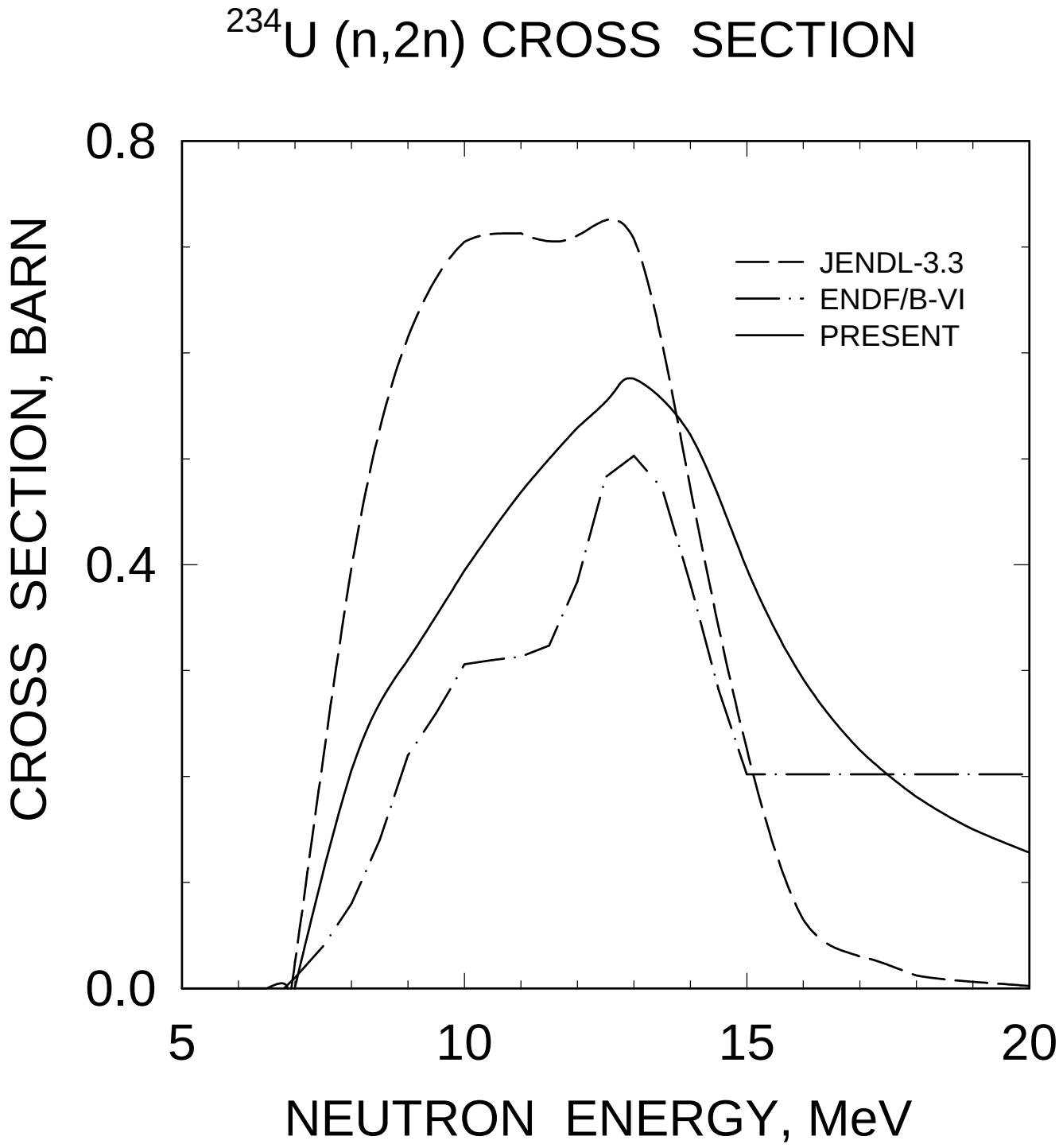
^{234}U (n,2n) CROSS SECTION
CROSS SECTION, BARN
0.8
0.4
0.0
5
10
15
20
NEUTRON ENERGY, MeV
JENDL-3.3
ENDF/B-VI
PRESENT

FIG. 58

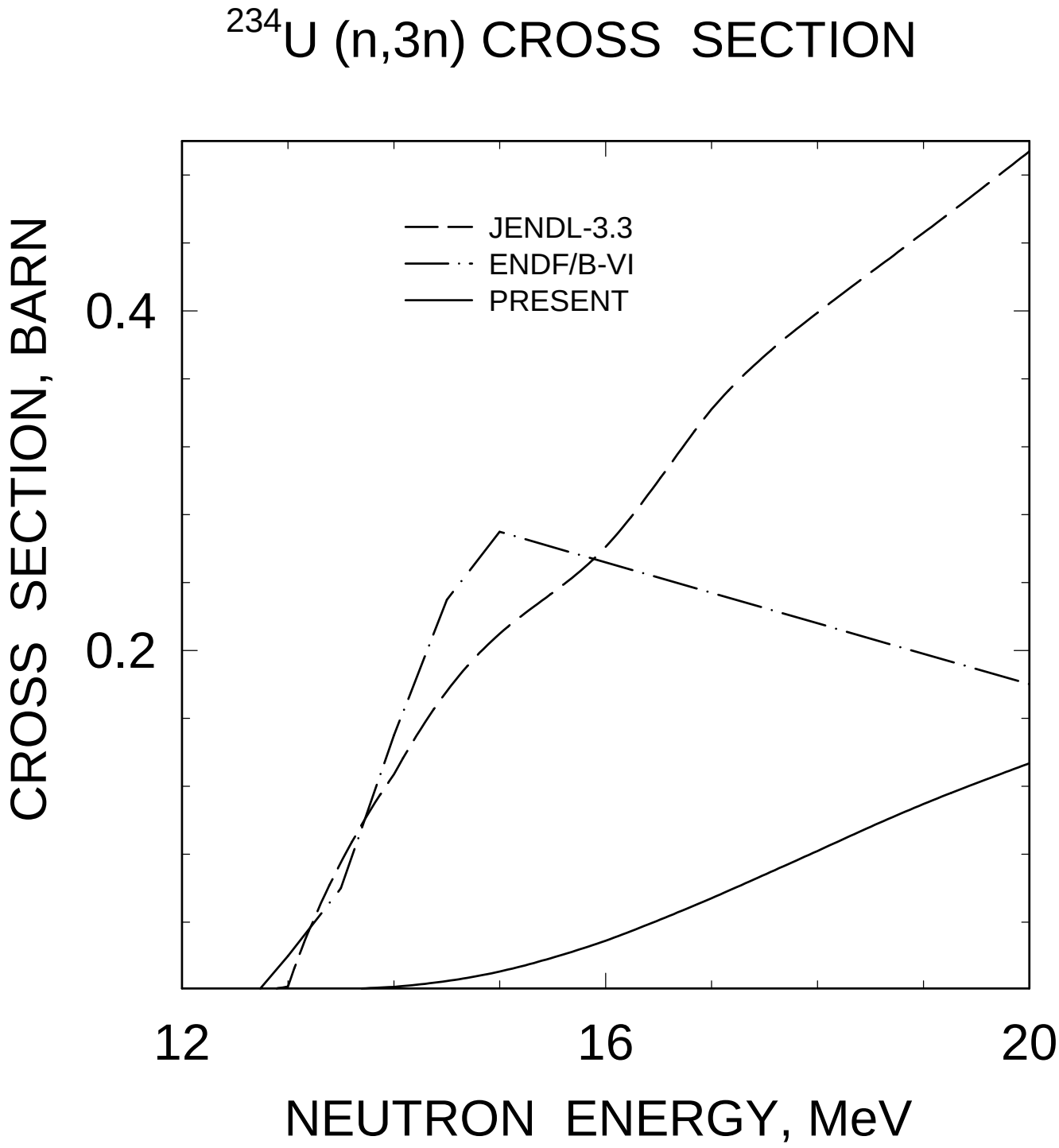
^{234}U (n,3n) CROSS SECTION
JENDL-3.3
ENDF/B-VI
PRESENT
CROSS SECTION, BARN
0.4
0.2
12
16
20
NEUTRON ENERGY, MeV

FIG. 59

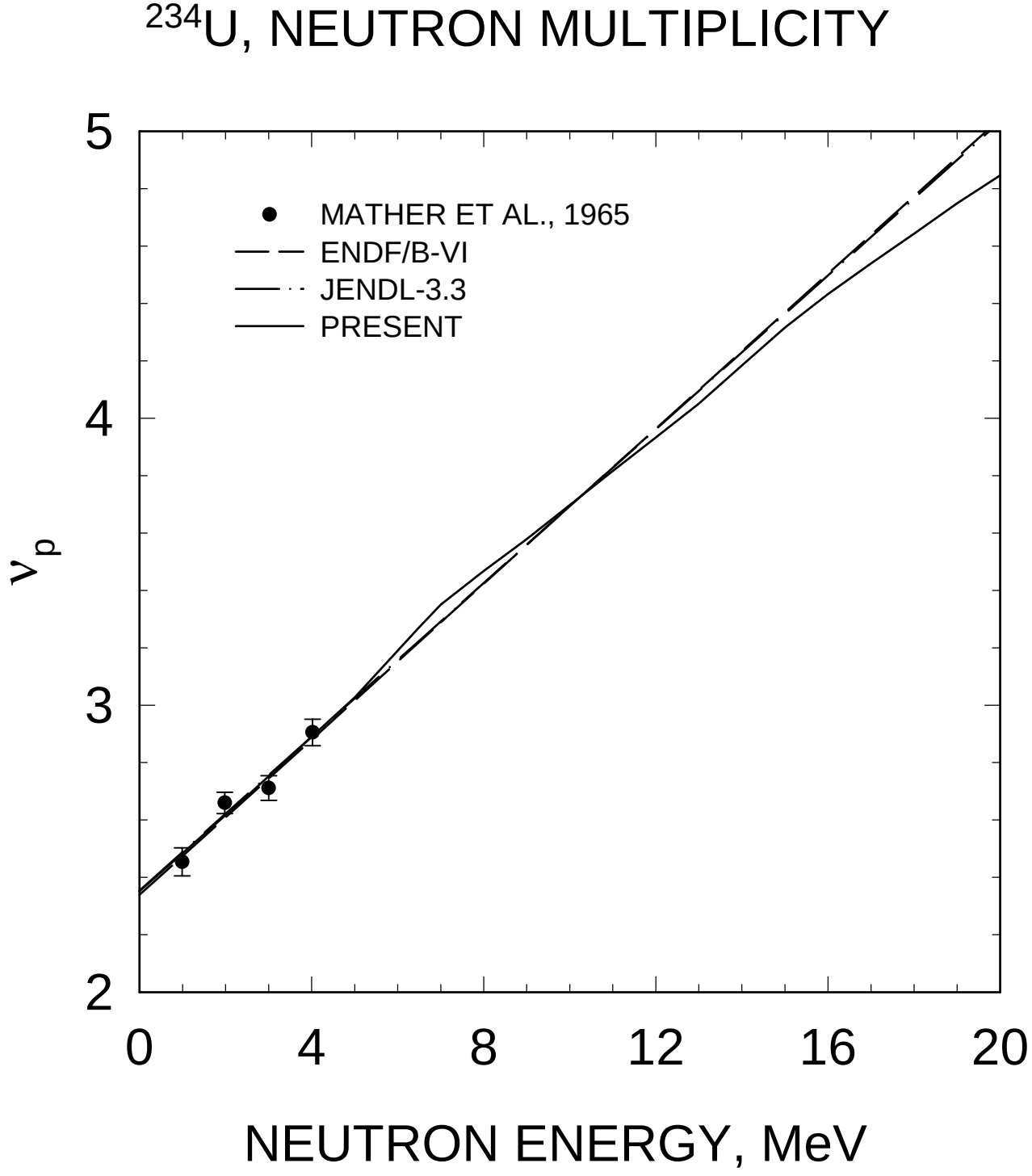
^{234}U, NEUTRON MULTIPLICITY
MATHER ET AL., 1965
ENDF/B-VI
JENDL-3.3
PRESENT
ν_p
5
4
3
2
0
4
8
12
16
20
NEUTRON ENERGY, MeV

FIG. 60

^{234}U, PARTIAL NEUTRON MULTIPLICITY

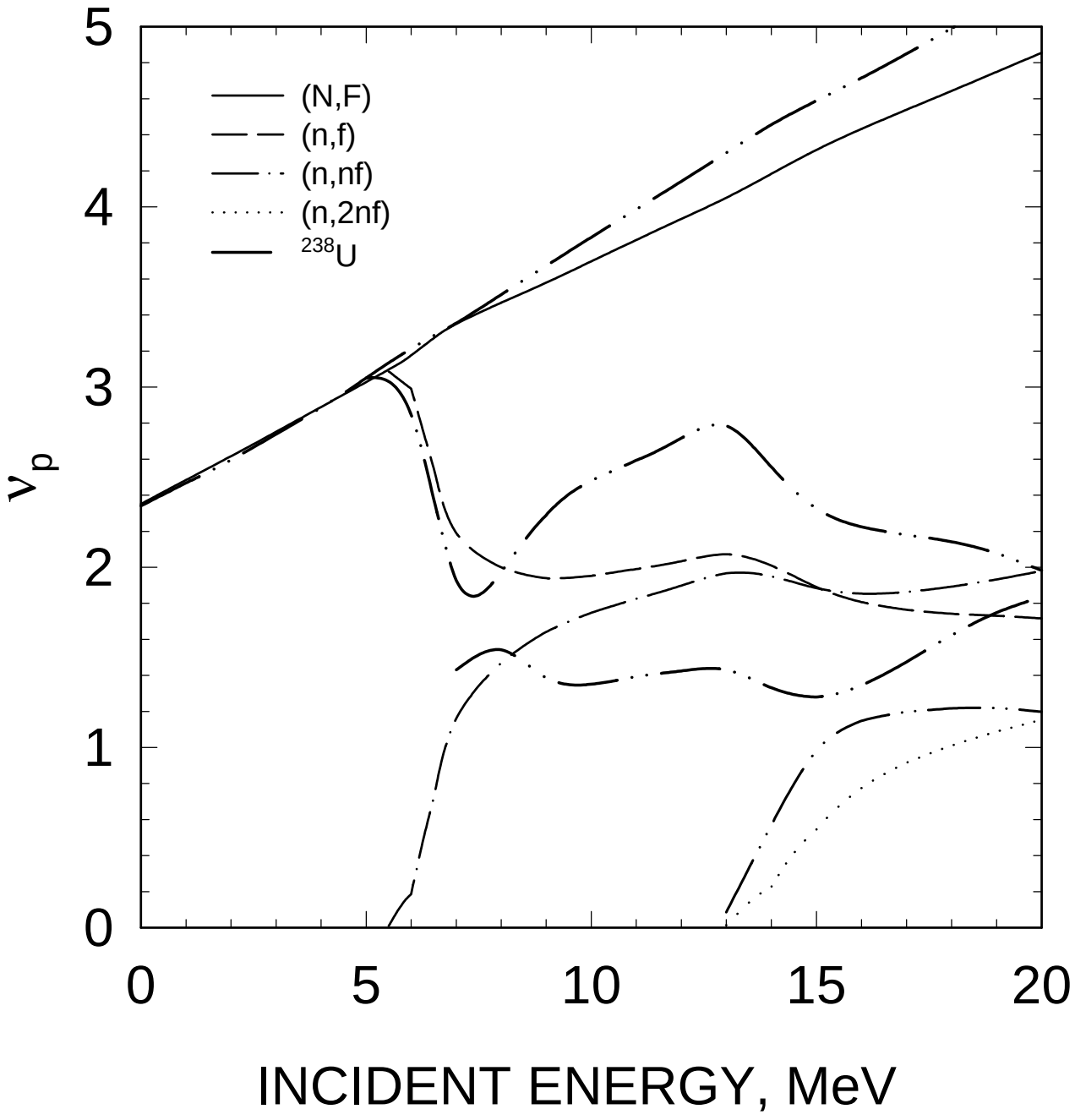

FIG. 61

^{234}U E_n=20 MeV

COMPONENTS OF FIRST NEUTRON SPECTRUM

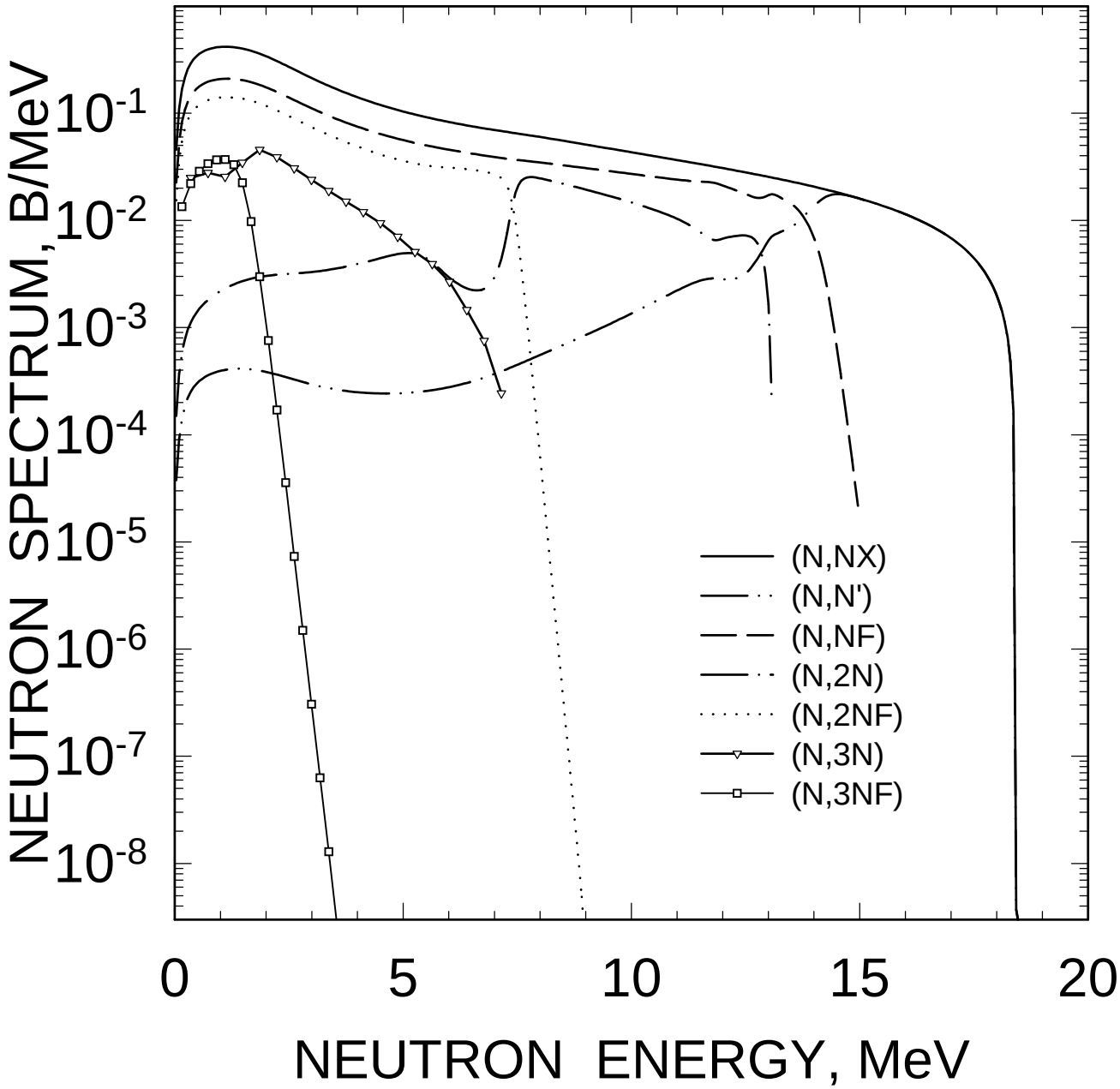

FIG. 62

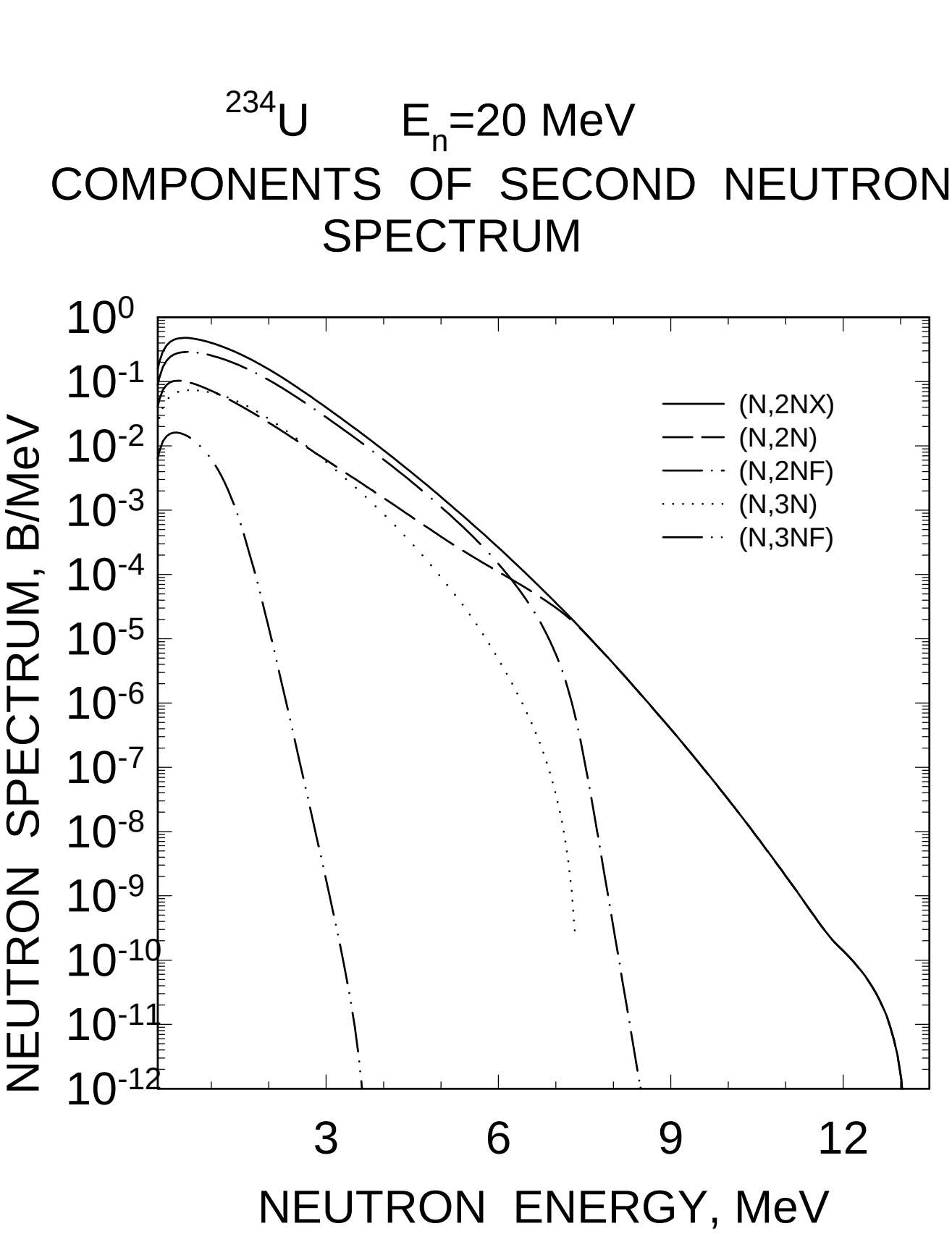
^{234}U E_n=20 MeV
COMPONENTS OF SECOND NEUTRON SPECTRUM
NEUTRON SPECTRUM, B/MeV
10^{0}
10^{-1}
10^{-2}
10^{-3}
10^{-4}
10^{-5}
10^{-6}
10^{-7}
10^{-8}
10^{-9}
10^{-10}
10^{-11}
10^{-12}
(N,2NX)
(N,2N)
(N,2NF)
(N,3N)
(N,3NF)
3
6
9
12
NEUTRON ENERGY, MeV

FIG. 63

^{234}U E_n=20 MeV

COMPONENTS OF THIRD NEUTRON SPECTRUM

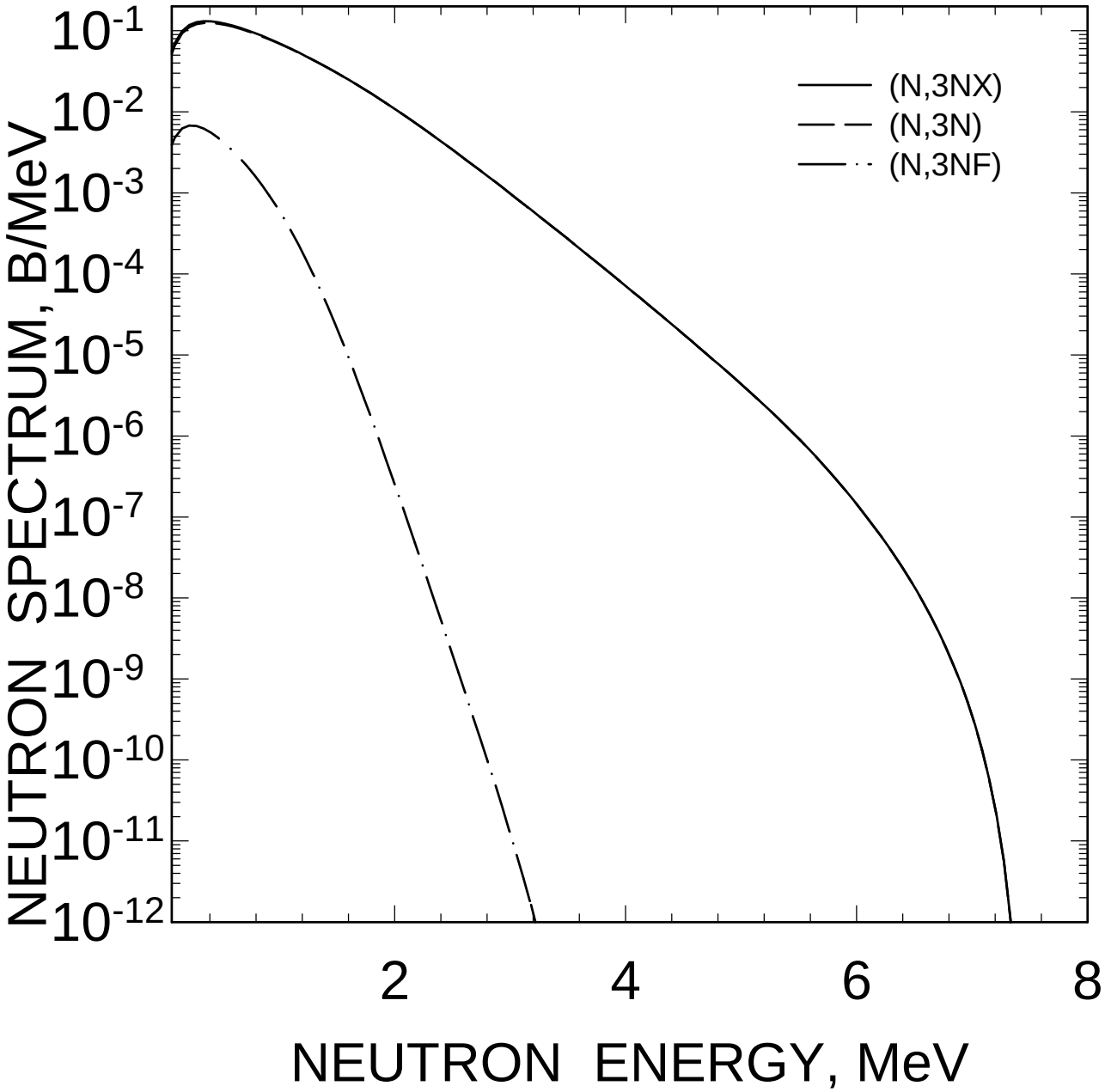

FIG. 64

^{234}U E_n=14 MeV

COMPONENTS OF FIRST NEUTRON SPECTRUM

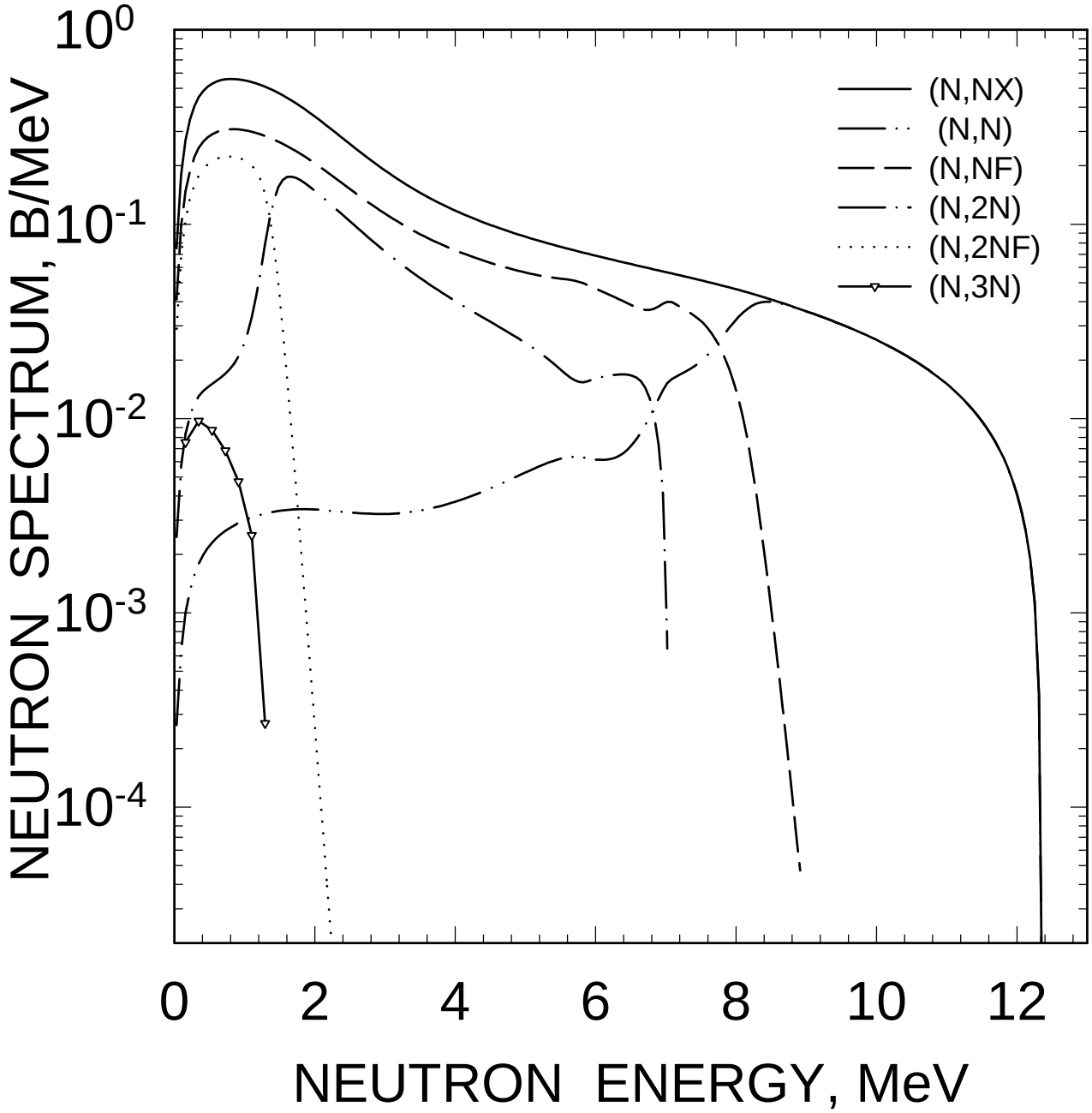

FIG. 65

^{234}U E_n=14 MeV

COMPONENTS OF SECOND NEUTRON SPECTRUM

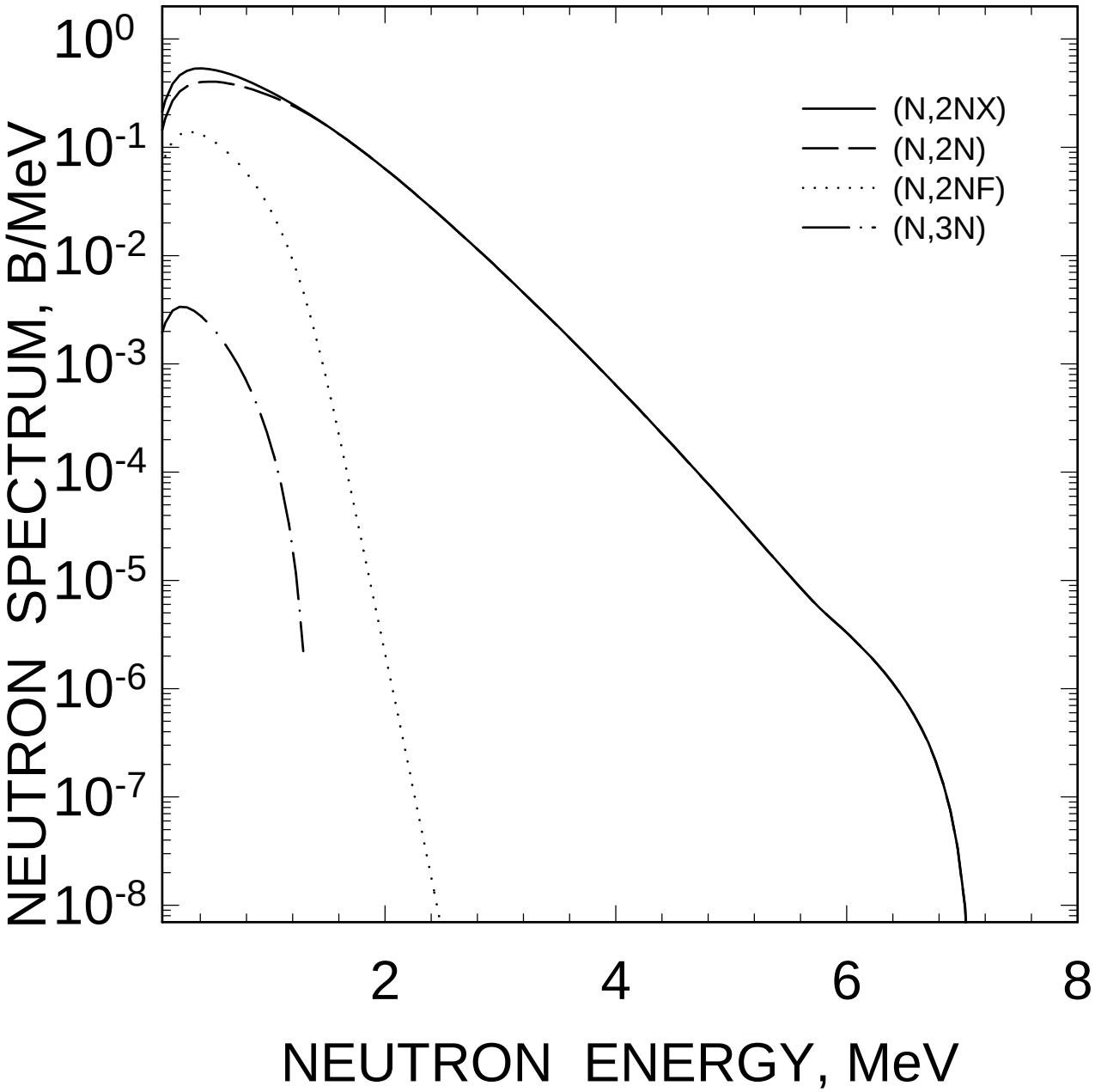

FIG. 66

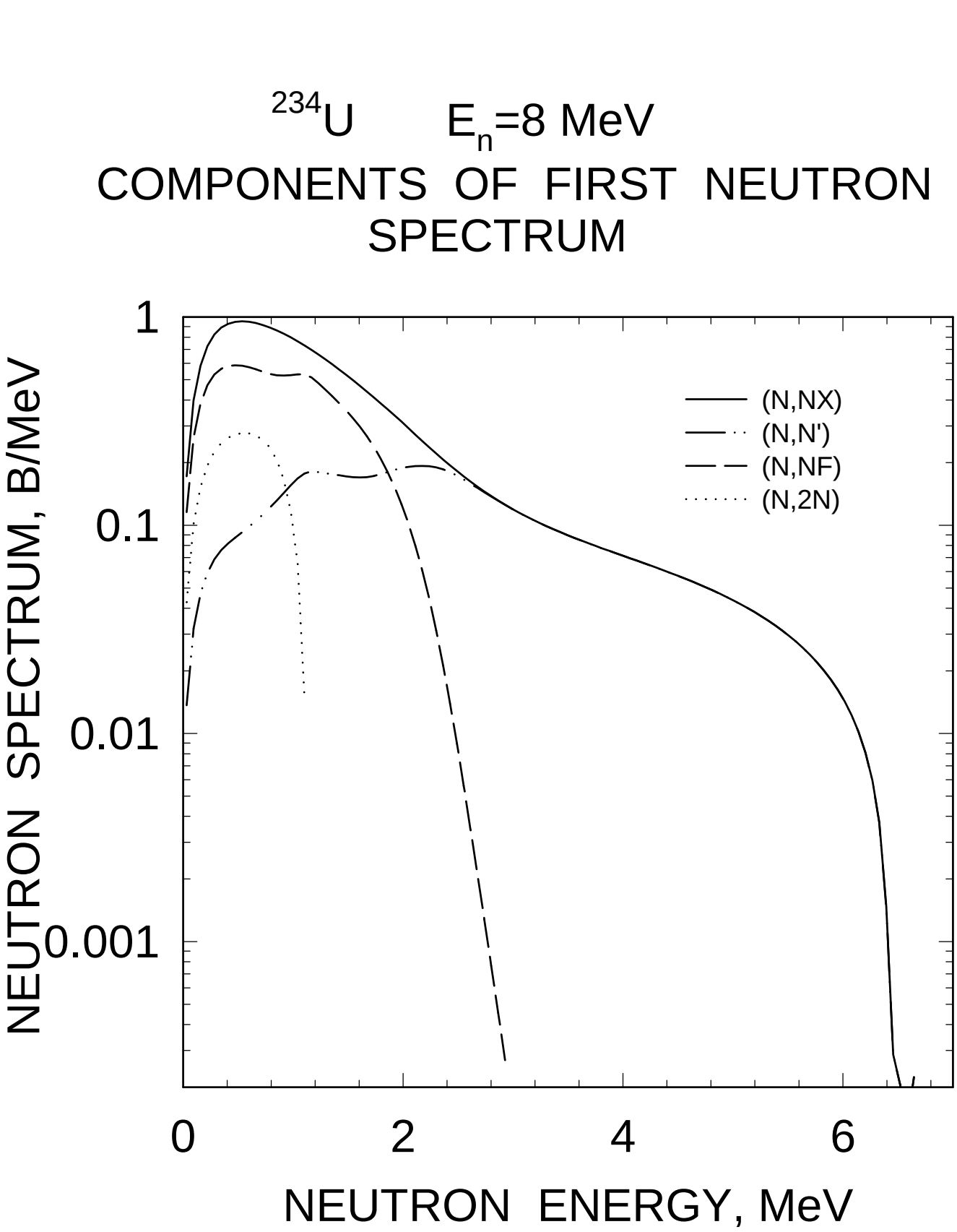
^{234}U E_n=8 MeV
COMPONENTS OF FIRST NEUTRON SPECTRUM
NEUTRON SPECTRUM, B/MeV
1
0.1
0.01
0.001
0
2
4
6
NEUTRON ENERGY, MeV
(N,NX)
(N,N')
(N,NF)
(N,2N)

FIG. 67

^{234}U E_n=8 MeV

COMPONENTS OF SECOND NEUTRON SPECTRUM

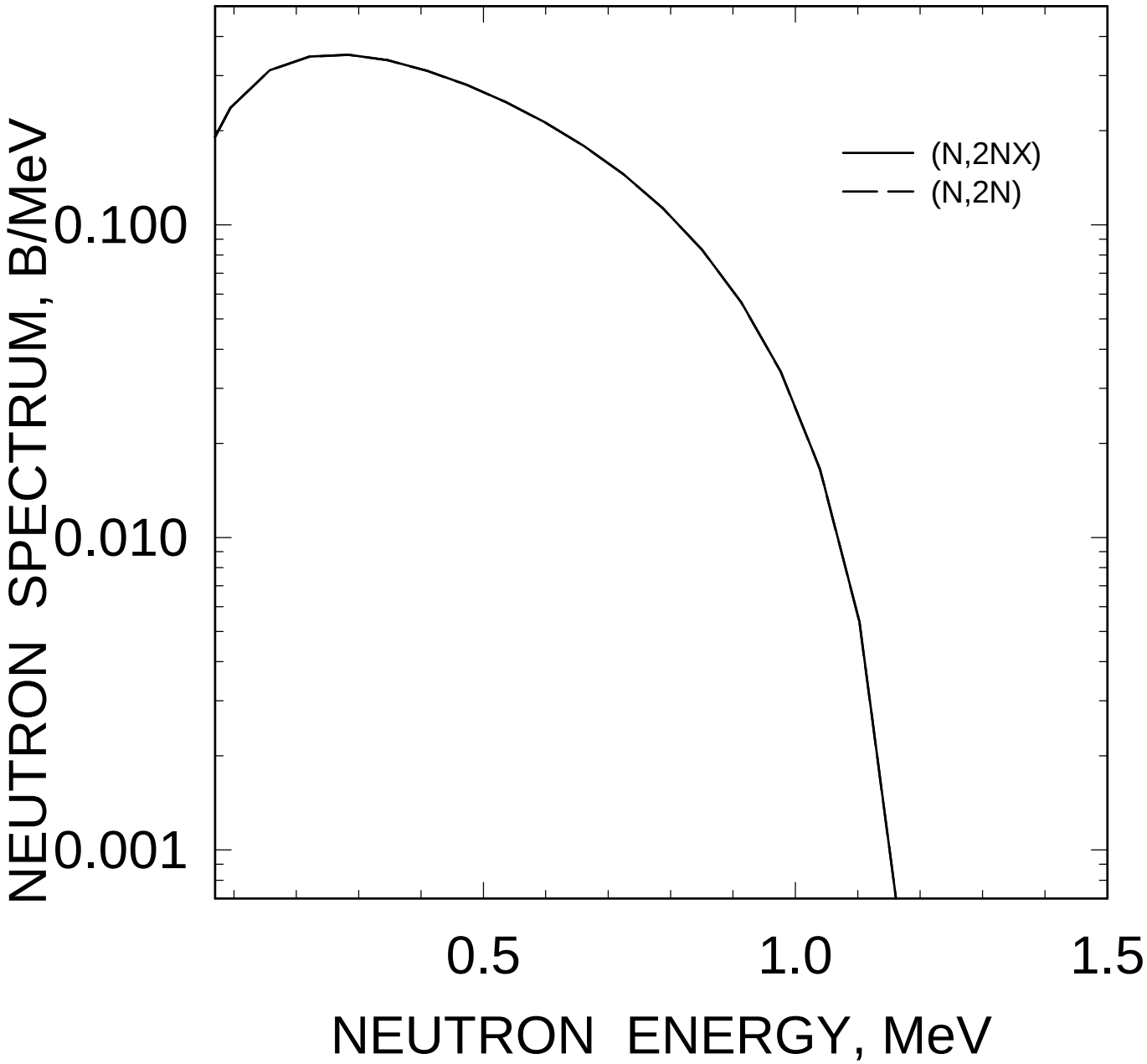

FIG. 68

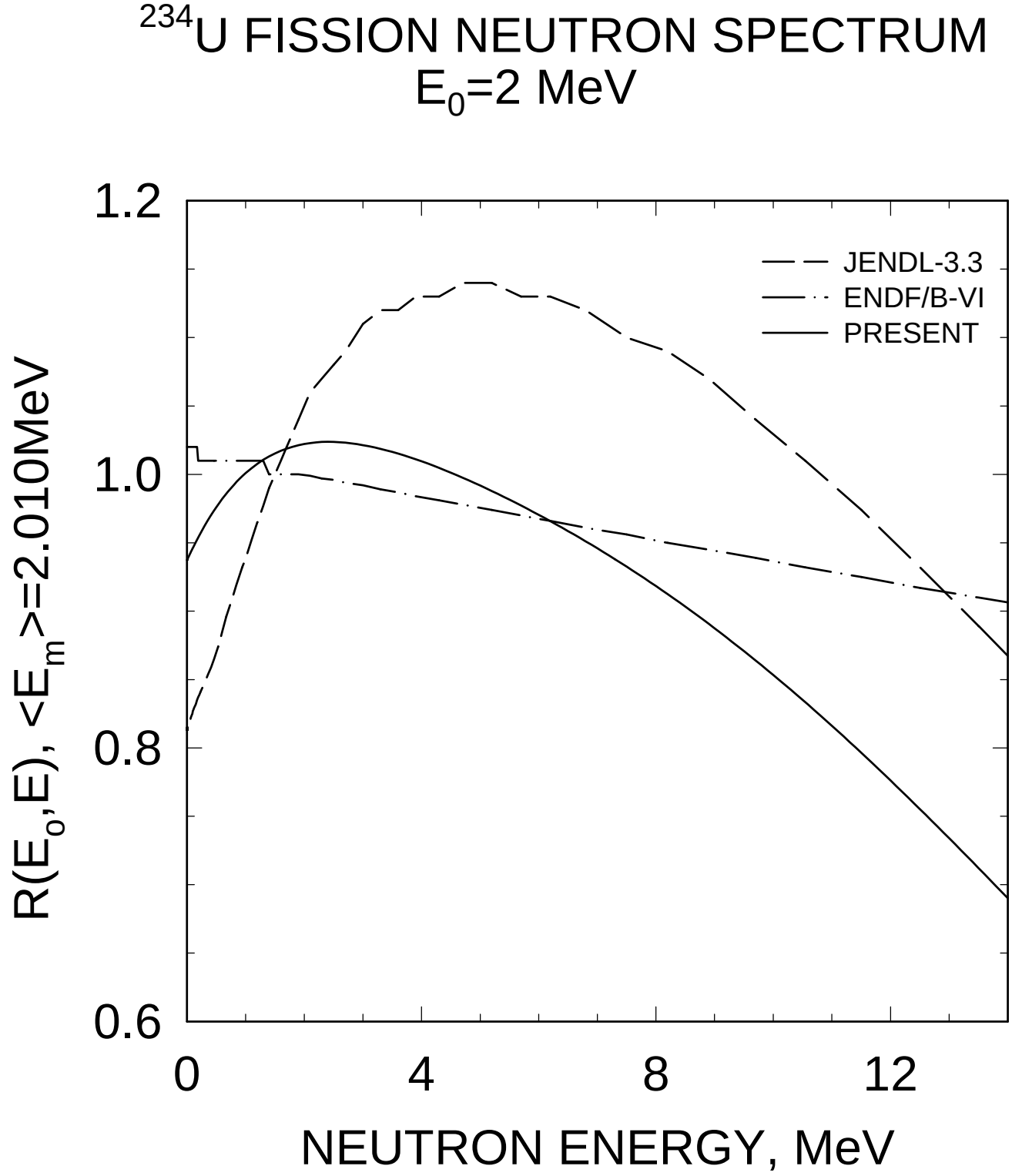
^{234}U FISSION NEUTRON SPECTRUM
E_0=2 MeV
1.2
1.0
0.8
0.6
0
4
8
12
R(E_o,E), <E_m>=2.010MeV
NEUTRON ENERGY, MeV
JENDL-3.3
ENDF/B-VI
PRESENT

FIG. 69

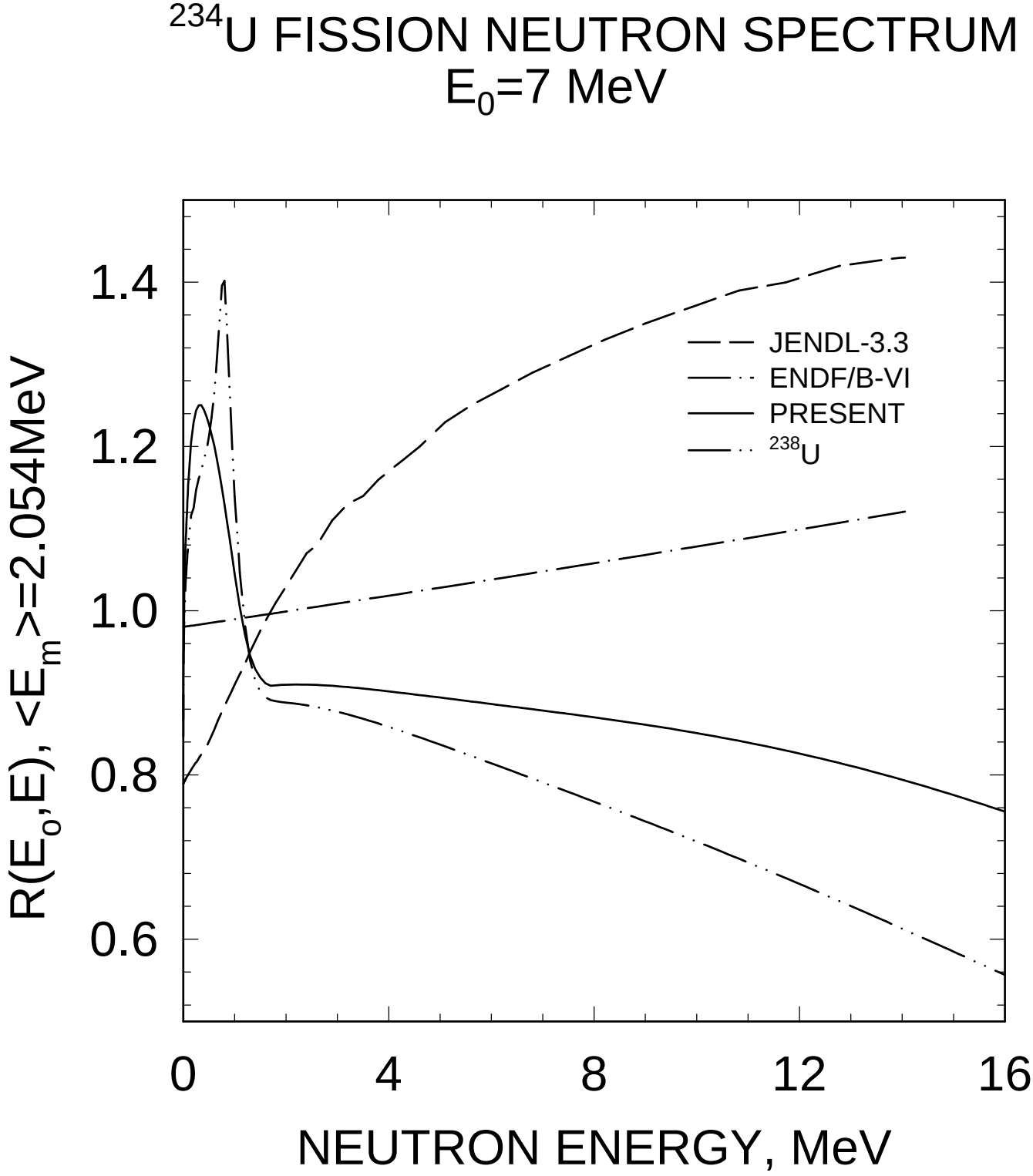
^{234}U FISSION NEUTRON SPECTRUM
E_0=7 MeV
R(E_o,E), <E_m>=2.054MeV
1.4
1.2
1.0
0.8
0.6
0
4
8
12
16
NEUTRON ENERGY, MeV
JENDL-3.3
ENDF/B-VI
PRESENT
^{238}U

FIG. 70

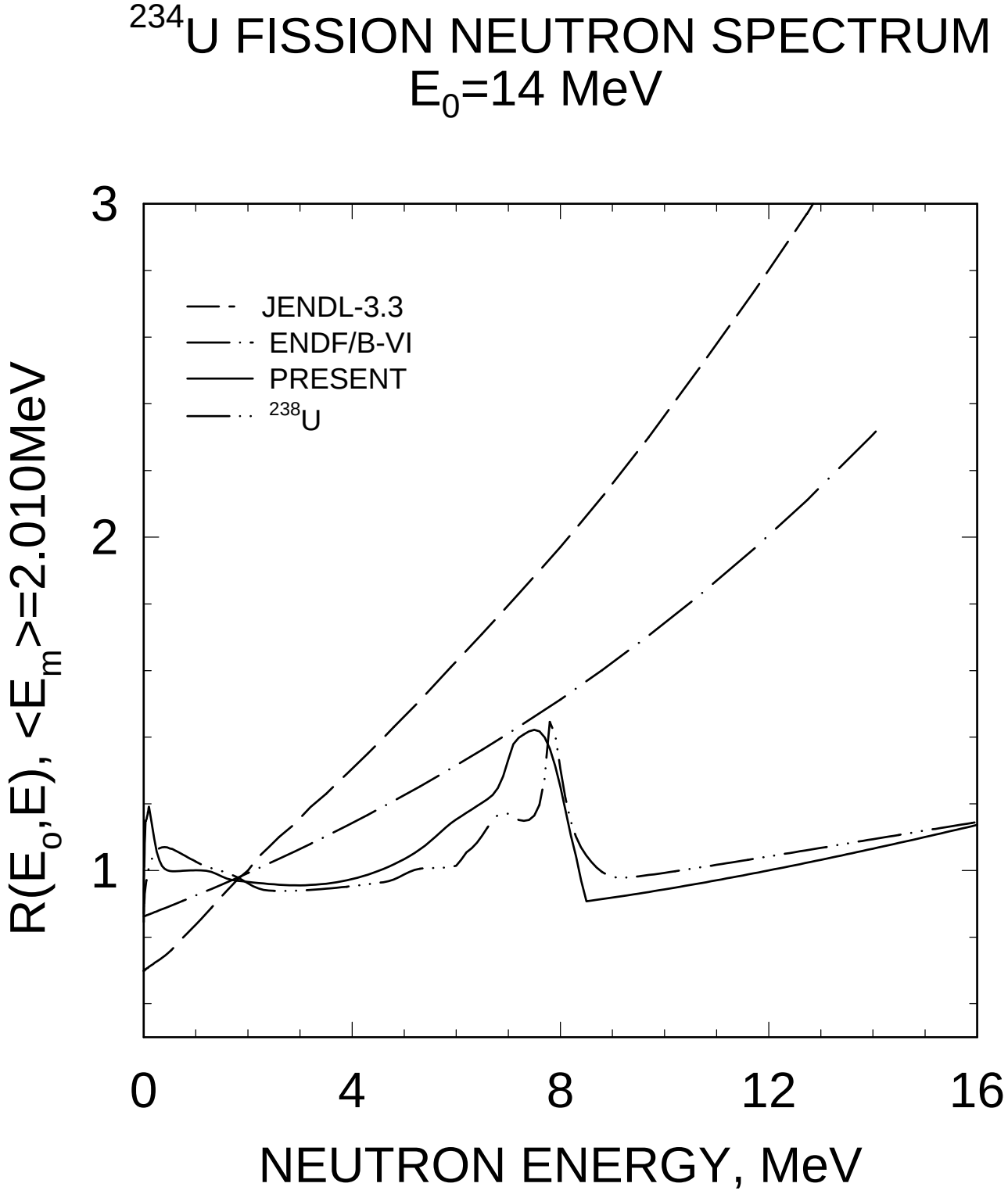
^{234}U FISSION NEUTRON SPECTRUM
E_0=14 MeV
JENDL-3.3
ENDF/B-VI
PRESENT
^{238}U
$R(E_o,E)$, $<E_m>$=2.010MeV
NEUTRON ENERGY, MeV
0
4
8
12
16
1
2
3

FIG. 71

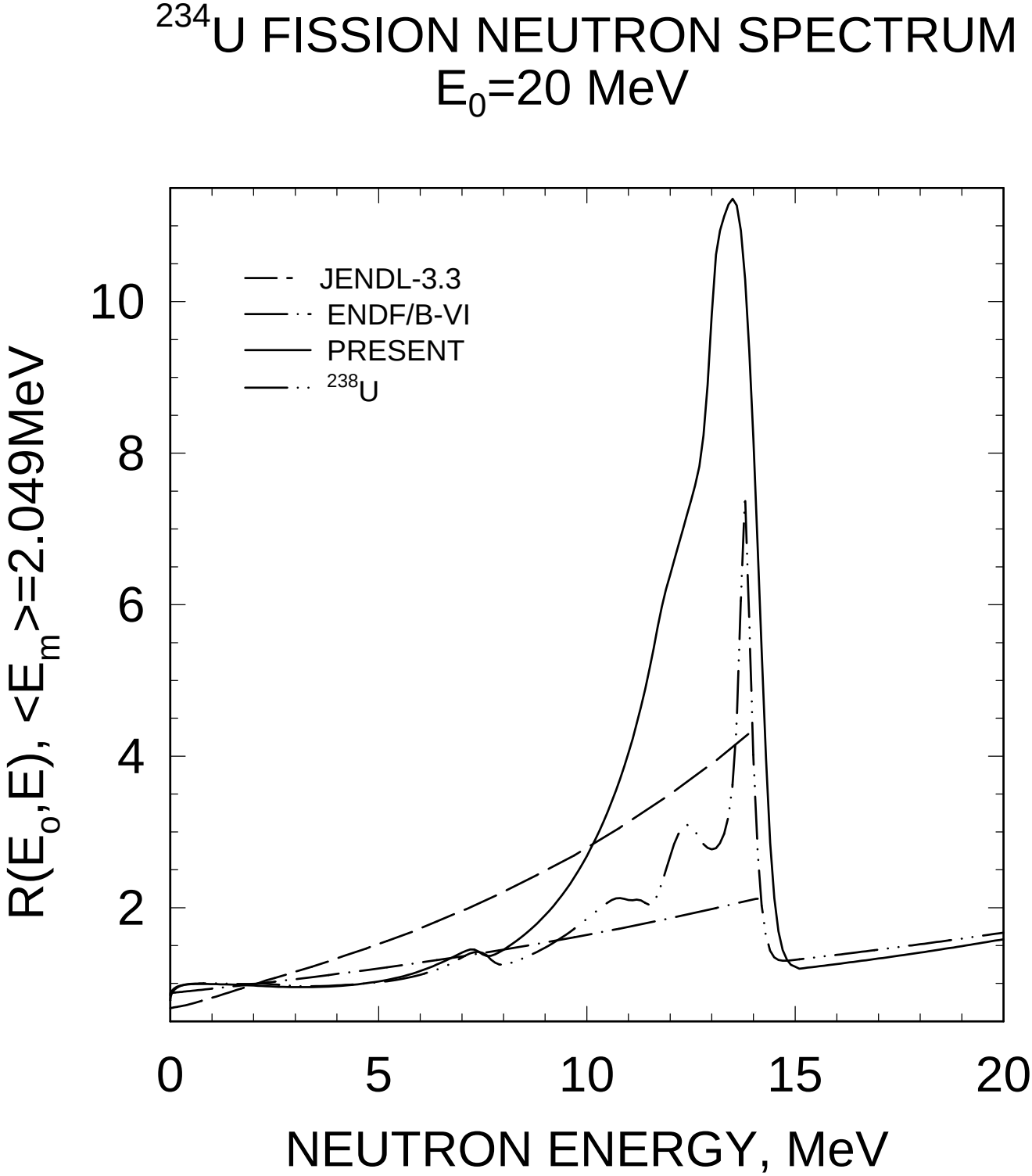
^{234}U FISSION NEUTRON SPECTRUM
E_0=20 MeV
JENDL-3.3
ENDF/B-VI
PRESENT
^{238}U
R(E_o,E), <E_m>=2.049MeV
2
4
6
8
10
0
5
10
15
20
NEUTRON ENERGY, MeV

FIG. 72

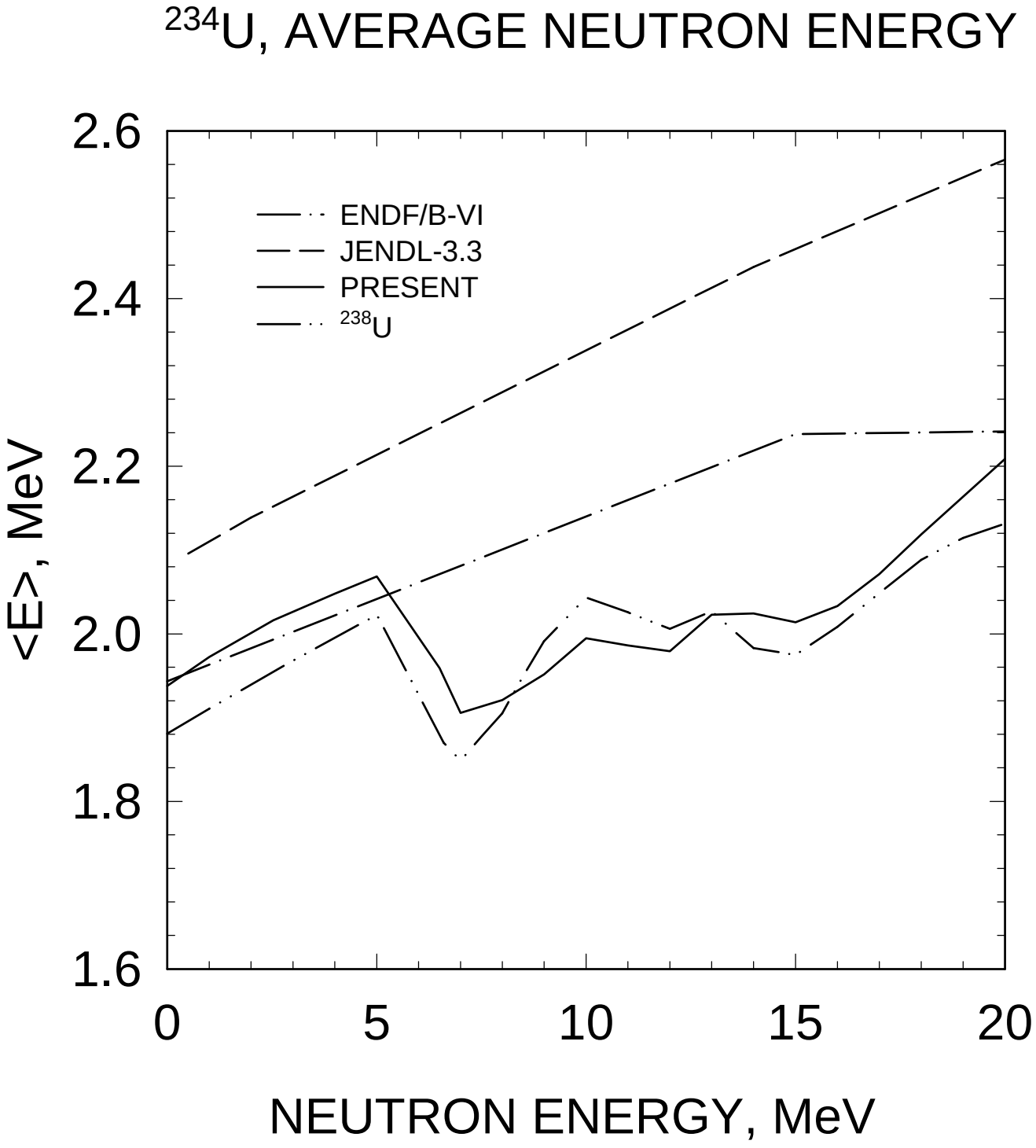
^{234}U, AVERAGE NEUTRON ENERGY
ENDF/B-VI
JENDL-3.3
PRESENT
^{238}U
<E>, MeV
2.6
2.4
2.2
2.0
1.8
1.6
0
5
10
15
20
NEUTRON ENERGY, MeV

FIG. 73

^{234}U: E_n=1.2 MeV

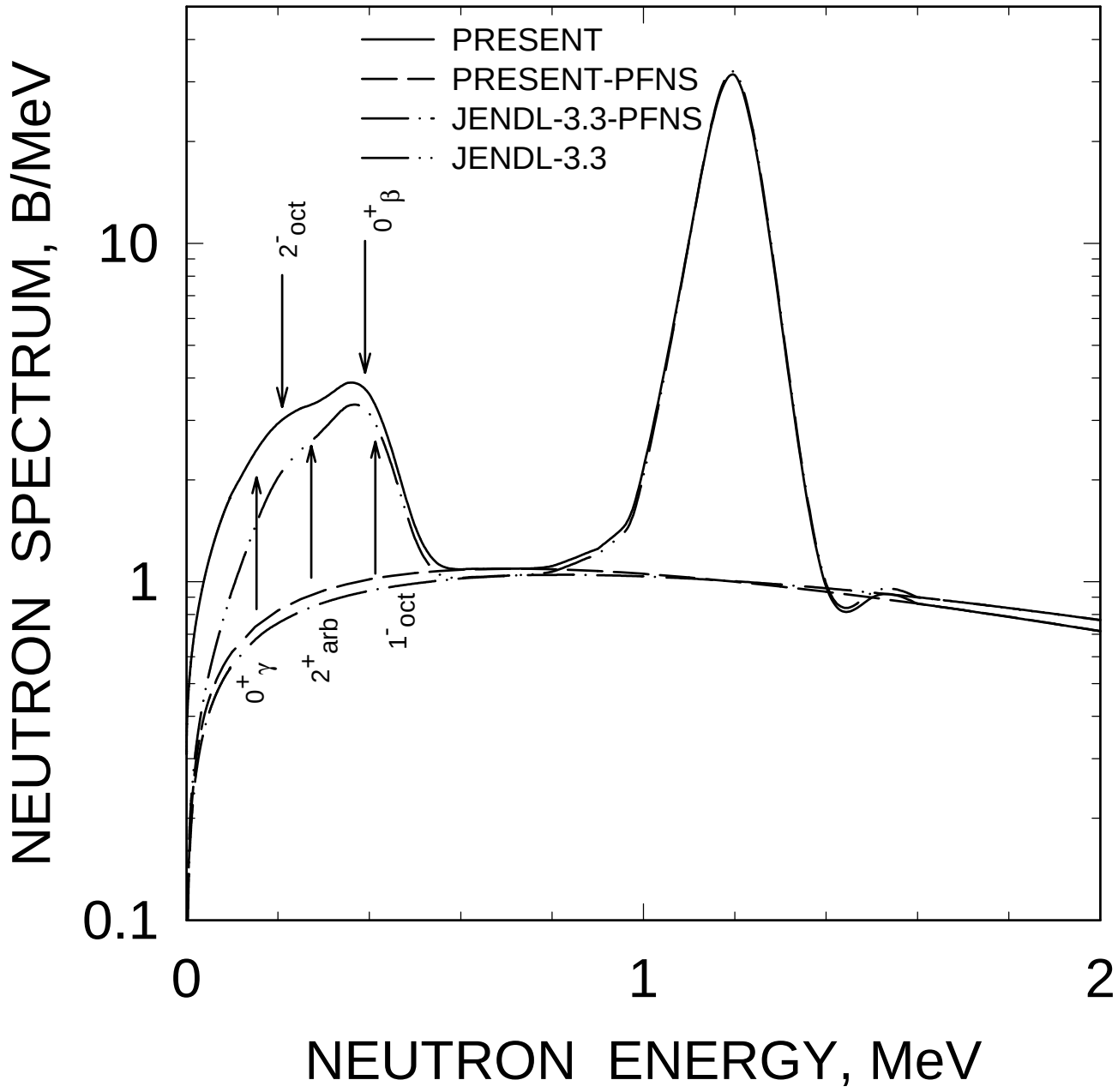

FIG.74

^{234}U: E_n=2.6 MeV

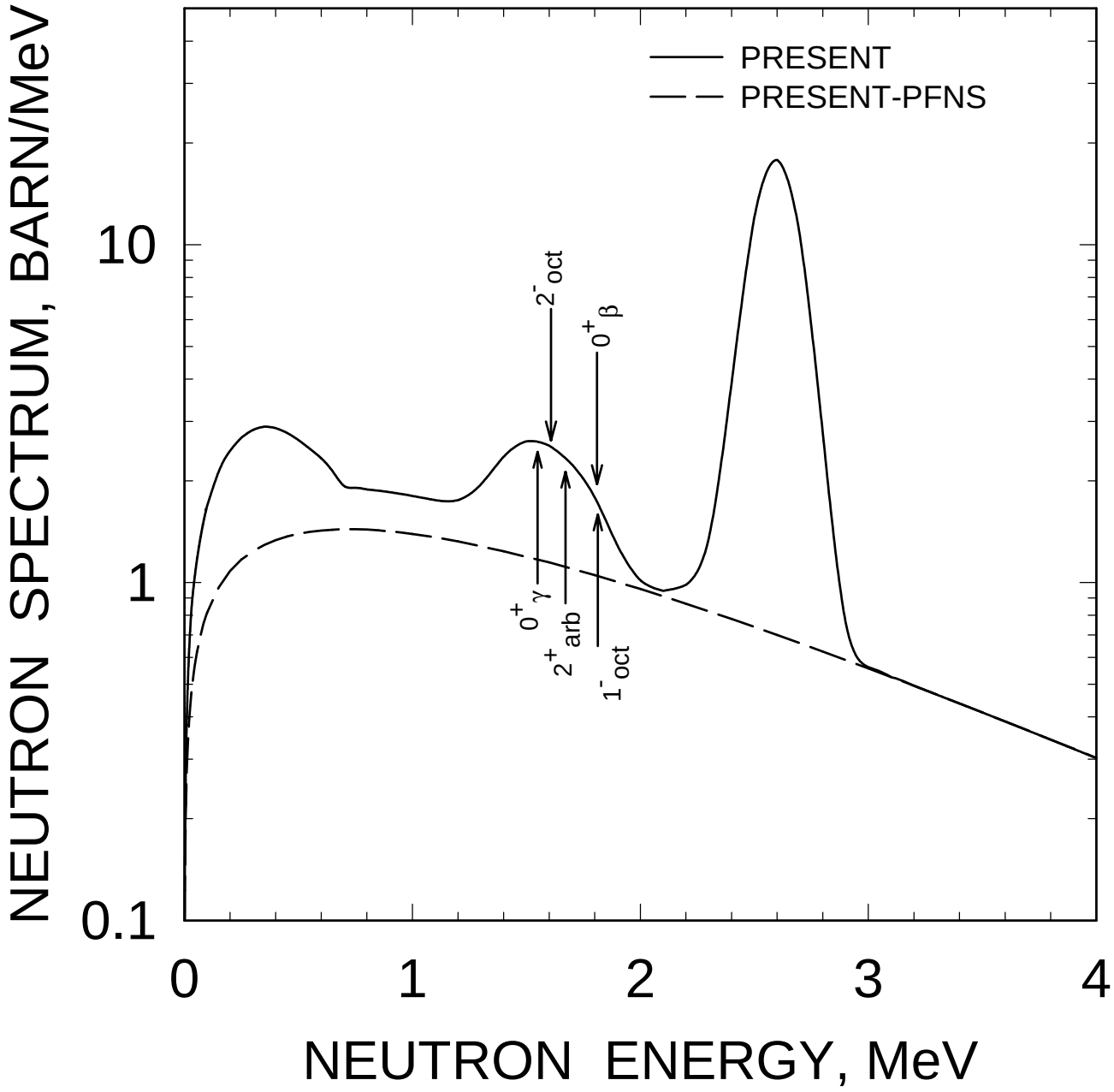

FIG.75

^{234}U: E_n=3.55 MeV

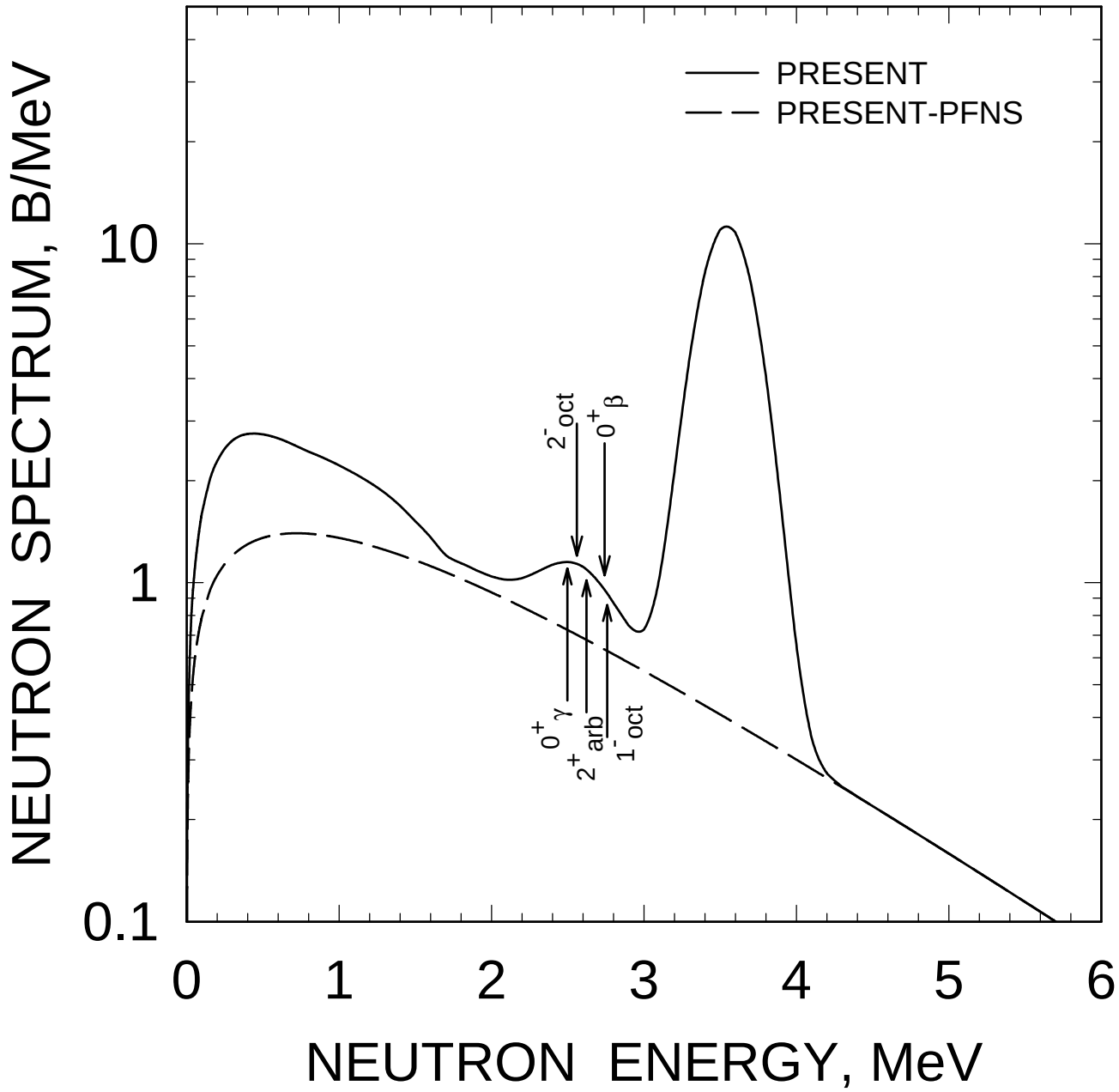

FIG.76

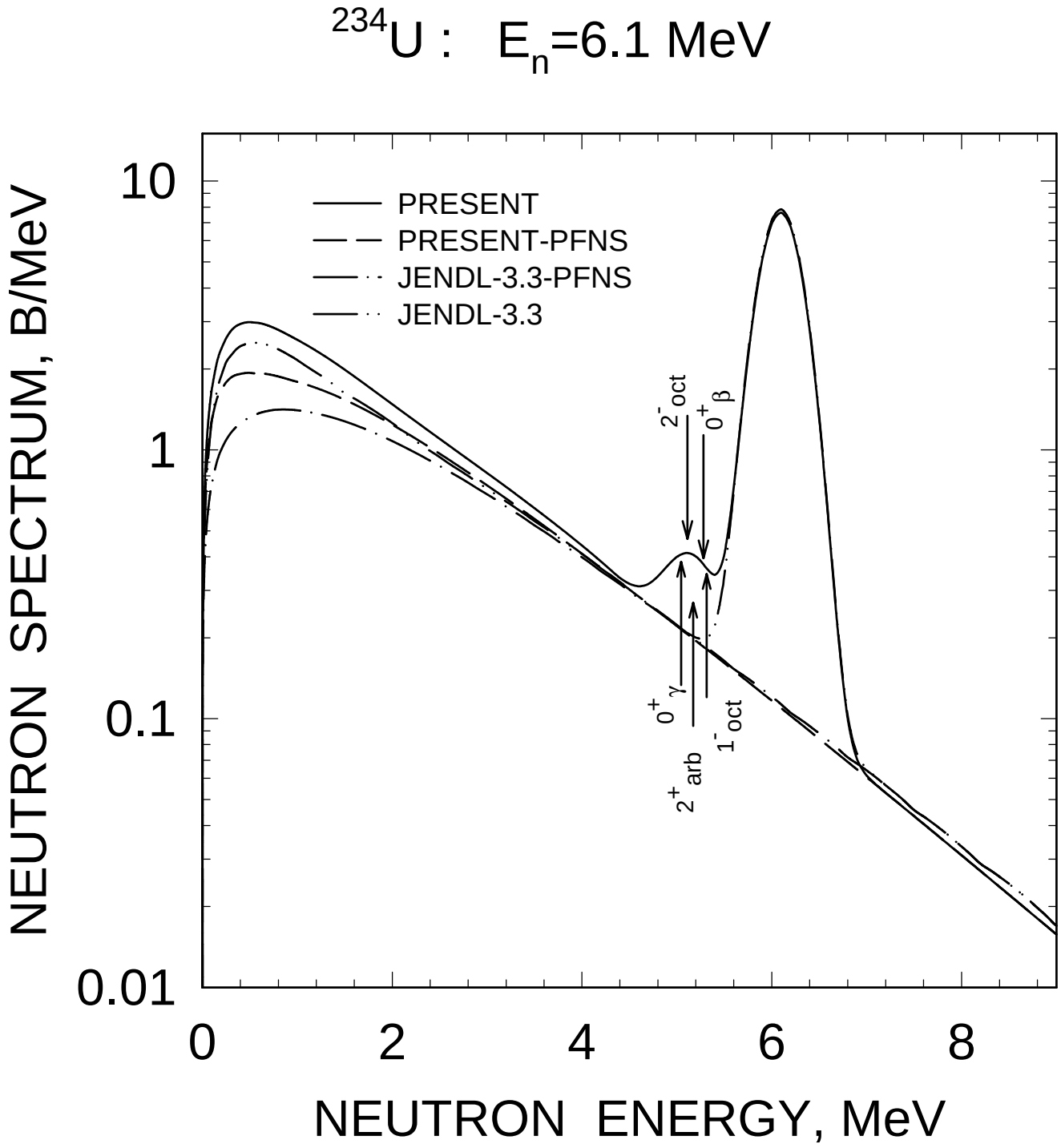
^{234}U : E_n=6.1 MeV
PRESENT
PRESENT-PFNS
JENDL-3.3-PFNS
JENDL-3.3
NEUTRON SPECTRUM, B/MeV
NEUTRON ENERGY, MeV
10
1
0.1
0.01
0
2
4
6
8
2^- oct
0^+ β
0^+ γ
2^+ arb
1^- oct

FIG.77

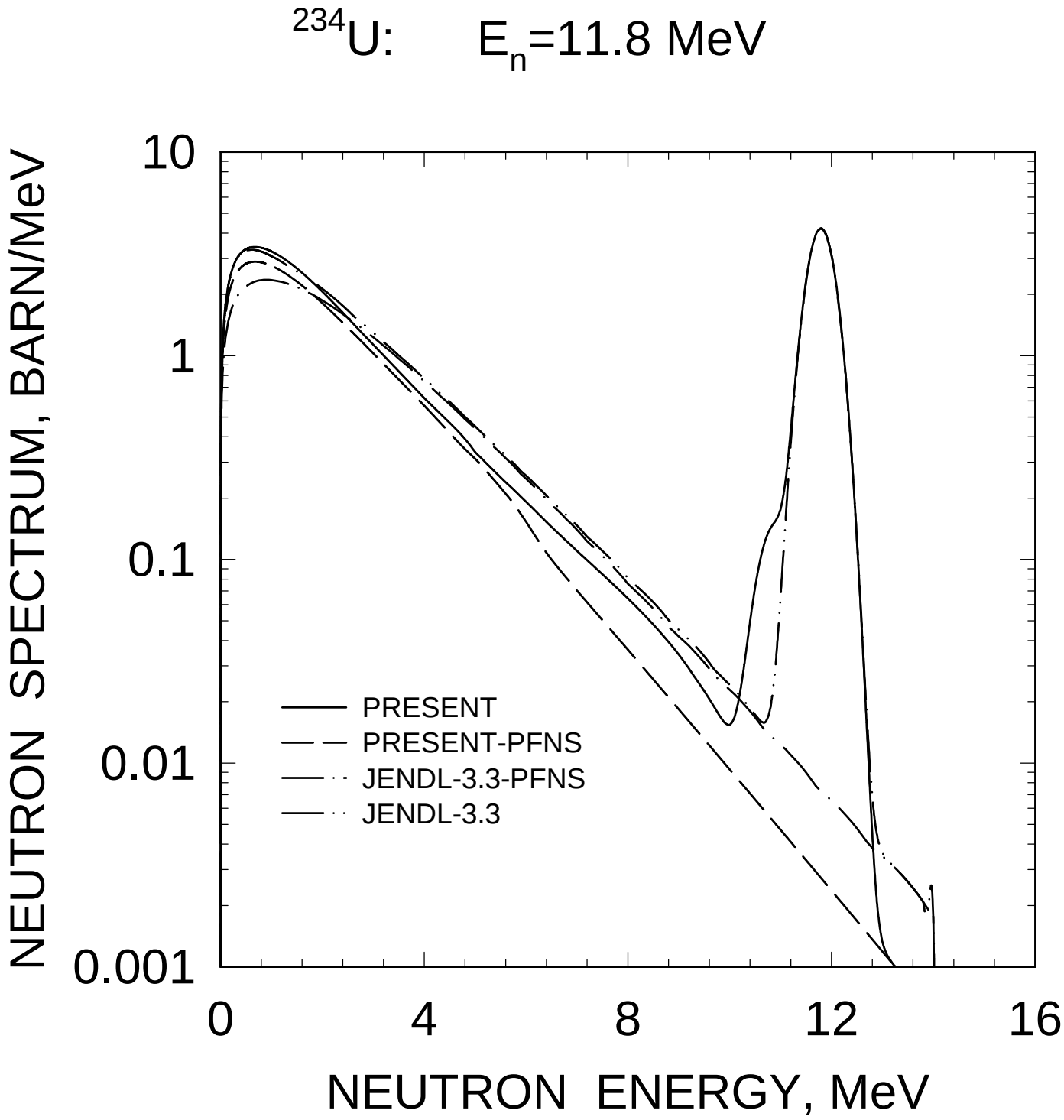
^{234}U: E_n=11.8 MeV
NEUTRON SPECTRUM, BARN/MeV
10
1
0.1
0.01
0.001
0
4
8
12
16
NEUTRON ENERGY, MeV
PRESENT
PRESENT-PFNS
JENDL-3.3-PFNS
JENDL-3.3

FIG.78

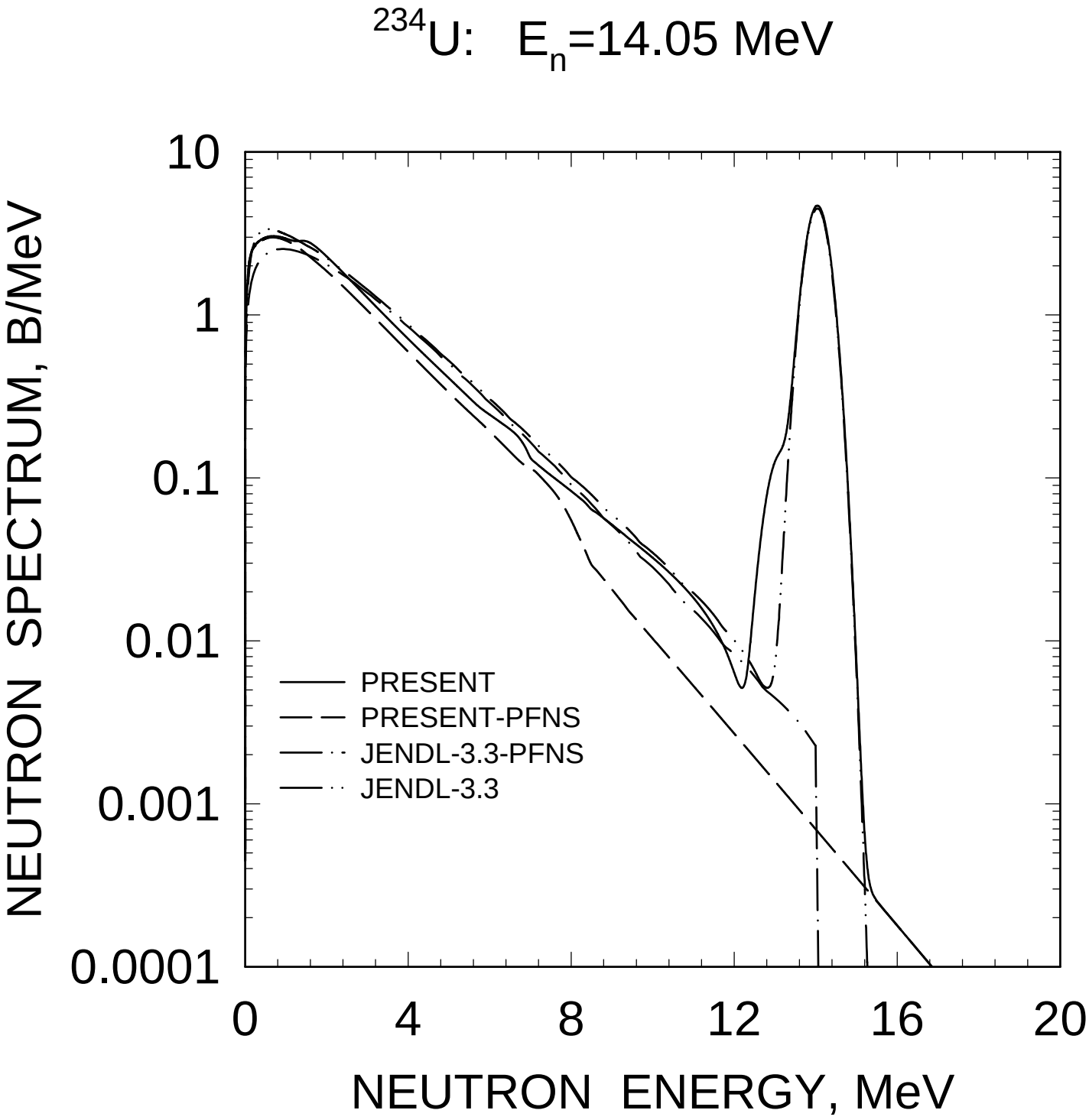
^{234}U: E_n=14.05 MeV
NEUTRON SPECTRUM, B/MeV
10
1
0.1
0.01
0.001
0.0001
0
4
8
12
16
20
NEUTRON ENERGY, MeV
PRESENT
PRESENT-PFNS
JENDL-3.3-PFNS
JENDL-3.3

FIG.79

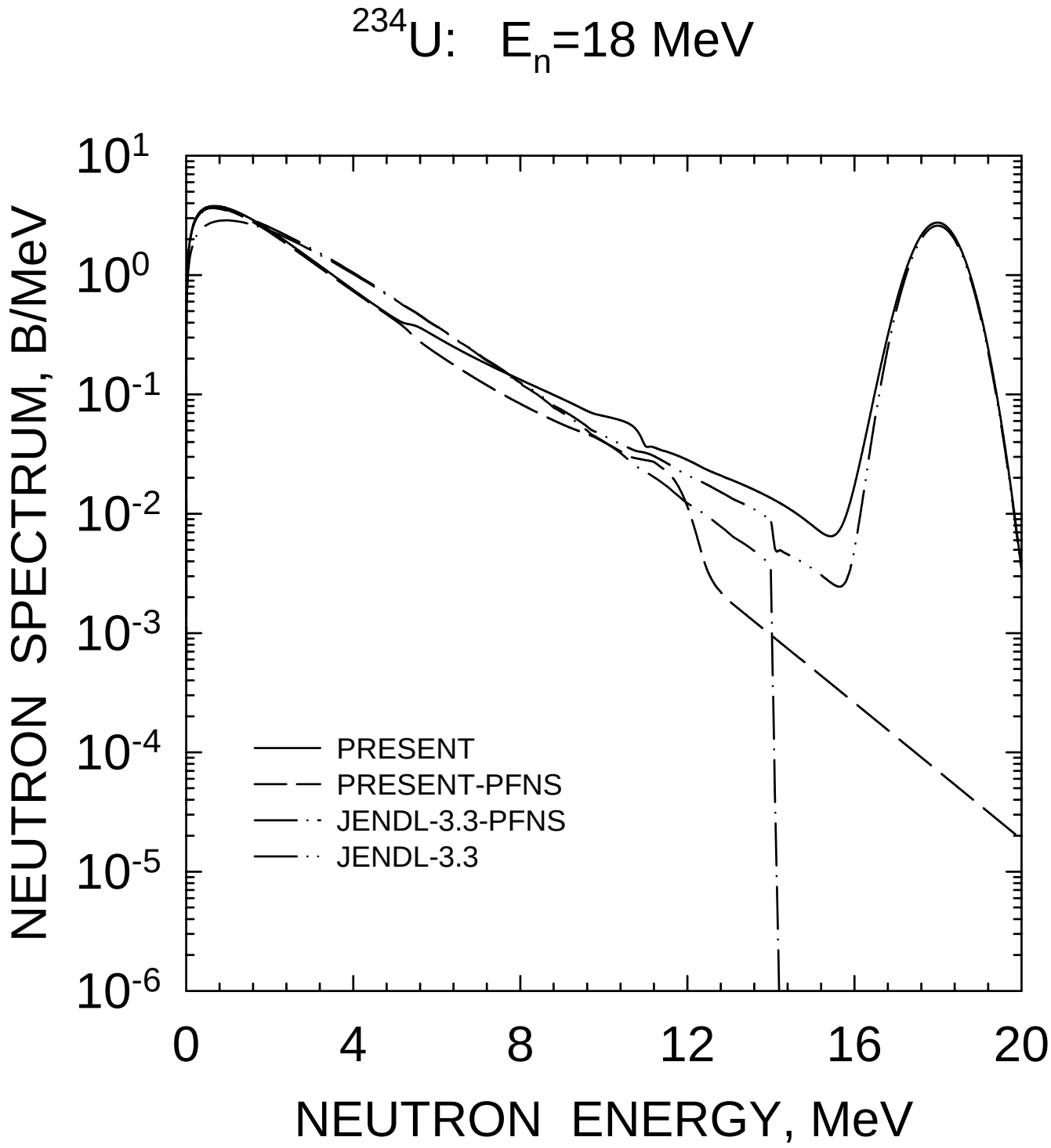
^{234}U: E_n=18 MeV
NEUTRON SPECTRUM, B/MeV
10^{1}
10^{0}
10^{-1}
10^{-2}
10^{-3}
10^{-4}
10^{-5}
10^{-6}
0
4
8
12
16
20
NEUTRON ENERGY, MeV
PRESENT
PRESENT-PFNS
JENDL-3.3-PFNS
JENDL-3.3

FIG. 80

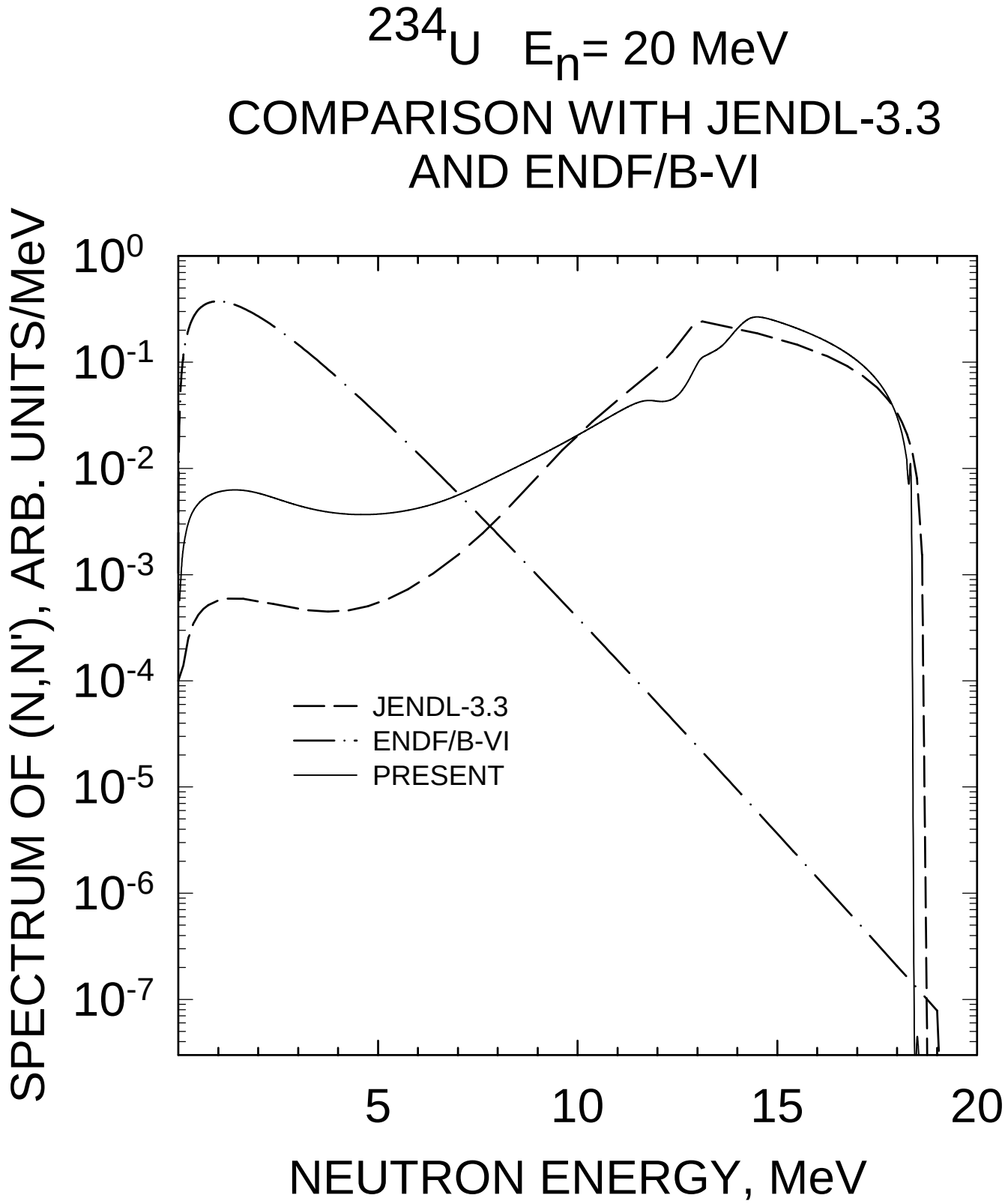
^{234}U E_n= 20 MeV
COMPARISON WITH JENDL-3.3
AND ENDF/B-VI
SPECTRUM OF (N,N'), ARB. UNITS/MeV
10^{0}
10^{-1}
10^{-2}
10^{-3}
10^{-4}
10^{-5}
10^{-6}
10^{-7}
JENDL-3.3
ENDF/B-VI
PRESENT
5
10
15
20
NEUTRON ENERGY, MeV

FIG. 81

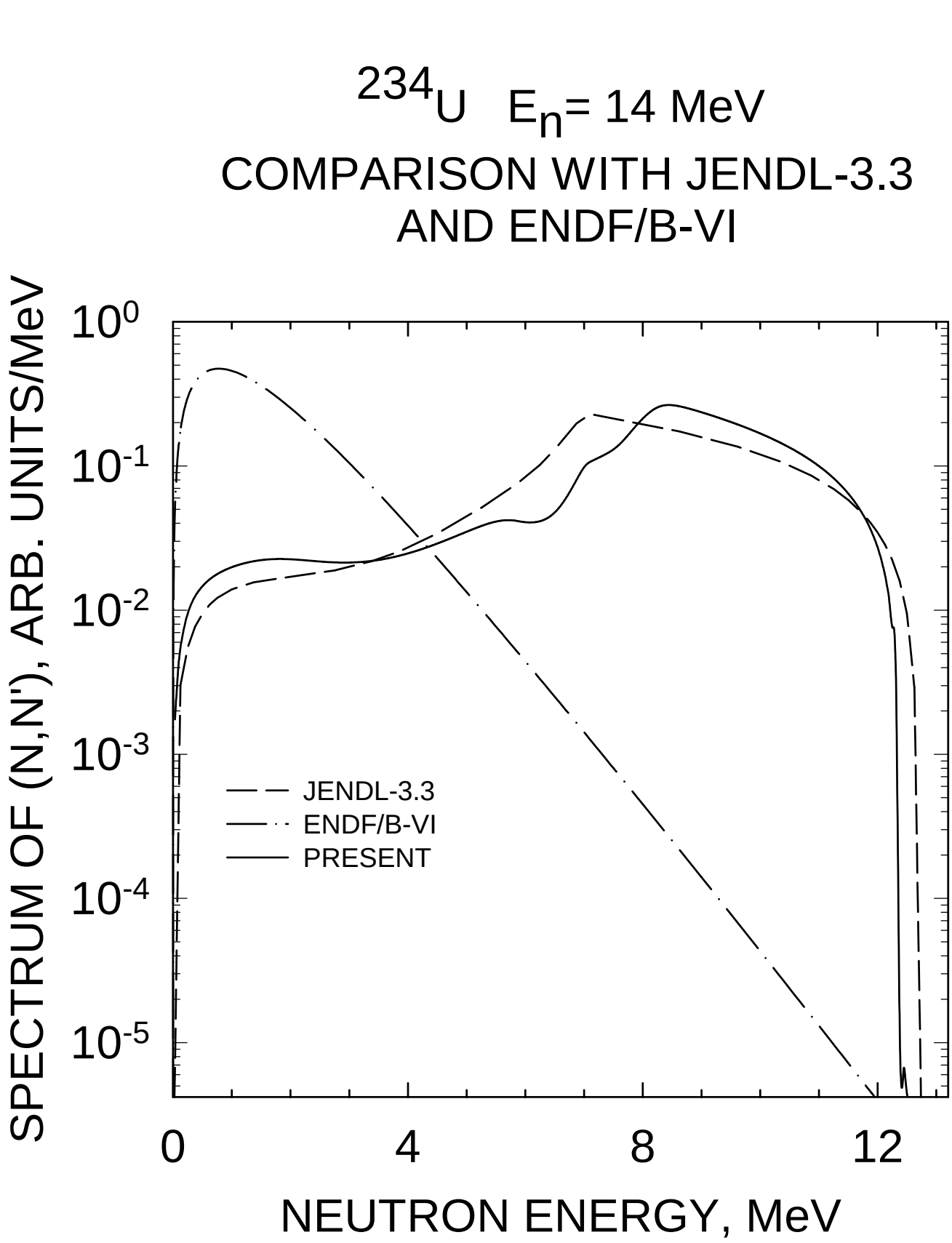
^{234}U E_n= 14 MeV
COMPARISON WITH JENDL-3.3
AND ENDF/B-VI
SPECTRUM OF (N,N'), ARB. UNITS/MeV
10^0
10^{-1}
10^{-2}
10^{-3}
10^{-4}
10^{-5}
JENDL-3.3
ENDF/B-VI
PRESENT
0
4
8
12
NEUTRON ENERGY, MeV

FIG. 82

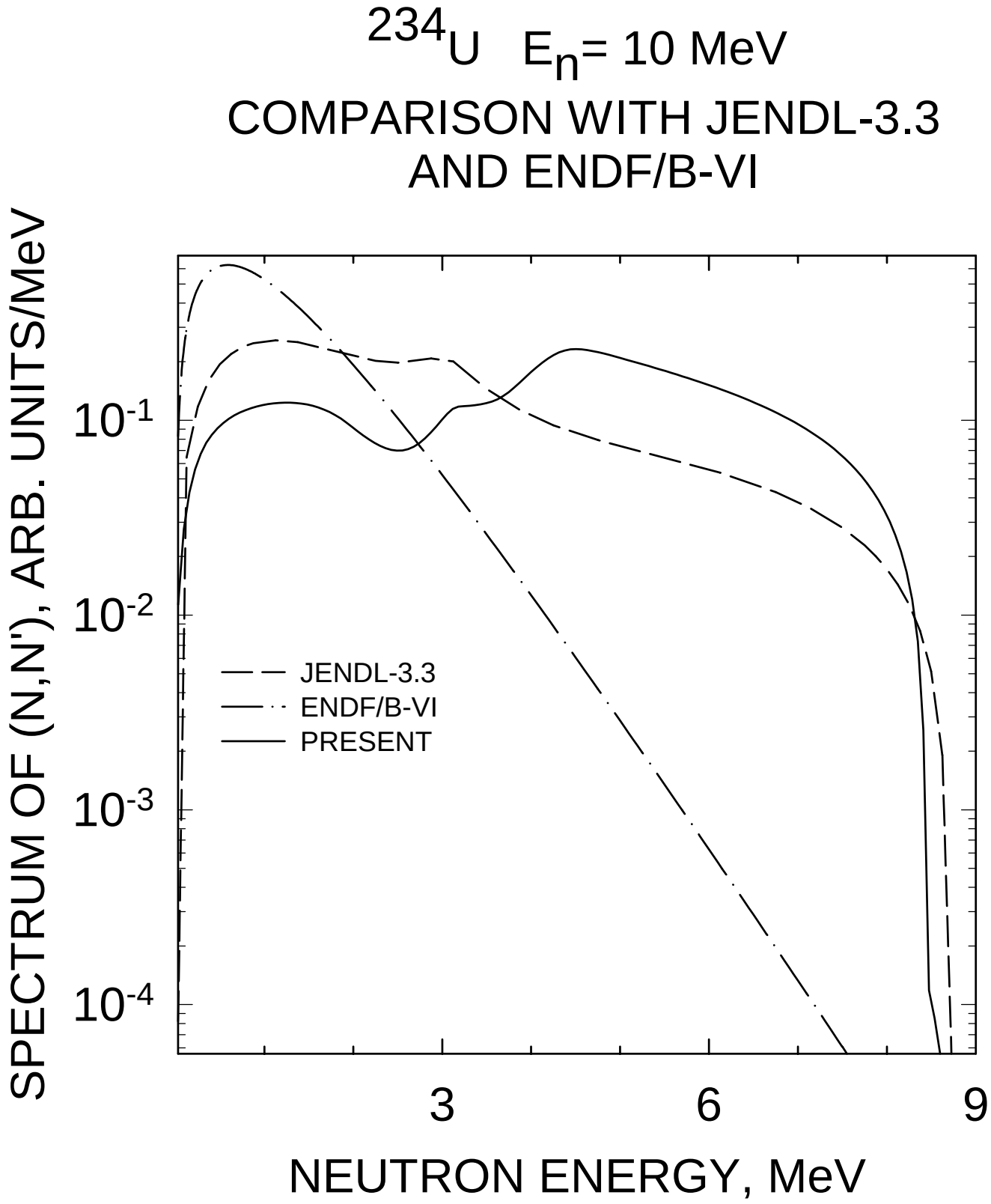
^{234}U E_n= 10 MeV
COMPARISON WITH JENDL-3.3
AND ENDF/B-VI
SPECTRUM OF (N,N'), ARB. UNITS/MeV
10^{-1}
10^{-2}
10^{-3}
10^{-4}
JENDL-3.3
ENDF/B-VI
PRESENT
3
6
9
NEUTRON ENERGY, MeV

FIG. 83

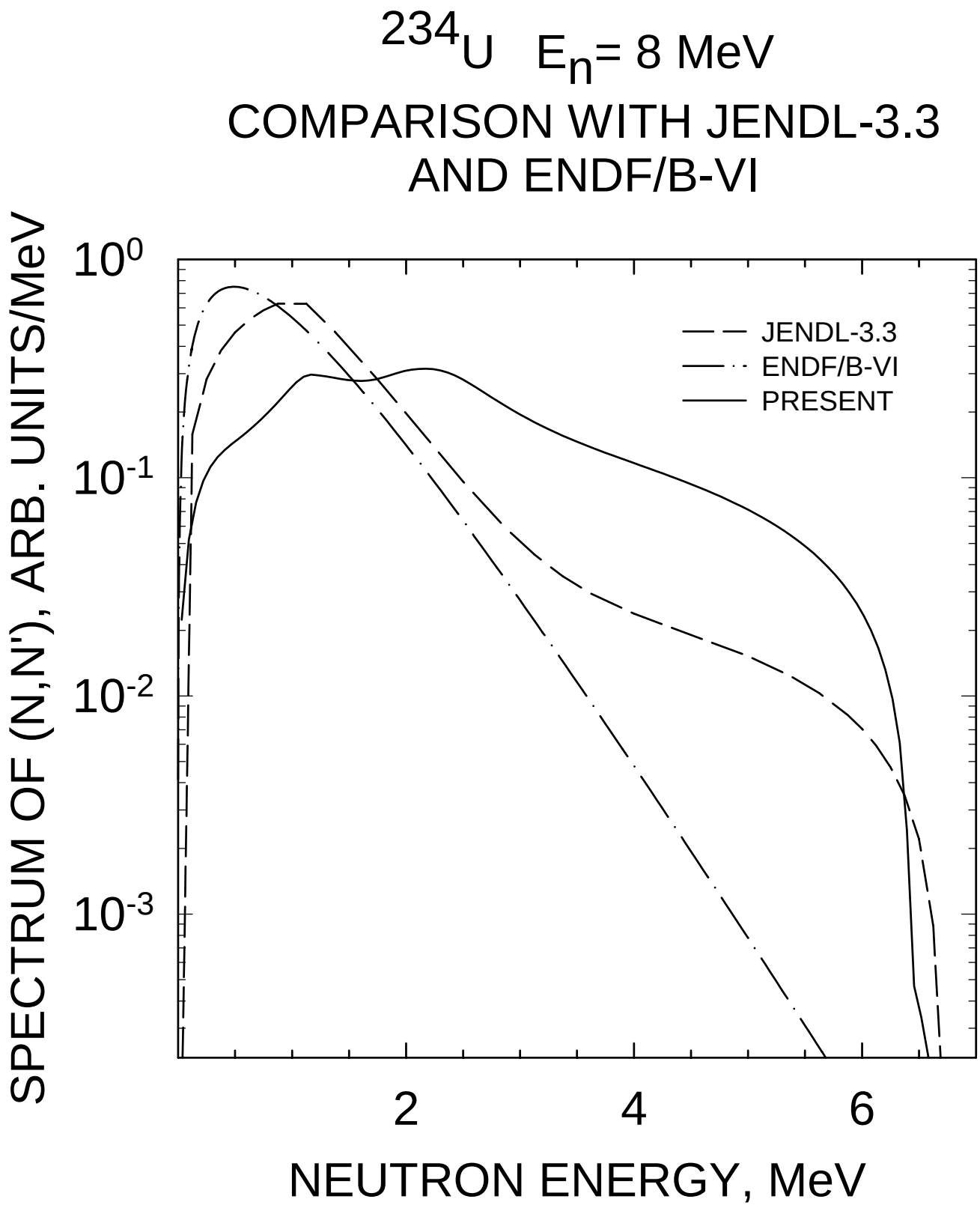
^{234}U E_n= 8 MeV
COMPARISON WITH JENDL-3.3
AND ENDF/B-VI
SPECTRUM OF (N,N'), ARB. UNITS/MeV
10^0
10^{-1}
10^{-2}
10^{-3}
JENDL-3.3
ENDF/B-VI
PRESENT
2
4
6
NEUTRON ENERGY, MeV

FIG. 84

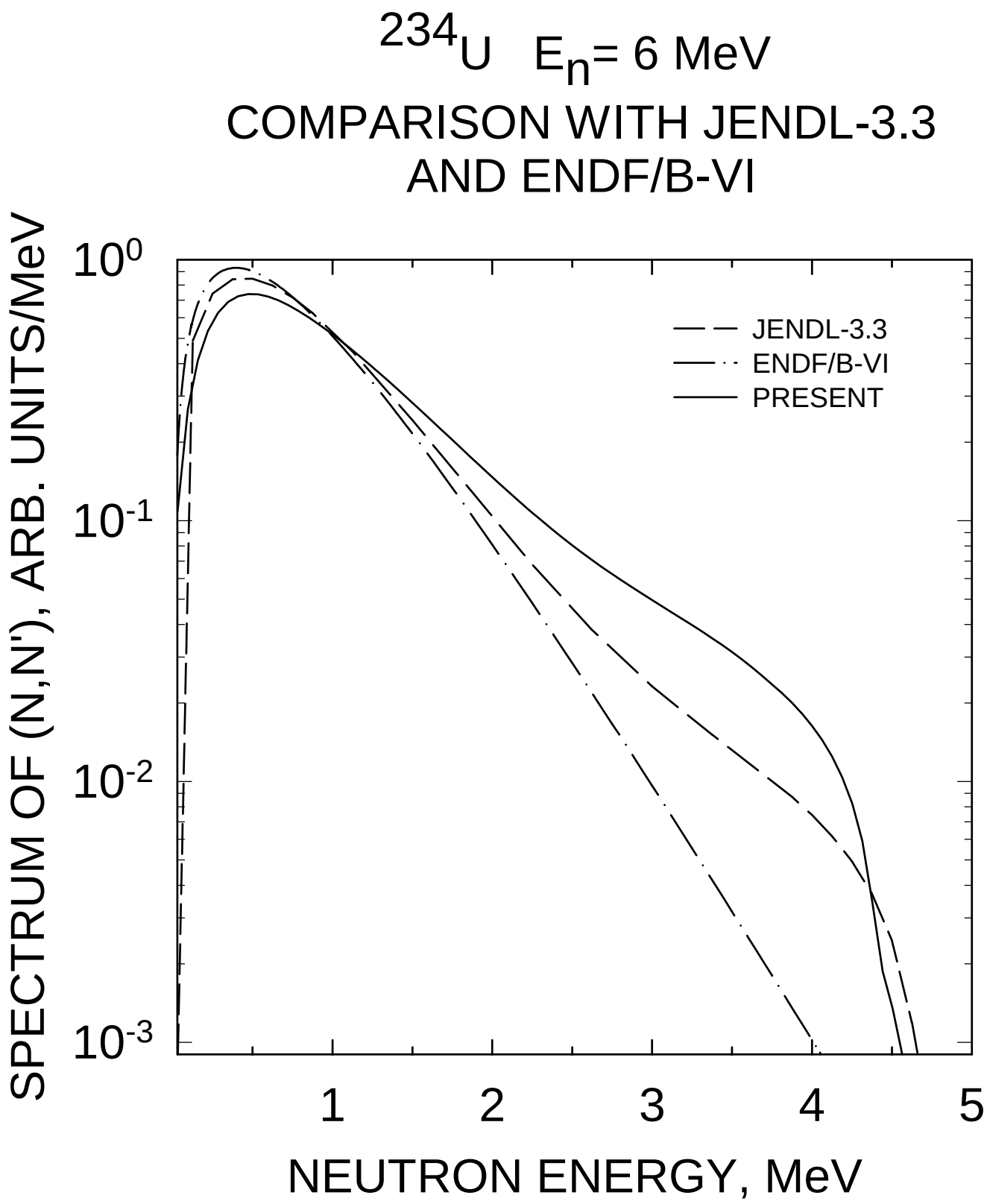
^{234}U E_n= 6 MeV
COMPARISON WITH JENDL-3.3
AND ENDF/B-VI
SPECTRUM OF (N,N'), ARB. UNITS/MeV
10^0
10^{-1}
10^{-2}
10^{-3}
JENDL-3.3
ENDF/B-VI
PRESENT
1
2
3
4
5
NEUTRON ENERGY, MeV

FIG. 85

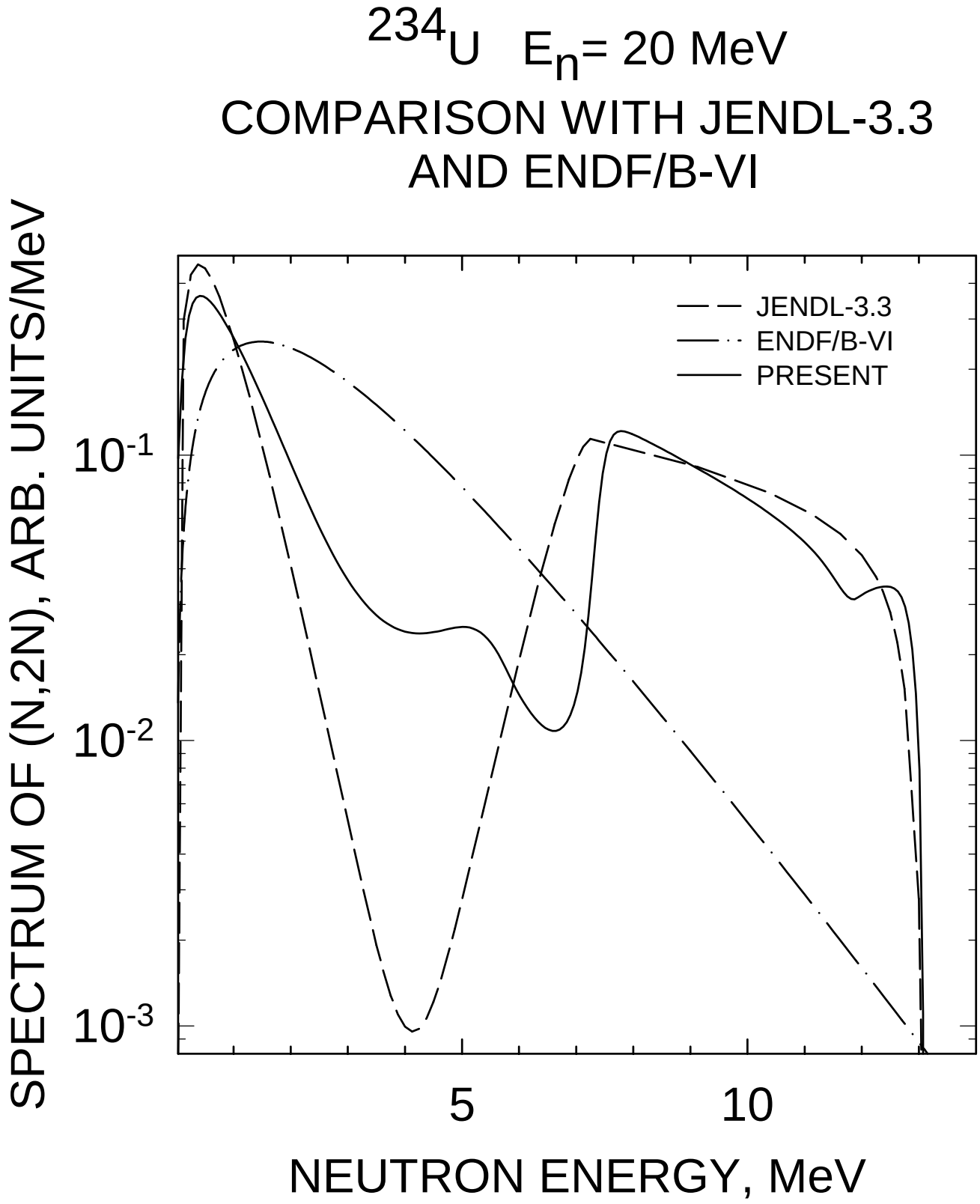
^{234}U E_n= 20 MeV
COMPARISON WITH JENDL-3.3
AND ENDF/B-VI
JENDL-3.3
ENDF/B-VI
PRESENT
SPECTRUM OF (N,2N), ARB. UNITS/MeV
10^{-1}
10^{-2}
10^{-3}
5
10
NEUTRON ENERGY, MeV

FIG. 86

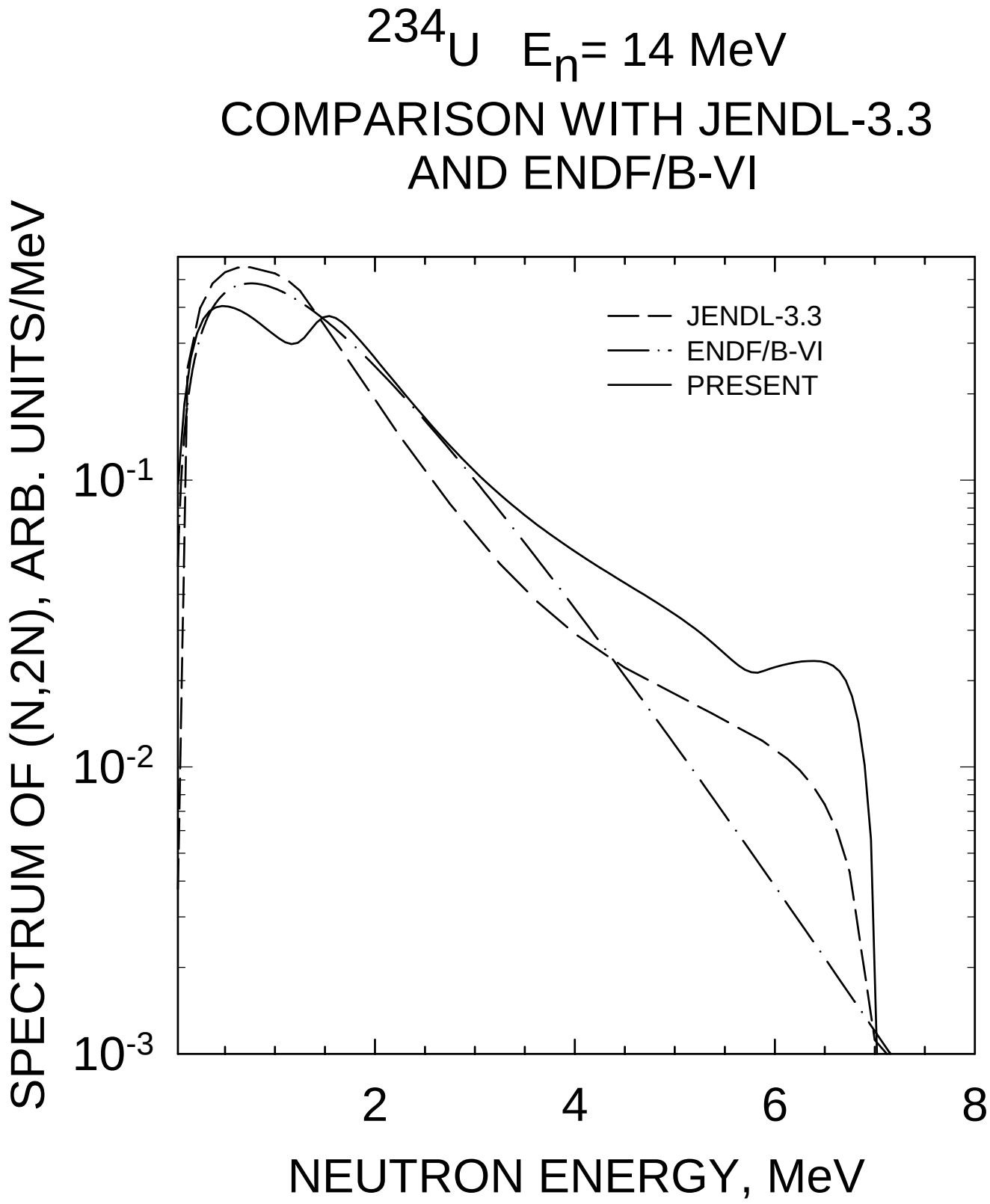
^{234}U E_n= 14 MeV
COMPARISON WITH JENDL-3.3
AND ENDF/B-VI
SPECTRUM OF (N,2N), ARB. UNITS/MeV
JENDL-3.3
ENDF/B-VI
PRESENT
10^{-1}
10^{-2}
10^{-3}
2
4
6
8
NEUTRON ENERGY, MeV

FIG. 87

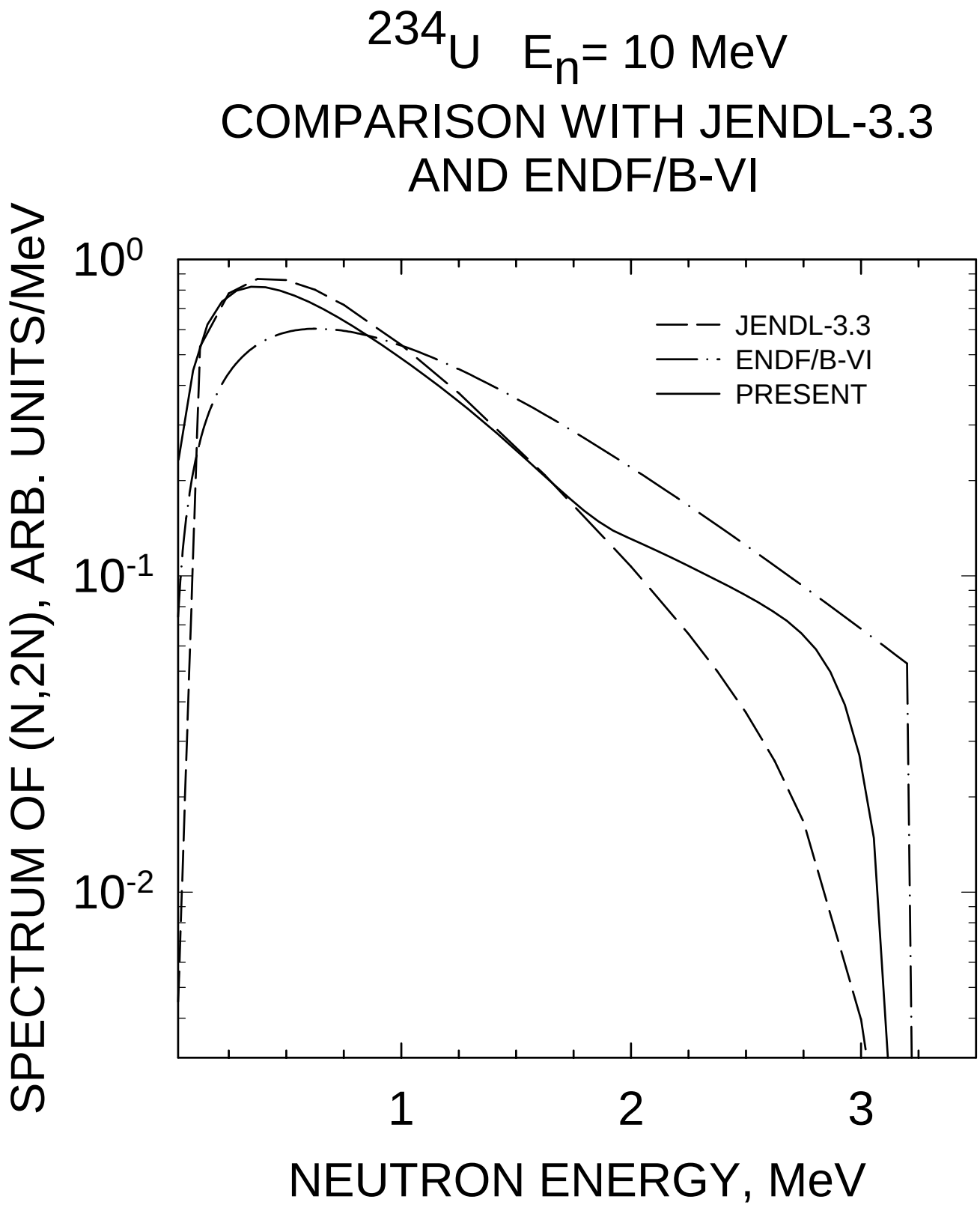
^{234}U E_n= 10 MeV
COMPARISON WITH JENDL-3.3
AND ENDF/B-VI
SPECTRUM OF (N,2N), ARB. UNITS/MeV
10^0
10^{-1}
10^{-2}
JENDL-3.3
ENDF/B-VI
PRESENT
1
2
3
NEUTRON ENERGY, MeV

FIG. 88

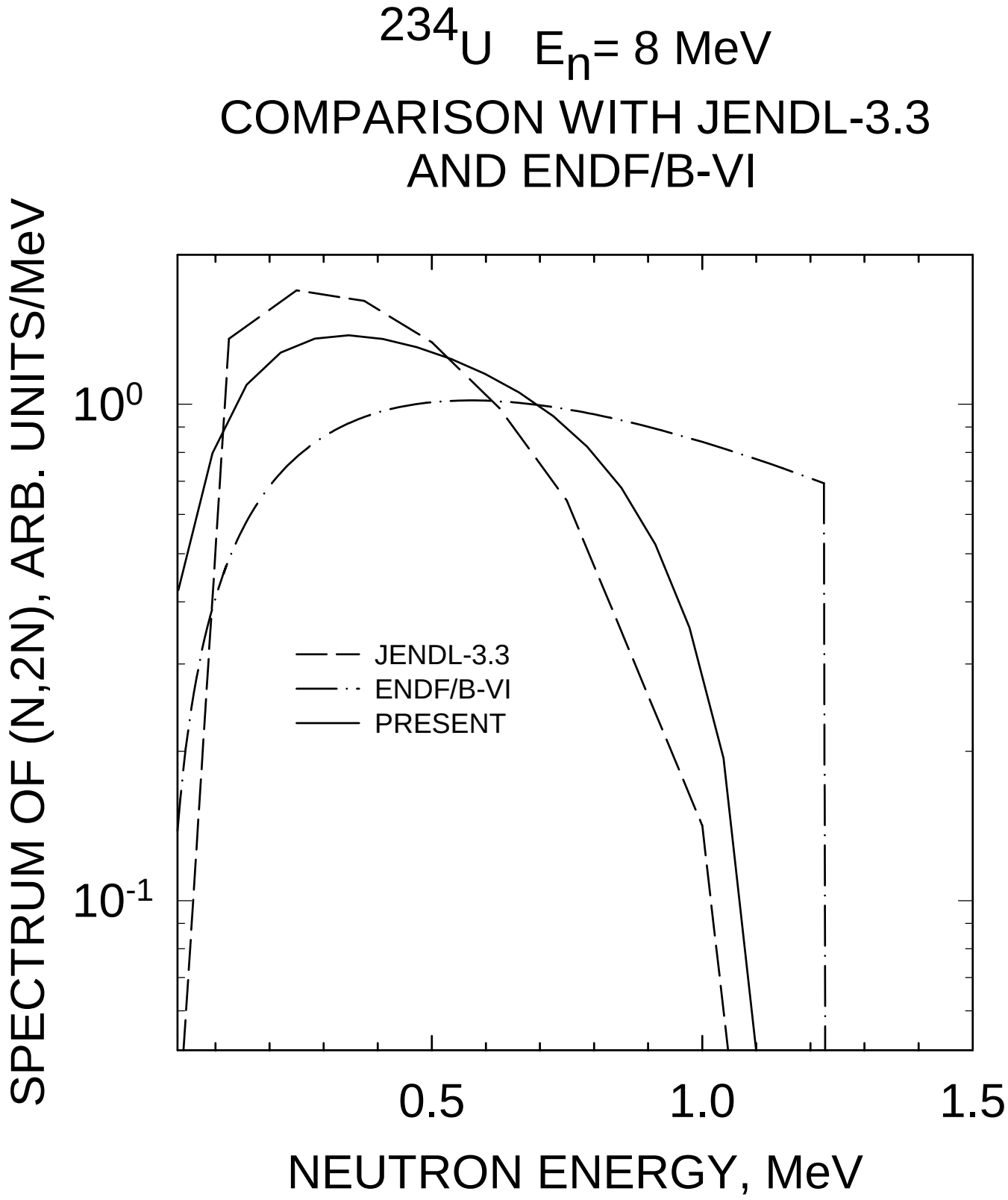
^{234}U E_n= 8 MeV
COMPARISON WITH JENDL-3.3
AND ENDF/B-VI
SPECTRUM OF (N,2N), ARB. UNITS/MeV
10^0
10^{-1}
JENDL-3.3
ENDF/B-VI
PRESENT
0.5
1.0
1.5
NEUTRON ENERGY, MeV

FIG. 89

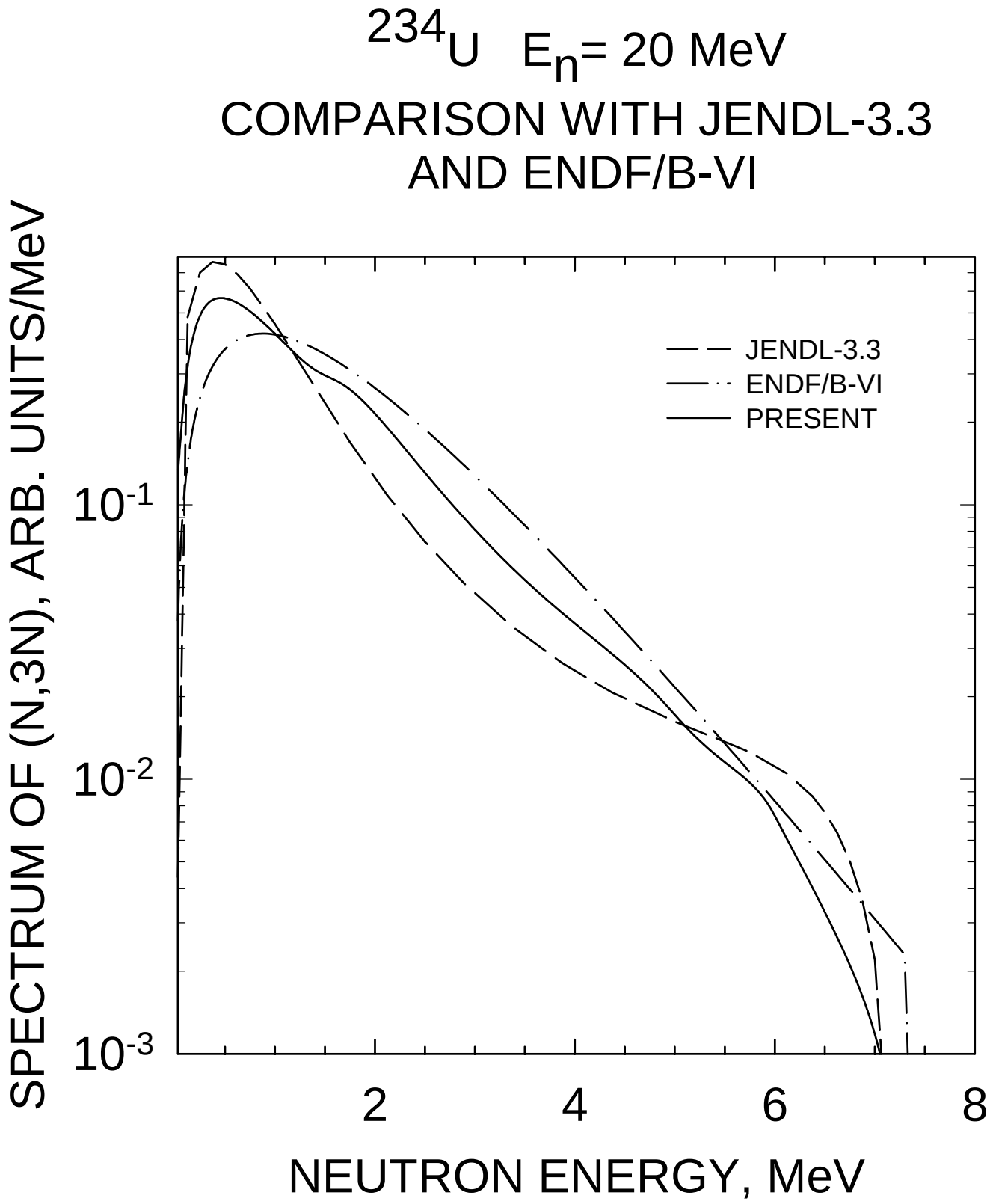
^{234}U E_n= 20 MeV
COMPARISON WITH JENDL-3.3
AND ENDF/B-VI
SPECTRUM OF (N,3N), ARB. UNITS/MeV
10^{-1}
10^{-2}
10^{-3}
JENDL-3.3
ENDF/B-VI
PRESENT
2
4
6
8
NEUTRON ENERGY, MeV

FIG. 90

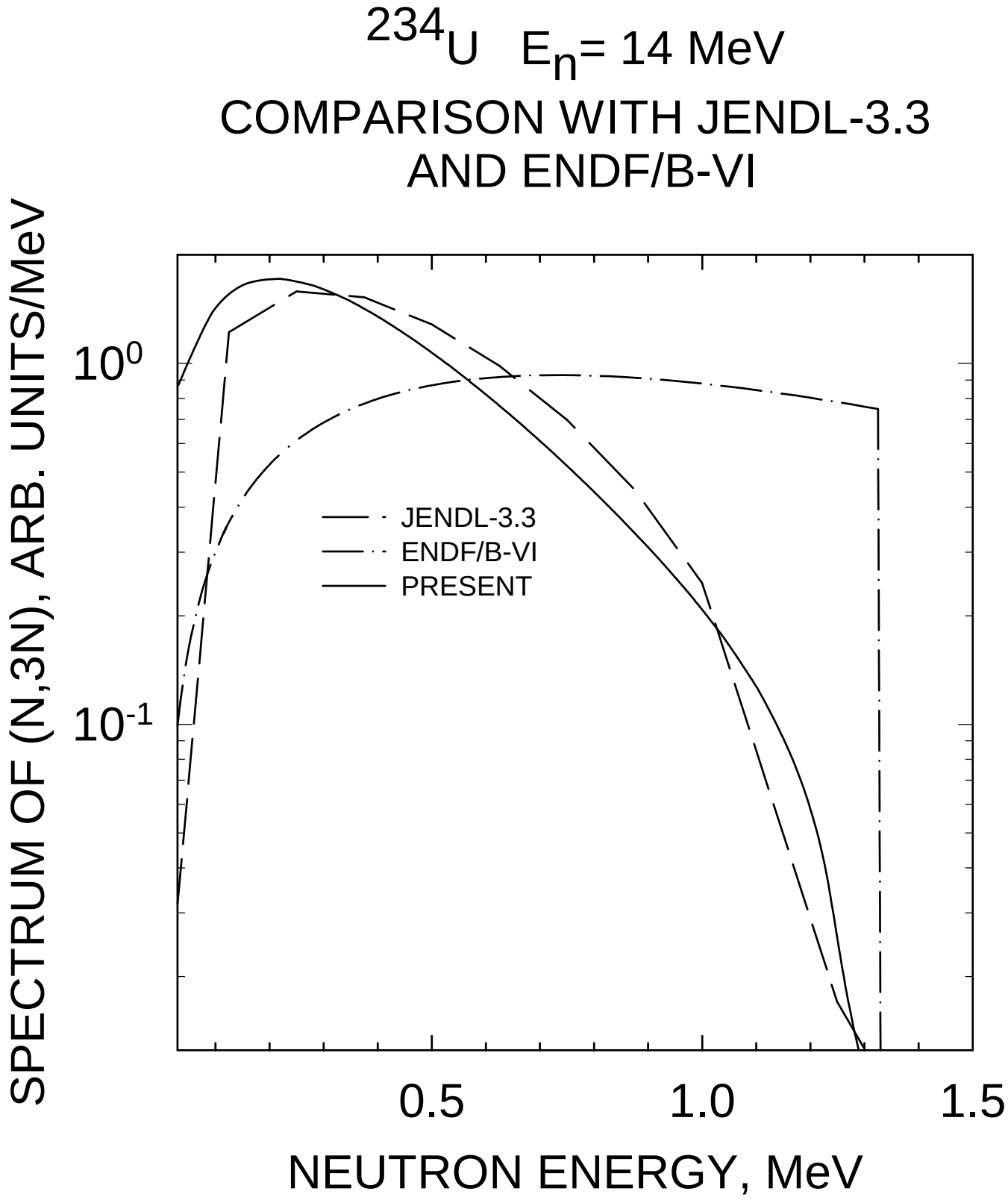
^{234}U E_n= 14 MeV
COMPARISON WITH JENDL-3.3
AND ENDF/B-VI
SPECTRUM OF (N,3N), ARB. UNITS/MeV
10^0
10^{-1}
JENDL-3.3
ENDF/B-VI
PRESENT
0.5
1.0
1.5
NEUTRON ENERGY, MeV

FIG. 91

Nuclear Data Section
International Atomic Energy Agency
P.O. Box 100
A-1400 Vienna
Austria

e-mail: services@iaeand.iaea.org
fax: (43-1) 26007
cable: INATOM VIENNA
telex: 1-12645
telephone: (43-1) 2600-21710

Online: TELNET or FTP: iaeand.iaea.org
username: IAEANDS for interactive Nuclear Data Information System
usernames: ANONYMOUS for FTP file transfer;
FENDL2 for FTP file transfer of FENDL-2.0;
RIPL for FTP file transfer of RIPL;
NDSONL for FTP access to files saved in "NDIS" Telnet session.
Web: http://www-nds.iaea.org